ABSTRACT

Title of dissertation: A COMPREHENSIVE STUDY OF THE
                           OUTSKIRTS OF GALAXY CLUSTERS
                           USING *SUZAKU*

                           Jithin Varghese George
                           Doctor of Philosophy, 2014

Dissertation directed by: Professor Richard Mushotzky
                            Department of Astronomy

Galaxy clusters, which contain up to tens of thousands of galaxies and which

are the largest virialized structures in the universe, serve as unique probes of cos-

mology. Most of their baryonic mass is in the form of hot gas that emits X-rays

via thermal bremsstrahlung radiation. The study of this emission from the outer,

least-relaxed portions of clusters yields valuable information about the hierarchical

assembly of large scale structure. In this thesis, we report on our X-ray analysis of

the outskirts of four clusters.

For this purpose, we *Suzaku* data, which is well-suited to the study of the

outsides of clusters. Accurate parameter estimates require reliable data and proper

analysis, so we focus on the 0.7–7.0 keV range because other studies have shown

that energies below or above this range are less reliable.

A key component of our analysis is our careful modeling of the background

emission as a thermal component plus a power law contribution. Our power law

model uses a fixed slope of 1.4, which is consistent with other clusters. We constrain

our thermal background component by fitting it to *ROSAT* data over the energy range 0.3–2.0 keV.

Using this method, we extract the temperature, density, and surface brightness from the *Suzaku* data. These parameters are somewhat different from the values obtained using *XMM-Newton* data but are consistent with other measurements using *Suzaku*. We then deprojected these quantities to estimate the total mass, entropy, pressure, and baryonic fraction. We find an entropy that is consistent with the previously suggested 'universal' entropy profile, but our pressure deviates from the 'universal' profile. We discuss some possible reasons for this discrepancy.

Consistent with previous observations but in contrast to what is expected from simulations, we infer that the outer parts of the clusters we study have baryon fractions in excess of the cosmic fraction. We suggest some explanations for this, focusing on clumping as a possibility. We then finish by discussing the role of our observations in cluster physics studies and by enumerating other avenues of exploration to attain a more complete picture of galaxy clusters.

A COMPREHENSIVE STUDY OF THE OUTSKIRTS OF GALAXY CLUSTERS USING *SUZAKU*

by

Jithin Varghese George

Dissertation submitted to the Faculty of the Graduate School of the
University of Maryland, College Park in partial fulfillment
of the requirements for the degree of
Doctor of Philosophy
2014

Advisory Committee:
Professor Richard Mushotzky, Chair/Advisor
Professor Chris Reynolds
Professor Coleman Miller
Dr. Eric Miller
Professor Robert Hudson (Dean's Representative)

Preface

The Suzaku data was obtained as part of the *Suzaku* Project titled "The Outer Limits of Rich Clusters: *Suzaku* Observations to r_{200}". The work presented here was done in close collaboration with the PI of this project, Dr. Eric Miller.

To science, to my family and to my friends.

Acknowledgments

It has been a wonderful ride these past few years, and there are countless people who have made it both fruitful and enjoyable.

First and foremost, I would like to thank my advisor Dr. Richard Mushotzky. He took a chance bringing me into his group and the experience for me has been life-altering. His constant prodding on ways to improve myself and my science have made me a better scientist and has made me produce fruit in the form of this thesis. He also helped provide opportunities to travel for the sake of science which were wonderful adventures.

Next I would like to thank Dr. Eric Miller, who has been my personal sounding board for all my science ideas and whose input has been invaluable in extracting the proper science. Dr. Mark Bautz is another person who has been critical to my research by providing timely comments and the all-important funding to continue research. I would also like to specifically mention Dr. Coleman Miller (or Lord Miller as he likes to be called). Thank you for the wonderful conversations over the years and the sharp elbows during basketball. To Dr. Alberto Bolatto and Dr. Derek Richardson: your timely chats about science, coding, 'mojo' and video games were very entertaining. Special thanks to my committee for taking the time out of their busy schedules.

The department of Astronomy has been a great place to work and I have made some lifelong friendships here. First I would like to thank all the faculty and administrative staff here. As an international student, I am sure I have been the

Table of Contents

List of Tables

List of Figures

ix

Chapter 1:   Introduction

Galaxy clusters are very important cosmological probes [Allen et al., 2011] because their size and total mass are very sensitive to cosmological parameters. These objects also present a unique opportunity of study as they are small enough to be mostly relaxed and in hydrostatic equilibrium [Sarazin, 1988] while also being massive. Thus clusters help to place constraints on structure formation since they can be observed out to high redshifts.

Clusters are the largest and most massive gravitationally bound systems and represent the location of peaks in the large scale matter density [Allen et al., 2011]. They consist of thousands of galaxies in a region of radius $\sim$2 Mpc, and total cluster masses range from 10^{14} to 10^{15} $M_\odot$. A cluster's mass is comprised of dark matter, the galaxies it contains as well as very hot intracluster gas ($T > 10^6$ K). The dominant component of galaxy clusters is dark matter: baryonic matter represents only about 15–25% of the total mass of the cluster [Vikhlinin et al., 2006]; however, the intracluster gas constitutes more of the cluster's baryonic mass than all of the cluster's galaxies combined and therefore radiation from the gas is a galaxy cluster's primary observable. The free electrons in the hot plasma are accelerated by encounters with heavier ions, resulting in thermal bremsstrahlung radiation. Because the

gas is so hot, this radiation emits primarily at very high energies and necessitates observations with X-ray satellites.

Previous studies of galaxy clusters have focused on the interior of galaxy clusters [Sarazin, 1986, Snowden et al., 2008], but in order to use clusters to probe larger cosmological questions, it is also necessary to understand the outskirts of clusters. The physics in cluster outskirts is governed primarily by cosmological processes and conditions. This thesis begins to characterize the heretofore poorly understood outskirts of galaxy clusters.

1.1   Cluster Outskirts

Observations of the outskirts of galaxy clusters offer insight into a more complete understanding of clusters and also provide the best view of the accretion processes onto the cluster and of large-scale structure formation in the early universe. These studies can help answer vital questions of how clusters grow and what the properties of accreting material are. Observations of these regions also probe areas where hydrostatic equilibrium begins to break down in the hot gas, thus enabling the study of accreting matter as it becomes virialized [Allen et al., 2011]. These cluster outskirts also contain plasma in exotic conditions: some of the lowest densities, highest entropies and longest electron-ion equilibration timescales ever measured. Typically these are regions beyond the virialization radius of the cluster. The virialization radius corresponds to $\sim r_{200}$, the radius at which the average density of the cluster enclosed is 200 times the critical density of the universe. To date, most

2

cluster studies have been limited to observations well within r_{200}, usually only extending to r_{500} (the radius at which the average density of the cluster enclosed is 500 times the critical density of the universe).

1.2 Entropy Deficit at Large Radii

The entropy profile of clusters has generated much interest because it determines the structure of the intra-cluster medium (hereafter ICM) and provides a record of the ICM's thermodynamic history. When the heated gas expands in a gravitational potential, its thermal energy can be converted into gravitational potential energy [Walker et al., 2012a]. This introduction of heat will cause the entropy to increase, while radiative cooling will cause the entropy to decrease.

Assuming a polytropic equation of state: $P(r) = K(r) \cdot n_e(r)^{5/3}$ for the cluster, the ideal gas equation yields a functional form for the entropy, $K(r)$. By defintion, the pressure in a cluster is calculated as:

$$P(r) = n_e(r)kT(r)$$

$$K(r) \cdot n_e^{5/3} = n_e(r)kT(r) \tag{1.1}$$

$$K(r) = kT(r)n_e(r)^{-2/3}$$

A simple yet realistic model for the density is the beta model with a value of $\beta = 2/3$ [Sarazin, 1988]:

$$n_e = n_0 \cdot \left(1 + \frac{r}{r_c}\right)^{-3\frac{\beta}{2}} \text{ (if } \beta = 2/3) \implies n_e = \frac{n_0}{1 + \left(\frac{r}{r_c}\right)^2} \tag{1.2}$$

Combining equations 1.1 and 1.2, the entropy profile for the simplest isothermal case reduces to a simple power law of the form $K(r) \propto r^{4/3}$.

Tozzi and Norman [2001] analytically modeled the entropy assuming a Navarro-Frenk White model for the density and temperature profiles. They presented theoretical studies of clusters of galaxies for the shock-dominated regime assuming a constant and homogeneous initial entropy in the external galactic medium. They find that for the shock-dominated regime, the slope of the derived entropy profile is independent of the initial value and follows:

$$\frac{d\ln(K)}{d\ln r} \simeq 1.1 \implies K \propto r^{1.1} \qquad (1.3)$$

which is similar to the isothermal case presented in equation 1.1

This work was followed up by simulations in Voit et al. [2005] using two differently simulated clusters. They were able to empirically fit these simulated clusters to the above power law and extracted the relationship:

$$\frac{K}{K_{200}} = 1.32 \cdot \left(\frac{r}{r_{200}}\right)^{1.1} \qquad (1.4)$$

for the regime $r > 0.2r_{200}$. For $r < 0.2r_{200}$, both simulations and observations find an excess of entropy when compared to the $r^{1.1}$ behavior. This central excess has been attributed to central heating caused by non-gravitational sources like AGN feedback. The few studies of well measured systems which have included cluster outskirts have also shown similar deviations from this baseline entropy profile [Walker et al., 2012a] (Figure 1.1).

Walker et al. [2012a] also observed another deviation from the baseline model: a flattening in the entropy profile at large radii. This flattening entropy profile can be attributed to several possible processes. Hoshino et al. [2010] cites the difference between the electron and ion temperatures inside the accretion shock as a possible
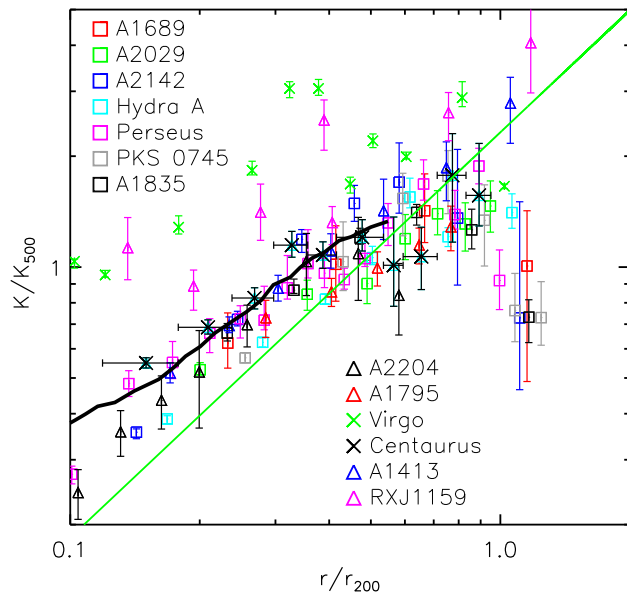
Figure 1.1: Entropy profiles of clusters outskirts explored with *Suzaku, XMM-Newton* and *Chandra*. The scaled radius r/r_{200} plotted over the scaled entropy K/K_{500}(refer Section 4.3.1.1). The solid green line shows the baseline entropy profile from Voit et al. [2005] The black line shows the median entropy profile from the REXCESS cluster sample in Pratt et al. [2010]. (From Walker et al. [2012a])

reason for this deviation. The temperature differential could arise because the heavier ions get thermalized immediately after the accretion shock whereas the much lighter electrons take longer to thermalize [Rudd and Nagai, 2009]. However, the inefficient transfer of energy to electrons through electron-ion collisions could also cause a similar separation in temperatures.

Another possible explanation for the flattening entropy profile is that the propagating accretion shock strength weakened as the cluster became older and more relaxed [Cavaliere et al., 2011]. As cosmological structure growth slows down at later

cosmic times, the accreting gas encounters a smaller potential drop as the accretion shock expands outwards. This weakening reduces the gain in entropy at the shock with the added effect of increasing the amount of energy passing across the shock [Lapi et al., 2010].

There is also the possibility of some of the accretion energy going into turbulence or cosmic ray acceleration as opposed to purely gravitational mechanisms, thus causing the entropy deficit. As an after effect of the increased energy passing through the shock, there will be an increase in the turbulence and non-thermal pressure support in the outskirts, causing deviations from hydrostatic equilibrium [Lau et al., 2009].

Finally, clumping in the outskirts of these clusters could also explain the observed deviation in the entropy profile. Assuming hierarchical formation, we expect to find structures like groups or galaxies at the very outer edges of clusters. These structures are sufficiently large that they have enough gravitational binding energy to be held together while being accreted onto the larger cluster. Such structures would not be immediately visible because of the surrounding cluster material, but would cause the gas density to be overestimated, thus causing the entropy to be underestimated [Nagai and Lau, 2011]. This phenomenon is expected to be most significant around r_{200}, beyond which we expect to see unvirialized cluster matter.

1.3 Baryonic Gas Fraction

In the study of cluster outskirts, another important goal is to ascertain the boundary between the virialized cluster and infalling material, beyond which any assumptions of hydrostatic equilibrium break down. Beyond this boundary, we should detect inhomogeneities in the ICM, specifically clumps or other such signatures of accretion.

The baryonic fraction – the ratio of the gas mass enclosed to the total mass enclosed within a particular radius – is a valuable cosmological probe to determine this boundary. Assuming hierarchical structure formation and the large size of clusters, the matter contained in clusters must have been accreted from regions which are now 8–40 co-moving Mpc [Takizawa and Mineshige, 1998]. Because it is so large, this region of accretion matter is a good sample of the mean matter content of the universe. The large masses of clusters ensure that clusters have enough gravitational binding energy to retain their gas over time. Additionally, there is no observed separation of the baryons and the dark matter over such large scales of several megaparsecs for relaxed clusters [Takizawa and Mineshige, 1998]. Thus, it is expected that clusters will have the same baryonic fraction as the one they began with: the cosmic baryonic fraction.

However, Simionescu et al. [2012] finds that for the *Perseus* cluster, the baryonic fraction increases to a much larger value than the cosmic baryonic fraction in the very outskirts of the cluster (Figure 1.2). This adds further evidence to the possibility of clumping in the outskirts, as clumping would bias the results of the

density observed, causing the cluster's gas mass calculation to be biased towards larger values.

1.4   Previous Cluster Outskirts Work

In spite of the scintillating science on cluster outskirts awaiting study, these regions have not been studied extensively. Until very recently, only up to the inner $\sim 10\%$ of a cluster's volume has been well studied [Reiprich et al., 2013] because obtaining robust observations and simulations is challenging in this regime. But advances in observation methods and theoretical techniques are quickly opening opportunities for deeper outskirts observations.

The surface brightness is the easiest quantity to characterize for clusters and, because it is directly related to density, is rich in physical information. The *ROSAT* Position Sensitive Proportional Counters (PSPC) has been heavily utilized for analyzing cluster surface brightness profiles due to its large field of view and low instrumental background [Vikhlinin et al., 1999]. A simple β-model was found to fit the surface brightness profile out to r_{180} with $\beta =$0.65–0.85 [Vikhlinin et al., 1999, Neumann, 2005]. The Chandra instrument has also been utilized to extract surface brightness profiles for regions $r > r_{500}$ yielding results similar to the ROSAT results [Roncarelli et al., 2006, Nagai and Lau, 2011]. The possible existence of density inhomogeneities in the outskirts of a large cluster sample was recently studied using the *ROSAT* instrument. Eckert et al. [2012] observes a steepening of the density profiles beyond $\sim r_{500}$, which can be modeled by accounting for gas clumping.
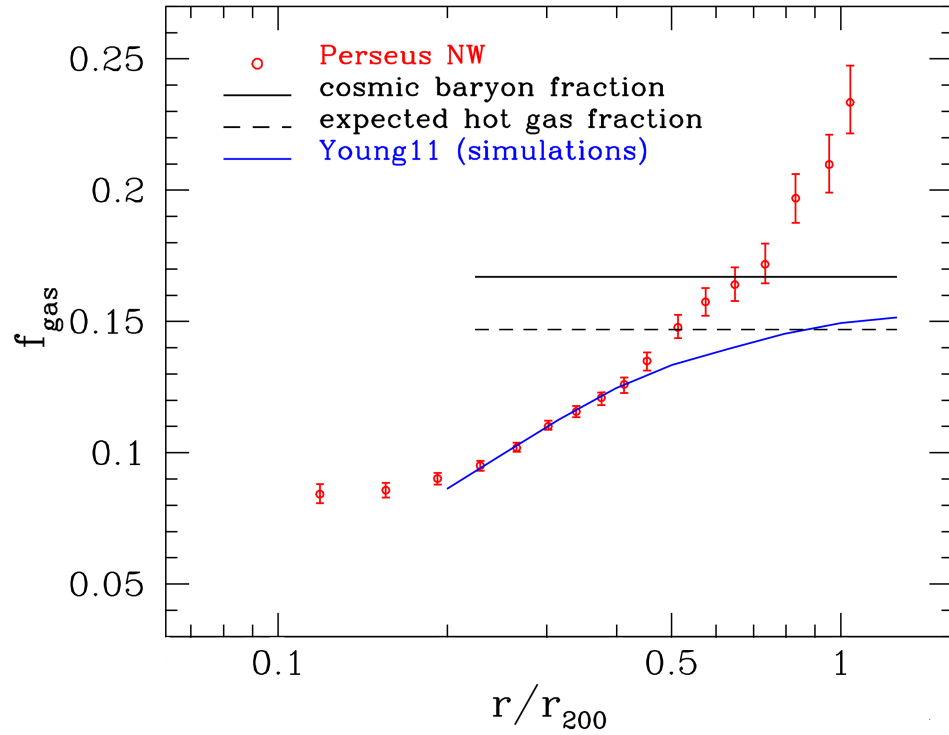
Figure 1.2: The integrated, enclosed gas mass fraction profile for the NW arm of the *Perseus* cluster. The cosmic baryonic fraction from WMAP values is indicated by the horizontal solid black line; accounting for 12% of the baryons being in stars gives the expected fraction of baryons in the hot gas phase, shown as a dashed black line. Predictions from numerical simulations are shown in blue.(From Simionescu et al. [2012])

Temperature measurements of the cluster outskirts are much harder to obtain because of large PSFs and high instrumental backgrounds. There have been temperature measurements of the outskirts using the *ASCA* instrument [Markevitch et al., 1998] and the *BeppoSAX* instrument [Irwin and Bregman, 2000] in spite of the poor, energy dependent point spread function. But for both *XMM-Newton* and *Chandra* which have much sharper PSFs, their high particle backgrounds prevent robust measurements of the temperature at the outskirts [Snowden et al., 2008, Allen et al., 2001].

XMM-Newton observations of the REXCESS sample, which is a representative sample of nearby clusters, suggest that the scaled pressure distribution follows a universal form [Pratt et al., 2009] suggested by simulations [Nagai et al., 2007a]. The *Planck* satellite has also made a similar observation [Planck Collaboration et al., 2013a] using the Sunyaev-Zeldovich effect. These studies combined suggest that such a profile exists up to $r > 3r_{500}$.

The baryonic gas fraction has been studied using the *ROSAT* PSPC as it was suitable for measuring gas density profiles out to the outskirts [Eckert et al., 2012]. Reiprich [2001] performed a study of about 58 *ROSAT* clusters and observed baryonic fraction values larger than expected in $\sim 10\%$ of the clusters.

1.5 Previous *Suzaku* Observations of Cluster Outskirts

Several of the observational issues mentioned in section 1.4 can be improved upon by using the *Suzaku* instrument. There have already been several studies of

galaxy clusters using the *Suzaku* instrument. Cluster PKS0745-191 [George et al., 2009, Walker et al., 2012b] exhibits a decrease in temperature by roughly 70% out to r_{200}. This cluster also exhibits a flattening of the entropy profile at large radii. Reiprich et al. [2009] was able to determine the temperature profile from the center out to r_{200} for Abell 2204 in high detail.

In the case of Abell 1795, Bautz et al. [2009] was able to use high resolution *Suzaku* data to extract temperature, density, entropy and pressure profiles. They observed a rapidly declining temperature profile and evidence for a deviation from hydrostatic equilibrium at radii as small as r_{500}. Hoshino et al. [2010] extends the previous measurements with *Chandra* and *XMM-Newton* for Abell 1413 using Suzaku data. They notice an entropy flattening at around 0.5 r_{200} and a temperature drop to about 3 keV around the virial radius.

Abell 1689 shows anistropic gas temperature and entropy distributions in the cluster outskirts. In the north-eastern outskirts, Kawaharada et al. [2010] find an excess of temperature and entropy which is attributed to an overdense filamentary structure. Deviations from hydrostatic equilibrium are only seen in the outskirts regions with low density voids. Abell 2142 [Akamatsu et al., 2011] also has a temperature drop in the profile and entropy flattening beyond 0.4 r_{200}.

The entropy flattening at the outskirts is confirmed for the cluster Hydra A [Sato et al., 2012] beyond r_{500}. They also notice that the ratio of the gas mass to hydrostatic mass (baryonic fraction) exceed the WMAP results by a large value and attribute this to a breakdown in hydrostatic equilibrium. Walker et al. [2012c] suggest that the assumptions for spherical symmetry and hydrostatic equilibrium are

responsible for the discrepant flattening in the entropy profile and the temperature anisotropies observed in Abell 2029.

Using high quality *Suzaku* data, Simionescu et al. [2012] discovered that the baryonic fraction exceeds the cosmic mean at large radii for the *Perseus* cluster, suggesting a clumpy distribution of gas. Entropy flattening is observed for the *Centaurus* cluster and an excess in the pressure in the outskirts which could be the result of an excess in the measured gas density possibly due to clumping [Walker et al., 2013]. Walker et al. [2013] find that the gas mass fraction does not exceed the mean cosmic baryonic fraction and that there is increased entropy in the central regions.

Simionescu et al. [2013] used a large mosaic of *Suzaku* observations of the *Coma* cluster to study cluster properties. The azimuthally averaged temperature profiles, the deprojected density, and the pressure profile all show the sharp drop in the values expected due to an outward propagating shock. There is no entropy flattening seen at high radii but the central excess is still observed here as well. The pressure profile observed is also consistent with the 'universal' pressure profile obtained using the *Planck* satellite. Finally, *Suzaku* data was used to study the fossil group RXJ 1159+5531 [Humphrey et al., 2012]. They find no evidence of flattening of the entropy profile or an excess of baryonic fraction in the outskirts, which is in sharp contrast to previous results.

There are currently several studies of other clusters trying to map out the baryonic gas fraction profiles to study whether *Perseus* is a unique cluster or whether there are other such anomalies [Gonzalez et al., 2013, Dai et al., 2010].

In this work, we will study the existing conditions of the ICM around r_{200} by extracting a variety of parameters from the *Suzaku* data beginning with the primary parameters of temperature, abundance, surface brightness and density; and then further on to secondary parameters like pressure, entropy, total mass and the baryonic fraction. We will compare these secondary parameter profiles to the theoretical 'universal' profiles for these parameters. This will give us clues about the viability of clumping as a possible explanation for the entropy flattening seen in the other clusters.

Chapter 2:   Data

2.1   *Suzaku* and `XIS` detectors

Suzaku is a Japanese satellite that conducts various observational studies for a wide variety of X-ray sources with higher energy resolution and a higher sensitivity over a wider energy range (from 0.3 to 600 keV) than other currently available X-ray satellites. The satellite carries five soft X-ray instruments and one hard X-ray instrument [Koyama et al., 2007]. For our purposes, we used the on-board X-Ray Imaging Spectrometer (`XIS`) instrument which is utilized for imaging and spectroscopy. The `XIS` instrument covers an energy range of 0.4-10 keV with a typical energy resolution of 60 eV to 200 eV; the exact resolution is dependent on the observation date (due to variation in contamination) and the energy regime. It consists of four X-Ray CCD cameras (`XIS`0-3), three of them front-illuminated and one back-illuminated. One of the front illuminated CCDs, `XIS`2 has seen heavy micro-meteorite damage and has become unusable since November 9, 2009 . For this reason, in two of the clusters only the other three CCD cameras were used for this thesis.

2.2 Sample Selection

For the study of cluster outskirts, the *Suzaku* satellite is the optimal choice. *Suzaku* has a low and stable background which, coupled with the large effective area, enables the observation of clusters out to the far outskirts. For a complete picture of the outskirts, we undertook a comprehensive program to observe a sample of twelve clusters in 2010 using *Suzaku*. These clusters are a subset of the sample of clusters observed in Snowden et al. [2008] which exhibit a variety of temperature profiles in the outer regions of the cluster (falling, flat, rising) and which also have high quality *XMM-Newton* data. The sample was also restricted to ensure that the clusters appeared relaxed in the *XMM-Newton* images. The Snowden et al. [2008] sample was selected empirically, by comparing *ROSAT* images for available *XMM-Newton* archival data. Clusters with 'reasonable' extent and brightness were included in the sample.

To maximize the efficiency of the observation, the sample was further confined to clusters with $r_{200} \lesssim 16'$ where $r_{200} = 2.77(1+z)^{-3/2}(kT_x/10 \ keV)^{1/2}h_{70}^{-1}$ Mpc assuming kT, the average temperature of the cluster. This ensures that the chosen cluster can be observed to a sufficient area beyond r_{200} for accurate background estimation. This analytic formulation of r_{200} was derived using the mass-temperature relationship explored in Henry et al. [2009], defined as:

$$0.7 \ E(z) \ h_{70} \ M_{500} = A_{MT} \ (kT)^{\alpha_{MT}} \tag{2.1}$$

where h_{70} is the present value of the Hubble parameter in units of 70 km s^{-1} Mpc^{-1},

$E(z) = \sqrt{\Omega_M(1+z)^3 + \Omega_\Lambda}$ for a redshift z, M_{500} is the total mass enclosed within r_{500}, and A_{MT} and α_{MT} refer to the normalization and the index of the power law used to characterize this mass-temperature relation. Starting from the definition of M_{200} (the total mass enclosed within a radius of r_{200} from the center of the cluster) and $\rho_{crit}(z) = \frac{3H_0 E(z)^2}{8\pi G}$, the critical density of the universe at the redshift z:

$$
\begin{aligned}
M_{200} &= \frac{4}{3}\pi r_{200}^3 \cdot 200\rho_{crit} \\
r_{200}^3 &= \left(\frac{15}{8\pi}\right) \cdot M_{200} \cdot \left(\frac{1}{500 \cdot \rho_{crit}}\right) \\
&= \left(\frac{15}{8\pi}\right)\left(\frac{M_{200}}{M_{500}}\right)\left(\frac{A_{MT}(kT)^{\alpha_{MT}}}{500 \cdot \rho_{crit} \cdot 0.7E(z)h_{70}}\right)
\end{aligned}
\tag{2.2}
$$

For the typical values of the parameters, $M_{200}/M_{500}=1.479$ (assuming a NFW profile for density), $\alpha_{MT} = 3/2$ and $A_{MT} = 10^{-3/2} \cdot 10^{15}$, equation 2.2 reduces to:

$$
r_{200} = 2.77(1+z)^{-3/2}(kT_x/10 \text{ keV})^{1/2}h_{70}^{-1} \text{ Mpc}
\tag{2.3}
$$

The large *Suzaku* point spread function (PSF) can cause X-rays from bright sources to scatter to large radii. Because of this, a few clusters had to be removed from the sample as they were either too compact or too centrally bright, causing scattered light to dominate cluster emission in the r_{500}–r_{200} region. Some of the remaining clusters already have archival data with sufficient exposure and the proper pointing to accurately determine the temperature and density profiles at the largest radii. Abell 1413 and Abell 2204 already had single offset pointings, which are supplemented with three additional pointings to provide the full azimuthal coverage.

As unresolved point sources in *Suzaku* data are the main source of background uncertainty, it is necessary to identify as many point sources as possible. For that reason, we also proposed for side-by-side snapshot *Chandra* observations for the same
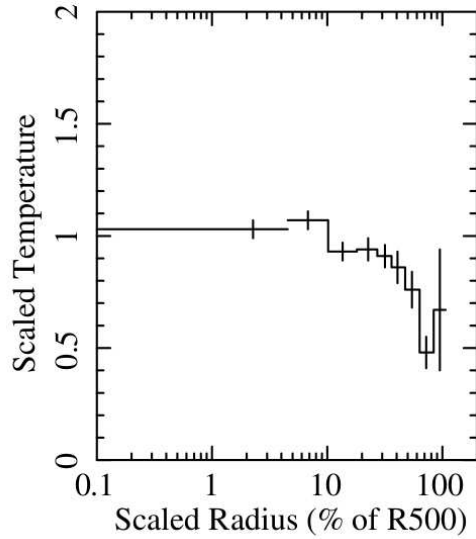
(a) Abell 1413
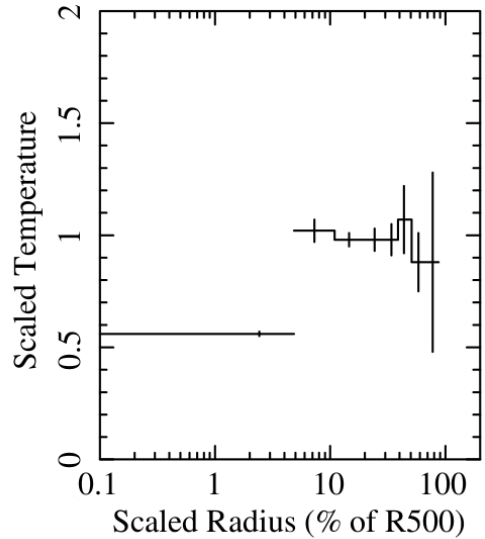
(b) Abell 2204
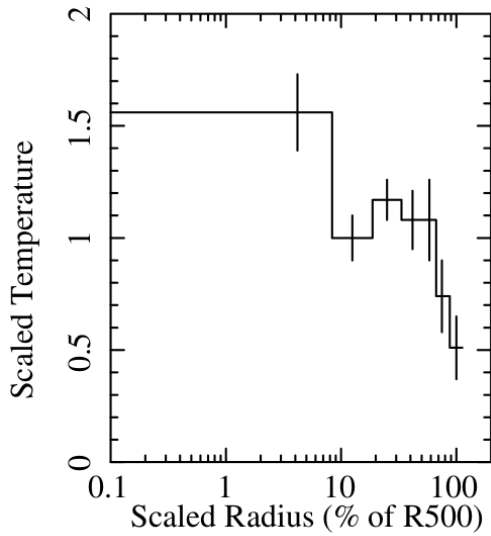
(c) Abell 773
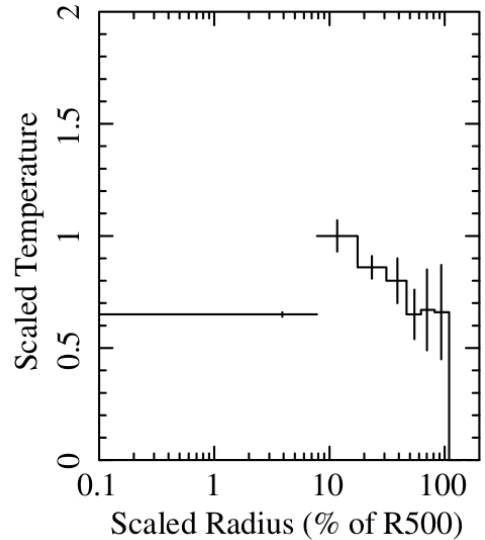
(d) Abell 383

Figure 2.1: *XMM-Newton* temperature profiles for Abell 1413, Abell 2204, Abell 773 and Abell 383 [Snowden et al., 2008]. Abell 1413 shows a rise in temperature beyond r_{500} while Abell 2204 shows a flat temperature profile out to r_{500}. Abell 773 and Abell 383 show the expected falling temperature profile at high radii.

Suzaku clusters to isolate the point sources for removal during analysis. Together, these data will help provide an accurate and comprehensive picture of these clusters. The clusters analyzed in this work are shown in Table 2.1, which is a subset of the larger sample of **twelve** clusters observed for the *Suzaku* outskirts project. These clusters were chosen to be a representative subset of the entire sample.

Cluster	z	r_{200}	t_{exp}
		(arcmin)	(ksec)
A1413	0.1427	14.8	170
A383	0.187	9.3	110
A2204	0.1523	11.8	140
A773	0.217	9.5	200

Table 2.1: The *Suzaku* Cluster Outskirts Project subsample: List of clusters, their redshifts z (from Snowden et al. [2008]), r_{200} (taken from literature) and the exposure time t_{exp}

While a major motivation for this sample is to study the non-axisymmetric nature of the cluster, the first step in the project is to verify the accuracy of our analysis method. And the best way to do so is to extract average profiles by assuming axisymmetry. By combining the multiple pointings, we are able to achieve greater signal-to-noise, enabling better comparisons to theoretical expectations and observed trends. This thesis focuses on this averaging step of the analysis. Once this has been achieved, the next step would be to study any non-axisymmetric effects.

2.3   Observations

Three of the clusters were observed in 2010: Abell 383 was observed in July 2010, Abell 1413 (Figure 2.2) was observed in May 2010 and Abell 2204 was observed in August 2010. The last one, Abell 773 was observed in May 2011. For Abell 1413, Abell 2204 and Abell 773, we had four overlapping pointings which together give a full view of the cluster. For Abell 1413 and Abell 2204, one of the pointings came from archival *Suzaku* data. For Abell 1413, we used an archival pointing of the northern region of the cluster observed in November 2005. The observation ID for the pointing is 800001010 and the analysis on this data set was published by Hoshino et al. [2010]. Similarily, for Abell 2204 we also utilized an archival pointing of the north-eastern region of the cluster observed in September 2006. The observation ID for the pointing is 801091010 and the analysis was published in Reiprich et al. [2009]. In the case of Abell 383, we only had three overlapping pointings but this is sufficient to cover the azimuthal range of the cluster.

We used the three detectors XIS 0, XIS 1 and XIS 3 for the analysis of all four clusters. For the case of Abell 1413 and Abell 2204, we include XIS 2 data for the two archival pointings. The XIS data was cleaned using the complete cleaning routine of aepipeline version 1.1.0. Both the 3×3 and 5×5 editing modes were merged for each pointing and the standard *Suzaku* filters were applied. The calibration source regions and regions of low effective area near the chip edges were masked out.
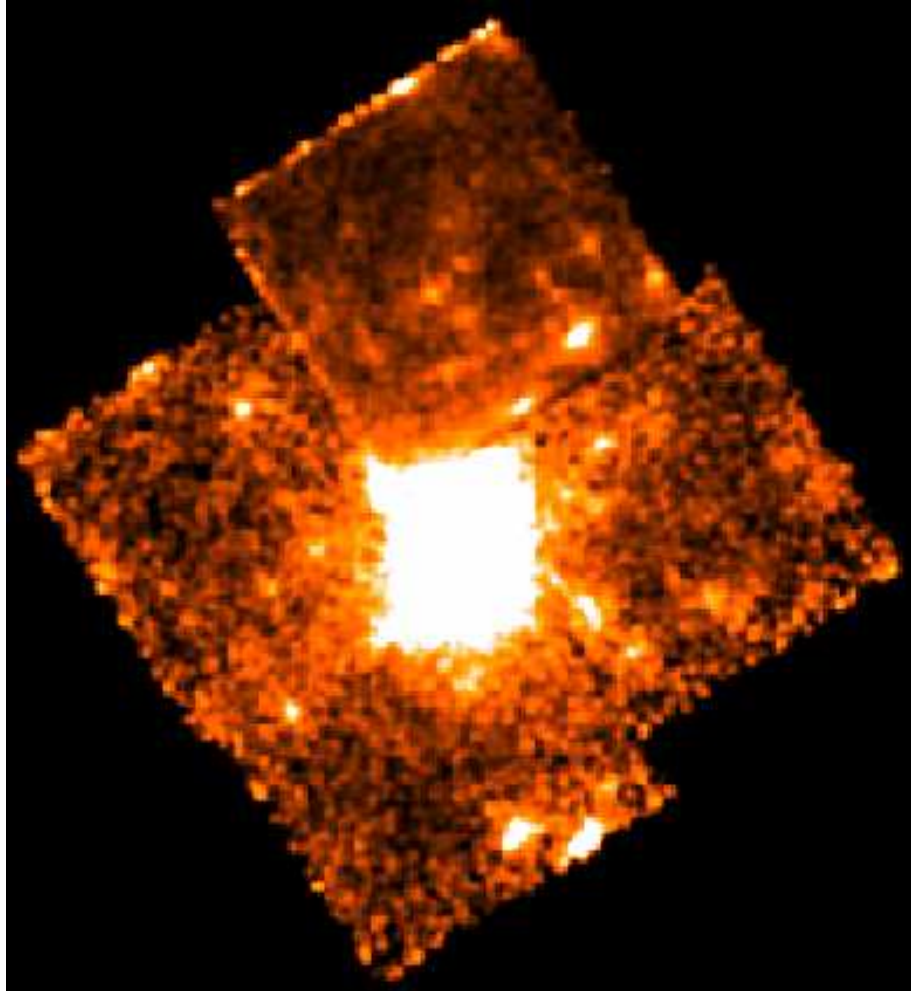
Figure 2.2: Sample *Suzaku* image of Abell 1413 showing the four different pointings mosaiced together. Each square represents a pointing which combined together gives azimuthal coverage of the cluster.

Chapter 3:   Analysis

3.1   Spatial Analysis

3.1.1   Attitude Corrections with *Suzaku*

The *Suzaku* data was initially checked for overall attitude errors in the expected orientation of the satellite with respect to the source. We created preliminary images for each pointing individually by extracting images in the 0.5–7 keV band (to minimize background and maximize point source signal) for each `XIS` and summing the images together. Each image was then compared with overlapping *XMM-Newton* data, which identified typically two to four comon point sources. From these point sources, we determined the average pointing offset. This pointing correction was then applied using a single correction for all `XIS` observations in a single field. The correction was typically less than the published 20" pointing accuracy of *Suzaku*, with a few deviations of 1' or more. From the uncertainty in the point source positions, we estimate that the residual astrometric accuracy of the *Suzaku* data is 5", registered to the *XMM-Newton* frame of reference.

3.1.2   Image Analysis

To produce exposure-corrected, mosaicked images of the clusters, we followed a similar procedure to Bautz et al. [2009]. Images from each detector and pointing were extracted in two bands (0.5-2 keV or "soft" and 2-8 keV or "hard") in sky coordinates. Normalized instrument maps were created for each image in detector coordinates, including the effects of bad pixels and the unusable region in post-2009 `XIS` 0 data. Vignetting maps were created in the same coordinate system, using as input two field-filling uniform spectral models in `xissim` to weight the maps: an absorbed thermal+power law model similar to the cosmic X-ray background model described in Section 3.3.1, and an absorbed 5 keV APEC (refer to section 3.2) model to represent cluster emission. These maps were created for both the soft and hard energy bands, thus resulting in four vignetting maps for each detector/pointing combination, representing the response of the telescope to two different spectral sources within two different energy bands. Each vignetting map was combined with the appropriate instrument map.

Using the *Suzaku* attitude table for each observation, the combined instrument+vignetting maps were projected onto the sky coordinate plane for each attitude time stamp, and finally combined and scaled by the exposure time to create exposure maps for each detector-pointing combination. For a typical cluster, this resulted in 48 individual exposure maps (4 fields times 3 detectors times 2 spectral model times 2 energy bands). Finally, the counts images and individual exposure maps were mosaicked onto a common re-gridded map, resulting in two mosaicked

counts images (one in each of 2 energy bands) and four mosaicked exposure maps (one in each of 2 energy bands, corresponding to each of 2 input source spectra).

Maps of the non-X-ray background (NXB) were produced for each pointing-detector combination using `xisnxbgen`, and were combined and mosaicked in the same way as the counts image, yielding two such maps in the soft and hard energy bands.

3.1.3   Attitude Corrections & Spurious Sources

We broke down each of the pointings into one kilo-second intervals and re-generated the images. We also checked for attitude errors and the existence of spurious and variable sources during the observation of each individual cluster. To illustrate these possible complications, we present here images from a similar cluster RXCJ0605.

- Errors in attitude: If there are attitude variations that happened during the course of the observations which are not accounted for, we run the risk of inaccurate region analysis and inaccurate point source removal. The problem is compounded when performing azimuthally averaged cluster analysis. This is shown in Figure 3.1

<center>(a)   (b)</center>
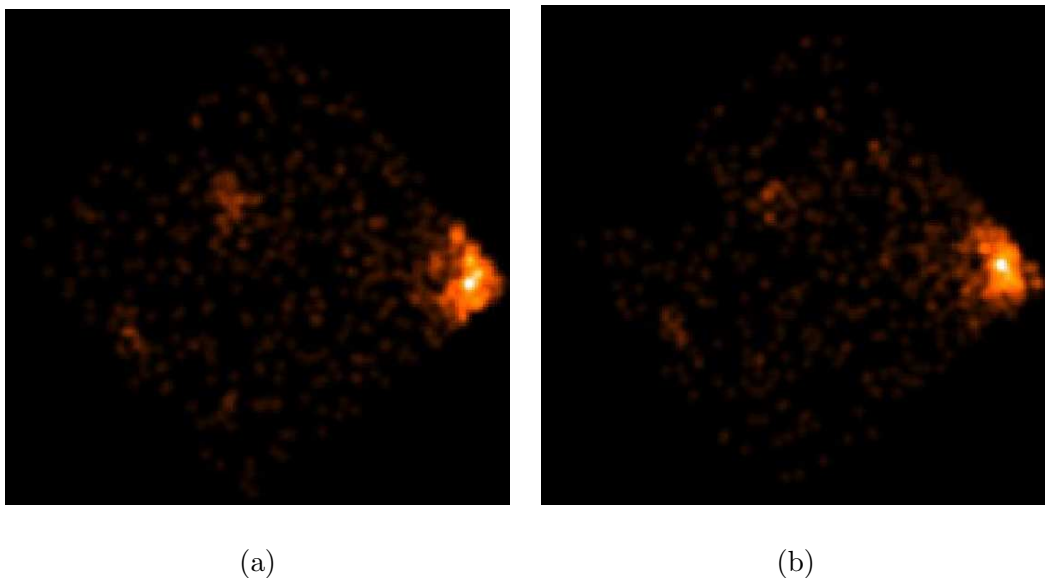
Figure 3.1: Attitude Errors in *Suzaku*. *Left (Before Correction):* The cluster source in the left corner of the image shows several point-like sources within the same area, all of which are technically the cluster center. *Right (After Correction):* The cluster source in the right corner of the image is confined to a single collated source after attitude correction.

- Spurious sources: We also identified a few spurious sources which initially appear as bright sources and then slowly dissipate away. Such occurrences can usually be attributed to cosmic rays or high-powered Fe ions hitting the detector. However, the time scales and spatial scales for this phenomenon in our samples are not consistent with what is observed. It is more likely these are an unknown transient source. In either scenario, the random nature of these sources will cause invalid fits to the cluster variables. This feature is shown in Figure 3.2

<center>24</center>

(a)   (b)
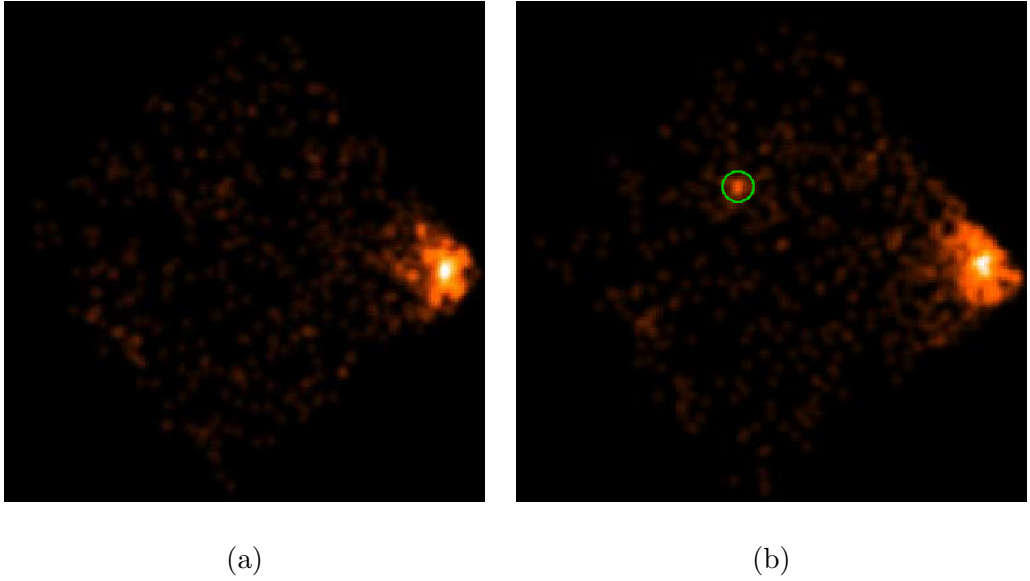
Figure 3.2: Spurious Sources: These two images were taken 1 kilo-second apart. The image in the left shows no source while the image in the right shows the sudden occurrence of a bright point source.

3.2 Spectral Analysis

Spectra were extracted from each of the clusters as a series of annuli specified in Table 3.1. These particular annuli definitions were chosen due to the relatively large *Suzaku* point spread function. These annuli have a minimum separation of $2.5'$ to account for the *Suzaku* half-power diameter (HPD) of $2'$. The annuli were extracted using the FTOOL `xselect` v2.4b directly from the cleaned event lists. In the case of Abell 773, we had to use a larger annulus for the outermost cluster annulus as we were unable to achieve enough signal to noise for accurate analysis. The annulus definitions are shown on the *Suzaku* image in Figure 3.3.

Annulus	Inner Radius	Outer Radius
1	$0'$	$2.5'$
2	$2.5'$	$5'$
3	$5'$	$7.5'$
4	$7.5'$	$10'$
5	$10'$	$12.5'$
6a	12.5'	$15'$
6b	12.5'	$17.5'$

Table 3.1: The inner and outer radii of annuli used for the cluster analysis
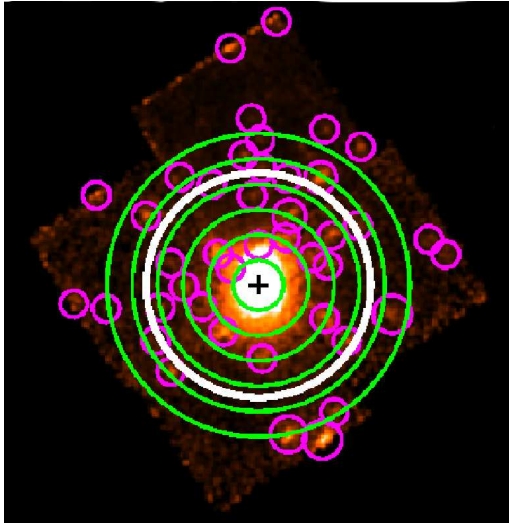
(a) Abell 1413: $r_{200} = 11.101837'$
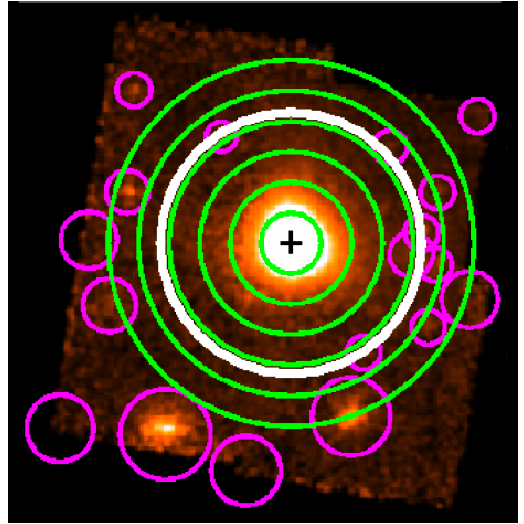
(b) Abell 2204: $r_{200} = 10.706187'$
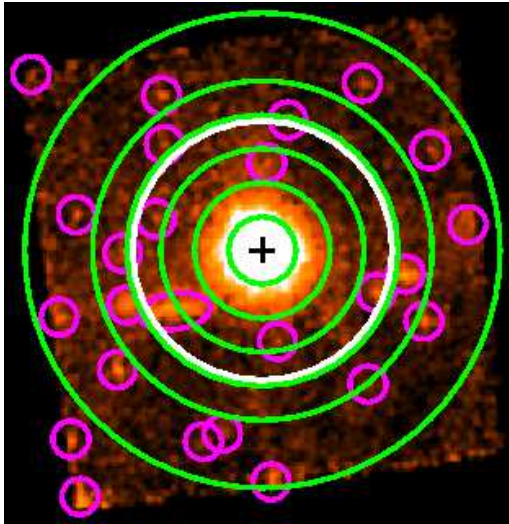
(c) Abell 773: $r_{200} = 9.7031247'$
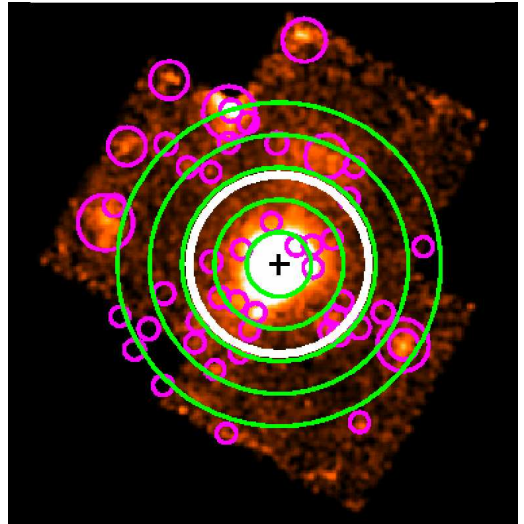
(d) Abell 383: $r_{200} = 6.9362954'$

Figure 3.3: *Suzaku* images of the clusters with annuli. The green concentric annuli represent the different annuli that were used to extract the parameter profiles. The magenta circles mark the point sources that were removed from the data. The white circle marks r_{200} to show the spatial scale of the images, the values of which are included below each cluster image.

For each of the annuli, the appropriate redistribution matrix files (RMF files) were created using the FTOOL `xisrmfgen` v2012-04-21. These files account for the time variation in the energy response for the particular XIS instrument being used. The ancillary response files (ARF files) for these annuli were generated using the FTOOL `xissimarfgen` v2010-11-05. This is a ray-tracing algorithm which accounts for the telescope vignetting, telescope structure blocking and scattering, filter transmission, molecular contamination absorption, and the point spread function for the source. The program generates tables which relate the energy of the incident photon to the spectral response of the instrument. We utilize two different ARFs for our analysis. The first kind was created using a $20'$ radius source of uniform brightness. This ARF is used in the analysis of the uniform background emission. The second ARF is created using a β model. The β model is an analytic approximation of the observed surface density for many clusters [Cavaliere and Fusco-Femiano, 1978]. Integrating this density distribution yields an Abel integral which has an analytic solution, in the bremsstrahlung limit, of the form:

$$S(R) = S_0(1 + (R/r_c)^2)^{-3\beta+0.5} \tag{3.1}$$

where S is the surface brightness and r_c is the core radius. The flux distribution used as input for these ARFs was produced by fitting the surface brightness profiles of Snowden et al. [2008] out to a radius of $6'$. This was used to construct an input image for `xissimarfgen`, with arbitrary normalization, representing the flux distribution of the cluster. Note that this means the beta model was extrapolated beyond $6'$. This ARF is used for fitting the cluster emission in each of the annuli (Figure 3.4).
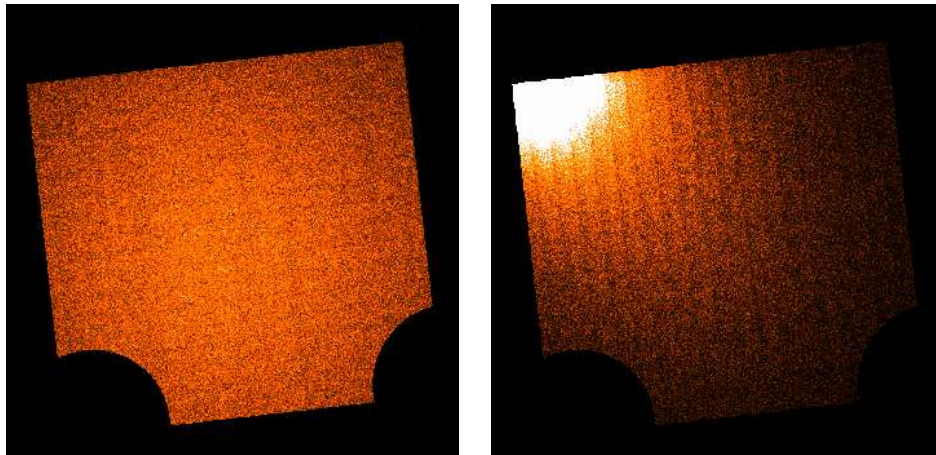
(a) Ray-traced image for the uni- form source

(b) Ray-traced image for the beta model

Figure 3.4: Images of Abell 773 produced by the ray tracing program `xissimarfgen` for the two kinds of ARFs.

The data from all the annuli and the three working `XIS` detectors were fit in `XSPEC` v12.8.0 using the C-statistic. The C-statistsic is a maximum likelihood function ideally suited for model fitting poisson distributed data. The spectral fitting was restricted to the 0.7–7.0 keV range as the response calibration is the best in this region. Restricting the energy range also helps constrain values better. The detailed effects of using this energy range is described in section 3.4.

A combination of an absorbed thermal plasma model (`APEC`) and a background model (described in section 3.3.1), is used to fit the emission from the annuli. In addition to this, a background region was chosen outside the cluster annuli to which just the background model was fit. A *ROSAT* data spectrum was also fit simultaneously to help constrain the background. The redshift for each of the clusters was fixed to the value obtained from Snowden et al. [2008]. For each of the cluster

fits, the cluster's heavy element abundance relative to cosmic values [Grevesse and Anders, 1989] was allowed to vary.

The *ROSAT* data spectrum was obtained using the HEASARC X-Ray background tool. The tool generates a FITS spectrum file for the specific region requested (typically an annulus between 0.4 and 1 degree). This helps to accurately calculate the X-ray background fluxes using the *ROSAT* data.

For our analysis, we assume a standard ΛCDM cosmology with $H_0 = 70$ km/s/Mpc, $\Omega_M = 0.27$ and $\Omega_\Lambda = 0.73$. All errors unless specifically stated are at the 1 σ level.

3.3   Background Analysis

Extracting information from annuli becomes increasingly difficult as one moves away from the center of the cluster to the outskirts. At the outskirts of galaxy clusters, the expected cluster flux (acquired from extrapolating the surface brightness profile) is less than 30% of the X-ray background [Bautz et al., 2009], making understanding and constraining the background a vital aspect of studying cluster outskirts accurately (Figure 3.5).

One source of background uncertainty is cosmic background variations. This comes from point sources just below the detection limit of the instrument that can still cause variations in the background as large as 40%. To address this issue, we excised point sources from the field using the already available data from *XMM-Newton* and *Chandra*, which are better at detecting point sources than *Suzaku* (Figure 3.6).

For typical *Suzaku* exposures (about 40 kilo-seconds), we can resolve and re-
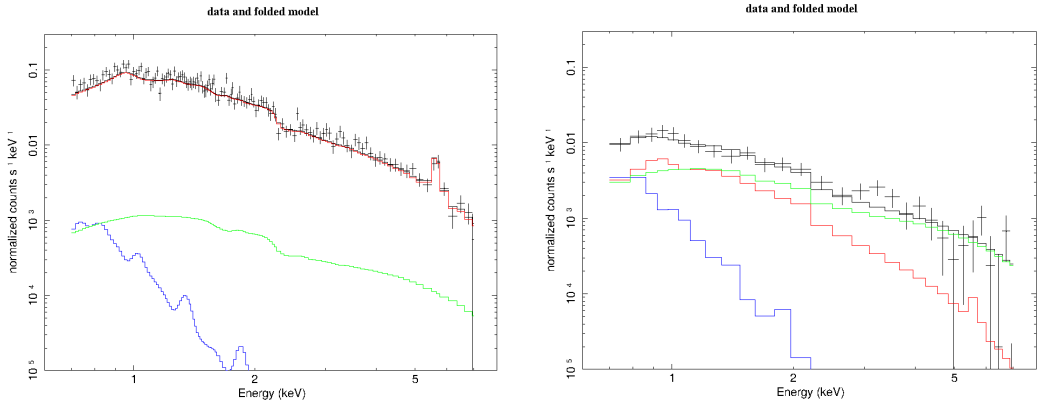
(a) Spectrum from 0' to 2.5'

(b) Spectrum from 5' to 7.5'
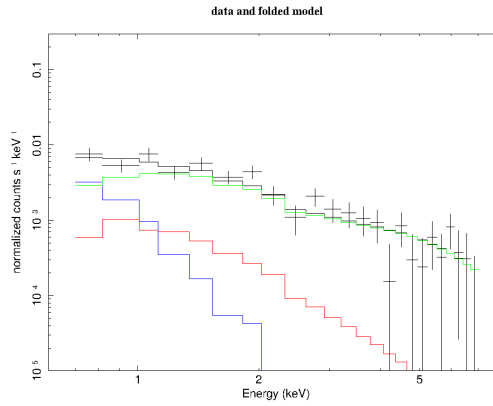
(c) Spectrum from 10' to 12.5'

Figure 3.5: The relative fractions of the various components as one moves from the center of the cluster Abell 383 to the outermost annuli. The *red* line depicts the contribution from the cluster emission, *blue* the galactic thermal background and *green* the extragalactic background. In the inner regions of the cluster (Figure 3.5a), emission from the cluster dominates. However, moving further out, the background components start to dominate over the cluster emission (Figure 3.5c). The relative fractions of the different components shown here are true for all other clusters in our sample as well.
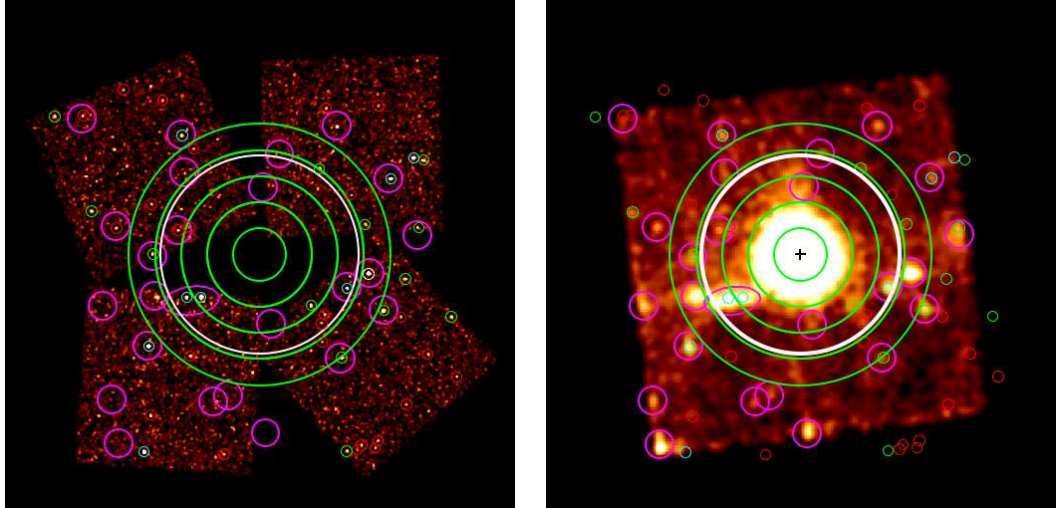
(a) *Chandra* data for Abell 773   (b) *Suzaku* data for Abell 773

Figure 3.6: Using the *Chandra* data, more of the point sources can be extracted than using *Suzaku* data alone, which will help to constrain the background better. In these images, the *Chandra* point sources are the smaller circles (with a size of approximately 10"), and the *Suzaku* annuli are in magenta circles (with a size of approximately 30"). Removal ensures that point sources are no longer a dominant component of the error in the background subtraction.

move point sources down to a threshold detection limit of $S_{excl} = 10^{-13}$ erg cm^{-2} s^{-1} for both the soft (0.5–2.0 keV) and the hard (2.0–10.0 keV) X-ray ranges [Bautz et al., 2009]. Using the point source distribution described in Moretti et al. [2003], one can calculate the expected surface brightness fluctuations of the background in the outskirts within a given solid angle (Ω) as described in the following equation from Walker et al. [2013]:

$$\sigma_{CXB}^2 = (1/\Omega) \int\limits_0^{S_{excl}} \left(\frac{dN}{dS}\right) \times S^2 dS \tag{3.2}$$

Here $\frac{dN}{dS}$ refers to the differential distribution of point sources at each flux as calculated in Moretti et al. [2003]; S refers to the flux and σ_{CXB} to the surface brightness fluctuations of the X-ray background expected after removing all point sources which have a flux above S_{excl}. For the *Suzaku* data, one can then expect surface brightness variations to be $\sigma_{CXB}^{Suzaku} = 3.3 \times 10^{-12} \Omega_{0.01}^{-1/2}$ erg cm^{-2} s^{-1} deg^{-2} in the soft band and $\sigma_{CXB}^{Suzaku} = 4.9 \times 10^{-12} \Omega_{0.01}^{-1/2}$ erg cm^{-2} s^{-1} deg^{-2} in the hard band. Here $\Omega_{0.01}^{-1/2}$ is the solid angle of the measurement region in units of 10^{-2} deg^{-2} which is the size of a typical annular extraction region in the outskirts used for spectral analysis.

Using the 5 kilo-second *Chandra* data, we are able to detect 95% of all sources above a detection limit of $S = 5 \times 10^{-15}$ erg cm^{-2} s^{-1} in the 0.5–2.0 keV range across most the of the field of view (Miller et al., in prep.). This immediately allows the background to be resolved to a threshold flux ~ 20 times lower than that achieved with just the *Suzaku* data. It also reduces the variations in the background flux by about a factor of 5.5 ($\sigma_{CXB}^{Chandra} = 6 \times 10^{-13} \Omega_{0.01}^{-1/2}$ erg cm^{-2} s^{-1} deg^{-2}). Additionally,

these values can be improved by increasing the solid angle of the extraction region – increasing the value of $\Omega_{0.01}^{-1/2}$. This, however would limit our ability to trace azimuthal variations.

3.3.1   Background Model

When studying clusters, background modeling is of prime importance and is known to have the following components [Kuntz and Snowden, 2001, Snowden et al., 2008, Bautz et al., 2009]:

- Instrumental Background: simulated as part of the data pipeline.

- A cool ($\sim$0.1 keV) unabsorbed thermal component which represents emission from the Local Hot Bubble.

- A cool ($\sim$0.1 keV) absorbed thermal component which represents emission from the cooler halo.

- A warmer ($\sim$0.25–0.7 keV) absorbed thermal component which represents emission from the hotter halo or the inter-galactic medium.

- An absorbed power law ($\alpha \sim 1.46$) for the sum of cosmological sources in the unresolved background.

Typically X-Ray data for clusters is modeled over the entire range of 0.5–10 keV, but due to calibration and signal-to-noise concerns, we model the data over the energy range of 0.7–7.0 keV. This choice is described in detail in Section 3.4.

We use *Suzaku* data beyond the extent of the cluster as regions with only background emission to constrain the background model. In addition to this, we also fit *ROSAT* data to help anchor the background. These backgound components are then simultaneously fit along with the cluster model.

3.3.1.1 Soft X-Ray Background

The soft X-Ray background for the cluster was modeled as a single temperature `APEC` model [Smith et al., 2001], which creates an emission spectrum from collisionally-ionized diffuse gas. The model uses atomic data to calculate spectral models for hot plasmas. The norms and the temperature for all the annuli and the *ROSAT* spectra for this background `APEC` model are linked together, ensuring that it is a uniform source across the field. We included an additional unabsorbed `APEC` model for just the *ROSAT* data to account for the fact that the *ROSAT* is modeled over the range of 0.3–2.0 keV. This additional range of the model will account for other thermal components that contribute to the emission within this energy range.

To study the effect of this particular component, we ran two iterations of the model fitting, one using a variable temperature value and the other using a fixed value of 0.18 keV, which is an expected median value (Yoshino et al. [2009]). This was to test the effect of variation in the thermal background on the cluster parameters. We do not see any significant variation in the parameters primarily because at this energy range (0.7–7.0 keV) lower energy components' contribution is minimal (Figure 3.7).
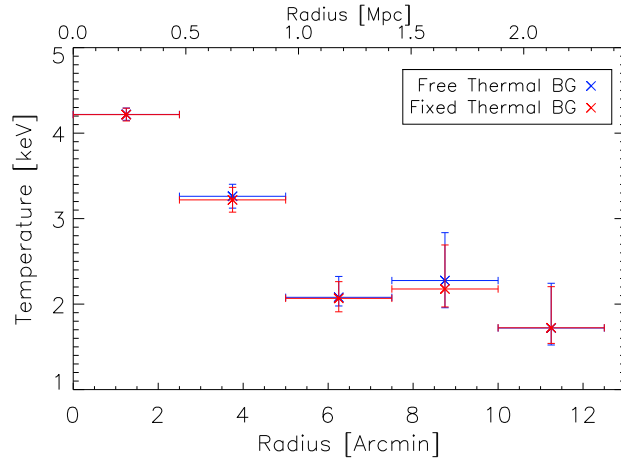
(a) Temperature profile modeled with fixed thermal background (*red*) and with free thermal background (*blue*)
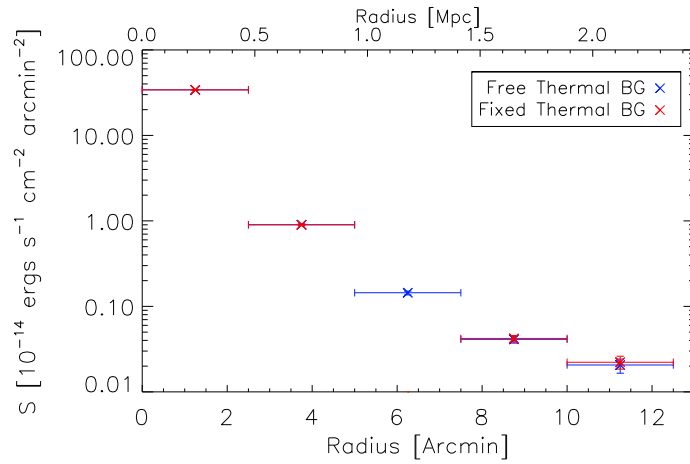
(b) Surface Brightness profile modeled with fixed thermal background (*red*) and with free thermal background (*blue*)

Figure 3.7: Analysis of the cluster Abell 383 using a variable temperature model and fixed temperature model for the Soft X-Ray Background. The variation between the two models in temperature and surface brightness is insignificant primarily due to the choice of energy range in modeling.

3.3.1.2 Non X-Ray Background

The non X-Ray Background is the sum total of all the non X-Ray components that are part of the data. To this end, the FTOOL `xisnxbgen` v2010-08-22 was used to generate the particle-induced non X-ray background spectra. This utilizes the night earth data: a database of spectra taken by pointing the satellite at the night earth; in addition to the latest contamination correction models to generate background spectra which are subtracted from each of the source spectra before cluster analysis.

3.3.1.3 Cosmic X-Ray Background

This is the most significant component of the background model and represents the sum of all cosmological sources in the unresolved background. This phenomenon is well studied by several surveys of the X-Ray sky [Jahoda et al., 1992, Gendreau et al., 1995], and between 1–10 keV, the background shape can be approximated by a power-law with an index of 1.4. This was further validated in Vasudevan et al. [2013] which deduced the same spectrum using a sample of local active galactic nuclei to calculate the background. We employ the same model with a single normalization for all the annuli due to the isotropic nature of this component.

3.4 Energy Range Considerations

In order to understand the effects of modeling the data between 0.5–10.0 keV and 0.7–7.0 keV, we simulate cluster data using the clusters Abell 383 and Abell 773

as a template for the other clusters in our sample. These particular clusters were used because their temperature and surface brightness values fall in the average value range for clusters [Snowden et al., 2008]. Since Abell 383 only has three pointings versus Abell 773 which has four, it will also help reveal any differences which stem from the number of pointings.

For both clusters, we simulate three separate cluster annuli: an inner annulus, an outer annulus, and an intermediate annulus in between the two. This translates to annuli 2, 4 and 6b for Abell 773 and annuli 1, 3 and 5 for Abell 383 (refer to Table 3.1). The cluster is simulated over the entire *Suzaku* energy range. In addition to this, we also simulate a *ROSAT* spectrum and a spectrum from a background *Suzaku* region which lies just beyond the cluster. We then model both sets of cluster data for two separate energy ranges 0.5–10.0 keV and 0.7–7.0 keV. We choose an upper limit of 7.0 keV because the cluster signal is not significant at lower energies, resulting in a low signal-to-noise ratio. Below 0.7 keV, there is uncertainty in the response matrices due to time variable contamination, and the contaminating contribution from the soft X-ray background is very large. Analyzing the data in this energy range (0.7-7.0 keV) is becoming more commonplace, as seen in Schellenberger et al. [2014]; however, the true test of the validity of these energy cutoffs lies in whether the physical parameters become better constrained within this range.

We initially fit the cluster over the entire range of 0.5–10.0 keV using all the different components of the model. These values are then used to simulate data using the `fakeit` command in `XSPEC`. This command creates spectrum files, where the model we supplied is multiplied by the *Suzaku* response curves. This product is

then added to a realization of the background to which statistical fluctuations are then injected to get the final output spectra. This fake data was fit over both the ranges of 0.5–10.0 keV and 0.7–7.0 keV and then the simulation and fitting were repeated 25 times. In one or two instances of these simulations, the fit obtained is very different from the expected values in either or both energy ranges. For the purposes of this study, these iterations were eliminated from analysis shown in the plots below (figures 3.8–3.13).

From these simulations, it is clear that there is no significant loss of information by restricting the analysis to between 0.7-7.0 keV. In all cases, it is seen that the values for the temperature and normalization are similarly or better constrained over this smaller range. This is manifested as smaller error bars on these parameters.

In some cases, we see larger deviations from the expected value of the temperature. This can be attributed to the random nature of the spectrum creation, especially of the background regions. This manifests as much larger deviations at higher radii where the fractional contribution of the background component is much larger than the inner regions. Such deviations could also arise because the fitting routine falsely finds a local minimum instead of global minimum because the normalization and the temperature of the cluster model are not independent parameters (Figures 3.14–3.16).
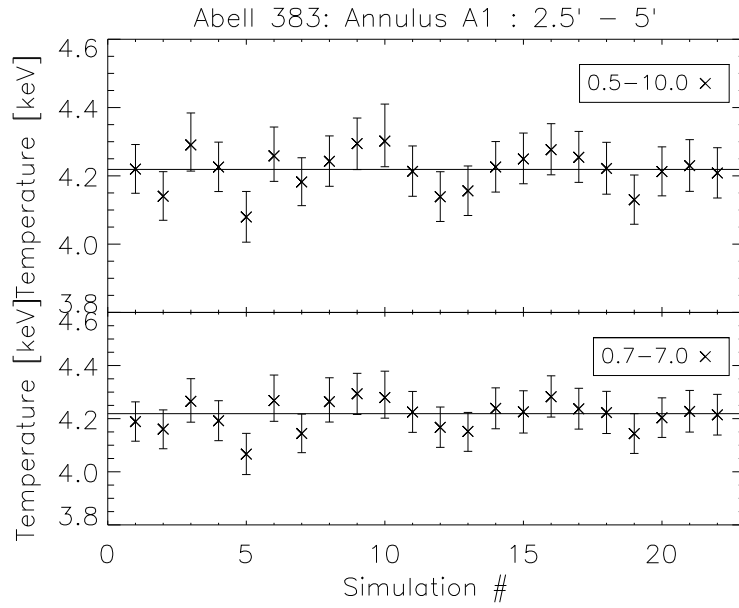
(a) *Top*: The results of simulations for the 0.5–10.0 keV regime.

Bottom: The results of simulations for the 0.7–7.0 keV regime. The

line represents the value used to simulate the data. The temperature

is plotted on a linear scale.
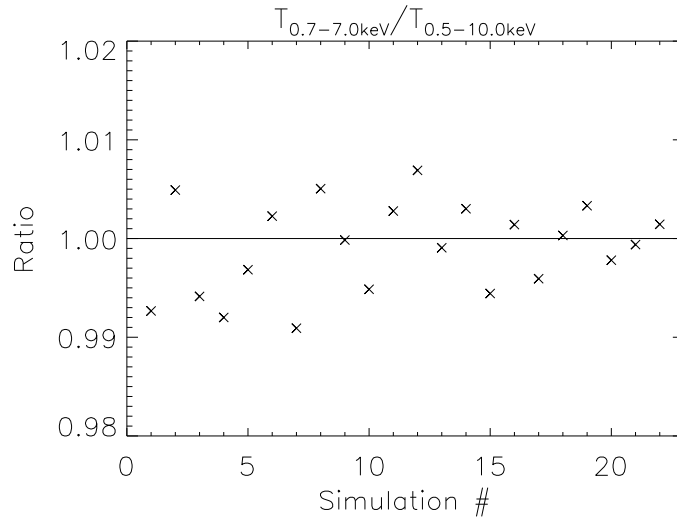
(b) Ratio of the values obtained in the two different energy

ranges.

Figure 3.8: Simulation of cluster Abell 383 over the innermost Annulus (0' − 2.5').
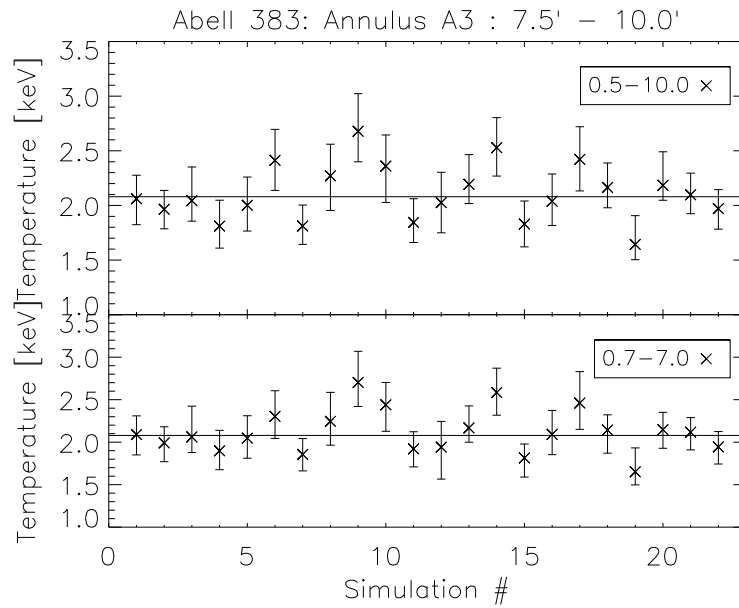
(a) *Top*: The results of simulations for the 0.5–10.0 keV regime.

Bottom: The results of simulations for the 0.7–7.0 keV regime. The

line represents the value used to simulate the data. The temperature

is plotted on a linear scale.
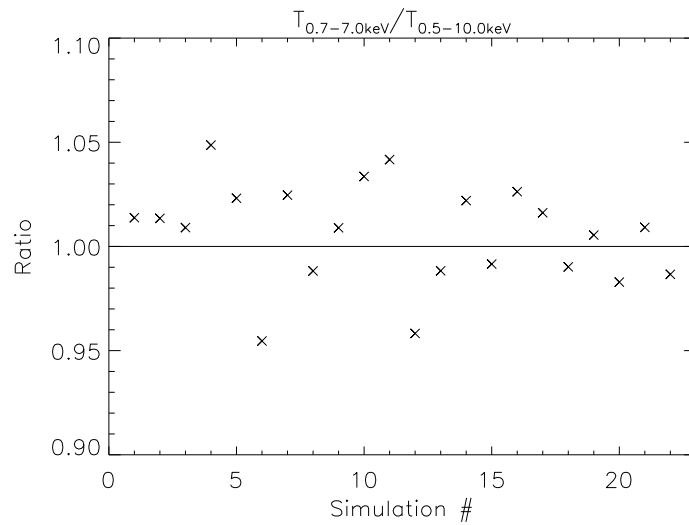
(b) Ratio of the values obtained in the two different energy

ranges.

Figure 3.9: Simulation of cluster Abell 383 over the intermediate Annulus (5.0' –

7.5').
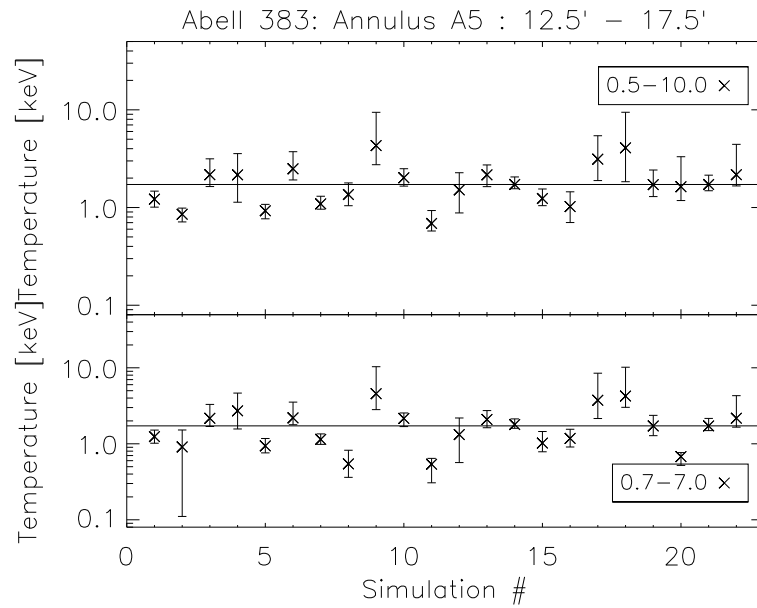
(a) *Top*: The results of simulations for the 0.5–10.0 keV regime.

Bottom: The results of simulations for the 0.7–7.0 keV regime. The line represents the value used to simulate the data. The temperature is plotted on a log scale.
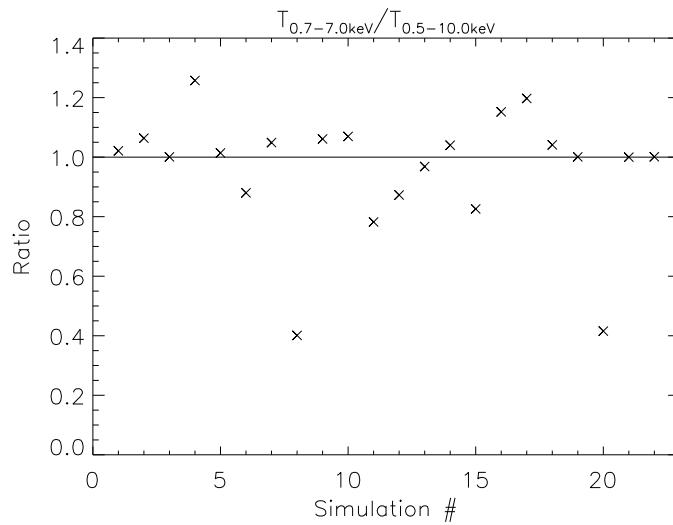
(b) Ratio of the values obtained in the two different energy ranges.

Figure 3.10: Simulation of cluster Abell 383 over the outermost Annulus (10.0' – 12.5').
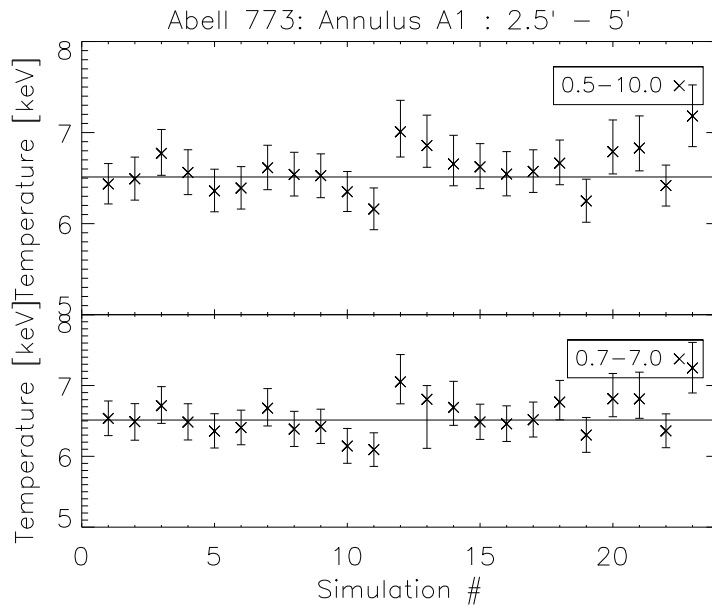
(a) *Top*: The results of simulations for the 0.5–10.0 keV regime.

Bottom: The results of simulations for the 0.7-7.0 keV regime. The line represents the value used to simulate the data. The temperature is plotted on a linear scale.
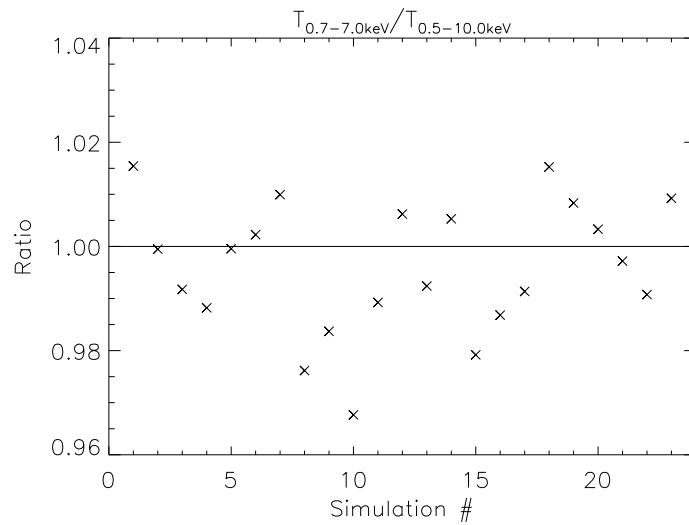
(b) Ratio of the values obtained in the two different energy ranges.

Figure 3.11: Simulation of cluster Abell 773 over the innermost Annulus (2.5' – 5.0').
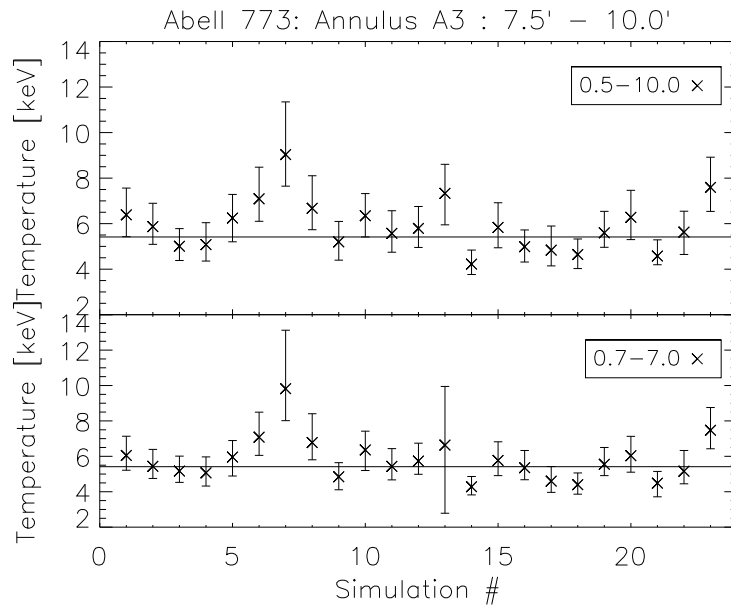
(a) *Top*: The results of simulations for the 0.5–10.0 keV regime.

Bottom: The results of simulations for the 0.7–7.0 keV regime. The

line represents the value used to simulate the data. The temperature

is plotted on a linear scale.
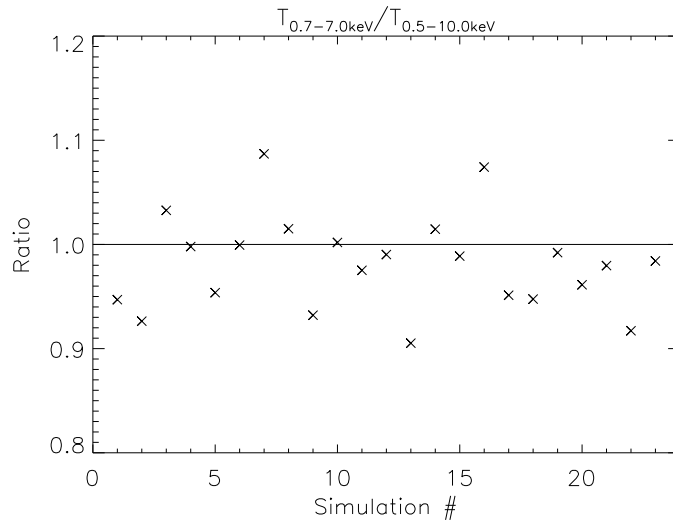
(b) Ratio of the values obtained in the two different energy

ranges.

Figure 3.12: Simulation of cluster Abell 773 over the intermediate Annulus (7.5' –
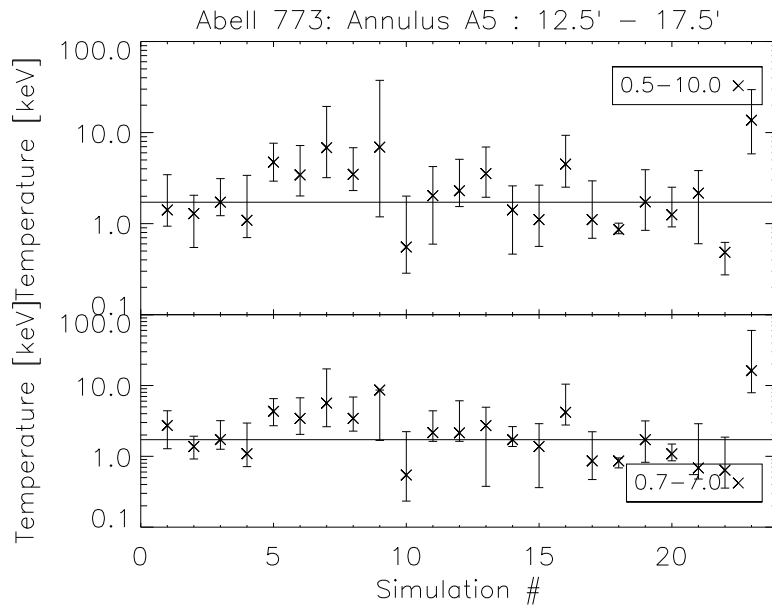
10.0').

(a) *Top*: The results of simulations for the 0.5–10.0 keV regime.
Bottom: The results of simulations for the 0.7–7.0 keV regime. The
line represents the value used to simulate the data. The temperature
is plotted on a log scale.
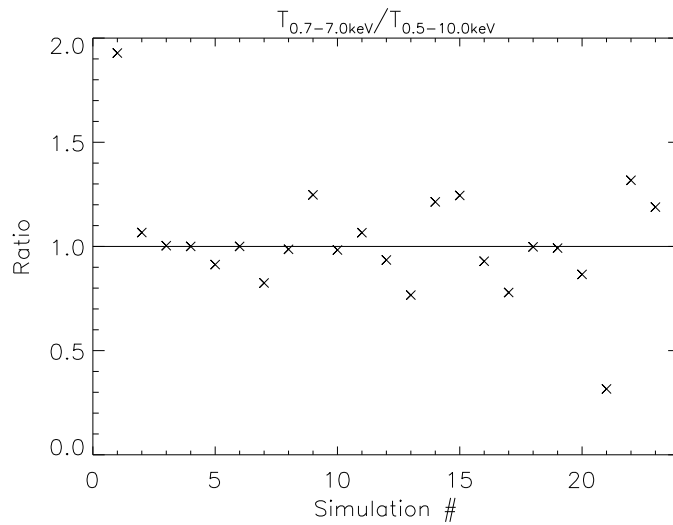
(b) Ratio of the values obtained in the two different energy
ranges.

Figure 3.13: Simulation of cluster Abell 773 over the outermost Annulus (12.5' –
17.5').
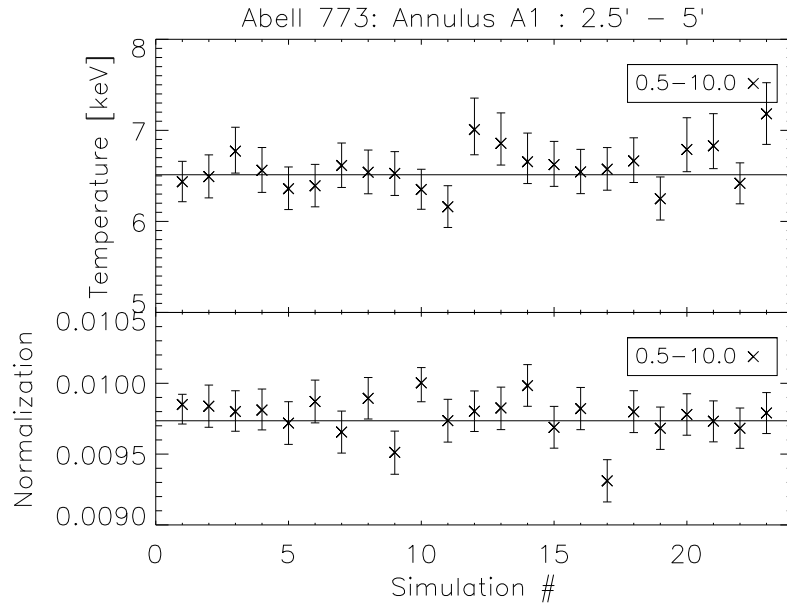
(a) The results of simulations for the 0.5–10.0 keV regime
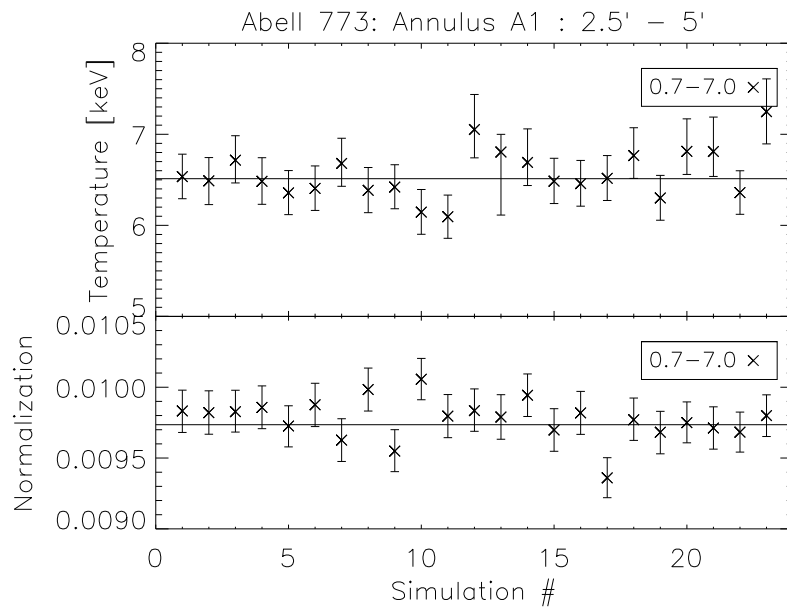
(b) The results of simulations for the 0.7–7.0 keV regime.

Figure 3.14: Comparison of the temperature and normalization for the simulation of cluster Abell 773 over the innermost Annulus (2.5'–5.0'). Both parameters are plotted on a linear scale.
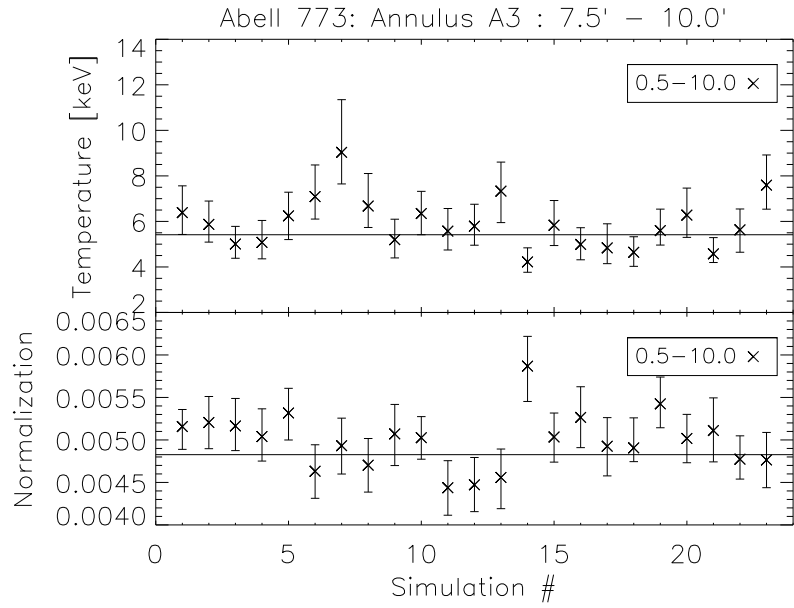
(a) The results of simulations for the 0.5–10.0 keV regime
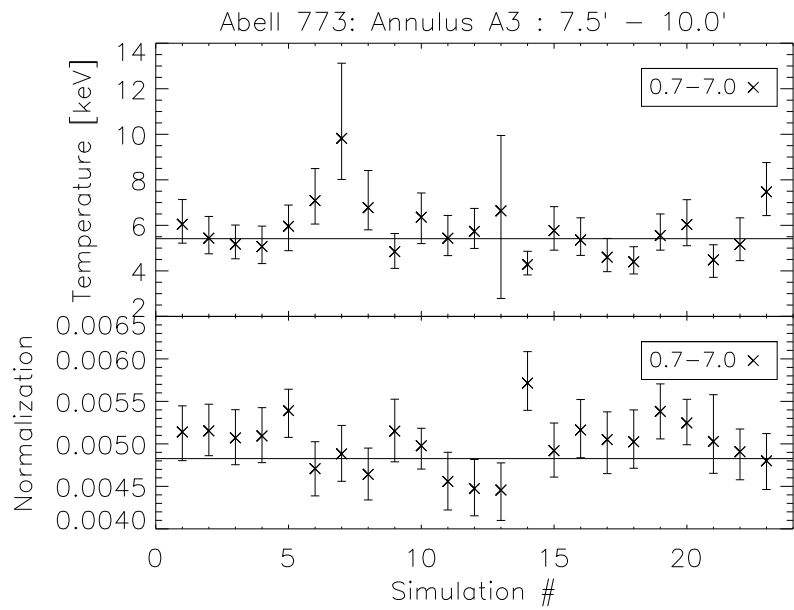
(b) The results of simulations for the 0.7–7.0 keV regime.

Figure 3.15: Comparison of the temperature and normalization for the simulation of cluster Abell 773 over the intermediate Annulus (7.5' – 10.0'). Both parameters are plotted on a linear scale.
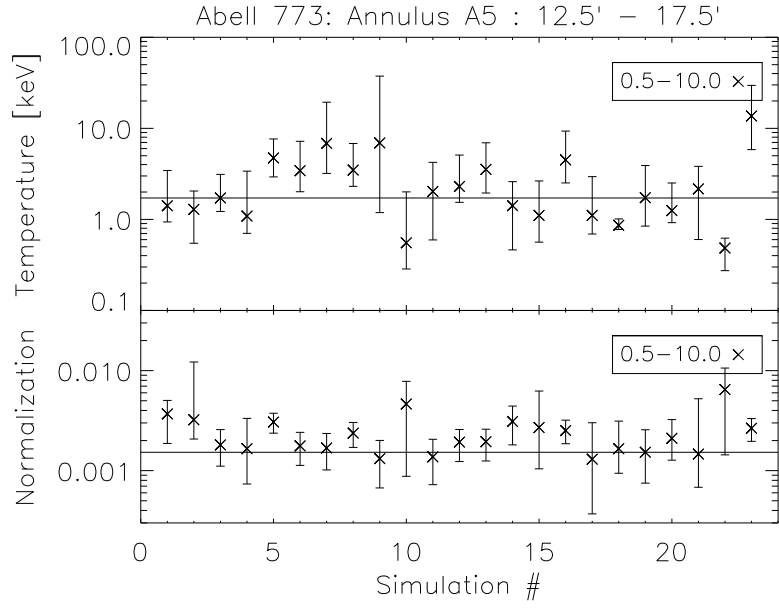
(a) The results of simulations for the 0.5–10.0 keV regime
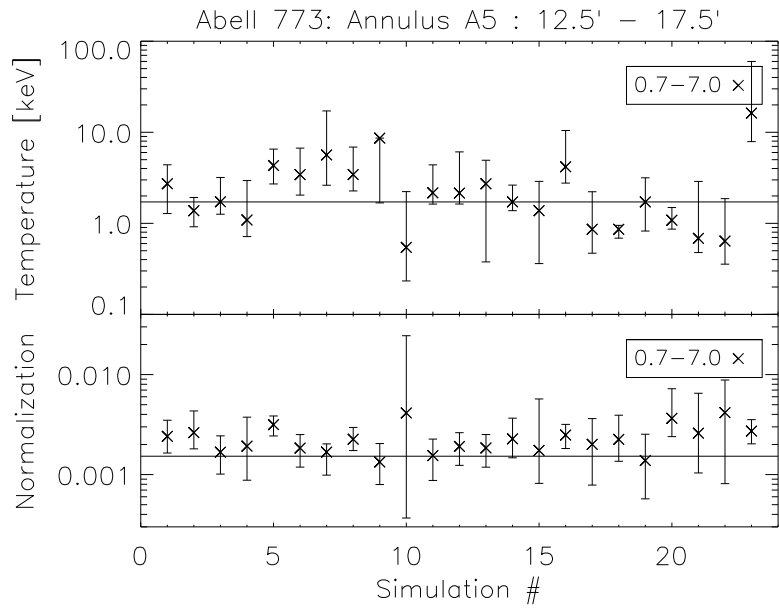
(b) The results of simulations for the 0.7–7.0 keV regime.

Figure 3.16: Comparison of the temperature and normalization for the simulation of cluster Abell 773 over the outermost Annulus (12.5'–17.5'). Both parameters are plotted on a log scale.

Chapter 4:   Results

The method outlined in Chapter 3 was used to analyze the four clusters from our sample, namely Abell 1413 ($z = 0.135$), Abell 2204 ($z = 0.151$), Abell 773 ($z = 0.216$) and Abell 383 ($z = 0.187$). We obtained the primary attributes temperature, metal abundance, surface brightness, and density as well as the secondary attributes pressure, entropy, total mass and baryonic fraction.

4.1   Primary Attributes

The temperature, abundance, surface brightness and density profiles for the afore-mentioned clusters are shown below in Figures 4.2 through 4.9 and in Table 4.1. As our sample enables a direct comparison with the results from Snowden et al. [2008], those values are also plotted in these figures.

For Abell 1413, we compared our results to Hoshino et al. [2010], which published values for the temperature, abundance, normalization and the surface brightness for the northern region of Abell 1413 using *Suzaku*. We extend and improve their results by incorporating four distinct pointings that cover the entire cluster, facilitating a better understanding of the cluster as a whole. Due to the fact that we are using four different pointings and are azimuthally averaging the data, we are

able to reduce our errors significantly more than in Hoshino et al. [2010]. Within errors, our results are still similar to the values produced in Hoshino et al. [2010].

For Abell 2204, we obtained newer *XMM-Newton* results for the cluster from Dave Davis' work [Davis, 2013]. These results account for changes in the *XMM-Newton* analysis due to improved extended emission analysis routines. The comparison of the older data and the newer are shown in Figure 4.1. We notice that our values disagree at high radii.
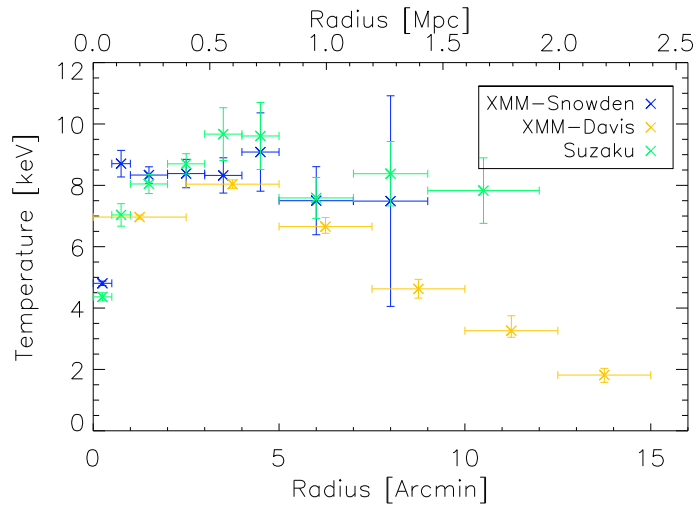
Figure 4.1: Comparison of *Suzaku* and *XMM-Newton* parameters for Abell 2204. The plot shows the older Snowden analysis and the newer Dave Davis analysis of *XMM-Newton* data for this cluster. The large disparity between the values shows unreliability of this instrument at large radii.

We have also compared our results to the *Suzaku* values in Reiprich et al. [2009], which provides temperature and abundance values for the north eastern region of Abell 2204 (Figure 4.2b). Our results are in agreement with their published

values.

For Abell 773, we see a discrepancy in temperature provided by Snowden et al. [2008] when compared to our results. For the two outermost *XMM-Newton* bins, the temperature is underestimated in their analysis. This suggests that *XMM-Newton* data fails to accurately describe the outskirts of the cluster. For Abell 383, like Abell 773, there is a temperature discrepancy in the *XMM-Newton* values in the outermost bins shown in Snowden et al. [2008].

Table 4.1: Detailed description of the cluster details: Temperature, Abundance, Surface Brightness. These quantities are directly fitted during analysis. Also shown are the 1 σ errors for each of the parameters.

Cluster	Annulus	kT [keV]	Abund[1]	S (0.3–10.0 keV) [10^{-14} ergs s^{-1} cm^{-2} arcmin^{-2}]
	3	$6.631^{+0.535}_{-0.368}$	$0.301^{+0.097}_{-0.090}$	$1.808^{+0.031}_{-0.039}$
	4	$4.254^{+0.361}_{-0.273}$	$0.445^{+0.127}_{-0.114}$	$0.575^{+0.011}_{-0.014}$
Abell 1413	5	$4.445^{+0.561}_{-0.556}$	$0.314^{+0.156}_{-0.143}$	$0.364^{+0.001}_{-0.012}$
	6a	$3.723^{+0.517}_{-0.714}$	$0.768^{+0.383}_{-0.326}$	$0.191^{+0.008}_{-0.001}$
	1	$6.965^{+0.067}_{-0.067}$	$0.391^{+0.011}_{-0.011}$	$182.209^{+0.590}_{-0.586}$
	2	$8.039^{+0.138}_{-0.137}$	$0.316^{+0.023}_{-0.022}$	$9.816^{+0.059}_{-0.074}$
Abell 2204				*continued on next page*

Cluster	Annulus	kT	Abund[1]	S (0.3–10.0 keV)
		[keV]		[10^{-14} ergs s^{-1} cm^{-2} arcmin^{-2}]
	3	$6.655^{+0.297}_{-0.218}$	$0.286^{+0.046}_{-0.044}$	$2.094^{+0.023}_{-0.027}$
	4	$4.625^{+0.312}_{-0.301}$	$0.238^{+0.075}_{-0.070}$	$0.689^{+0.015}_{-0.016}$
	5	$3.262^{+0.488}_{-0.214}$	$0.441^{+0.127}_{-0.113}$	$0.426^{+0.014}_{-0.015}$
	6a	$1.817^{+0.218}_{-0.238}$	$0.682^{+0.480}_{-0.327}$	$0.169^{+0.007}_{-0.027}$
	2	$6.512^{+0.255}_{-0.244}$	$0.173^{+0.045}_{-0.043}$	$3.348^{+0.051}_{-0.051}$
	3	$7.537^{+0.909}_{-0.825}$	$0.222^{+0.118}_{-0.112}$	$0.738^{+0.025}_{-0.029}$
Abell 773	4	$5.415^{+0.991}_{-0.650}$	$0.200^{+0.120}_{-0.200}$	$0.312^{+0.015}_{-0.020}$
	5	$3.633^{+1.203}_{-0.649}$	-	$0.136^{+0.015}_{-0.018}$
	6b	$1.719^{+0.319}_{-0.612}$	-	$0.021^{+0.014}_{-0.014}$
	1	$4.219^{+0.076}_{-0.069}$	$0.408^{+0.036}_{-0.035}$	$34.112^{+0.351}_{-0.418}$
	2	$3.262^{+0.141}_{-0.139}$	$0.264^{+0.067}_{-0.061}$	$0.902^{+0.019}_{-0.023}$
Abell 383	3	$2.080^{+0.244}_{-0.101}$	$0.178^{+0.094}_{-0.081}$	$0.144^{+0.007}_{-0.008}$
	4	$2.276^{+0.560}_{-0.318}$	-	$0.042^{+0.003}_{-0.004}$
	5	$1.721^{+0.523}_{-0.199}$	-	$0.021^{+0.004}_{-0.004}$

[1]Abundances are with respect to Anders and Grevesse [1989]

4.2 Deprojection

The parameters in Table 4.1 were obtained by projecting the three dimensional cluster as a two dimensional object onto the plane of the sky. To accurately understand cluster physics, one needs to deproject these parameters before calculating physical quantities such as entropy and pressure. We deprojected the temperature and density values using the three-dimensional models used in Vikhlinin et al. [2006].

These equations were proven to accurately represent the three-dimensional temperature and gas density of clusters generated from high resolution numerical simulations [Nagai et al., 2007b, Vikhlinin et al., 2006]. The large number of variables ensures that this model works over multiple radii regimes. However, the *Suzaku* data is not adequate to derive all 14 parameters in these models. For this reason, we must either eliminate some terms or fix the values of some of these parameters.

The equations are shown below:

$$
\begin{aligned}
n_e n_p &= n_0^2 \cdot n_1 \cdot n_2 + n_3 \\
n_e n_p &= n_0^2 \frac{(r/r_c)^{-\alpha}}{(1 + (r/r_c)^2)^{3\beta - \alpha/2}} \frac{1}{(1 + (r/r_s)^\gamma)^{\epsilon/\gamma}} + \frac{n_{0,2}^2}{(1 + (r/r_{c,2})^2)^{3\beta_2}}
\end{aligned} \tag{4.1}
$$

$$
\begin{aligned}
T_{3D} &= T_0 \cdot T_1 \cdot T_2 \\
T_{3D} &= T_0 \frac{(r/r_{cool})^{a_{cool}} + (T_{min}/T_0)}{(r/r_{cool})^{a_{cool}} + 1} \frac{(r/r_t)^{-a}}{(1 + (r/r_t)^b)^{c/b}}
\end{aligned} \tag{4.2}
$$

In equation 4.1, n_1 and n_2 are dimensionless fractions, while n_0 and n_3 have units of density [cm^{-3}]. In equation 4.2, T_1 and T_2 are dimensionless fractions, while T_0 have units of temperature [keV].

In equation 4.1, n_1 describes the central density of relaxed clusters which are typically modeled as a power-law-type cusp similar to Pointecouteau et al. [2004]. Here, r_c refers to the radius of the central core while α and β refer to the slope variation in this region. n_2 models the steepening in the slope of the density profile beyond $r > 0.3r_{200}$ relative to the slope at smaller radii [Neumann, 2005]. In n_2, ϵ refers to the change in slope which occurs around the radius r_s. The parameter γ sets the width of the transition range over which the slope steepens. For the sample of the ten relaxed clusters fit in Vikhlinin et al. [2006] a fixed value of $\gamma = 3$ provided acceptable fits. We therefore use the same value. The final term n_3 is an additional β-model component with a smaller core radius $r < r_c$ to increase the models capability to accurately constrain cluster centers. However, considering the quality of our data at cluster centers this term is unnecessary for our modeling as it probes regions much smaller than the *Suzaku* PSF, so we set $n_3 = 0$. These considerations reduce equation 4.1 to:

$$n_e n_p = n_0^2 \frac{(r/r_c)^{-\alpha}}{(1 + (r/r_c)^2)^{3\beta - \alpha/2}} \frac{1}{(1 + (r/r_s)^3)^{\epsilon/3}} \qquad (4.3)$$

Similarly for the three dimensional temperature model (equation 4.2), T_1 models the temperature decline seen moving from the temperature peak at around 0.1–0.2 r_{200} towards the center of the cluster [Allen et al., 2001]. r_{cool} constrains the radius of this cooling region while α_{cool} determines the slope of the temperature decline moving towards the center. T_{min} is defined as the temperature at the very center of the cluster and T_0 scales the power-law dependence. For our analysis, we set the ratio of T_{min}/T_0 as a variable and the slope value as $\alpha_{cool} = 2$. Since our

Suzaku clusters are not well sampled at these small radii, fixing this slope does not bias our results significantly. Beyond this central cooling region, the temperature profile is well-modeled by a broken power-law with a transition region from the cooling region represented by the term T_2. This term is parametrized by r_t, the scaling radius beyond which the transition from the cooling region occurs, and by the power-law indices a, b and c which determine the slopes for this region. While testing the effect of these variables, we noticed that the temperature profile in this regime can be effectively modeled by assuming a single slope without a transition region. This reduces the T_2 term to a beta model where $a = 0$ and $b = c = 2$. The final equation for the deprojected temperature then becomes:

$$T_{3D} = T_0 \frac{(r/r_{cool})^2 + (T_{min}/T_0)}{(r/r_{cool})^2 + 1} \frac{1}{(1 + (r/r_t)^2)} \tag{4.4}$$

We project these three-dimensional models described by equations 4.3 and 4.4 onto the observational plane in order to fit the projected models to the temperature and density profiles previously determined. This fit then allows us to generate deprojected profiles for the temperature and density. Errors for these deprojected values are determined by performing a Monte Carlo search of the parameter space.
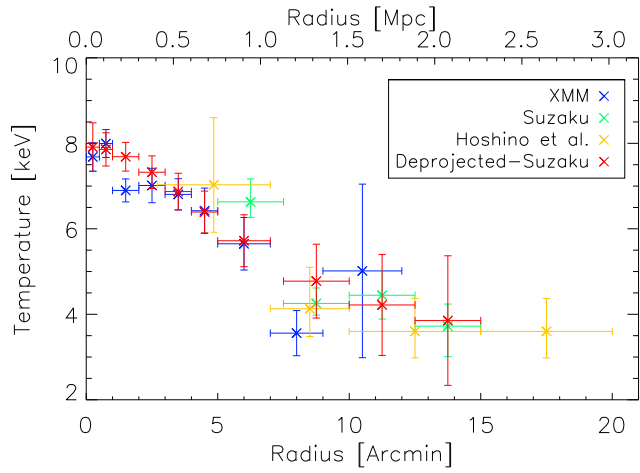
(a) **Abell 1413**: Our values agree with the Snowden et al. [2008] *XMM-Newton* values except at the outer bins, where we see a continuation of the falling temperature profile. Our profile agrees with the Hoshino et al. [2010] *Suzaku* values.
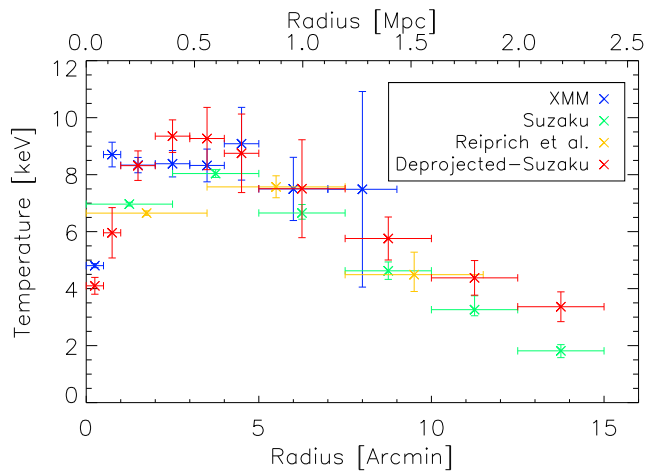
(b) **Abell 2204**: Our values agree with the Snowden et al. [2008] *XMM-Newton* values and with the *Suzaku* values of Reiprich et al. [2009]. We observe a continuation of the falling temperature profile to the outskirts.

Figure 4.2: The Temperature profiles for the clusters (Part 1)
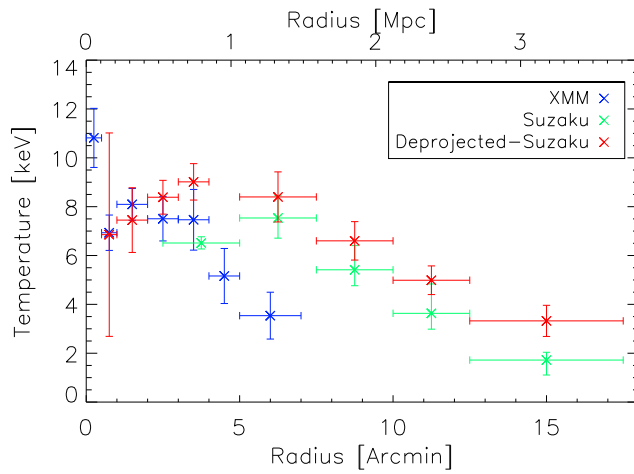
(a) **Abell 773**: Our values do not agree with the Snowden et al. [2008] *XMM-Newton* values, which have underestimated temperature values.
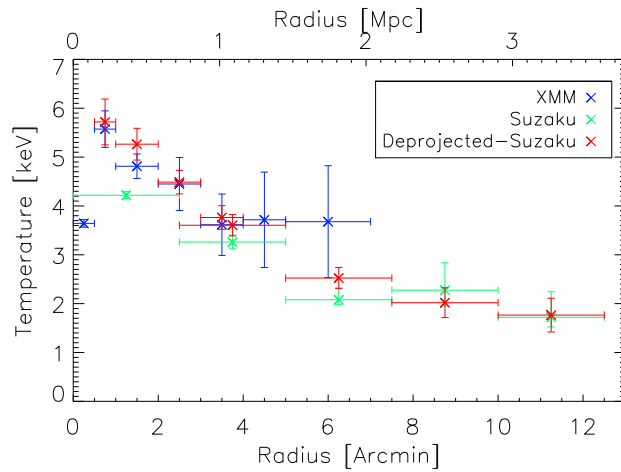
(b) **Abell 383**: Our values agree with the Snowden et al. [2008] *XMM-Newton* values within errors. While the individual values are overestimated for *XMM-Newton*, these values have very large errors

Figure 4.3: The Temperature profiles for the clusters (Part 2)
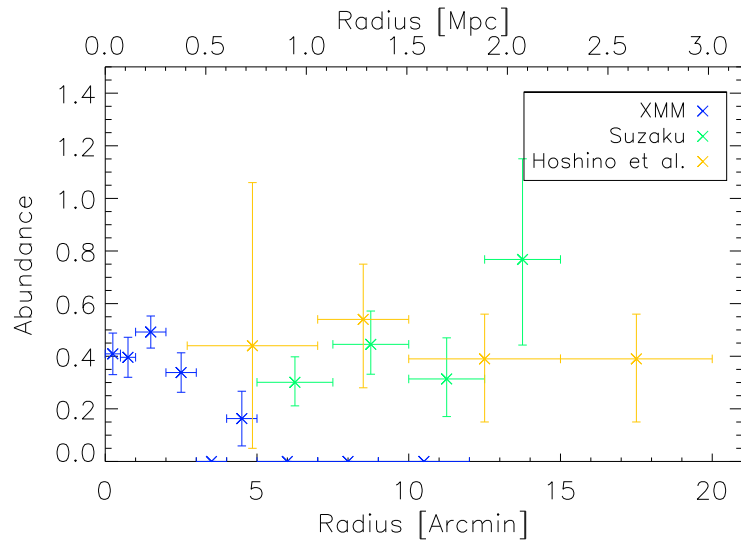
(a) **Abell 1413**: Our values disagree with the Snowden et al. [2008] *XMM-Newton* values but agree with the Hoshino et al. [2010] *Suzaku* values. Our profile suggests a flat metal abundance out to the outskirts.
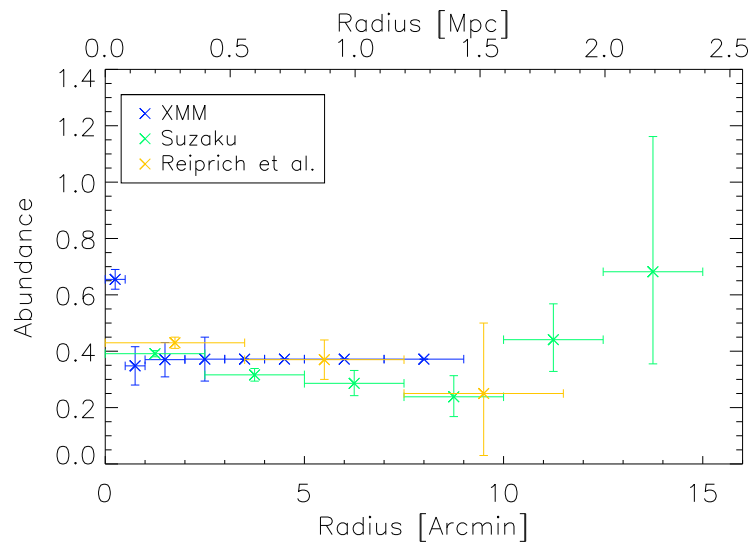
(b) **Abell 2204**: Our values disagree with the Snowden et al. [2008] *XMM-Newton* values but agree with the Reiprich et al. [2009] *Suzaku* values. Once again we observe a flat metal abundance out to the outskirts.

Figure 4.4: The Abundance profiles for the clusters (Part 1)
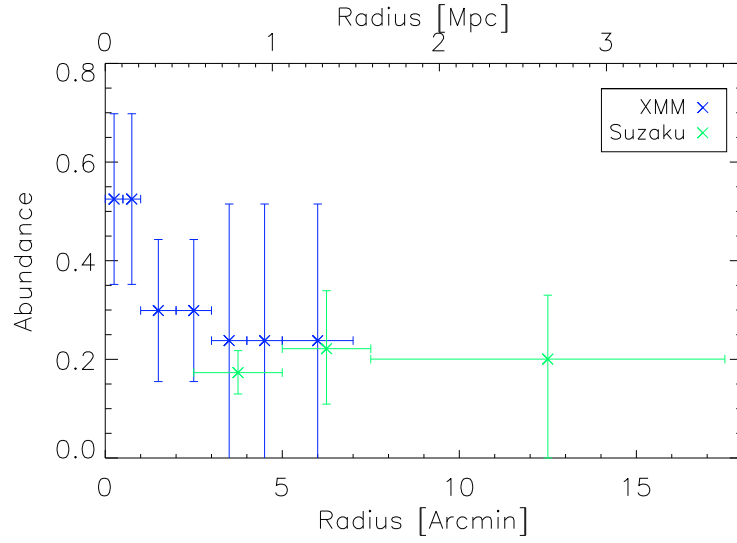
(a) **Abell 773**: Our values agree with the Snowden et al. [2008] *XMM-Newton* values. Once again, we observe a flat metal abundance out to the outskirts.
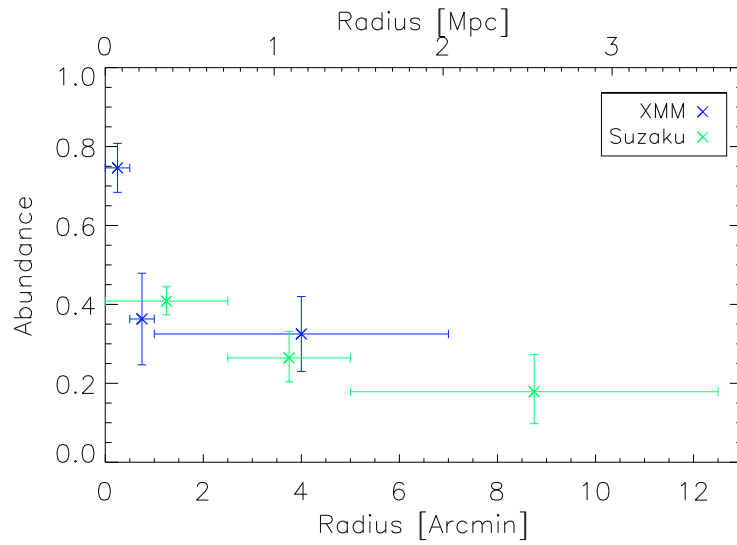
(b) **Abell 383**: Our values agree with the Snowden et al. [2008] *XMM-Newton* values. Here we notice a slightly falling metal abundance profile.

Figure 4.5: The Abundance profiles for the clusters (Part 2)
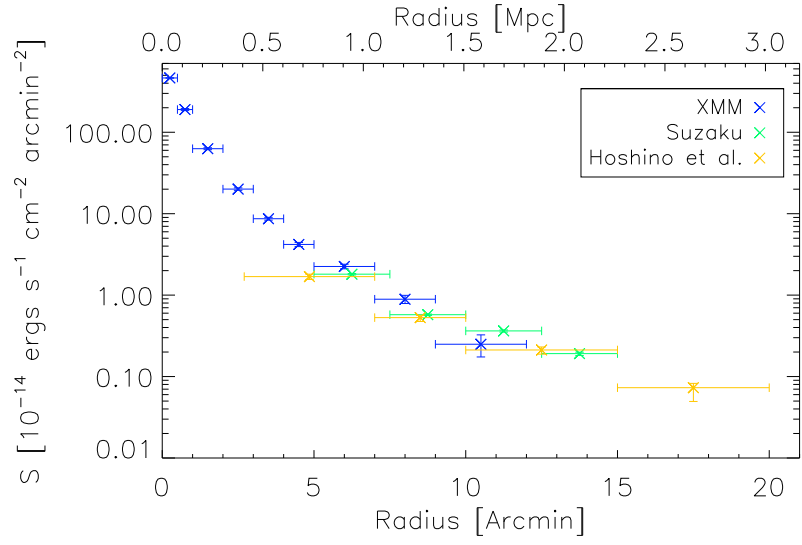
(a) **Abell 1413**: Our values agree with the Snowden et al. [2008] *XMM-Newton* values and the Hoshino et al. [2010] *Suzaku* values.
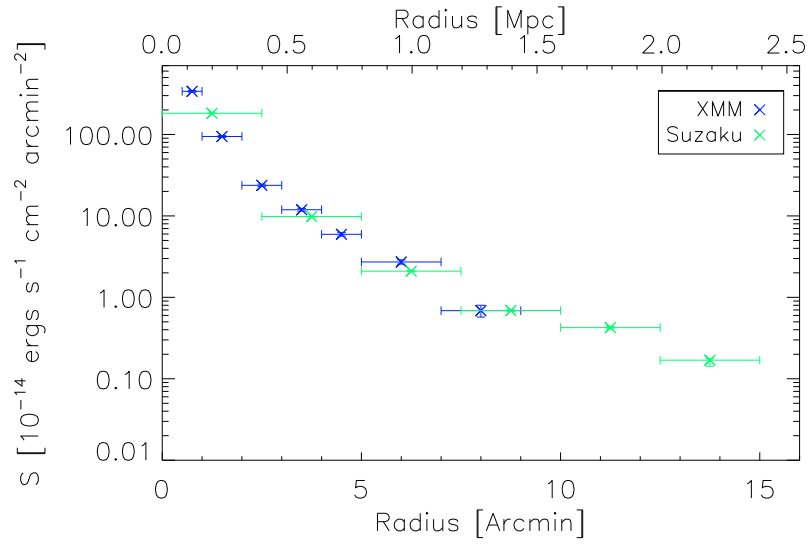
(b) **Abell 2204**: Our values agree with the Snowden et al. [2008] *XMM-Newton* values.

Figure 4.6: The Surface Brightness profiles for the clusters (Part 1)
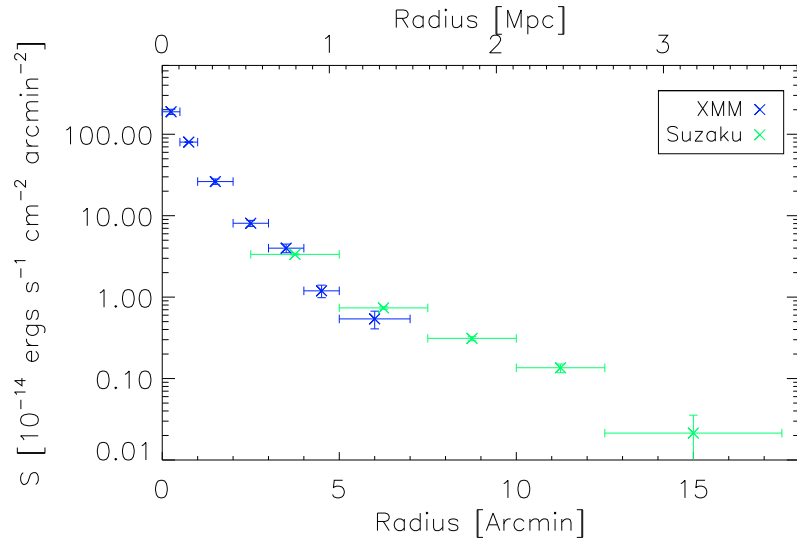
(a) **Abell 773**: Our values agree with the Snowden et al. [2008] *XMM-Newton* values.
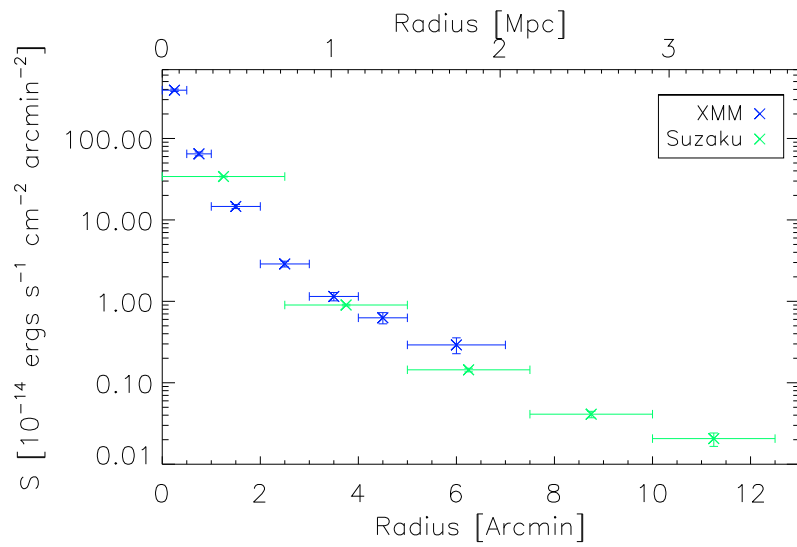
(b) **Abell 383**: Our values agree with the Snowden et al. [2008] *XMM-Newton* values.

Figure 4.7: The Surface Brightness profiles for the clusters (Part 2)
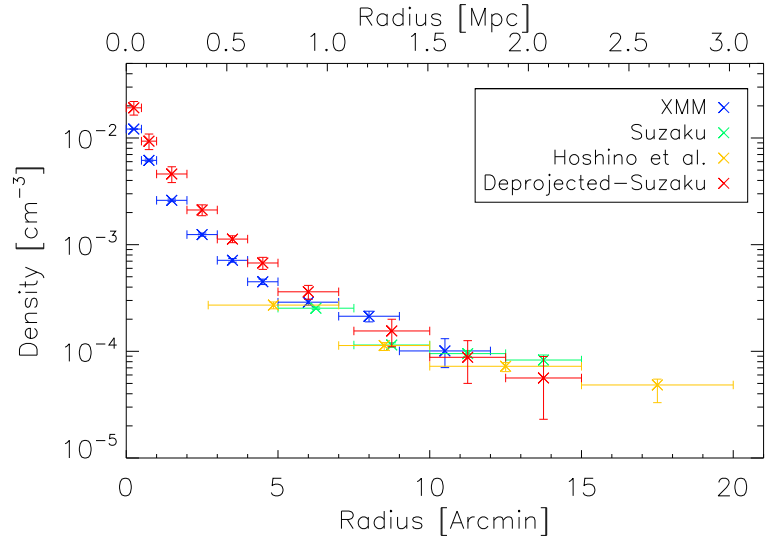
(a) **Abell 1413**: Our values agree with the Snowden et al. [2008] *XMM-Newton* values and the Hoshino et al. [2010] *Suzaku* values.
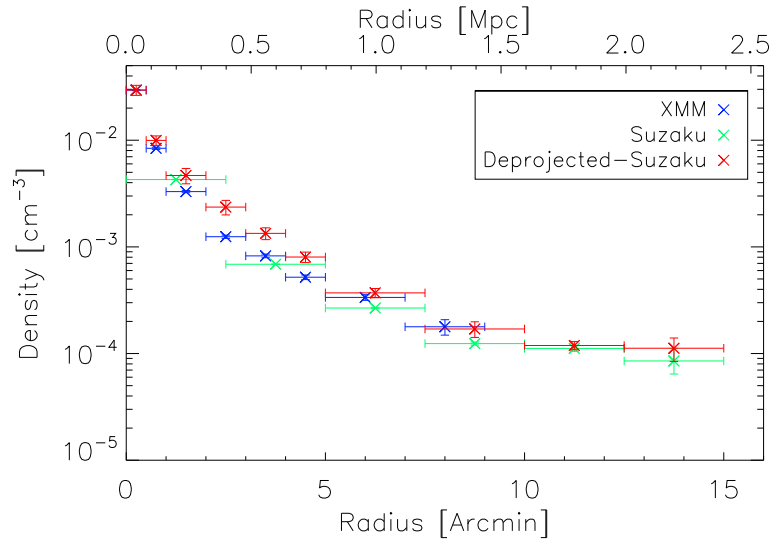
(b) **Abell 2204**: Our values agree with the Snowden et al. [2008] *XMM-Newton* values.

Figure 4.8: The Density profiles for the clusters (Part 1)
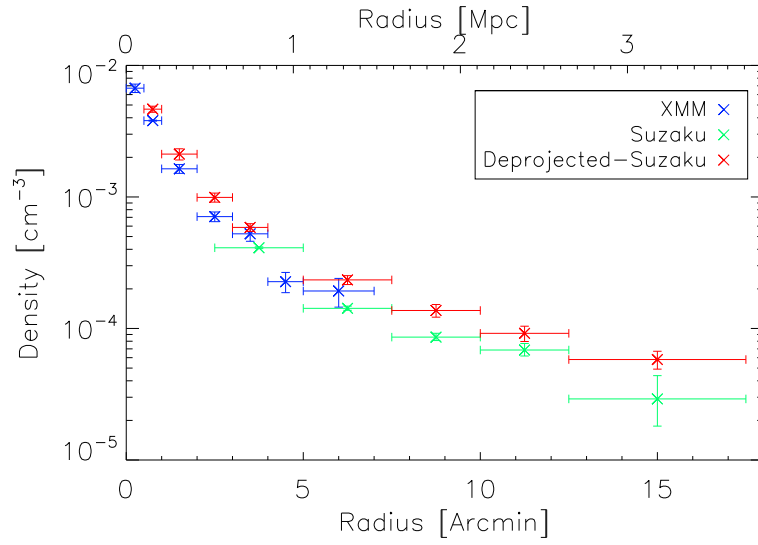
(a) **Abell 773**: Our values agree with the Snowden et al. [2008] *XMM-Newton* values.
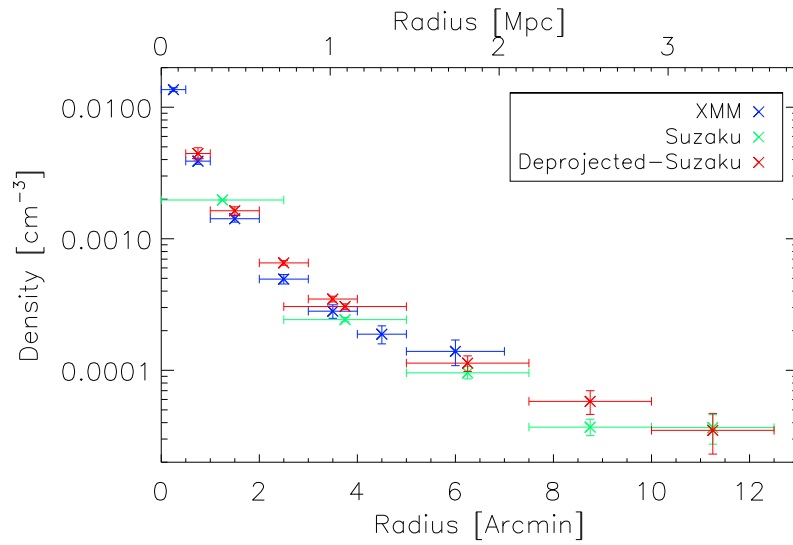
(b) **Abell 383**: Our values agree with the Snowden et al. [2008] *XMM-Newton* values.

Figure 4.9: The Density profiles for the clusters (Part 2)

4.3 Secondary Attributes

4.3.1 Total Mass

The total mass profiles for these clusters were calculated using two different methods. Both of our chosen methods were chosen for their ability to account for dark matter as well.

- **Method 1** (Thermal Model): This is the simplest and most common method for determining the total mass which includes both baryonic and dark matter. We use the analytic profiles of the deprojected temperature and density to calculate the mass using the hydrostatic equilibrium formula for the total mass enclosed at that radius [Vikhlinin et al., 2006].

$$M(< r) = -3.68 \times 10^{13} M_\odot \left[\frac{T(r)}{1 \ keV} \right] \left(\frac{r}{1 \ Mpc} \right) \left(\frac{d \log \rho_g}{d \log r} + \frac{d \log T}{d \log r} \right) \quad (4.5)$$

Here, $T(r)$ refers to the average temperature of the annulus in keV, r is the distance of the annulus from the center of the cluster and ρ_g is the mass density of the ICM. We assume the mean molecular weight of the ICM to be $\mu = 0.62$ [Vikhlinin et al., 2006].

- **Method 2** (NFW Model): We choose to use a second model in part to evaluate the validity of the commonly assumed thermal model. We choose the following model because it does not assume hydrostatic equilibrium and because it accurately accounts for dark matter [Navarro et al., 1997]. We use the deprojected temperature and density values to collectively fit a generalized

Navarro-Frenk White [Navarro et al., 1997] model (henceforth referred to as the NFW model; shown below) to the cluster density. We then use this NFW model for density to evaluate the total mass using the NFW model for density.

$$\rho(r) = \frac{\rho_0}{\frac{r}{R_s}\left(1 + \frac{r}{R_s}\right)^2}$$

$$M = \int_0^{R_{max}} \rho_r dV$$

(4.6)

Here, ρ_0 is a normalization parameter and R_s refers to a scaling radius.

This analysis was done using a script written by Helen Russell and Stephen Walker which fits the deprojected temperature to the following equation [Ettori et al., 2010].

$$T(r) = T_0 \frac{n_{gas,0}}{n_{gas}(r)} - \frac{\mu m_a G}{k_B n_{gas}(r)} \int_{r_0}^{r} \frac{n_{gas} M_{tot} dr}{r^2}$$

(4.7)

where n_{gas} is the gas density, $n_{gas,0}$ and T_0 are the density and temperature at the 'reference' radius r_0, k_B is Boltzmanns constant and M_{tot} is the total mass enclosed within the radius r.

Both the thermal and NFW methods give us similar results (Figures 4.10 and 4.11) except in the case of Abell 2204. In Abell 2204 (Figure 4.10b), the thermal model predicts that the total mass enclosed decreases within increasing radii, which is unphysical. This points directly to a breakdown in hydrostatic equilibrium at these radii possibly due to clumping, which would completely bias the results for the total mass. Sanders et al. [2009] also finds the existence of large cavities in the northern and southern regions of the clusters which could also bias our results. We

are confident in our Abell 2004 results since the *XMM-Newton* and *Suzaku* results are consistent.

4.3.1.1   Calculation of scaling parameters

There are two different size scales which are used to characterize any given cluster: r_{500} and r_{200}. These spatial scales refer to regions that compare the density at that radius to the critical density of the universe at that particular redshift. r_{500} is the radius from the center of the cluster at which the average density of the cluster enclosed is 500 times the critical density of the universe; r_{200} is the radius from the center of the cluster at which the average density of the cluster enclosed is 200 times the critical density of the universe. Similarly, M_{500} and M_{200} correspond to the total mass enclosed within r_{500} and r_{200} respectively.

The values of r_{500} and r_{200} are solved for iteratively using equation 4.5 and the total mass at these radii which is calculated as:

$$M_\delta = \frac{4}{3}\pi r_\delta^3 \delta \rho_{crit} \tag{4.8}$$

where ρ_{crit} is the critical density of the universe at a particular redshift and δ is 200 or 500 depending on the variable being calculated.

The results of this calculation are shown in Table 4.2. These values are biased by assuming hydrostatic equilibrium, which may not be accurate. This is especially important in the calculation of r_{200} and M_{200}, where a breakdown in equilibrium is expected, as evidenced in Abell 2204 where we see a lower value for M_{200} than M_{500}. This bias is also highlighted in Table 4.3 which compares the values of r_{200}
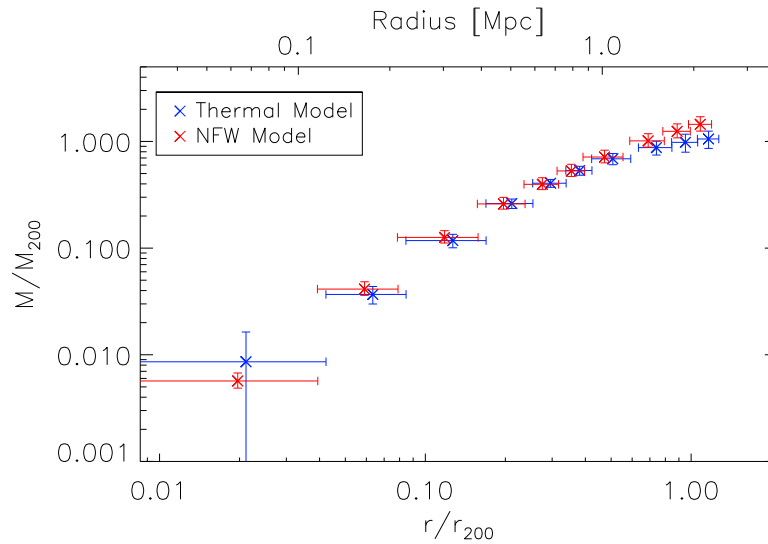
(a) **Abell 1413**: Both the thermal and the NFW models agree with each other. We see a slight discrepancy at large radii for the thermal model, suggesting a breakdown in the assumption of hydrostatic equilibrium.
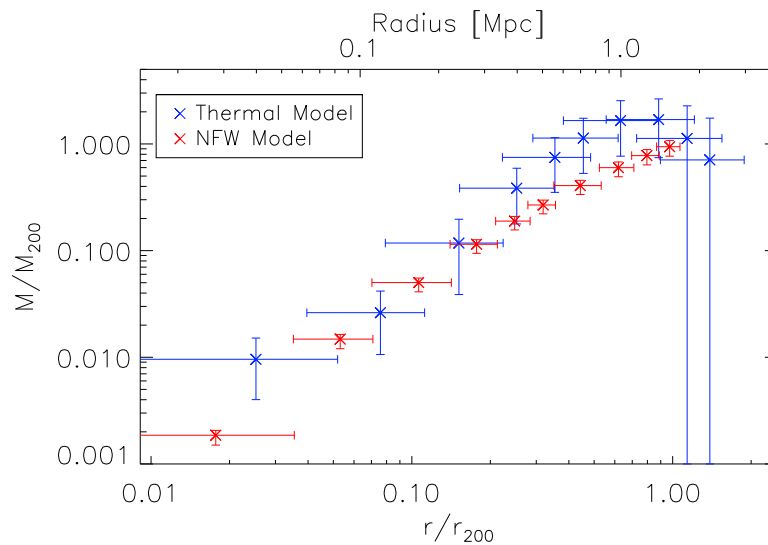
(b) **Abell 2204**: The calculation of the total mass using the thermal model gives very biased and unphysical results in the cluster outskirts, namely a lower total mass at large radii. This points to a breakdown in hydrostatic equilibrium.

Figure 4.10: The Total Mass profiles for the clusters (Part 1)

67
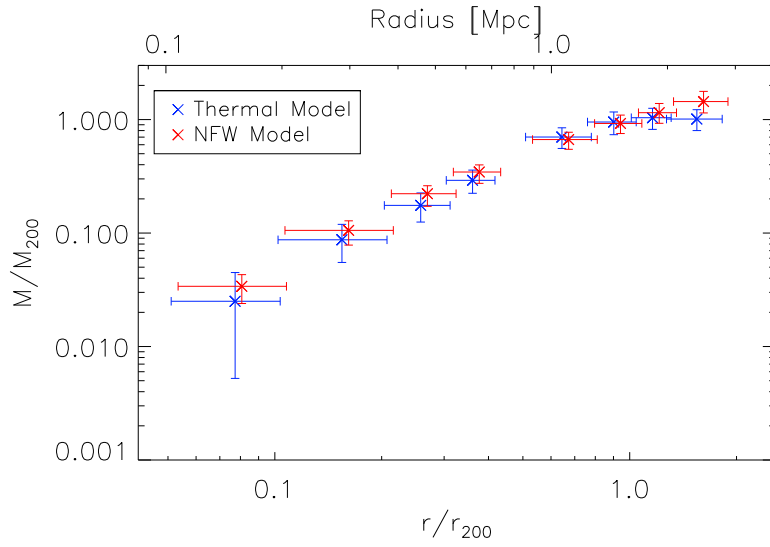
(a) **Abell 773**: Both the thermal and the NFW models agree with each other. We see a slight discrepancy at high radii for the thermal model, suggesting a breakdown in the assumption of hydrostatic equilibrium.
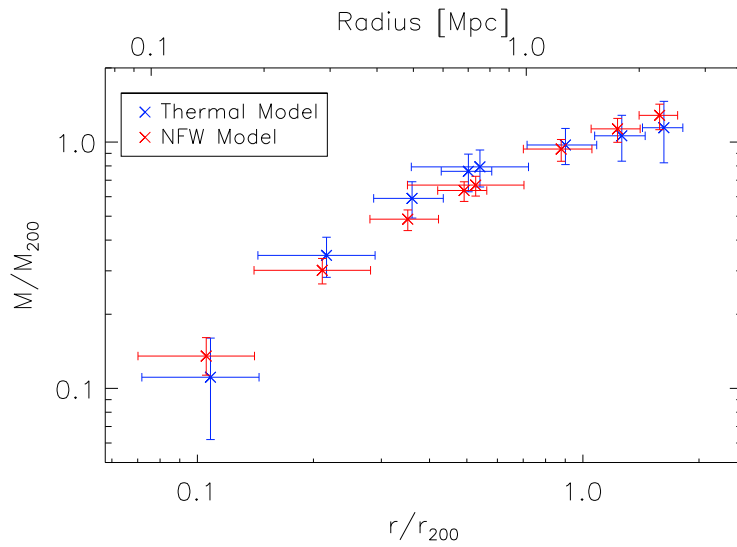
(b) **Abell 383**: Both the thermal and the NFW models agree with each other.

Figure 4.11: The Total Mass profiles for the clusters (Part 2)

and M_{200} for the two different mass calculation methods mentioned in section 4.3.1.

Cluster	r_{500} (arcmin)	M_{500} $10^{14}\ M_\odot$	r_{200} (arcmin)	M_{200} $10^{14}\ M_\odot$
A1413	8.24 ± 0.06	6.2 ± 0.15	11.8 ± 0.21	7.3 ± 0.37
A2204	8.7 ± 0.41	8.7 ± 0.98	10.7 ± 0.54	6.0 ± 1.4
A773	6.4 ± 0.56	8.0 ± 2.6	9.7 ± 0.63	12.0 ± 2.6
A383	4.9 ± 0.25	2.7 ± 0.36	6.9 ± 0.31	3.0 ± 0.44

Table 4.2: The values of r_{500} and r_{200}: and the corresponding values of M_{500} and M_{200} calculated using the thermal model (equation 4.5), which assumes hydrostatic equilibrium.

These scaling parameters are also extremely sensitive to the type of data being used. The Planck Collaboration et al. [2013b] studied instrumental effects on the observed values of the Sunyaev-Zeldovich (SZ) flux which is then used for determining the scaling parameters. They note the systematic differences in SZ flux values obtained using the two different satellites *Chandra* and *XMM-Newton*, and investigate the possible causes of the difference between the two data sets. They suggest that the uncertainties in the X-Ray measurements are dominated by errors in the temperature uncertainties caused by calibration issues. The *Chandra* values for the SZ flux were systematically larger than the *XMM-Newton* values. They also study a discrepancy in values obtained from different analysis methods which stems from different treatments of background estimation and the effect of point sources in

Cluster	$r_{200}^{Thermal}$	$M_{200}^{Thermal}$	r_{200}^{NFW}	M_{200}^{NFW}
	(arcmin)	$10^{14}\ M_\odot$	(arcmin)	$10^{14}\ M_\odot$
A1413	11.8 ± 0.21	7.3 ± 0.37	$12.7^{+0.60}_{-0.45}$	$7.0^{+1.01}_{-0.69}$
A2204	10.7 ± 0.54	6.0 ± 1.4	$14.1^{+0.42}_{-0.84}$	$15.0^{+1.3}_{-2.5}$
A773	9.7 ± 0.63	12.0 ± 2.6	$9.3^{+0.39}_{-0.55}$	$11.0^{+1.4}_{-1.8}$
A383	6.9 ± 0.31	3.0 ± 0.44	$7.1^{+0.17}_{-0.22}$	$3.2^{+0.24}_{-0.29}$

Table 4.3: The values of r_{200} and M_{200} as calculated using the thermal and NFW methods described in section 4.3.1.

the analysis. A similar bias is expected between the values we calculated using the *Suzaku* data when compared to other satellites. We, however, do not have enough data values to completely quantify this bias.

4.3.2   Pressure

The pressure profiles for each of these clusters were calculated as $P = n_e kT$ where P is pressure, n_e is electron density, and kT is temperature. The characteristic scale for cluster pressure, P_{500} is calculated as:

$$P_{500} = 1.65 \times 10^{-3} h(z)^{8/3} \times \left[\frac{M_{500}}{3 \times 10^{14} h_{70}^{-1} M_\odot} \right]^{2/3} h_{70}^2 \text{ keV cm}^{-3} \qquad (4.9)$$

where $h(z)$ is the ratio of the Hubble constant at redshift z to its present value.

As the normalization P_{500} is directly proportional to M_{500} and thus r_{500}, these values heavily influence the cluster pressure profile.

The scaled pressure profile is typically characterized using the analytical formulation for the generalized Navarro-Frenk White profile [Navarro et al., 1997, Nagai et al., 2007a]:

$$\mathbb{P}(x) = \frac{P_0}{(c_{500}x)^\gamma \left[1 + (c_{500}x)^\alpha\right]^{(\beta-\gamma)/\alpha}} \tag{4.10}$$

where $\mathbb{P}(x) = \frac{P}{P_{500}}$ and $x = \frac{r}{r_{500}}$ and where P_0, c_{500}, α, β and γ are respectively the pressure normalization, the concentration parameter defined at r_{500}, the slope defined in the intermediate region ($x \sim 1/c_{500}$), the slope defined in the outer regions ($x >> 1/c_{500}$) and the slope defined in the central region ($x << 1/c_{500}$). However, observations of real pressure profiles systematically deviate from this NFW model. The systematic deviation can be expressed as a function of the total mass. Adding this mass dependence to the pressure model can generate a model that now accurately describes all clusters which we shall henceforth dub a 'universal' pressure profile.

Currently there are two possible models that take into account this mass dependence: the Planck Pressure Profile and the Arnaud Pressure Profile.

Planck Collaboration et al. [2013a] defines a 'universal' pressure profile as:

$$\frac{P(r)}{P_{500}} = \mathbb{P}(x) \left[\frac{M_{500}}{3 \times 10^{14} h_{70}^{-1} M_\odot}\right]^{0.12} \tag{4.11}$$

with the parameters for equation 4.10 $[P_0, c_{500}, \gamma, \alpha, \beta]$ set as [6.41, 1.81, 0.31, 1.33, 4.13]. This is plotted against our pressure profiles in Figure 4.12.

We notice that our values do not agree with this version of the pressure profile. There is mismatch in the shape of the profile versus our values causing our values to deviate to larger values at low radii, but not see quite a large deviation at large
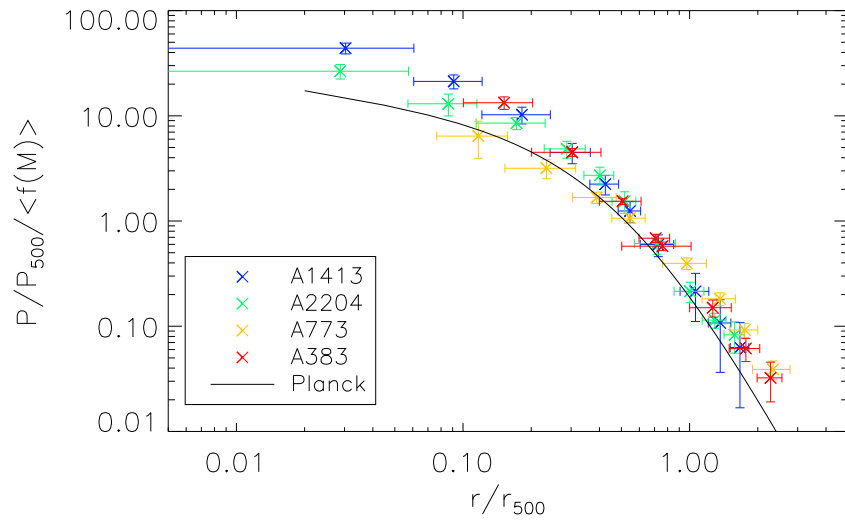
Figure 4.12: Comparison of Suzaku data to the Universal Planck Pressure Profile: The colored points refer to the individual clusters studied in this paper. The line refers to the Planck Pressure Profile (equation 4.11).

radii. This can be attributed to the fact that *Planck* PSF is quite large causing the points to be not well sampled at low radii. There is also a large dispersion seen in the *XMM-Newton* pressure values at low radii, which have also been included in Planck Collaboration et al. [2013a].

Arnaud et al. [2010] defines a slightly different 'universal' pressure profile which includes an additional radial dependence for the mass dependence in the pressure profiles as shown below:

$$\frac{P(r)}{P_{500}} = \mathbb{P}(x) \left[\frac{M_{500}}{3 \times 10^{14} h_{70}^{-1} M_\odot} \right]^{\alpha_p + \alpha_p'(x)} \tag{4.12}$$

with the parameters for equation 4.10 $[P_0, c_{500}, \gamma, \alpha, \beta]$ set as [8.403, 1.177, 0.3081, 1.0510, 5.4905]. The additional parameters α_p and $\alpha_p'(x)$ are defined as:

$$\alpha_p = 0.12$$
$$\alpha_p'(x) = 0.10 - (\alpha_p + 0.10 \frac{(x/0.5)^3}{1 + (x/0.5)^3} \tag{4.13}$$

This is compared to our scaled pressure profiles in Figure 4.13.

Here too, we see that our values are not in good agreement with Arnaud et al. [2010] profile. But unlike previously, we see a problem in the normalization of the profile versus our values. This bias too can be explained by the sample utilized in Arnaud et al. [2010]: large deviations at low radii from the *XMM-Newton* values and their extrapolation to high radii by using simulated data.

The values we observed in our clusters are also systematically higher than both the Planck and Arnaud 'universal' profiles. This is likely due to the bias in the values of r_{500} and M_{500} introduced by clumping. Such a bias would create a normalization error and not an error in the overall shape of the profile. While our
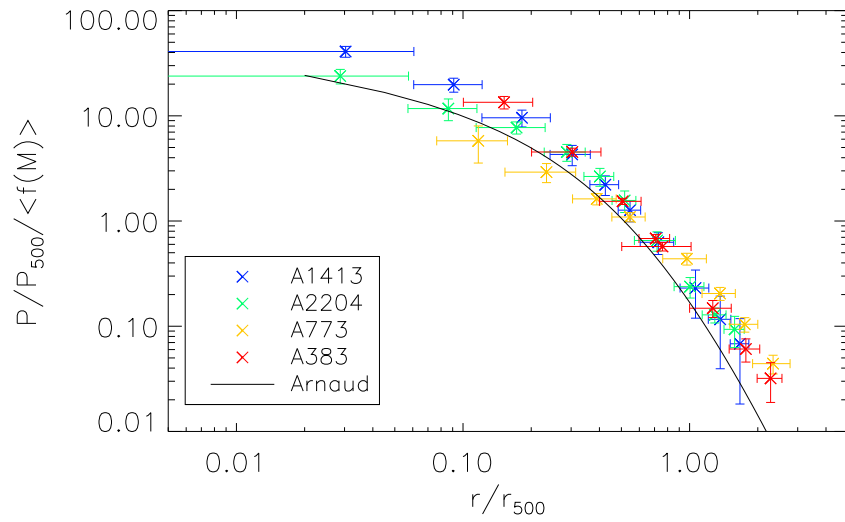
Figure 4.13: Comparison of Suzaku data to the Universal Arnaud Pressure Profile: The colored points refer to the individual clusters studied in this paper. The line refers to the Arnaud Pressure Profile (equation 4.12).

data show an offset to both the Planck and Arnaud profiles, the Arnaud pressure profile gives a better fit to the data, suggesting the existence of radial dependence in pressure profiles as seen in the Arnaud profile.

4.3.3   Entropy

We also calculated the entropy profile for these clusters using $S = kTn_e^{-2/3}$, where kT and n_e refer to the temperature and the electron density respectively. As derived in section 1.2, Voit et al. [2005], Walker et al. [2012a] both present a picture of the entropy profile which can be described as a power law that obeys $r^{1.1}$.

Voit et al. [2005] describes a universal entropy profile given by:

$$\frac{S}{S_{200}} = 1.32 \left(\frac{r}{r_{200}}\right)^{1.1} \tag{4.14}$$

The entropy normalization S_{200} is defined as $S_{200} \equiv T_{200}\overline{n_e}^{-2/3}$, where $\overline{n_e}$ is the mean electron density of the universe inside r_{200} and T_{200} is the characteristic temperature scale defined as $T_{200} \equiv \frac{GM_{200}\mu m_p}{2r_{200}}$. This has been plotted in Figure 4.14.

In Figure 4.14 we see an excess in the entropy values at smaller radii. This excess has been observed and well studied as an extra mass dependence [Voit et al., 2005] not included in numerical simulations that include only gravity. This mass dependence disappears at larger radii. This central excess has also been seen as a possible signature of AGN feedback at the cores of clusters. There is also a slight flattening of the entropy profile at larger radii in our analysis.

These deviations are corrected when we apply the universal entropy profile
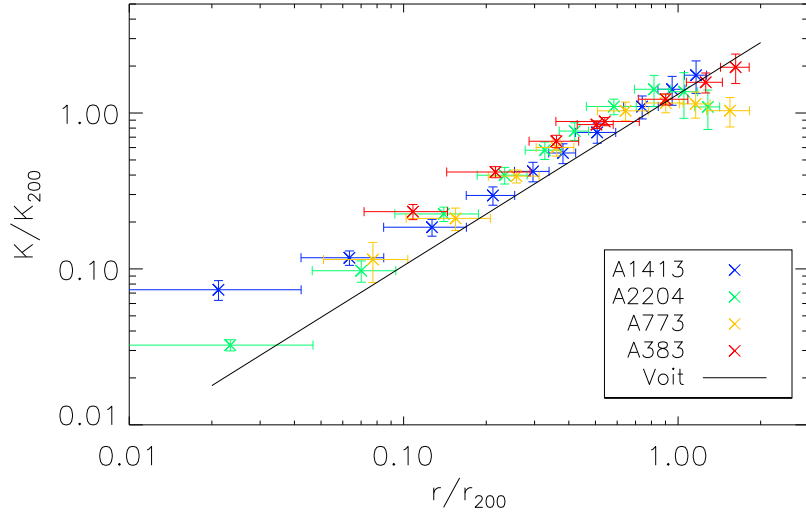
Figure 4.14: Comparison of Suzaku data to the Universal Entropy Profile [Voit et al., 2005]: The scaled entropy of each of the clusters plotted as a function of r/r_{200}. The solid line represents the Universal Entropy Profile as described in Voit et al. [2005].

defined in Walker et al. [2012a]:

$$\frac{S}{S(0.3r_{200})} = 4.4 \left(\frac{r}{r_{200}} \right)^{1.1} e^{-(r/r_{200})^2} \tag{4.15}$$

Unlike the Voit profile, the entropy values in the Walker profile are scaled to $S(0.3\ r_{200})$, which is the entropy calculated at $0.3r_{200}$. This profile models a turnover of the entropy profile at high radii as shown in Figure 4.15.

While we do not see as strong a turnover in the entropy profile in our data as expected from the Walker profile, the flattening seen is indicative of additional phenomena occurring at these outer regions of the clusters. This flattening could occur as a result of a weakening of accretion shock for older clusters. A similar situation can arise due to clumps of gas in the outskirts of clusters, which would

76
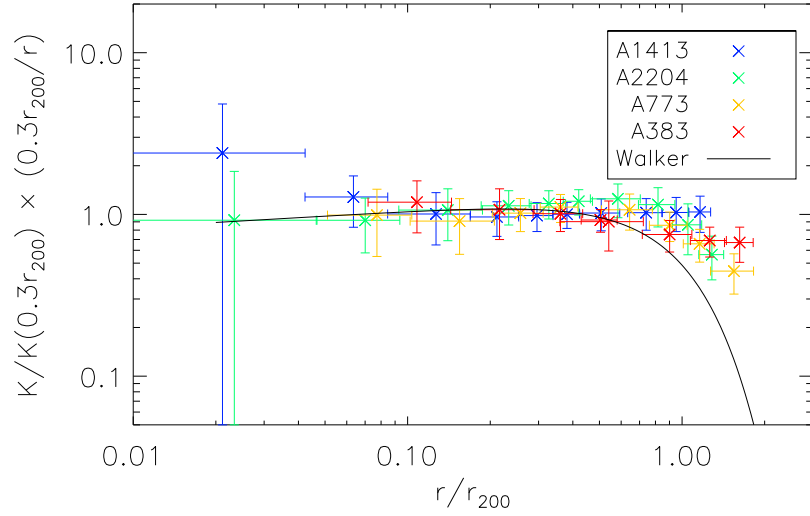
Figure 4.15: Comparison to the Universal Entropy Profile [Walker et al., 2012a]: The scaled entropy of each of the clusters plotted as a function of r/r_{200}. The solid line represents the Universal Entropy Profile as described in Walker et al. [2012a].

cause a bias towards higher density measurements. A third alternative is that the entropy deficit in the outskirts is caused by low electron temperatures. Shock fronts heat the ions instantaneously, while electrons gain equilibrium on a much larger equilibrium timescale [Simionescu et al., 2012]. Determining the exact cause of this observed flattening requires additional studies in the future with larger data sets or high resolution studies of nearby clusters (refer to section 5.2).

While the precise mechanism causing deviations in the profile is not obvious from our study, it is clear that the central excess indicates non-thermal heating and that the flattening at large radii indicates additional non-gravitational processes occurring in cluster outskirts.

4.3.4 Baryonic Gas Fraction

We also calculate the baryonic gas fraction, the ratio of the gas mass to the total mass enclosed within a particular radius. These values were calculated separately for the two different methods of measuring the total mass and are shown in Figures 4.16 and 4.17. In all cases, it is observed that the baryonic fraction does increase beyond the cosmic fraction value. This suggests the existence of clumps in these outer regions of clusters [Eckert et al., 2013] because our models will overestimate the density if they do not account for clumping.

The case of Abell 2204 is particularly unique in this data group. As seen in Figure 4.10, there is a breakdown in the hydrostatic equilibrium manifested as a decreasing total mass at larger radii. This causes the anomalous profile seen in Figure 4.16b. While Abell 2204 is the most extreme example, all our clusters defy expectation by exhibiting baryonic fractions that exceed the cosmic value in the outskirts.

4.4 Clumping

Clumping in the outskirts has been predicted by numerical simulations [Roncarelli et al., 2006] and may explain the anomalous behavior exhibited by these clusters in the outskirts. It is the most convincing explanation for all of the observed discrepancies between our data and the universal profiles.

Our overestimated density values is rooted in the way we observed the intensity of the bremsstrahlung radiation. This intensity is related to the average of the
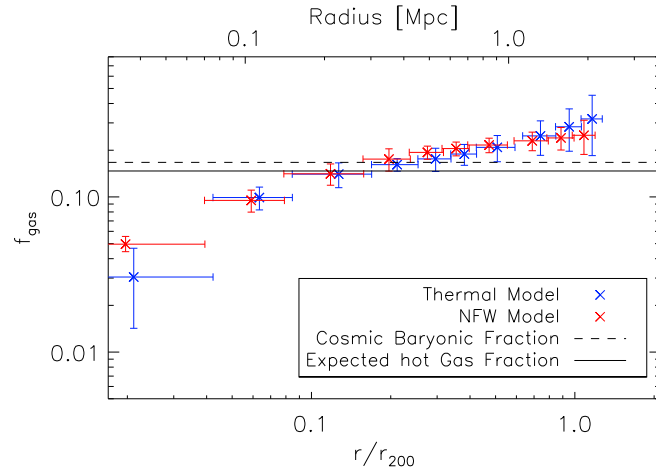
(a) **Abell 1413**: The gas fraction derived using both thermal and NFW methods agree with each other. However, in both cases, the fraction increases to a value higher than the cosmic baryonic fraction.
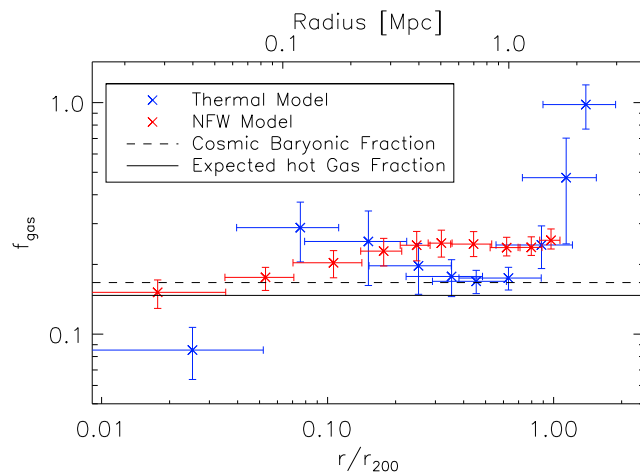
(b) **Abell 2204**: Like the total mass calculation of Abell 2204 (Figure 4.10b), there is a discrepancy between the two calculation methods. Once again, we observe that the fraction increases to a value higher than the cosmic baryonic fraction, this time beginning at low radii.

Figure 4.16: The baryonic gas fraction profiles for the clusters (Part 1). Also plotted are the values of the Cosmic Baryonic Fraction.
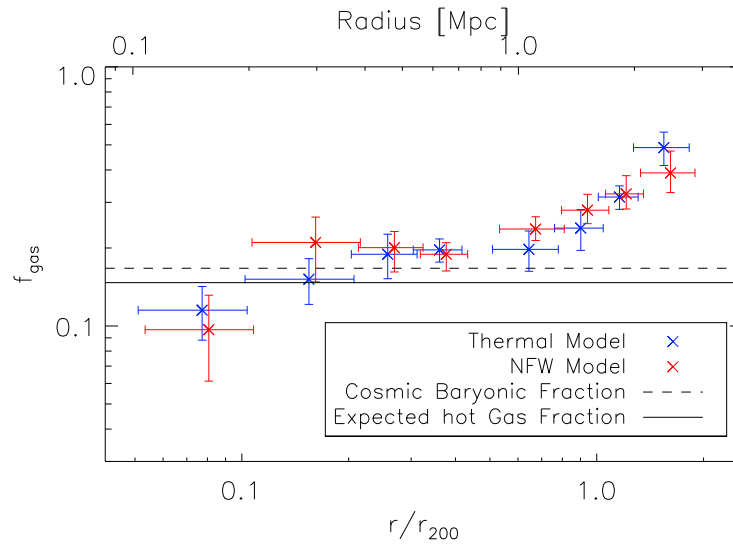
(a) **Abell 773**: The gas fraction derived using both methods agree with each other. Similar to Abell 2204 (Figure 4.16b), this profile shows an anomalous behavior with the fraction increasing beyond the cosmic baryon fraction at very low radii.
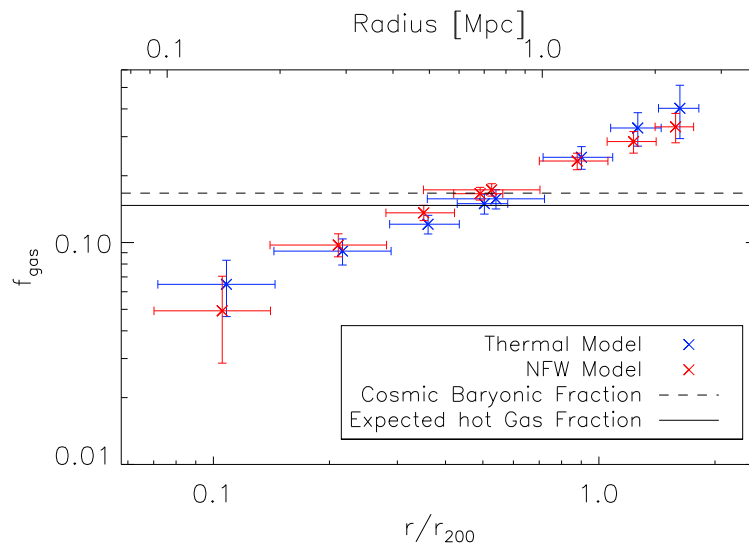
(b) **Abell 383**: The gas fraction derived using both methods agree with each other. However, in both cases, the fraction increases to a value higher than the cosmic baryonic fraction.

Figure 4.17: The baryonic gas fraction profiles for the clusters (Part 2). Also plotted are the values of the Cosmic Baryonic Fraction.

density squared $< n_e^2 >$ rather than the average density, $< n_e >$.

$$I_\nu \propto \int n_e^2 T^{-1/2} dl \qquad (4.16)$$

So if the gas is clumpy, the average density estimated by this method will be over-estimated. This would in turn cause an underestimation of the entropy calculated ($\propto n_e^{-2/3}$) as well as an over-estimation of the pressure ($\propto n_e$) and the baryonic gas fraction calculated.

Clumping in the outskirts could also introduce another bias in our corrections. Urban et al. [2011] has discovered that if gas clumping is present and if these clumps are in pressure equilibrium with their surroundings, they would be at a lower temperature than their surroundings. This would could cause the average temperature to be biased to lower values. However, Walker et al. [2013] notices no such biases in the analysis of the *Centaurus* cluster. We have not compared our data to temperature models, so we cannot definitively say whether our data also show these biases.

In the case of Abell 2204, there have been observed cavities in the northern and southern regions of the clusters. This would also cause a bias in the density and temperature calculations for this cluster. The unphysical values calculated for this cluster can be attributed to these cavities which we have not modeled for.

Chapter 5:   Conclusions

This thesis examines the very outer regions, or the outskirts, of galaxy clusters using X-ray spectroscopy. We have been able to achieve unique insights into the physics governing these regions as well identify some of the key issues involved in the processing of these low signal to noise data.

5.1   Summary of Results

We utilized *Suzaku* data for four clusters (Abell 1413, Abell 2204, Abell 773 and Abell 383) to draw generalized profiles for temperature, density, entropy, pressure and baryonic fraction.

In Chapter 3, we outlined the various data effects one must consider while analyzing cluster data. Of particular importance was the proper analysis of the background and the various issues involved in the spectral and image analysis of the data. In order to get a better handle on the background diagnostics, we utilize *Chandra* data to remove point sources, which helps constrain the cosmological background.

We chose to model the data between 0.7–7.0 keV to account for data limitations and to eliminate regions where contamination is poorly modeled. To further under-

stand the effect this has on the analysis, we ran simulations of the clusters Abell 773 and Abell 383 over the ranges of 0.5–10.0 keV and 0.7–7.0 keV. We notice no significant deviations between the two energy ranges. We modeled the background using an APEC model for the thermal components and a power law to account for the unresolved point sources in the cosmic background. We notice that the exact value of the thermal background has little effect on the parameters. The proper modeling of the cosmic background is very significant as it becomes the dominant source of error.

Using this analysis, we were able to directly obtain temperature, surface brightness, abundance, and density for the clusters. All of the values agree with latest available literature within errors. However, we do see deviations from the older *XMM-Newton* results, highlighting the effects of erroneous extended emission analysis.

These primary parameters were then deprojected using three dimensional models for temperature and density [Vikhlinin et al., 2006]. Using these deprojected values, we compared our calculated values of entropy and pressure to their respective universal profiles.

The pressure profiles we compiled for the clusters yield higher values than the expected universal pressure profile [Arnaud et al., 2010, Planck Collaboration et al., 2013a]. We believe that this deviation can be attributed to the bias we observed with the calculations of the scaling parameters, r_{500}, M_{500}, r_{200} and M_{200}. This bias occurs due to the variation in the parameters obtained using different methods of analysis and different instruments [Planck Collaboration et al., 2013b]. Similarly,

we calculated the entropy profile for each of the clusters, and compared the same to the universal profile. Here, we see agreement with previously observed deviations from the universal profile. We also observe an excess in entropy values at smaller radii when compared to the universal entropy profile according to Voit et al. [2005]. While the Walker et al. [2012a] profile accounts for the observed turnover at large radii, our results do not see as strong a turnover at larger radii as seen in this Walker et al. [2012a] profile.

Finally, we calculated the baryonic fraction profiles for each of the clusters. For all the clusters, we observe values that significantly exceed the expected cosmic baryonic fraction at r_{200}. This seems to suggest the existence of clumps in the outskirts of clusters. Of particular interest is the cluster Abell 2204, where we observe an obvious breakdown in hydrostatic equilibrium in the very outskirts, which could be due to clumping. Our unphysical observation that $M_{200} < M_{500}$ is likely due to the breakdown in the assumption of hydrostatic equilibrium in the calculation of these scaling parameters.

We have shown that, in spite of the variety of the temperature profiles chosen (falling, rising, constant) seen in the *XMM-Newton* [Snowden et al., 2008], all of our clusters actually having a fall ling temperature profile out to the outskirts which matches up to the theoretical expectations. It also highlights the inaccuracies seen in modeling cluster outskirts using *XMM-Newton* data. For the first time, we also carried out side-by-side calculations of the total mass using two different methods: the assumption of hydrostatic equilibrium and the modeling using the NFW model. Comparing these, we notice that the assumption of hydrostatic equilibrium

to characterize the outskirts may be false. This is especially obvious in the case of Abell 2204, where we obtain unphysical results while calculating the mass using the assumption of hydrostatic equilibrium.

Our comparisons to the two forms of the 'universal' pressure profile, show that there are deviations in both the shape and normalization for our data. This suggests the possibility of addition mass and radial dependencies that need to be accounted for to make it truly 'universal'. We also compared our results to the 'universal' $r^{1.1}$ entropy profile. In line with previous literature, we too observe a central excess in the entropy that suggests non-thermal heating processes and a flattening of the profile in the outskirts. Our calculations of the baryonic gas fraction not only suggest that the gas fraction in the outskirts is indeed much higher than expected, but that this may be the case even at lower radii. Clumping is the most convincing possibility that could explain some (if not all) of the discrepancy seen at large radii, as this could account for an over-estimation of the pressure, an under-estimation of the entropy and over-estimation of the baryonic gas fraction.

5.2   Future Science

This thesis helps to answer the question of how temperature varies in the cluster outskirts and the question of why observed cluster profiles deviate from previously developed universal models. However, there are still unanswered questions, some of which are:

- Is the background characterization accurate?

- Are the universal profiles for entropy and pressure truly universal?

- Is clumping the true solution to the increased baryonic fraction in the very outskirts?

- What role do the metallic abundances of the clusters in the outskirts play?

To answer these questions and more requires a two-pronged approach: detailed observations of nearby clusters to maximize resolution of the clusters and larger surveys of multiple clusters.

For this purpose, we have already obtained *Suzaku* data for several more clusters. We hope to extend our analysis to complete the entire sample. This will help us to improve our statistics when studying the validity of the universal profiles for entropy and pressure. This will also help to pick out anomalous behavior of individual galaxy clusters. In addition to extending this axisymmetric study of clusters, we can also study the non-axisymmetry found in some clusters. The aforementioned sample, however, only includes relaxed clusters. Similar surveys should be done which includes unrelaxed clusters to complete a universal sample.

Another topic which has been untouched in this thesis is the role of chemical abundance in the evolution of clusters. There has been indication of early metal enrichment in the outskirts of clusters, and the implications of such a scenario are manifold:

- All massive clusters would have a level of enrichment similar to the cosmic value at $\frac{1}{3}$ of the solar metallicity.

- The warm-hot intergalactic medium in large-scale structure filaments connecting to massive clusters would be metal-rich, which will be detectable using high-spectral resolution instruments.

- If the material currently falling into massive clusters is iron-rich, this indicates that the accreting material is being accelerated by the accretion shocks. This makes cluster accretion an important source of high energy cosmic rays.

Looking further out into the future, the *Astro-H* mission, which will be launched in 2015, promises great results in this area. The satellite houses two soft X-ray systems: the Soft X-ray Spectroscopy System and the Soft X-ray Imager (SXI). The satellite will have a similar low background orbit as the *Suzaku* satellite. The spectroscopy system will have a X-ray Calorimeter Spectrometer (XCS) which will have a much better energy resolution than XIS. The big advantage will be the X-ray Imaging system which provides a better field of view, that can be exploited to provide views of more clusters out to r_{200}. The better angular resolution is also helpful as it helps minimize the area lost to bright point sources and to maximize the depth of the observations which will help to minimize cosmic variance.

This thesis is the first important step in creating a fiducial data set for more detailed comparisons to high resolution simulations to further our understanding cluster outskirts. More in-depth studies of the full *Suzaku* sample will shed more light on the 'universality' of parameter profiles and on the physical processes occurring in outskirts.

Appendix A: Spectral Fits of the Cluster Data

This section shows the fits achieved for each of the clusters using the method outlined in 3.2. We present the spectra extracted from each annulus, for each pointing and for each `XIS` detector used and the corresponding model fit. In each case, the *red* line depicts the contribution from the cluster emission, *blue* the galactic thermal background and *green* the extragalactic background. The *black* solid line represents the total model i.e. the sum of all the individual components. The spectra are shown over the modeled range of 0.7–7.0 keV. In some cases, the spectra are cut-off at 5.5 keV. This was done to excise the two ^{55}Fe calibration sources (Mn I Kα and Kβ) that appear at 5.9 keV and 6.5 keV.

A.1 Abell 1413

Presented below are the *Suzaku* pointings for Abell 1413 we utilized for this analysis. The observation details are shown below in Table A.1.

Pointing #	Observation ID	Comments
1	805059010	Proposed Data
2	805060010	Proposed Data
3	800001010	Archival Data [Hoshino et al., 2010]
4	805061010	Proposed Data

Table A.1: The *Suzaku* data on Abell 1413 used for this analysis

For pointings 1, 2 and 4, we use only detectors `XIS` 0, `XIS` 1 and `XIS` 3 for the analysis. For pointing 3, we used the `XIS` 2 detector in addition to `XIS` 0, 1 and 3 as it was observed before the detector was damaged.

(a) XIS 0

(b) XIS 1

(c) XIS 3
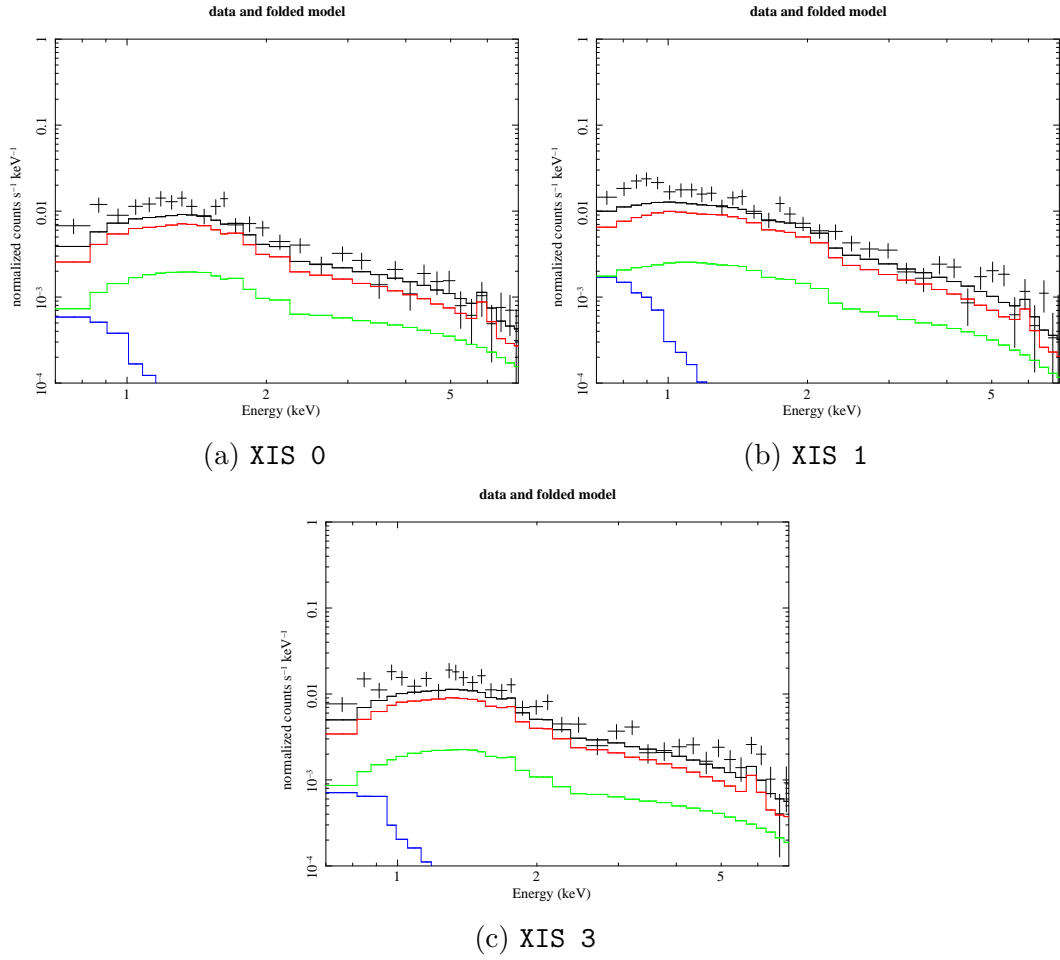
Figure A.1: The spectral fits for Annulus 3 (refer Table 3.1) of Abell 1413 for the first pointing

(a) XIS 0

(b) XIS 1

(c) XIS 3
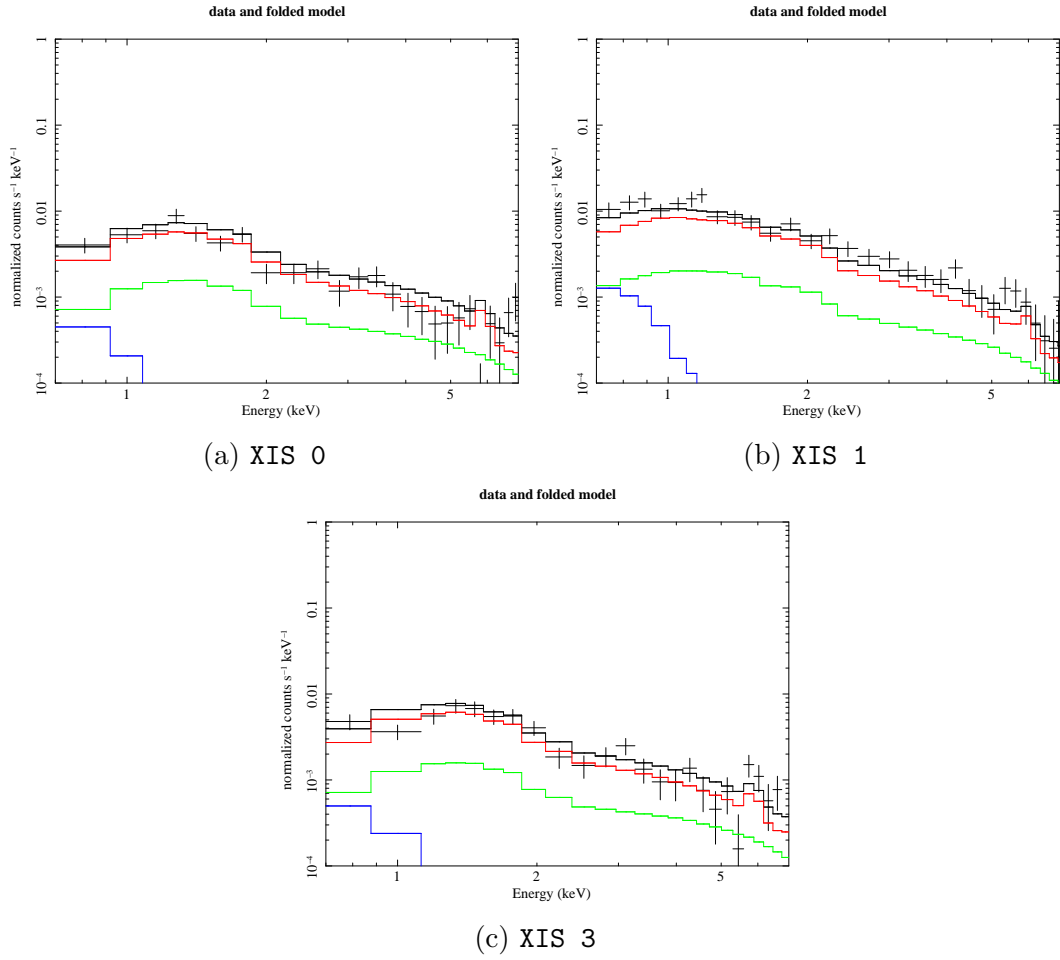
Figure A.2: The spectral fits for Annulus 3 (refer Table 3.1) of Abell 1413 for the second pointing

(a) XIS 0

(b) XIS 1

(c) XIS 2

(d) XIS 3
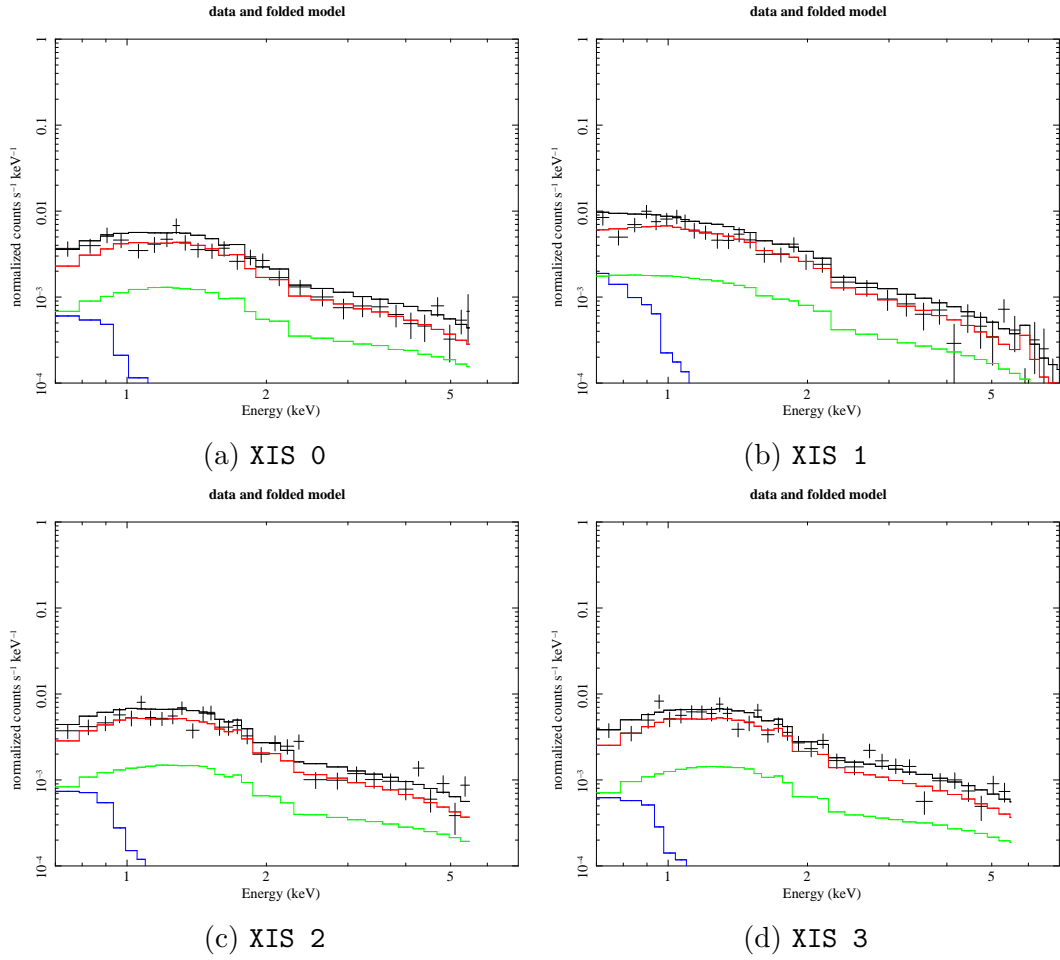
Figure A.3: The spectral fits for Annulus 3 (refer Table 3.1) of Abell 1413 for the third pointing

(a) XIS 0

(b) XIS 1

(c) XIS 3
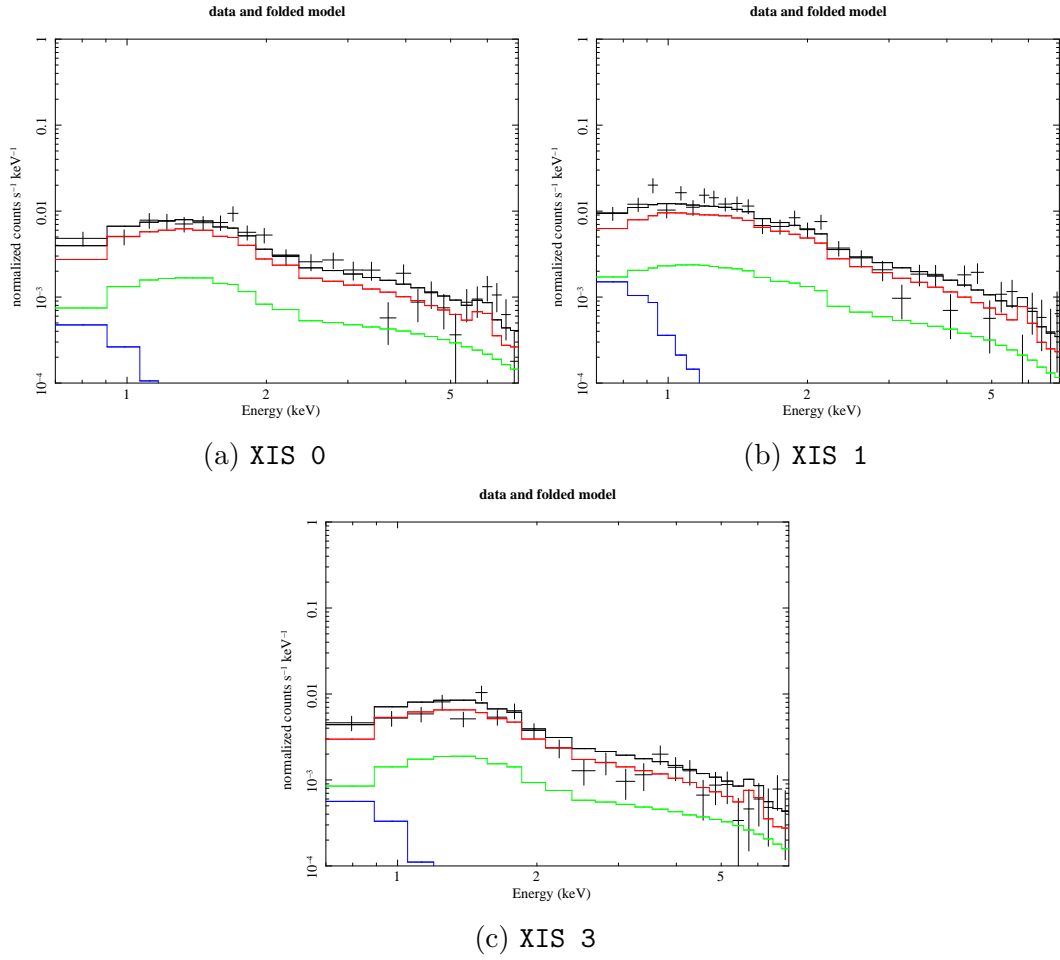
Figure A.4: The spectral fits for Annulus 3 (refer Table 3.1) of Abell 1413 for the fourth pointing

(a) XIS 0

(b) XIS 1

(c) XIS 3
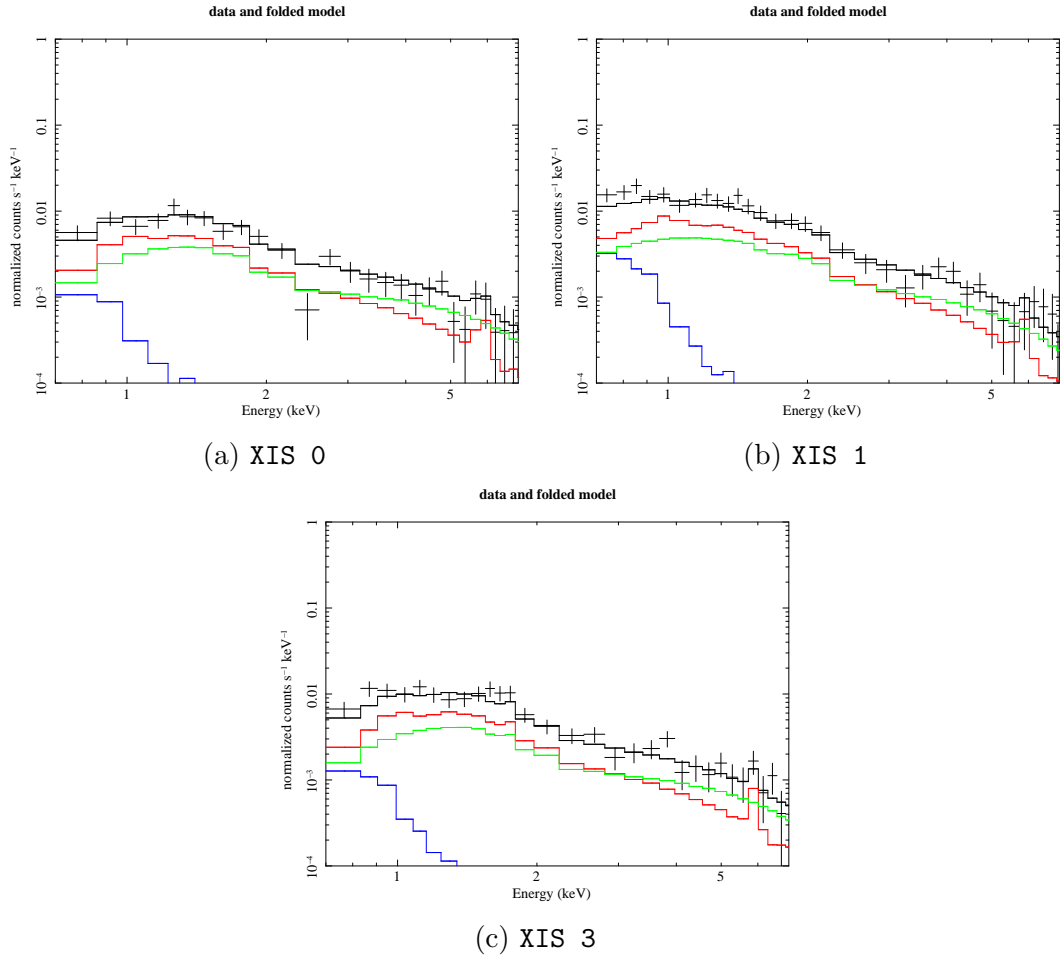
Figure A.5: The spectral fits for Annulus 4 (refer Table 3.1) of Abell 1413 for the first pointing

94

(a) XIS 0

(b) XIS 1

(c) XIS 3
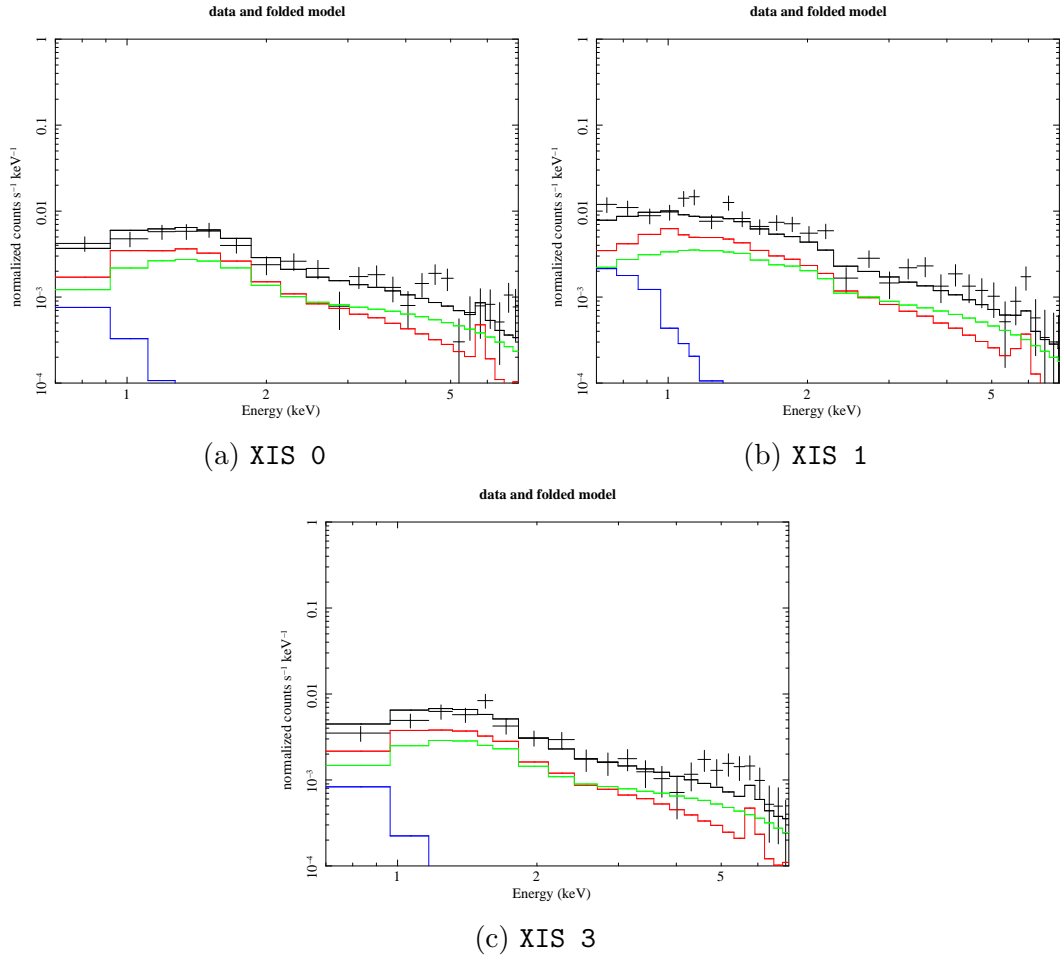
Figure A.6: The spectral fits for Annulus 4 (refer Table 3.1) of Abell 1413 for the second pointing

(a) XIS 0

(b) XIS 1

(c) XIS 2

(d) XIS 3
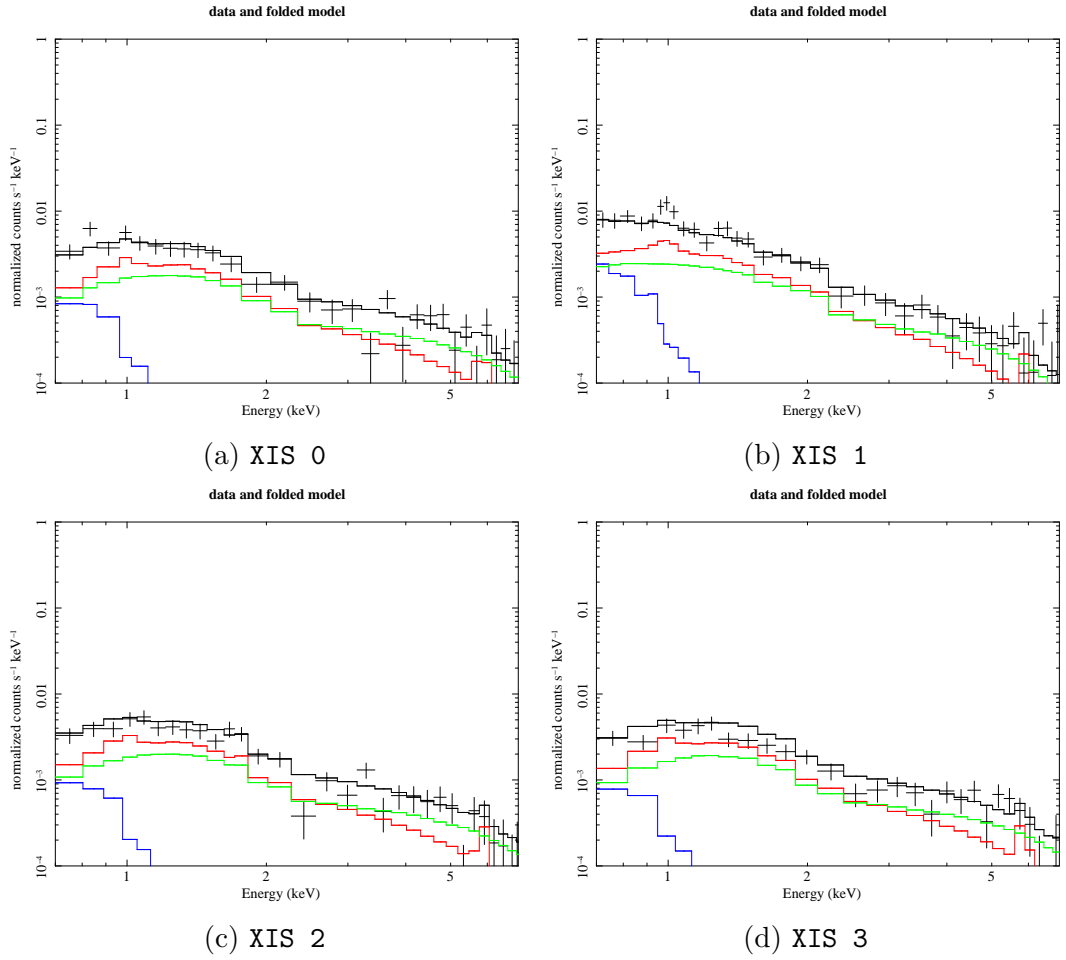
Figure A.7: The spectral fits for Annulus 4 (refer Table 3.1) of Abell 1413 for the third pointing

(a) XIS 0

(b) XIS 1

(c) XIS 3
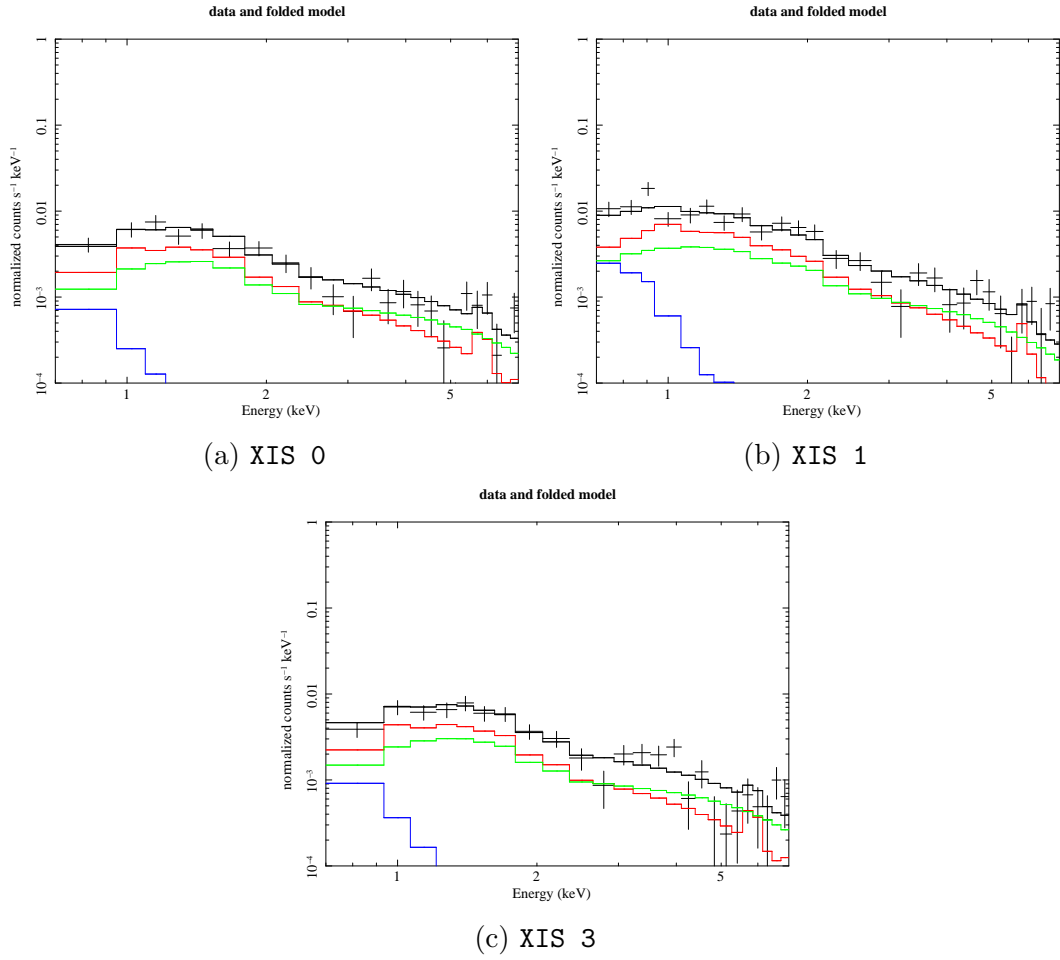
Figure A.8: The spectral fits for Annulus 4 (refer Table 3.1) of Abell 1413 for the fourth pointing

(a) XIS 0

(b) XIS 1

(c) XIS 3
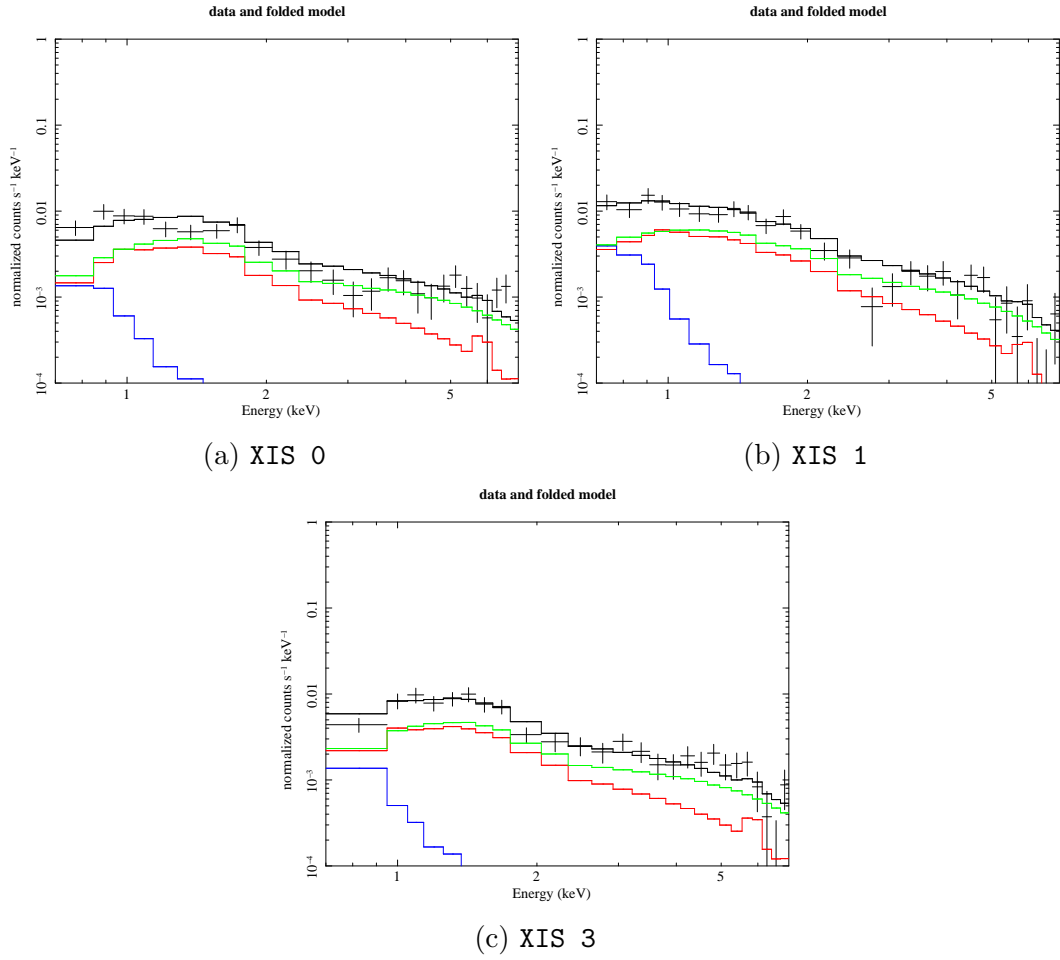
Figure A.9: The spectral fits for Annulus 5 (refer Table 3.1) of Abell 1413 for the first pointing

(a) XIS 0   (b) XIS 1

(c) XIS 3
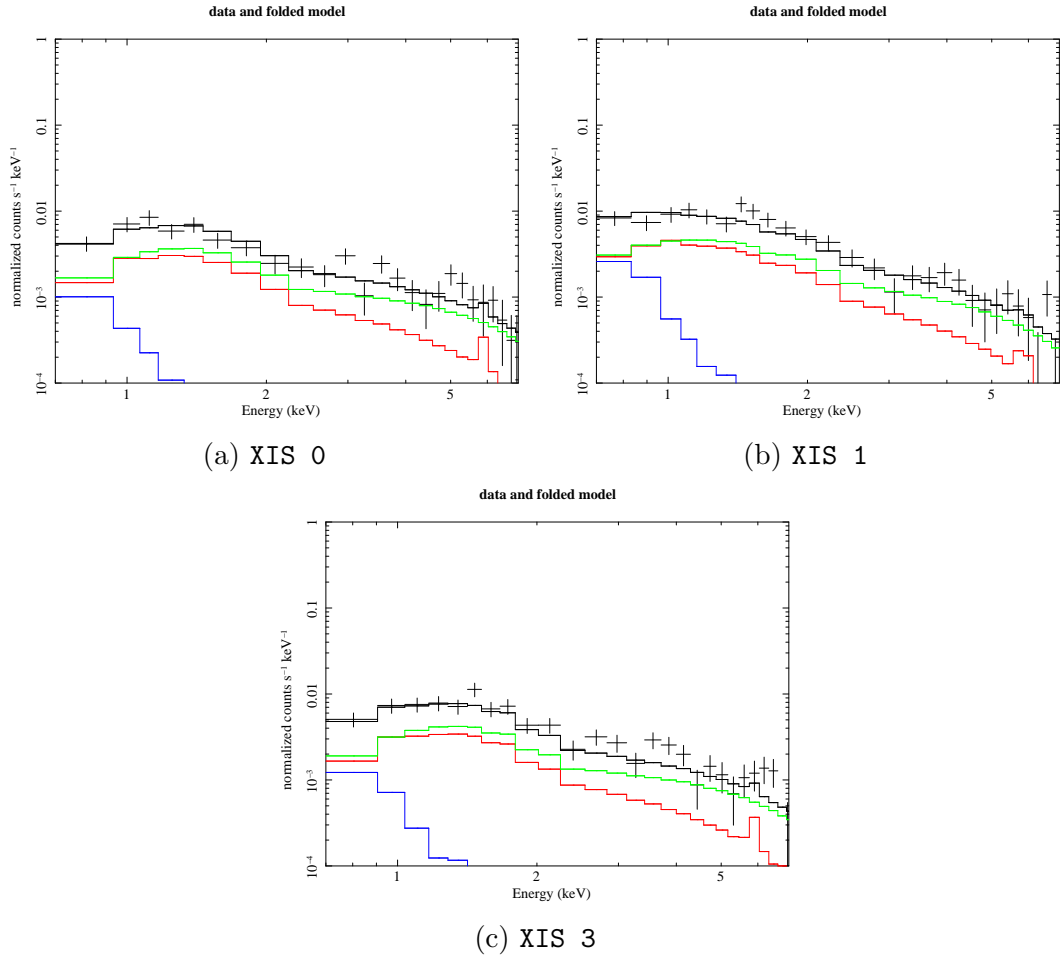
Figure A.10: The spectral fits for Annulus 5 (refer Table 3.1) of Abell 1413 for the second pointing

(a) XIS 0

(b) XIS 1

(c) XIS 2

(d) XIS 3
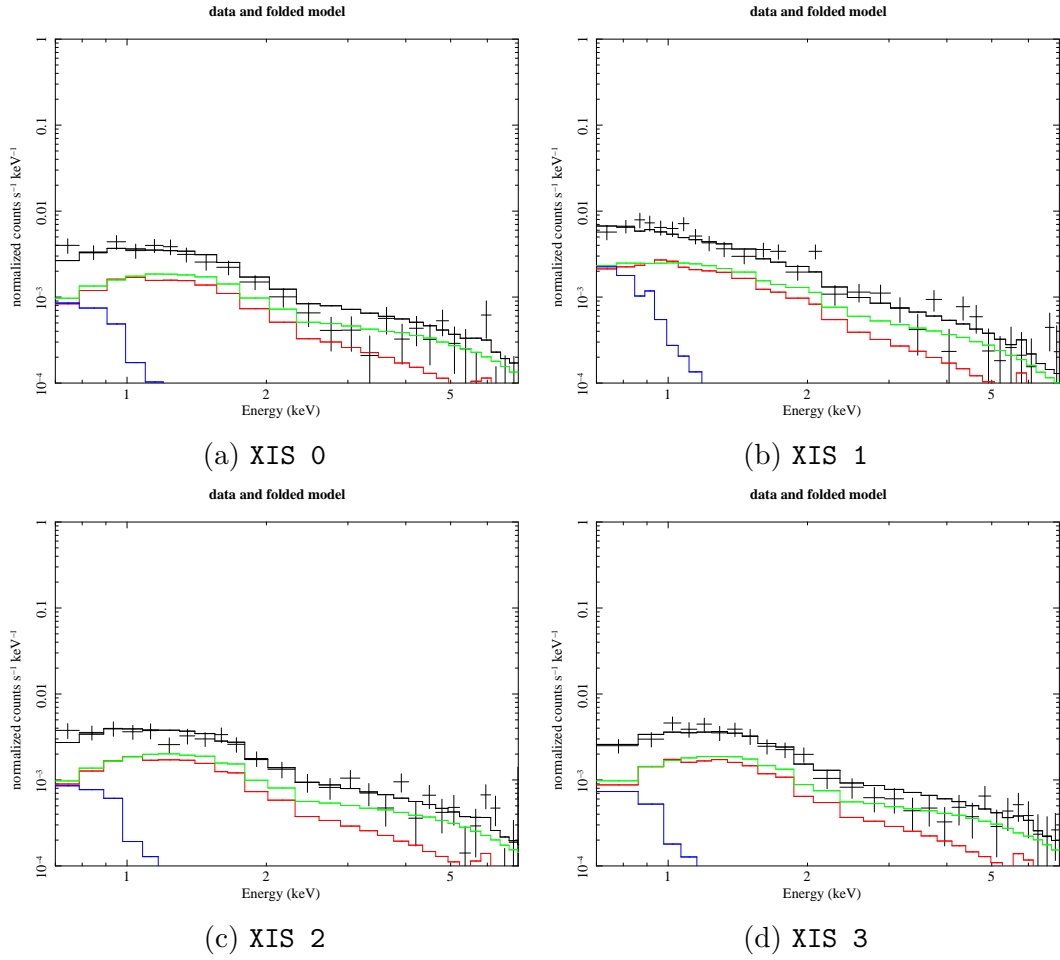
Figure A.11: The spectral fits for Annulus 5 (refer Table 3.1) of Abell 1413 for the third pointing

(a) XIS 0

(b) XIS 1

(c) XIS 3
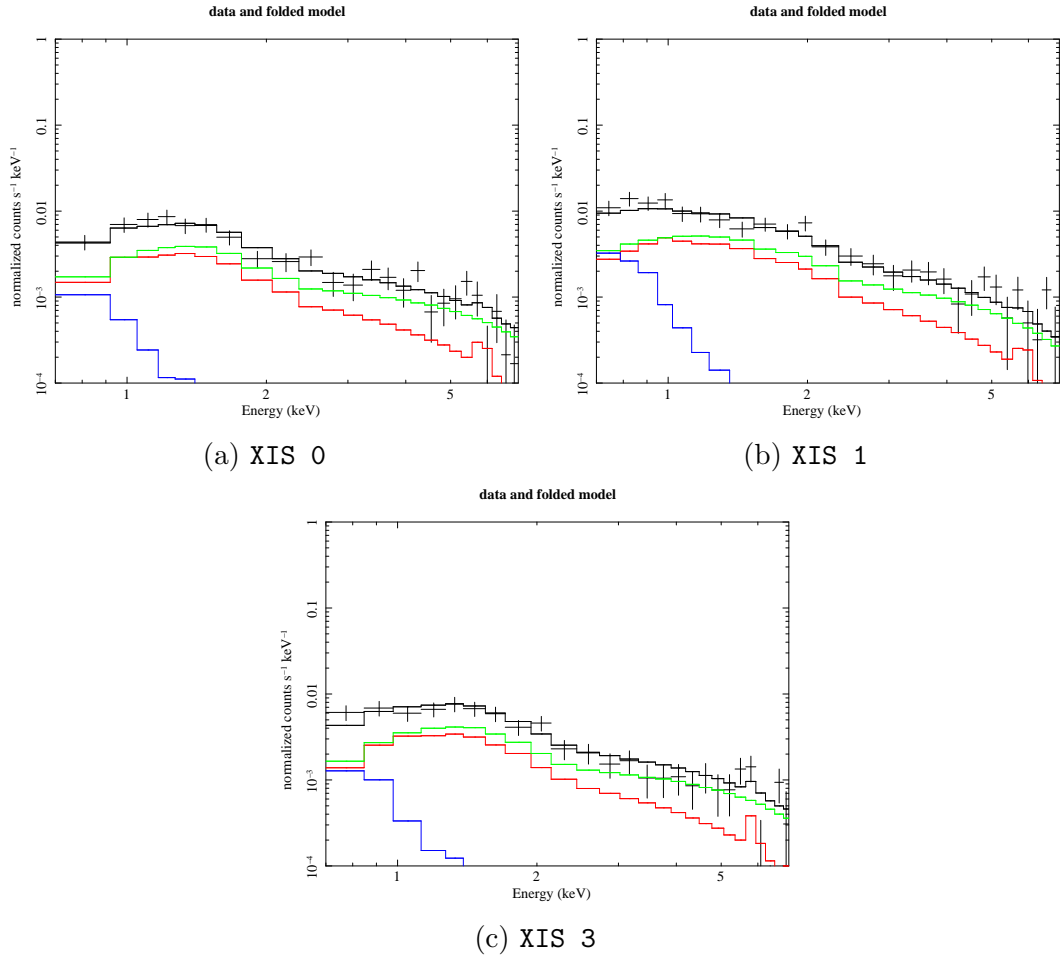
Figure A.12: The spectral fits for Annulus 5 (refer Table 3.1) of Abell 1413 for the fourth pointing

(a) XIS 0

(b) XIS 1

(c) XIS 3
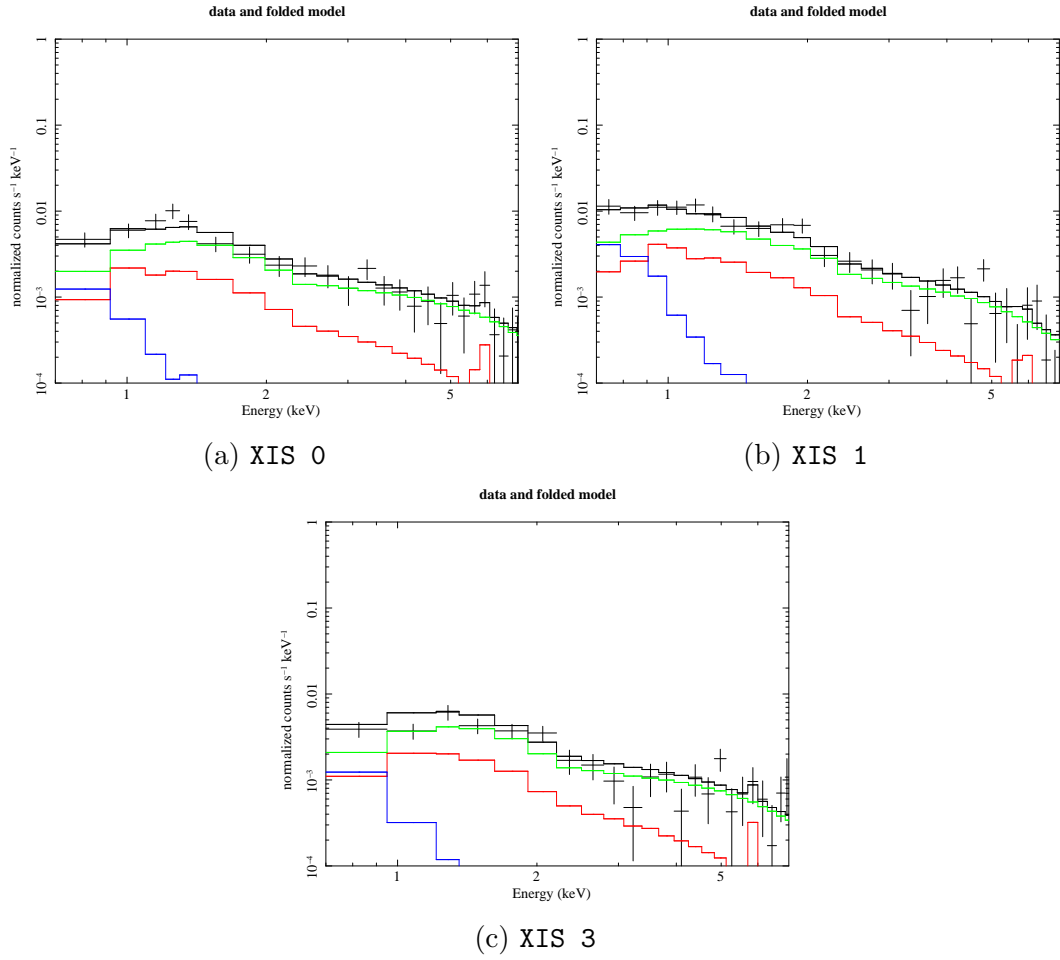
Figure A.13: The spectral fits for Annulus 6a (refer Table 3.1) of Abell 1413 for the first pointing

(a) XIS 0

(b) XIS 1

(c) XIS 3
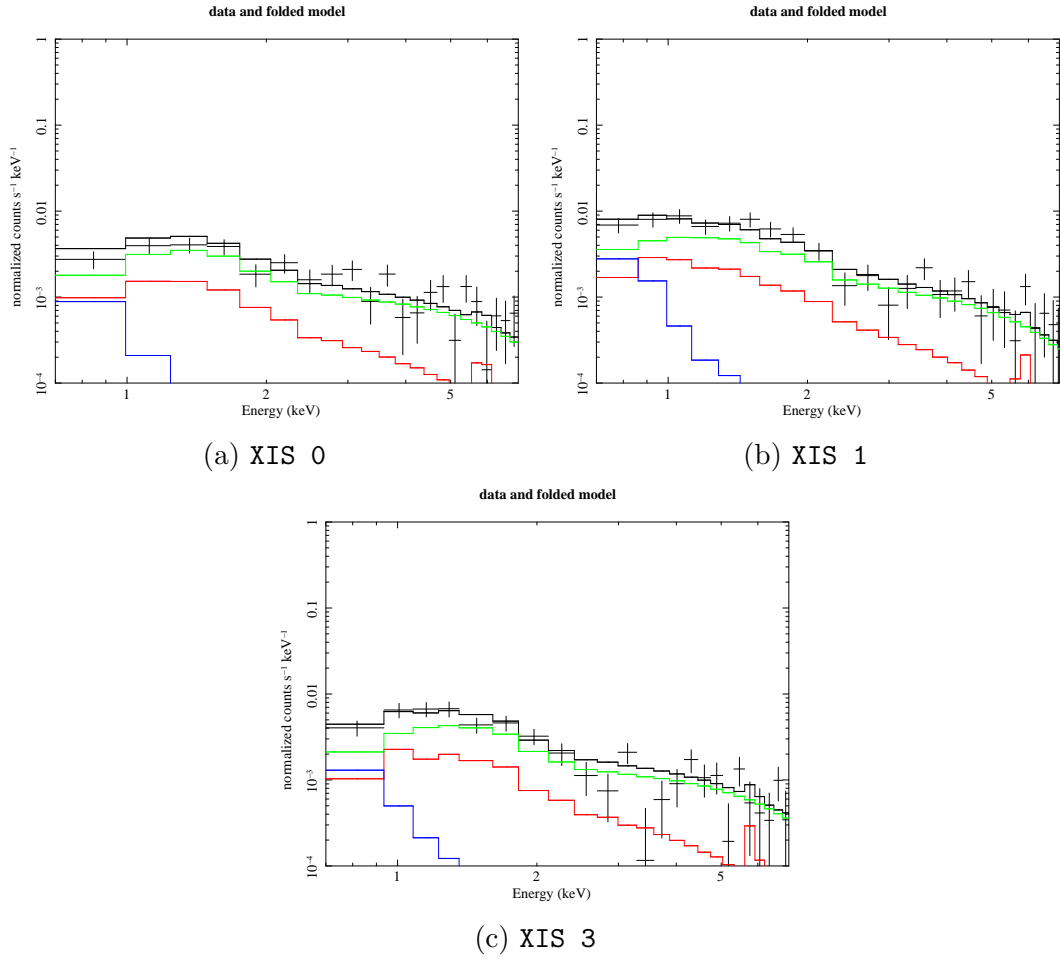
Figure A.14: The spectral fits for Annulus 6a (refer Table 3.1) of Abell 1413 for the second pointing

(a) XIS 0

(b) XIS 1

(c) XIS 2

(d) XIS 3
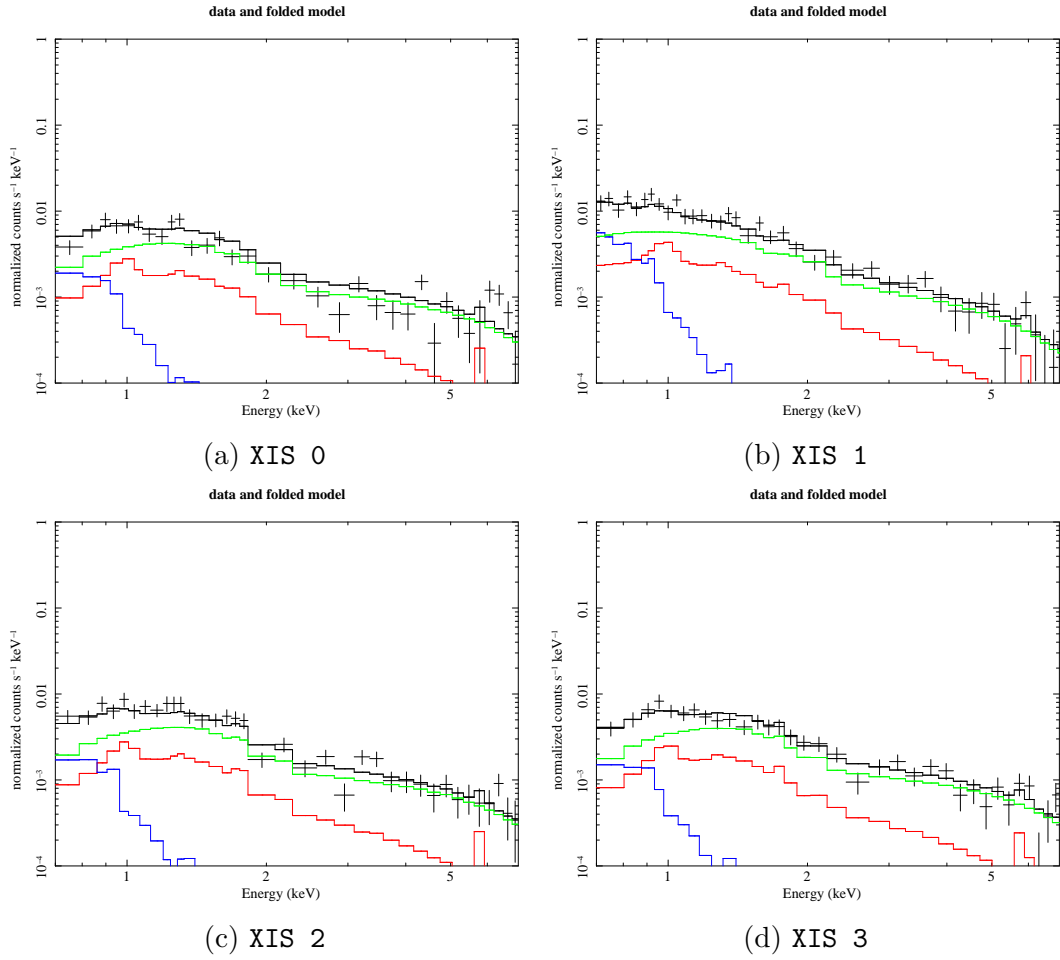
Figure A.15: The spectral fits for Annulus 6a (refer Table 3.1) of Abell 1413 for the third pointing

104

(a) XIS 0

(b) XIS 1

(c) XIS 3
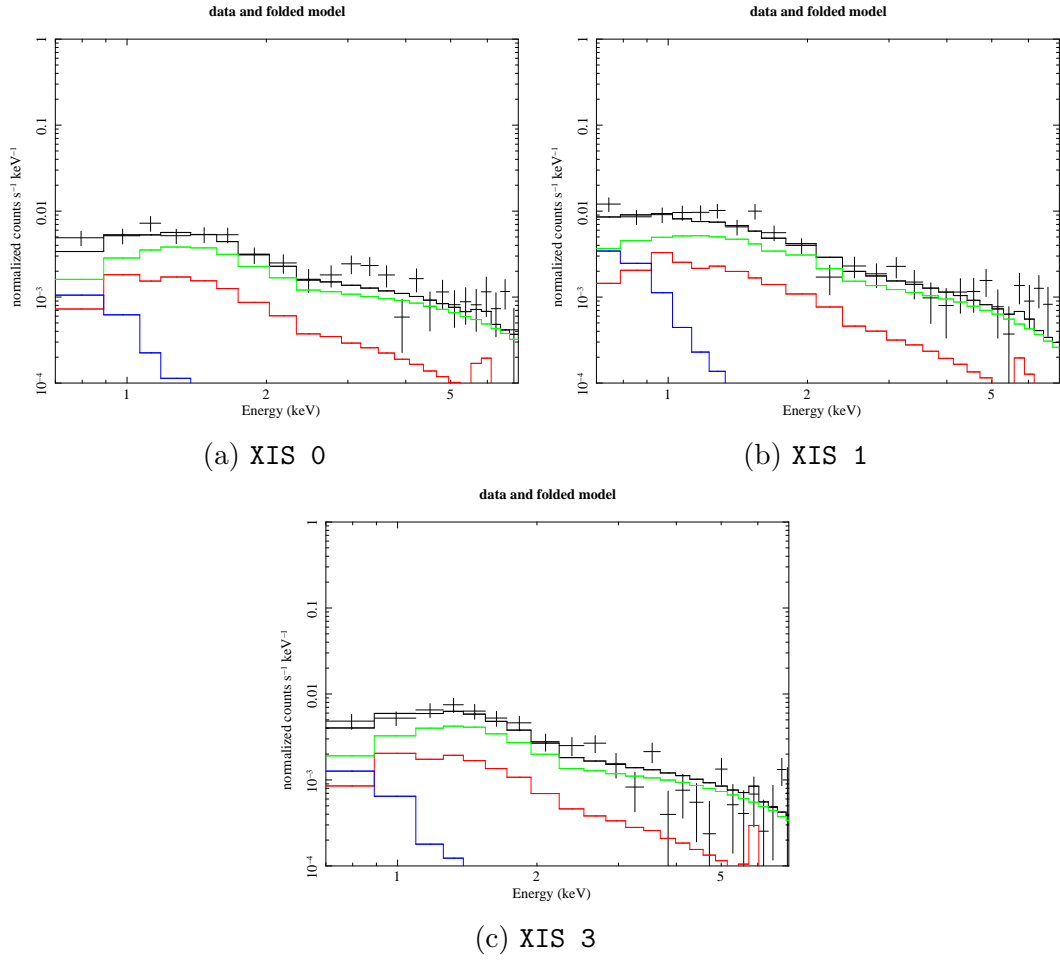
Figure A.16: The spectral fits for Annulus 6a (refer Table 3.1) of Abell 1413 for the fourth pointing

A.2 Abell 2204

Presented below are the *Suzaku* pointings for Abell 2204 we utilized for this analysis. The observation details are shown below in Table A.2.

Pointing #	Observation ID	Comments
1	801091010	Archival Data [Reiprich et al., 2009]
2	805056010	Proposed Data
3	805057010	Proposed Data
4	805058010	Proposed Data

Table A.2: The *Suzaku* data on Abell 2204 used for this analysis

For pointings 2, 3 and 4, we use only detectors XIS 0, XIS 1 and XIS 3 for the analysis. For pointing 1, we used the XIS 2 detector in addition to XIS 0, 1 and 3 as it was observed before the detector was damaged. For the first annulus, we did not use the data from the third pointing and the data from the XIS 0 and XIS 3 detectors, as these regions directly overlapped with the calibrator regions.

(a) XIS 0

(b) XIS 1

(c) XIS 2

(d) XIS 3
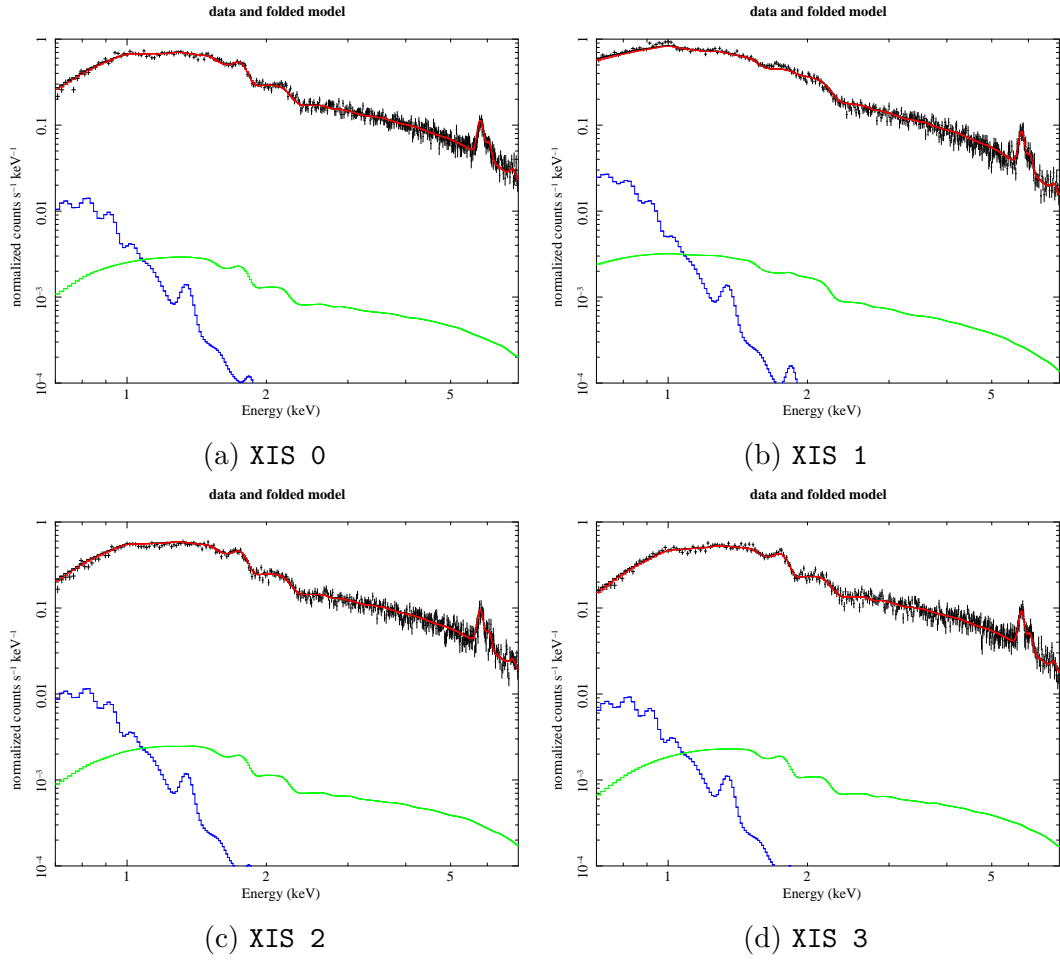
Figure A.17: The spectral fits for Annulus 1 (refer Table 3.1) of Abell 2204 for the first pointing

107

(a) XIS 0

(b) XIS 1

(c) XIS 3
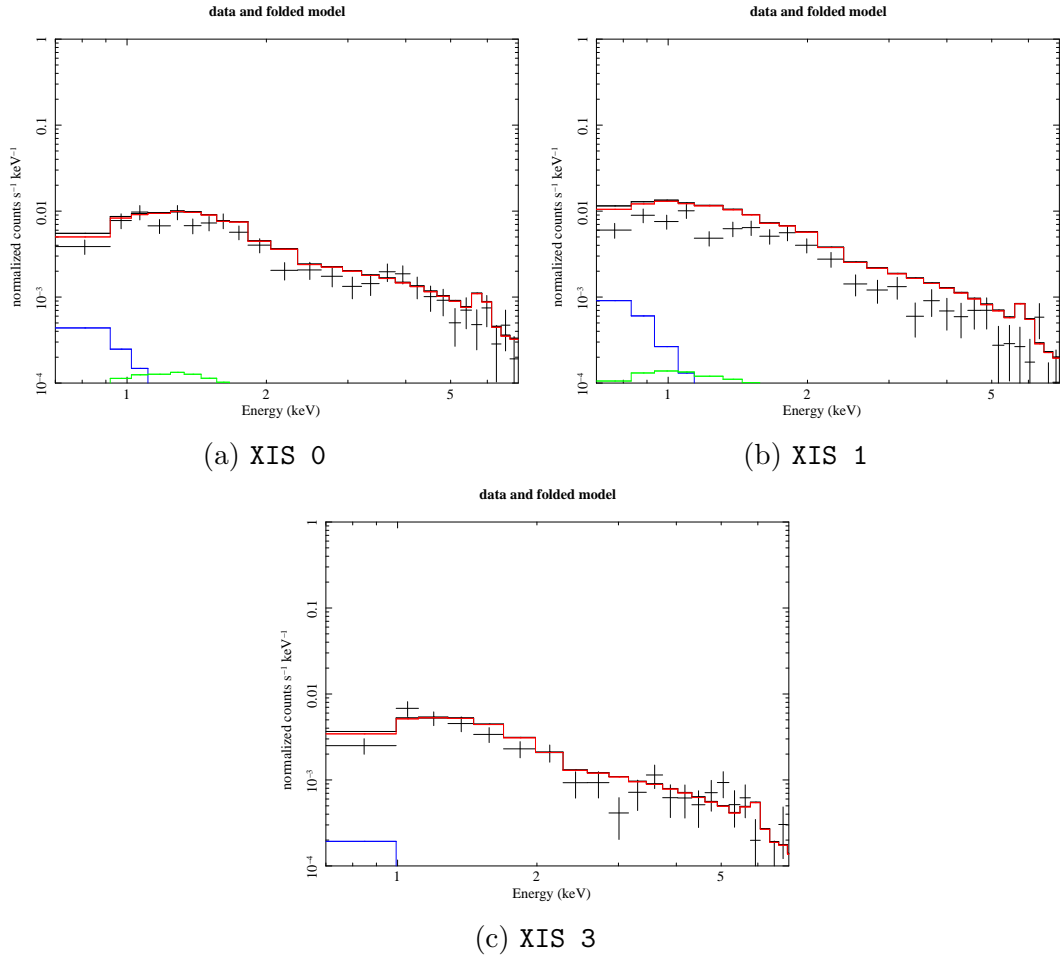
Figure A.18: The spectral fits for Annulus 1 (refer Table 3.1) of Abell 2204 for the second pointing

data and folded model
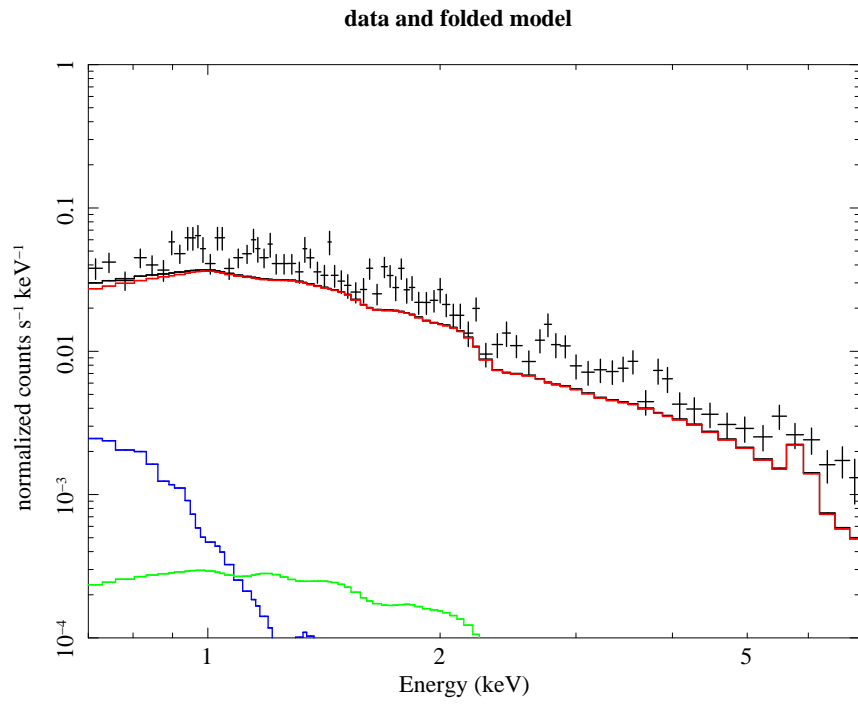
Figure A.19: The spectral fits for Annulus 1 (refer Table 3.1) of Abell 2204 for the fourth pointing in `XIS1`

(a) XIS 0

(b) XIS 1

(c) XIS 2

(d) XIS 3
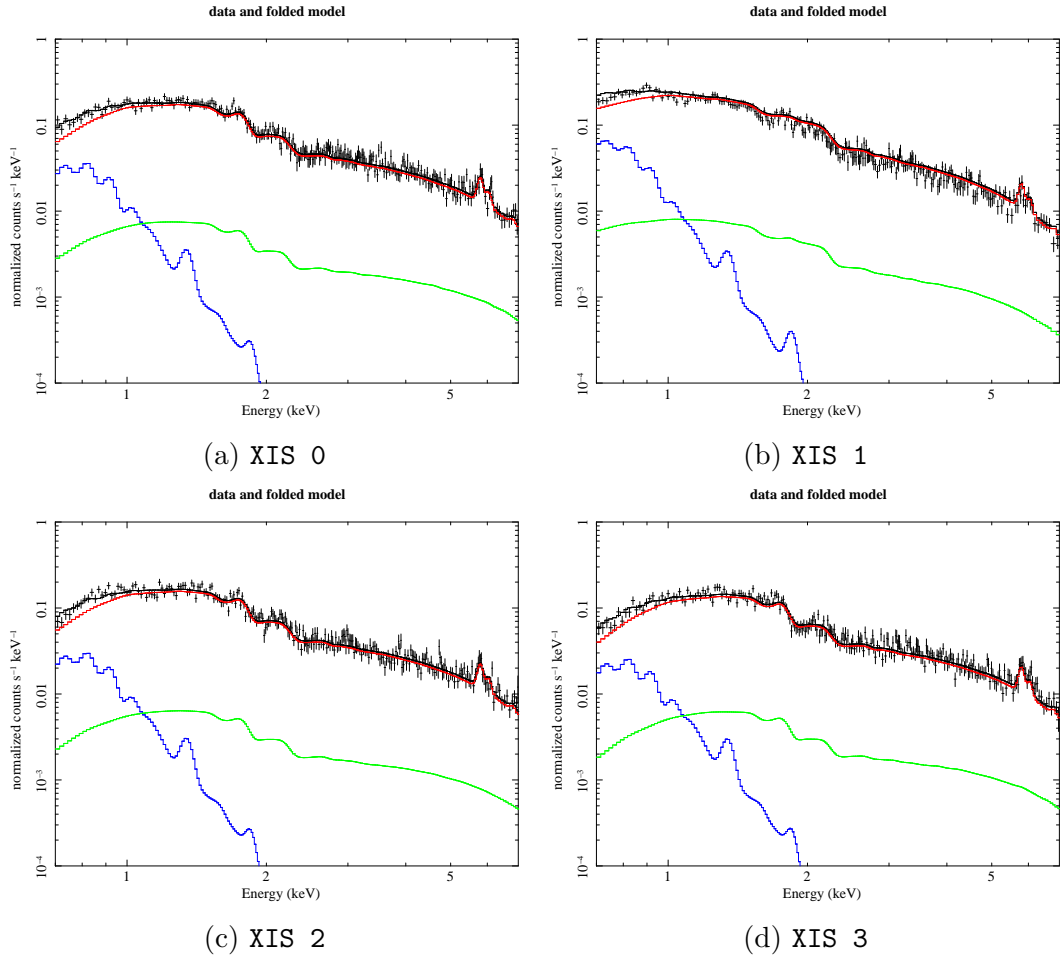
Figure A.20: The spectral fits for Annulus 2 (refer Table 3.1) of Abell 2204 for the first pointing

110

(a) XIS 0

(b) XIS 1

(c) XIS 3
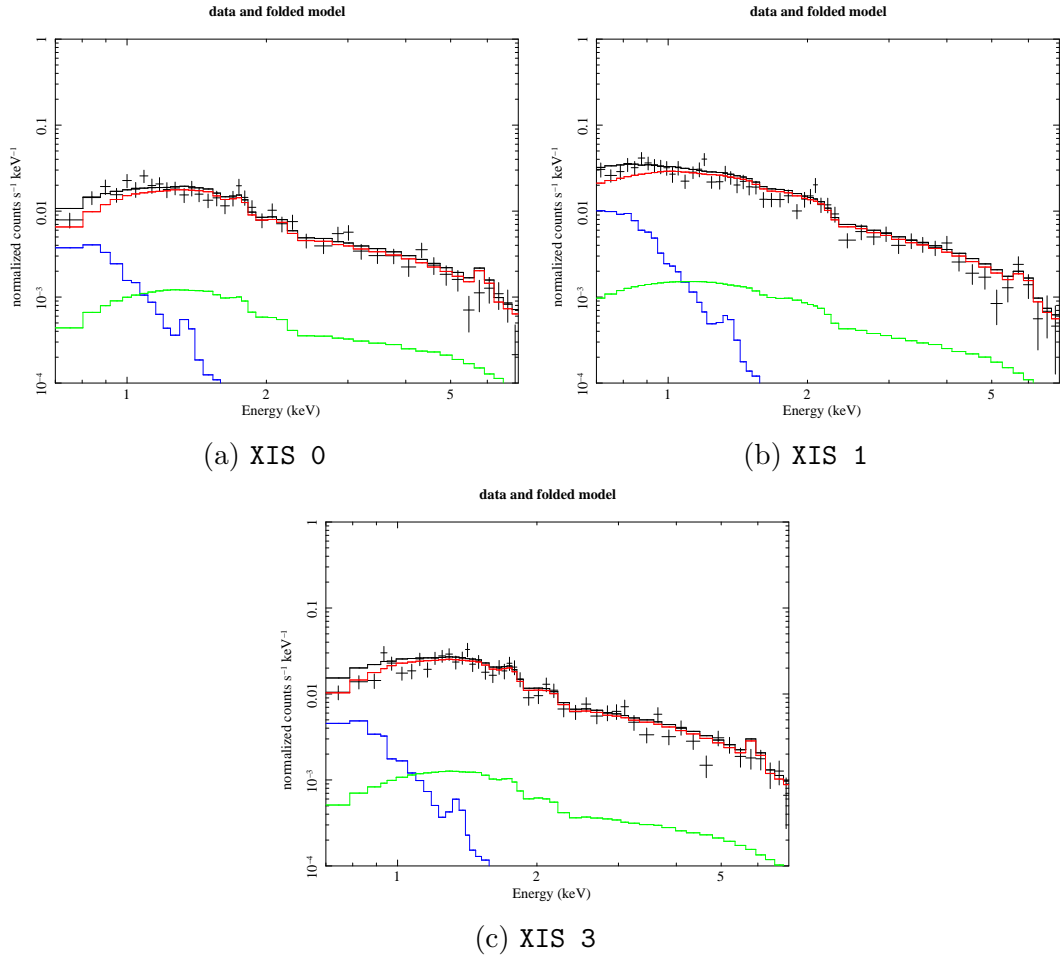
Figure A.21: The spectral fits for Annulus 2 (refer Table 3.1) of Abell 2204 for the second pointing

(a) XIS 0

(b) XIS 1

(c) XIS 3
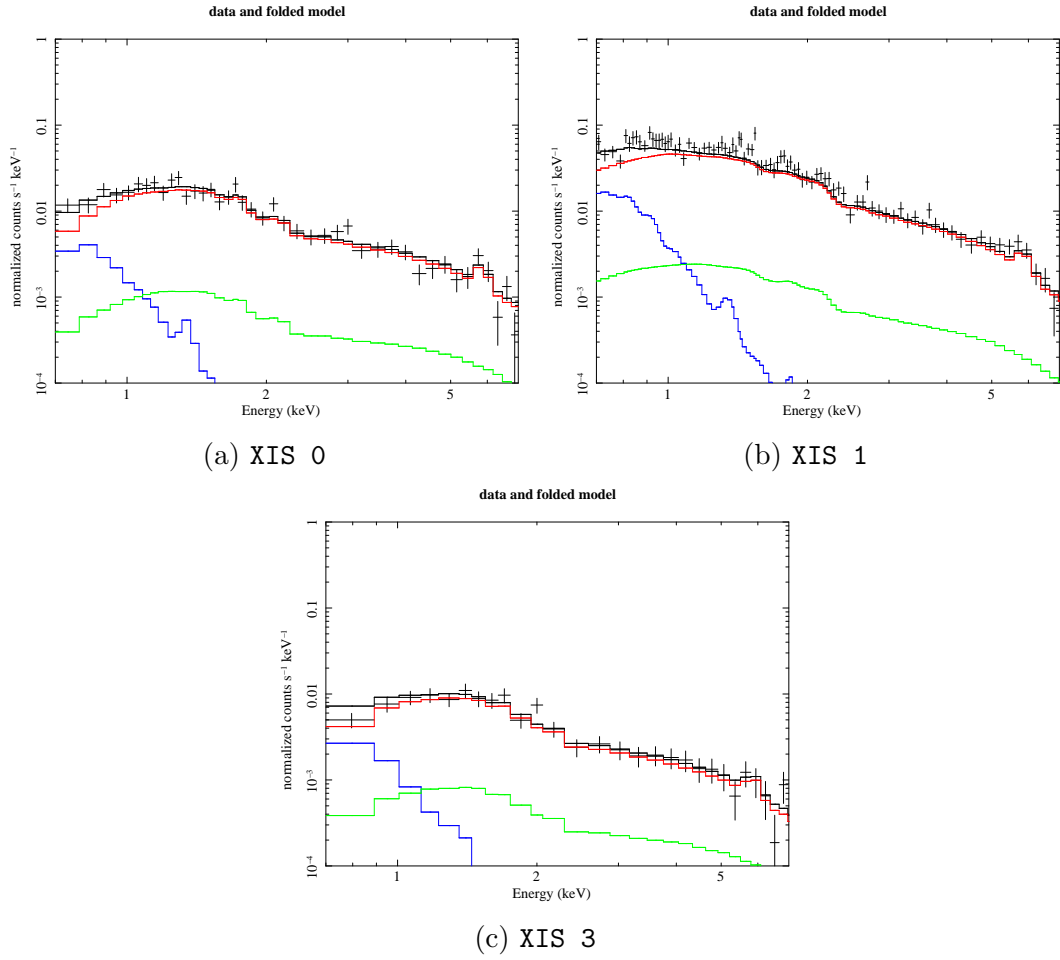
Figure A.22: The spectral fits for Annulus 2 (refer Table 3.1) of Abell 2204 for the third pointing

(a) XIS 0

(b) XIS 1

(c) XIS 3
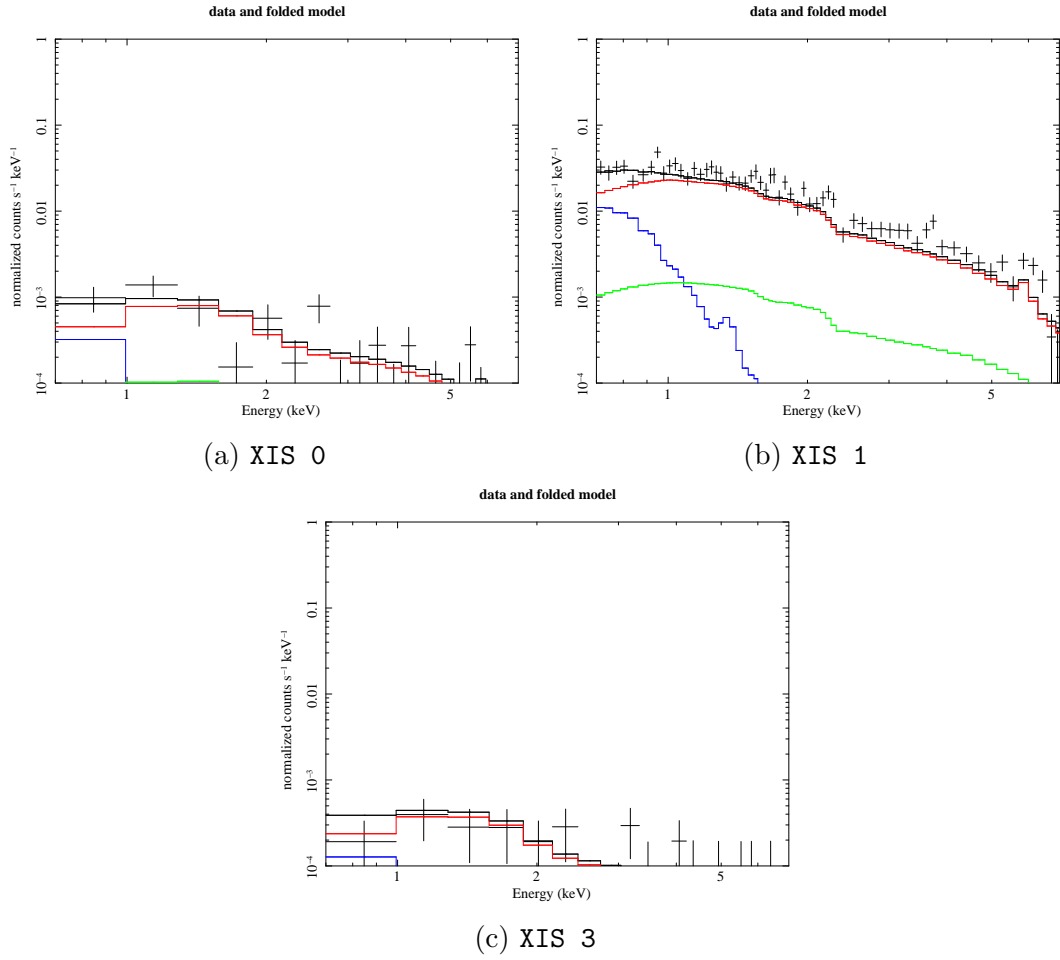
Figure A.23: The spectral fits for Annulus 2 (refer Table 3.1) of Abell 2204 for the fourth pointing

113

(a) XIS 0

(b) XIS 1

(c) XIS 2

(d) XIS 3
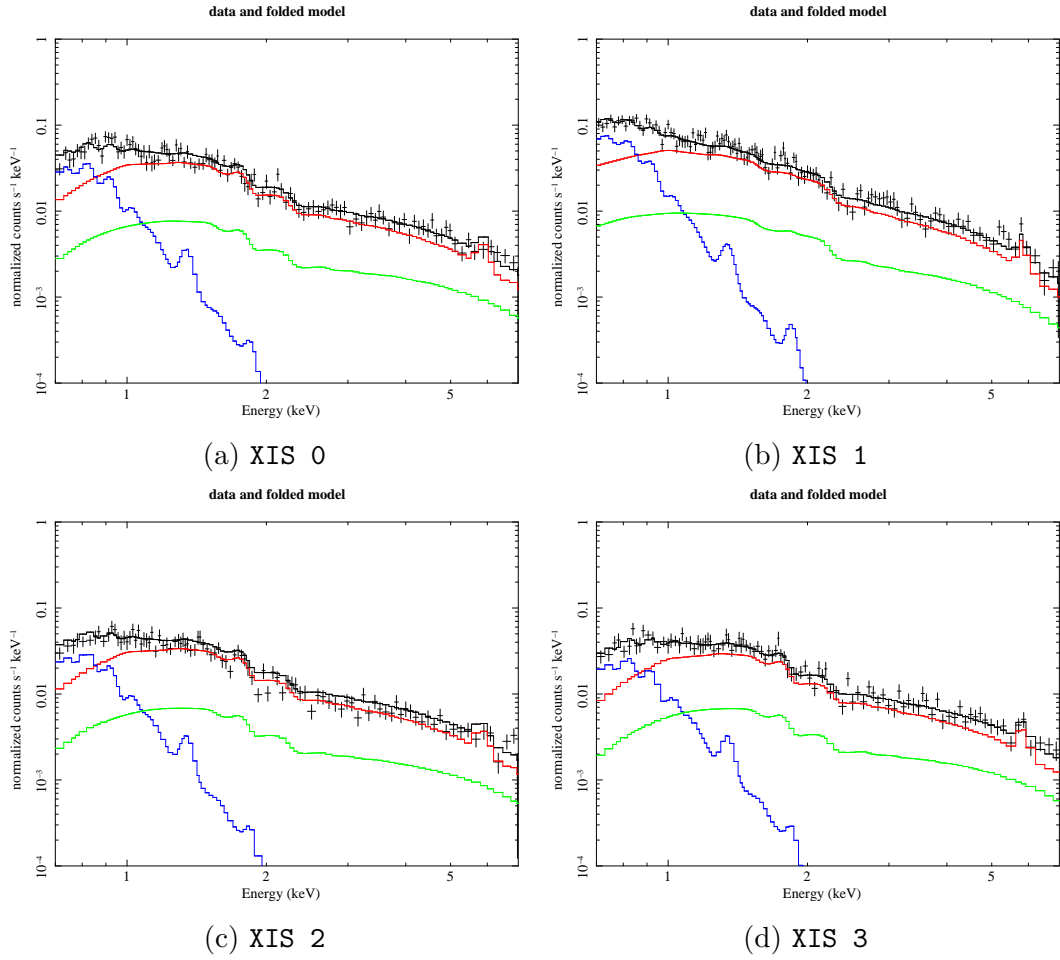
Figure A.24: The spectral fits for Annulus 3 (refer Table 3.1) of Abell 2204 for the first pointing

114

(a) XIS 0

(b) XIS 1

(c) XIS 3
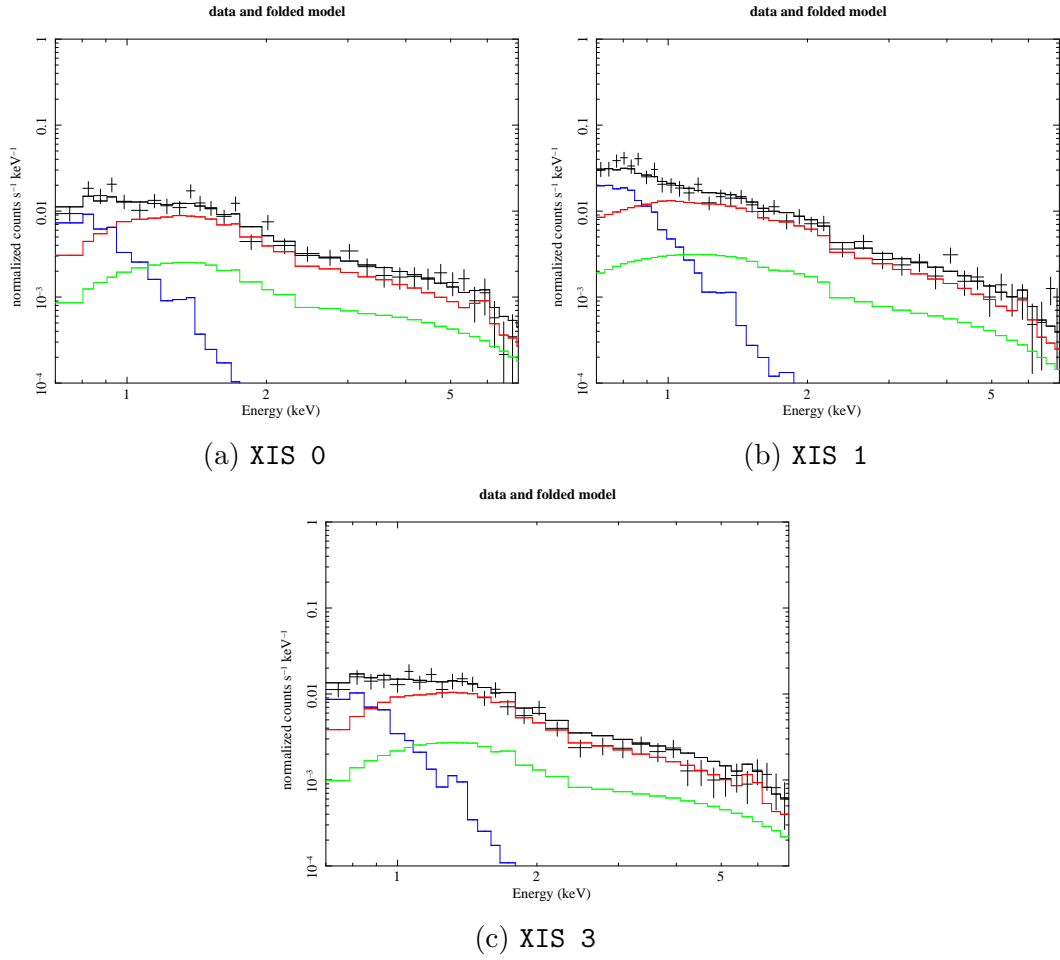
Figure A.25: The spectral fits for Annulus 3 (refer Table 3.1) of Abell 2204 for the second pointing

(a) XIS 0

(b) XIS 1

(c) XIS 3
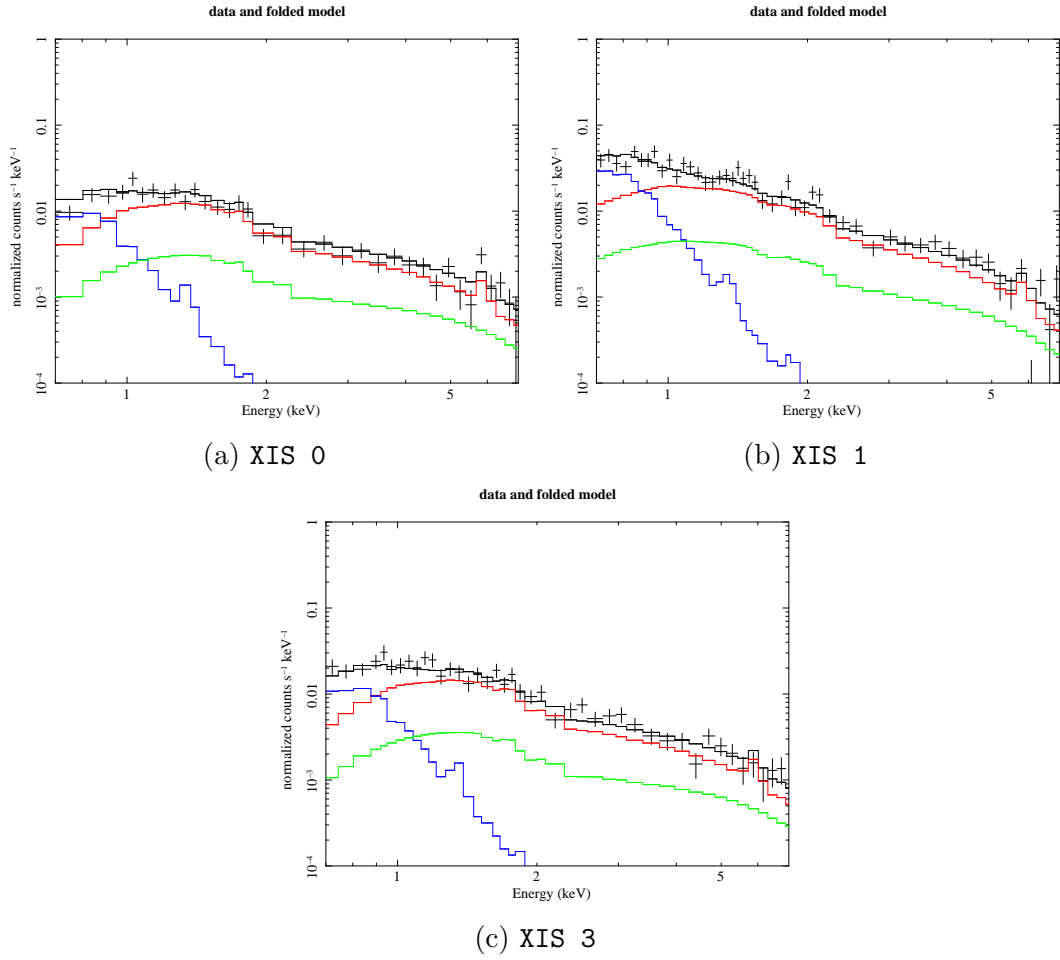
Figure A.26: The spectral fits for Annulus 3 (refer Table 3.1) of Abell 2204 for the third pointing

(a) XIS 0

(b) XIS 1

(c) XIS 3
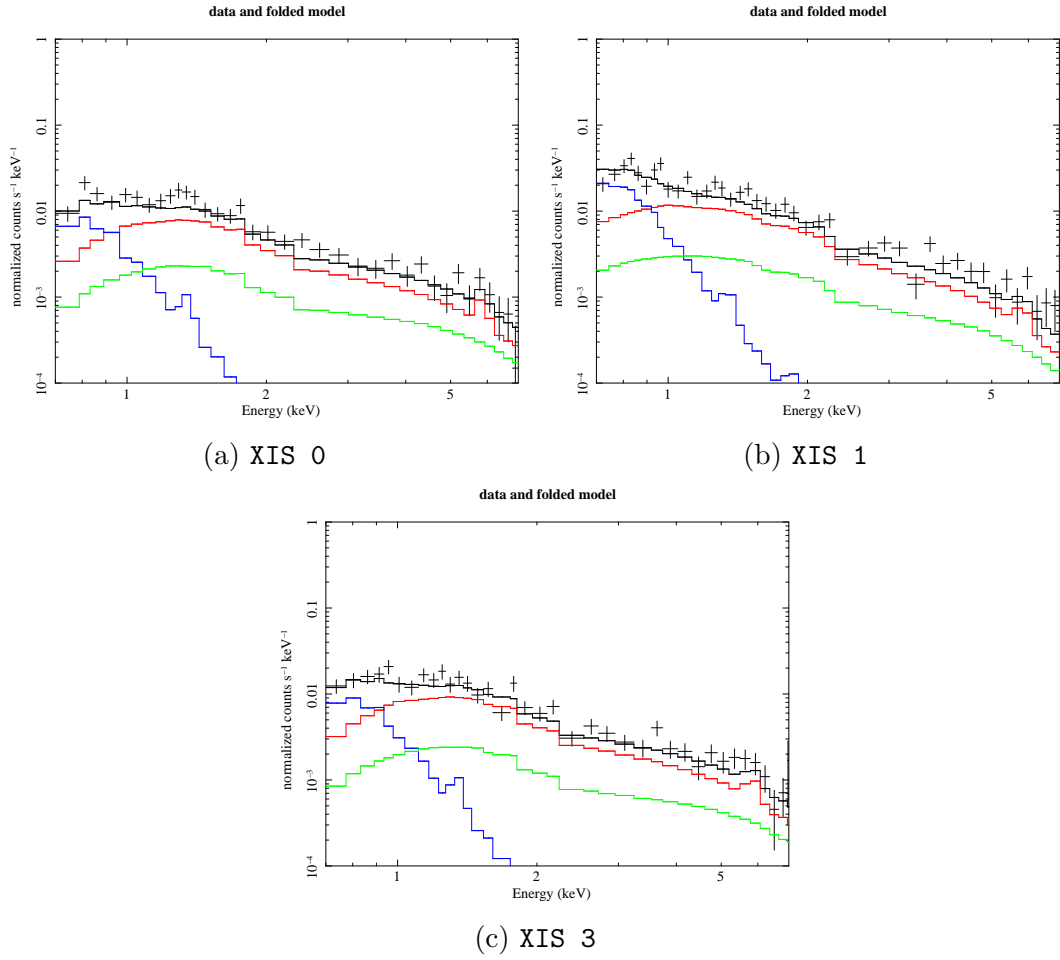
Figure A.27: The spectral fits for Annulus 3 (refer Table 3.1) of Abell 2204 for the fourth pointing

(a) XIS 0

(b) XIS 1

(c) XIS 2

(d) XIS 3
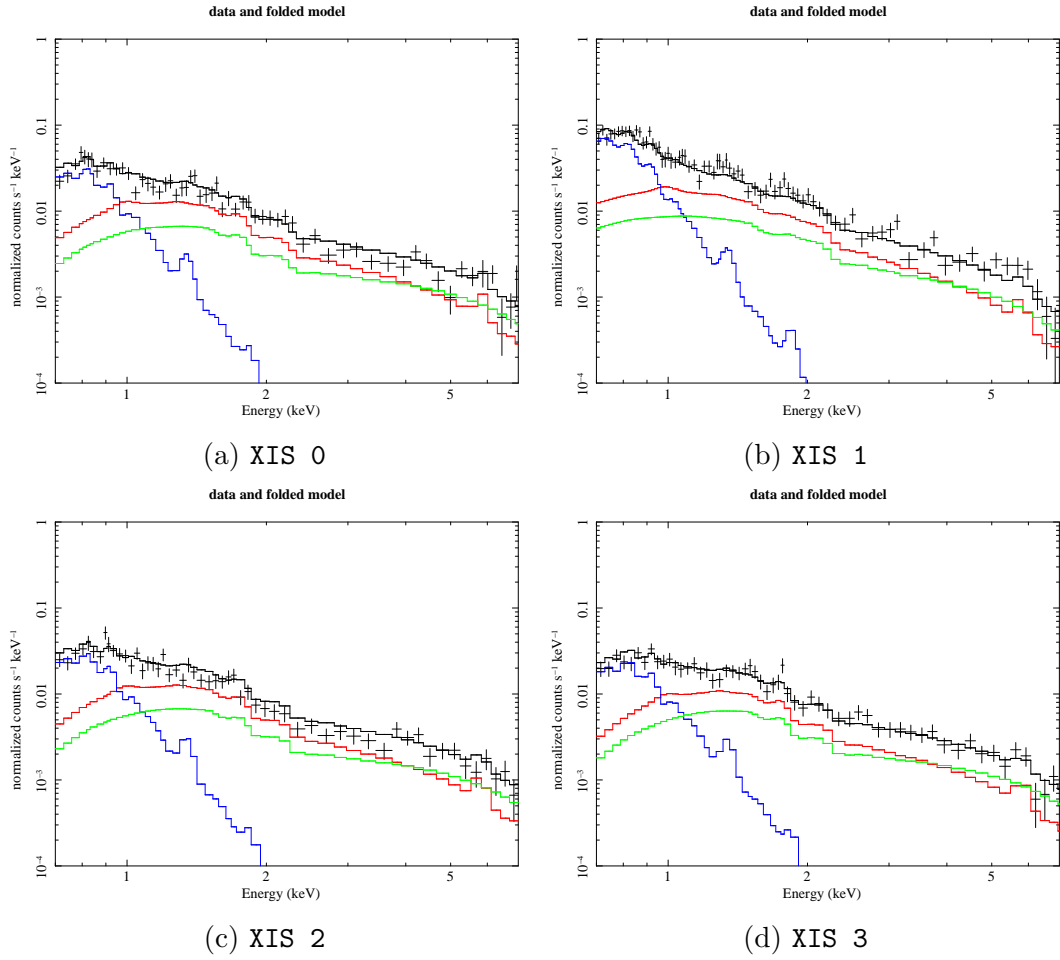
Figure A.28: The spectral fits for Annulus 4 (refer Table 3.1) of Abell 2204 for the first pointing

118

(a) XIS 0

(b) XIS 1

(c) XIS 3
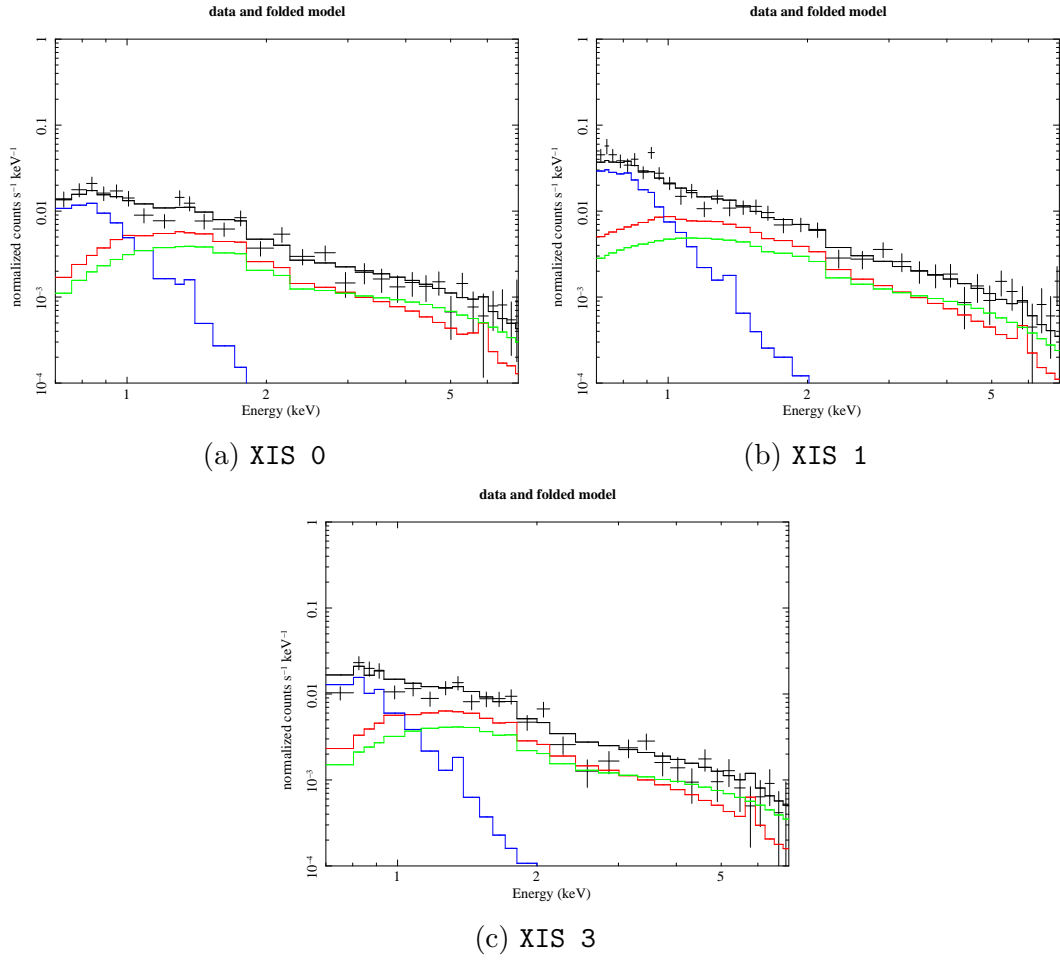
Figure A.29: The spectral fits for Annulus 4 (refer Table 3.1) of Abell 2204 for the second pointing

(a) XIS 0

(b) XIS 1

(c) XIS 3
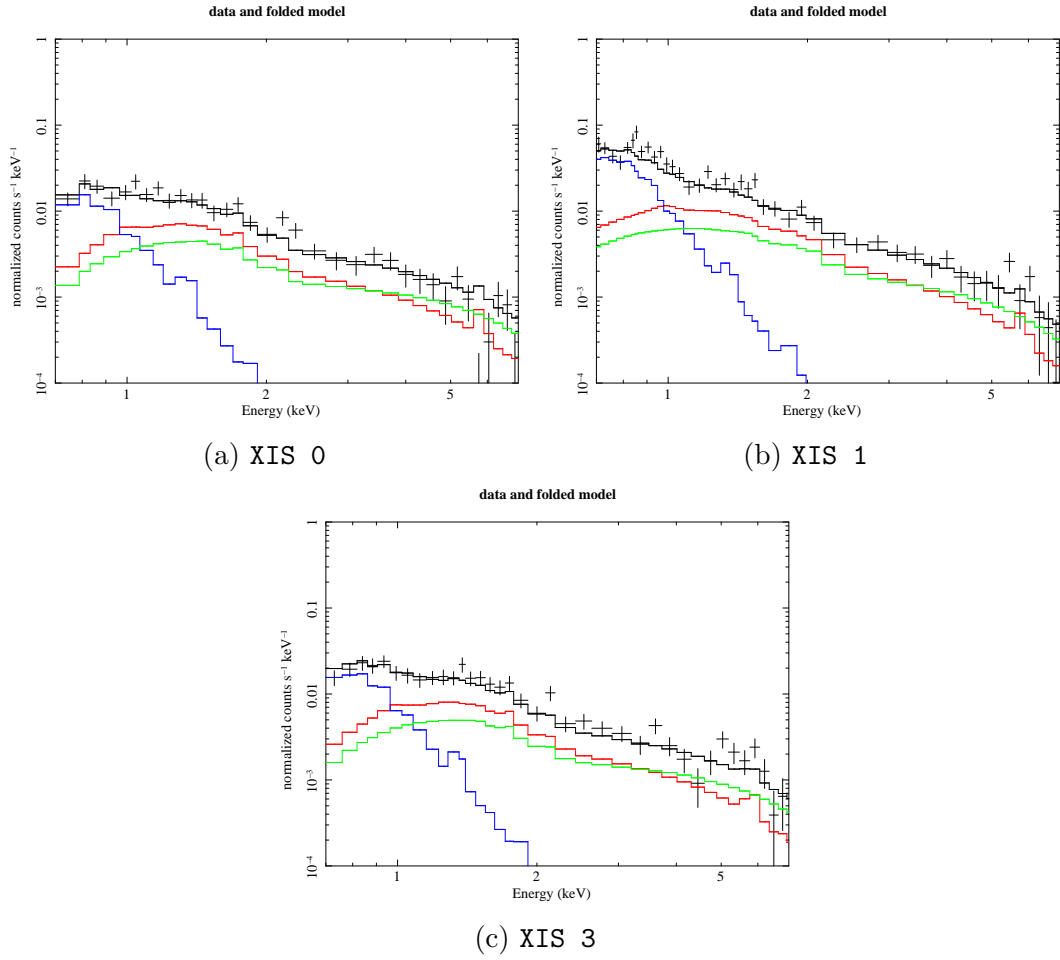
Figure A.30: The spectral fits for Annulus 4 (refer Table 3.1) of Abell 2204 for the third pointing

(a) XIS 0

(b) XIS 1

(c) XIS 3
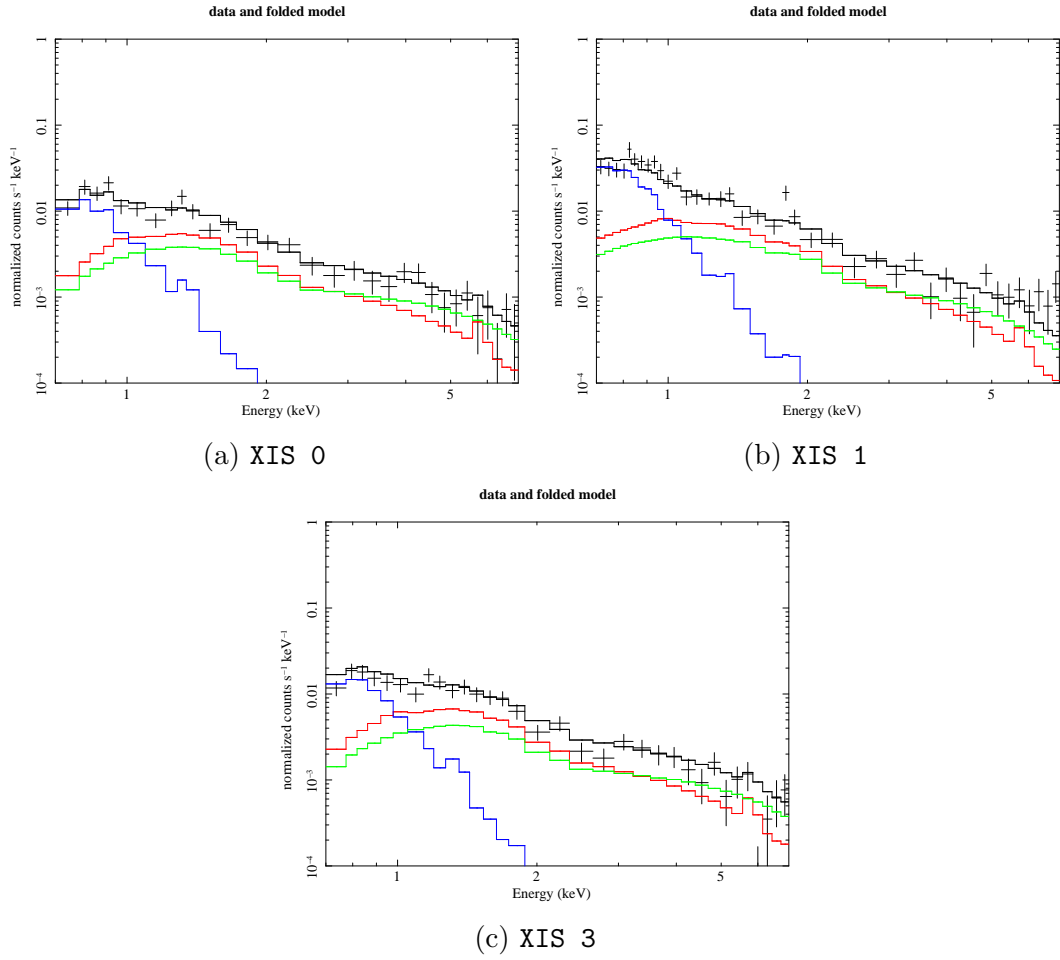
Figure A.31: The spectral fits for Annulus 4 (refer Table 3.1) of Abell 2204 for the fourth pointing

(a) XIS 0

(b) XIS 1

(c) XIS 2

(d) XIS 3
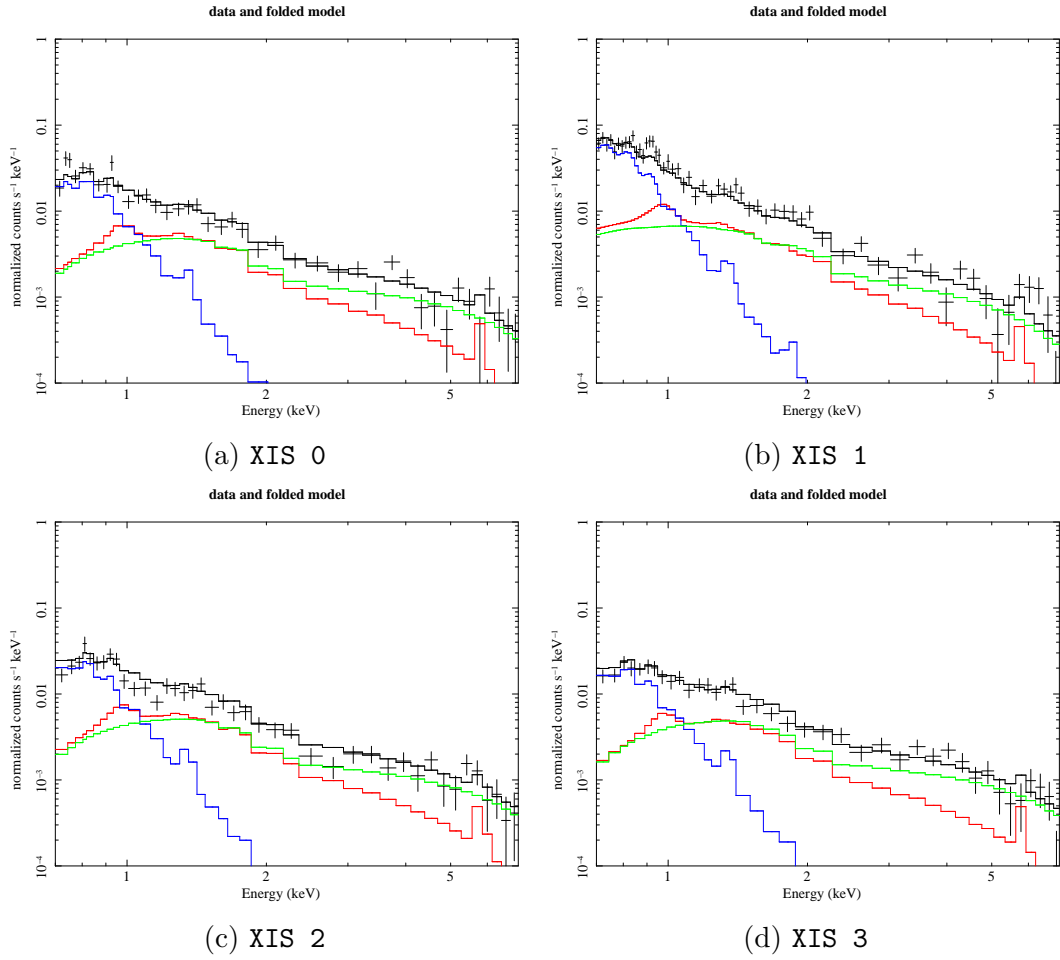
Figure A.32: The spectral fits for Annulus 5 (refer Table 3.1) of Abell 2204 for the first pointing

(a) XIS 0

(b) XIS 1

(c) XIS 3
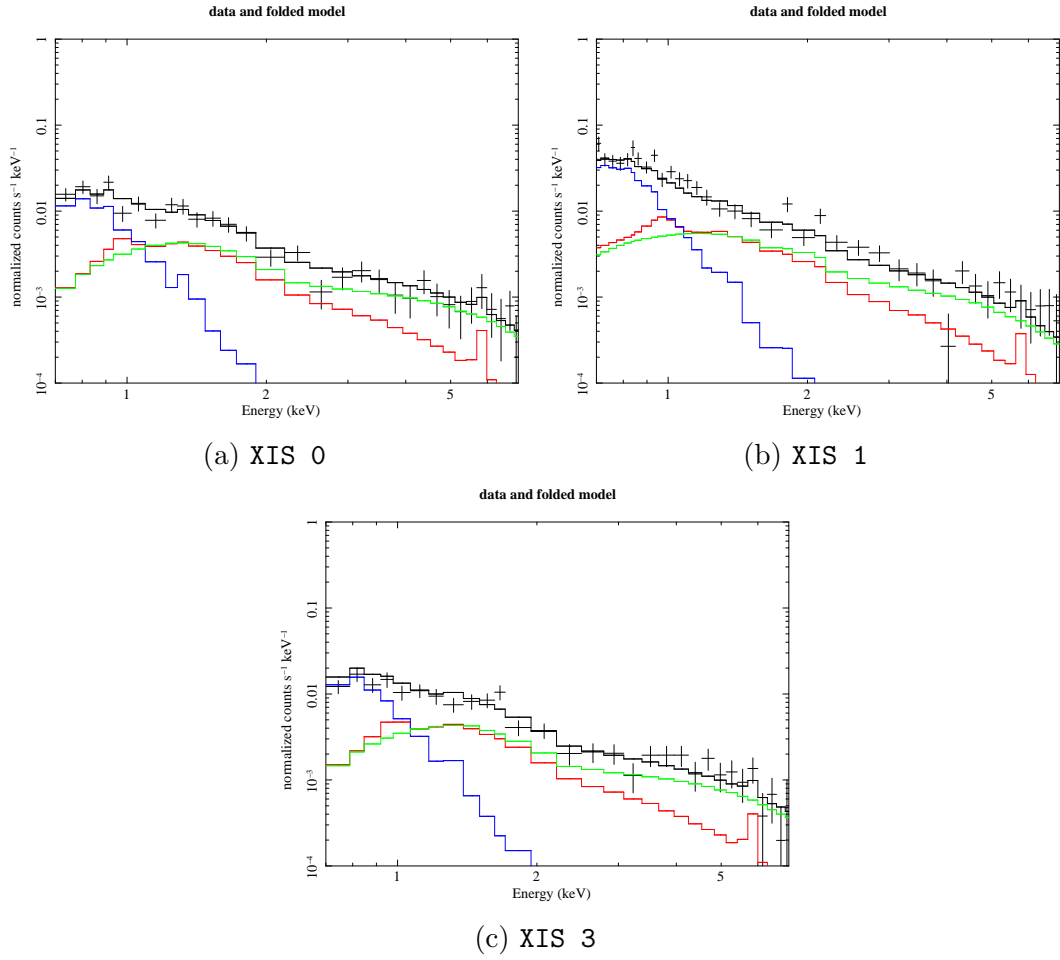
Figure A.33: The spectral fits for Annulus 5 (refer Table 3.1) of Abell 2204 for the second pointing

(a) XIS 0

(b) XIS 1

(c) XIS 3
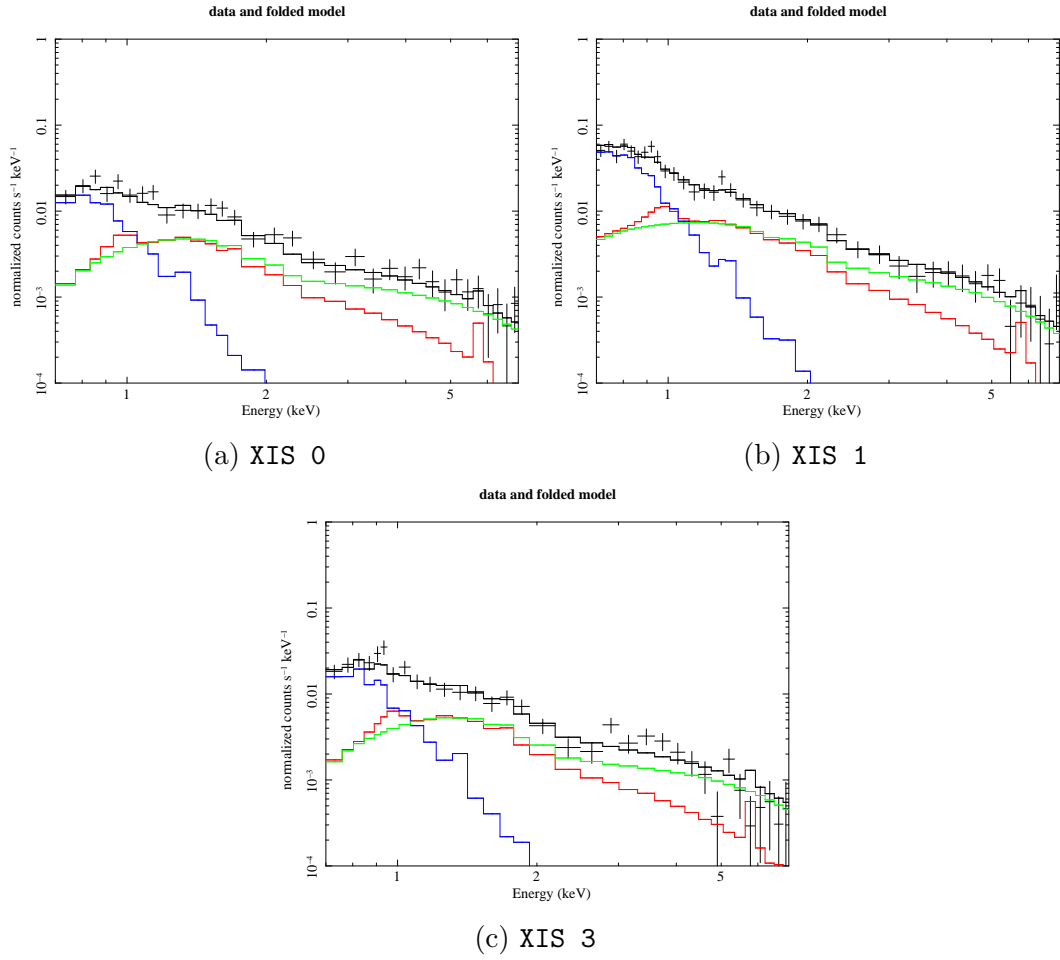
Figure A.34: The spectral fits for Annulus 5 (refer Table 3.1) of Abell 2204 for the third pointing

(a) XIS 0

(b) XIS 1

(c) XIS 3
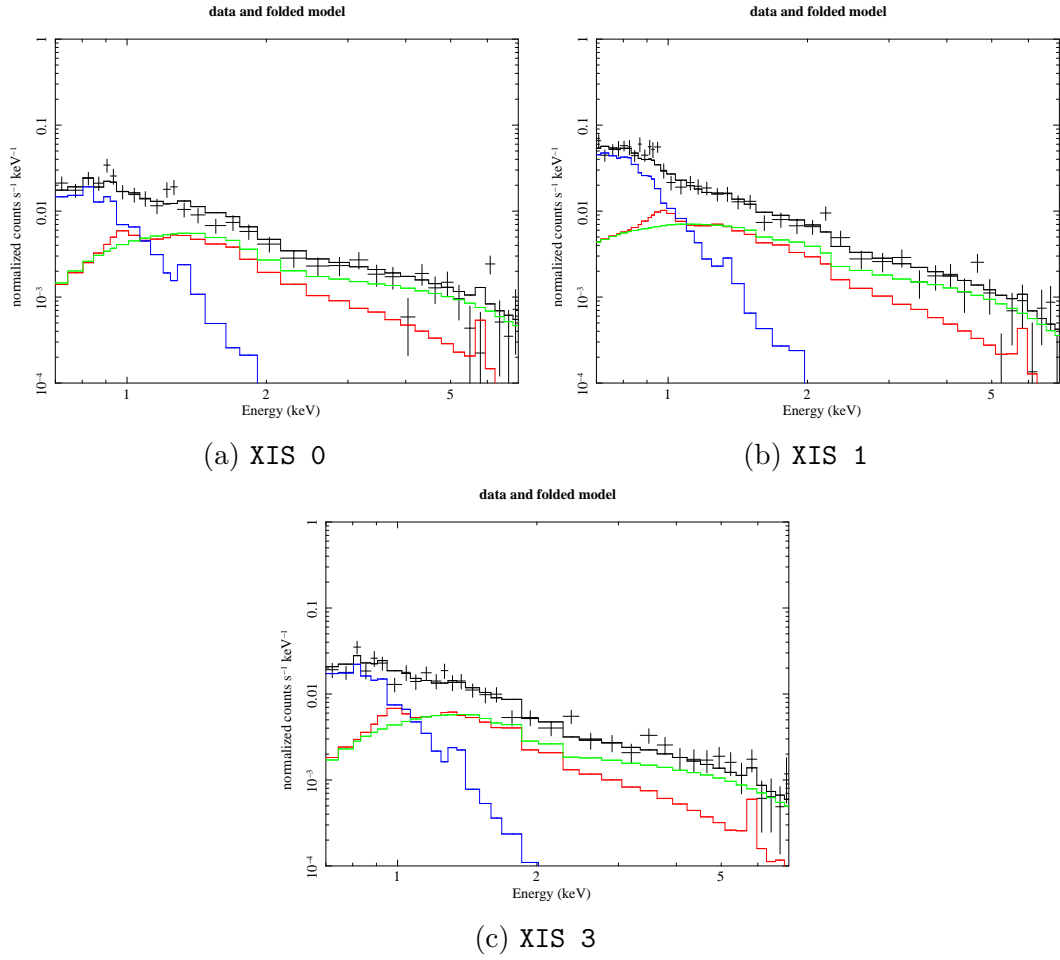
Figure A.35: The spectral fits for Annulus 5 (refer Table 3.1) of Abell 2204 for the fourth pointing

125

(a) XIS 0

(b) XIS 1

(c) XIS 2

(d) XIS 3
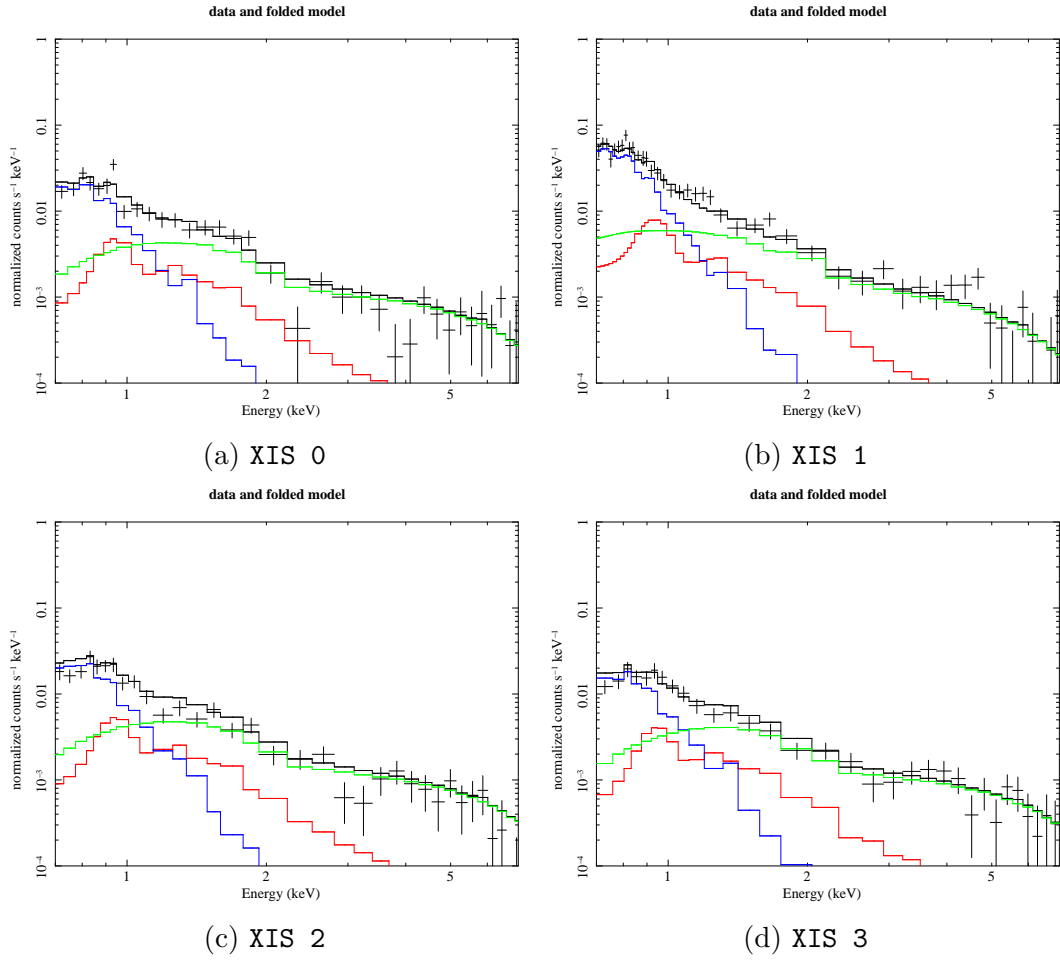
Figure A.36: The spectral fits for Annulus 6a (refer Table 3.1) of Abell 2204 for the first pointing

(a) XIS 0

(b) XIS 1

(c) XIS 3
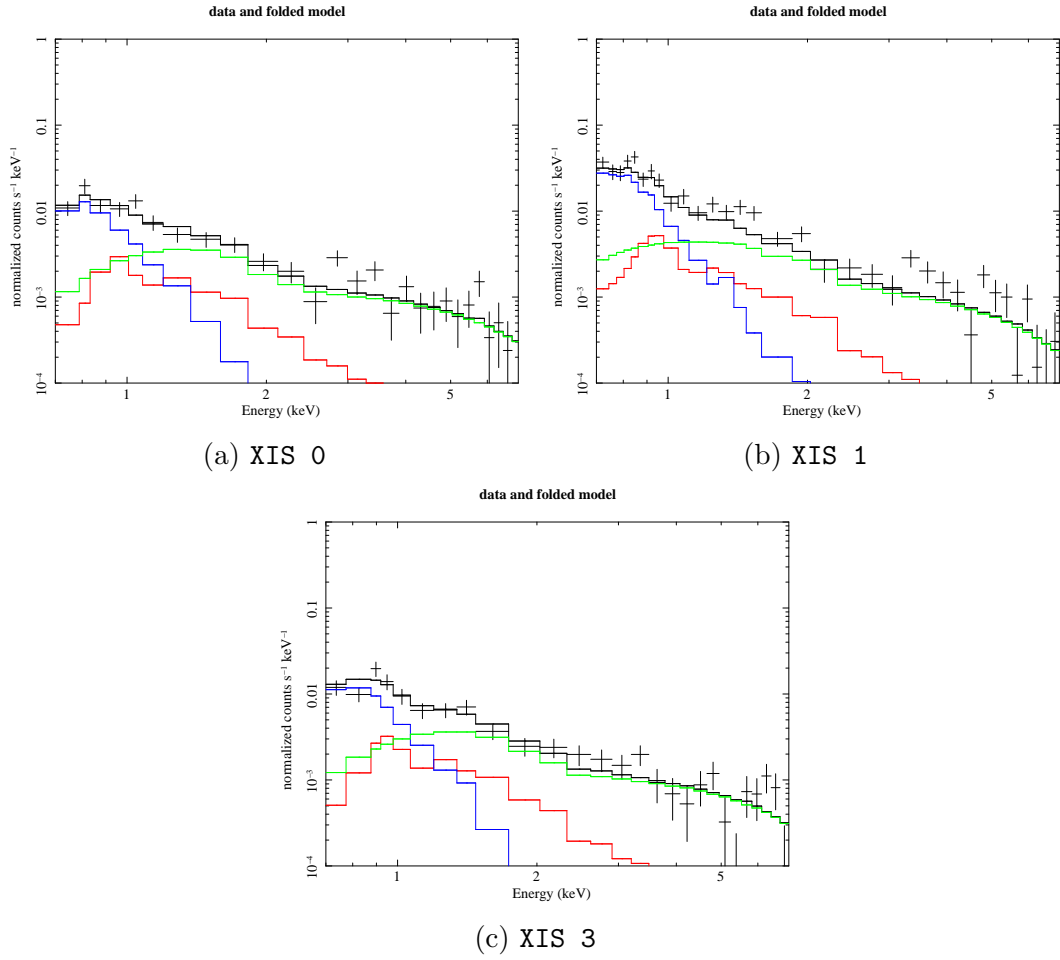
Figure A.37: The spectral fits for Annulus 6a (refer Table 3.1) of Abell 2204 for the second pointing

(a) XIS 0

(b) XIS 1

(c) XIS 3
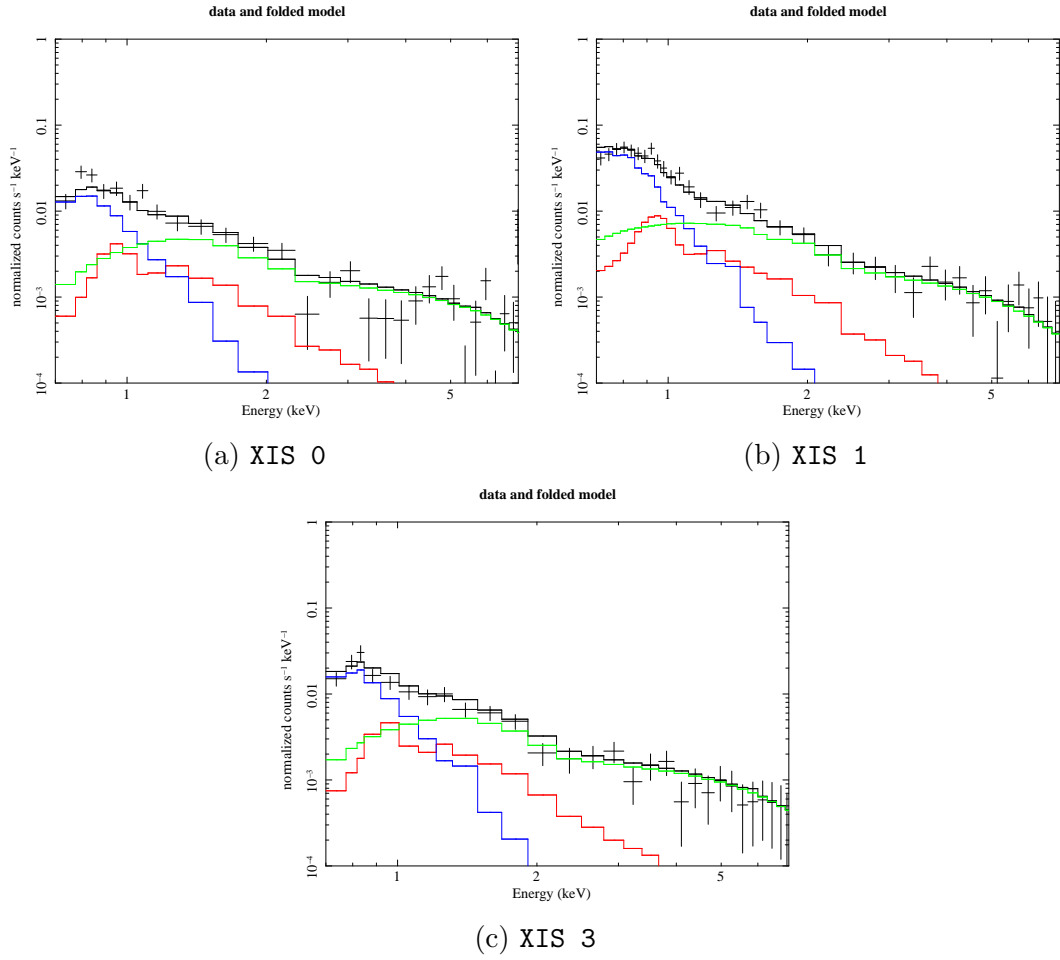
Figure A.38: The spectral fits for Annulus 6a (refer Table 3.1) of Abell 2204 for the third pointing

data and folded model

(a) XIS 0

data and folded model

(b) XIS 1

data and folded model

(c) XIS 3
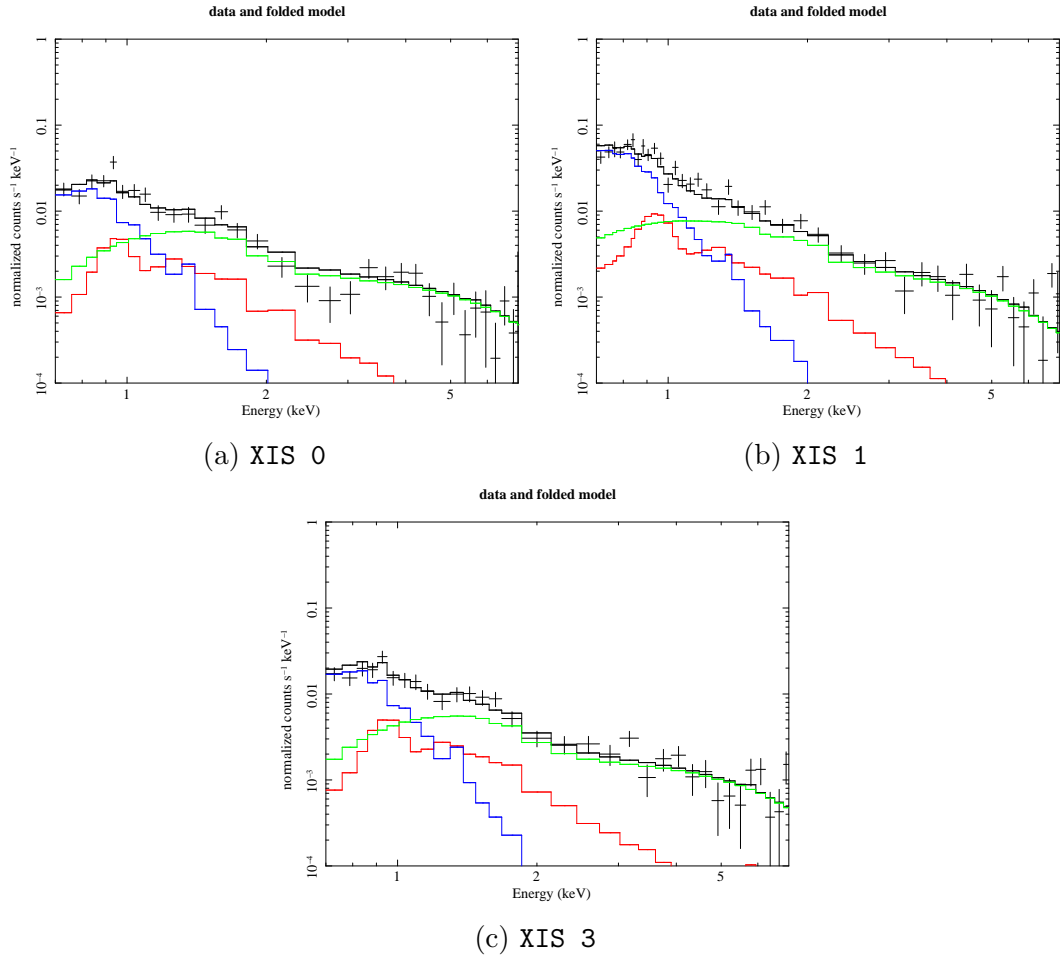
Figure A.39: The spectral fits for Annulus 6a (refer Table 3.1) of Abell 2204 for the fourth pointing

A.3 Abell 773

Presented below are the *Suzaku* pointings for Abell 773 we utilized for this analysis. The observation details are shown below in Table A.3.

Pointing #	Observation ID	Comments
1	806027010	Proposed Data
2	806027020	Proposed Data
3	806027030	Proposed Data
4	806027040	Proposed Data

Table A.3: The *Suzaku* data on Abell 773 used for this analysis

For all pointings, we use only detectors XIS 0, XIS 1 and XIS 3 for our analysis.

(a) XIS 0

(b) XIS 1

(c) XIS 3
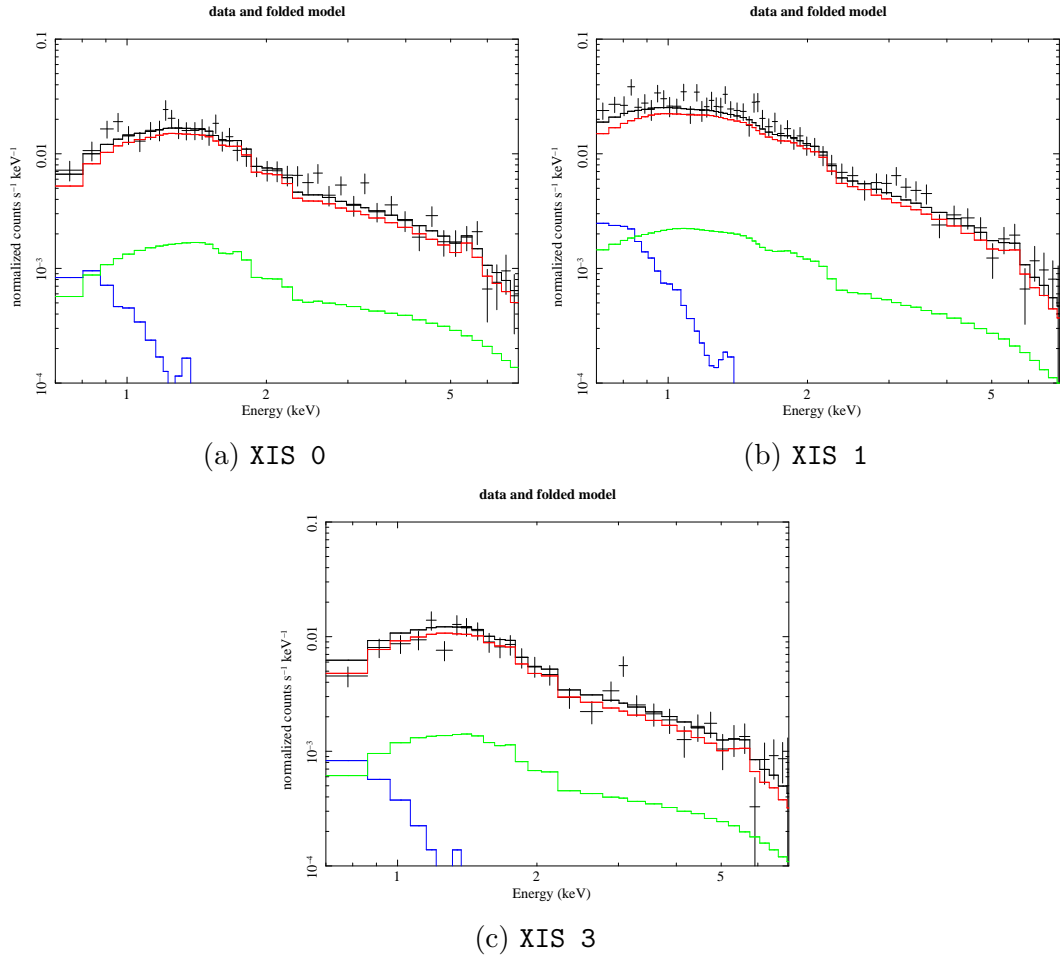
Figure A.40: The spectral fits for Annulus 2 (refer Table 3.1) of Abell 773 for the first pointing

(a) XIS 0

(b) XIS 1

(c) XIS 3
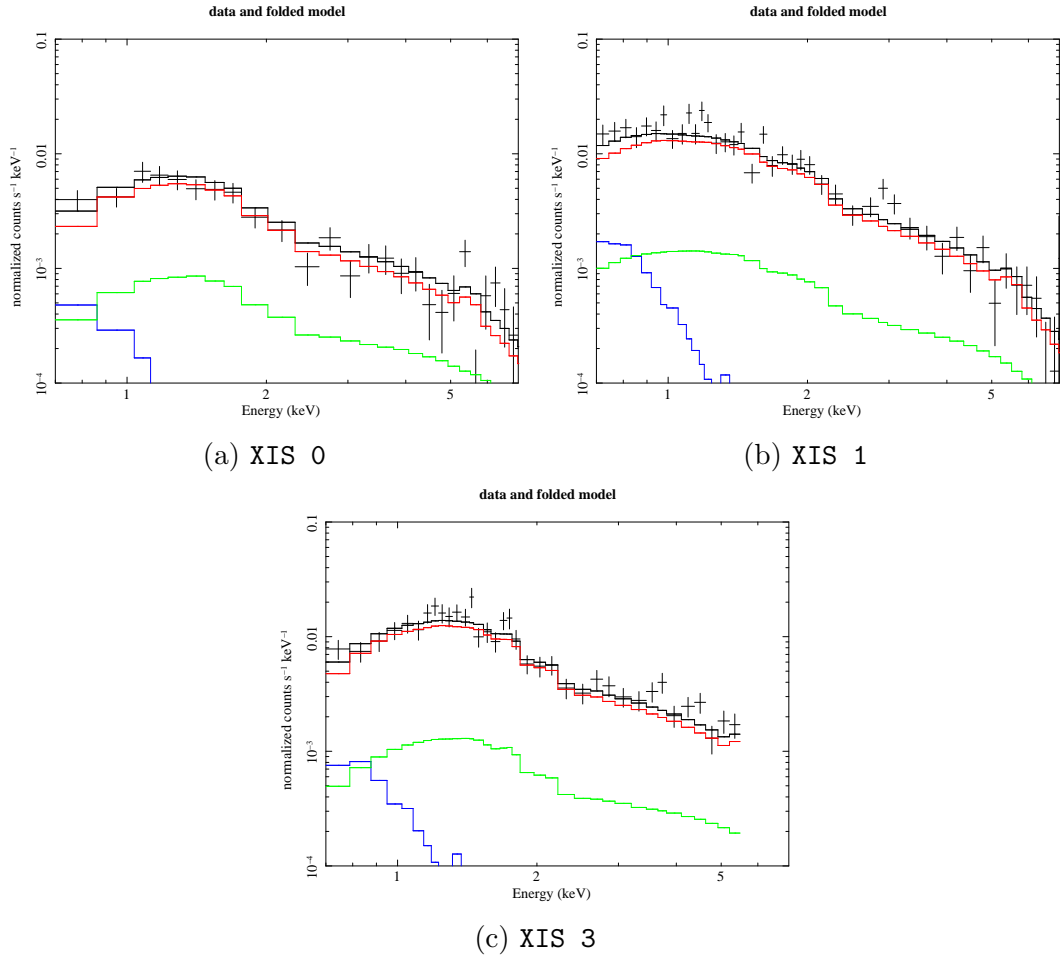
Figure A.41: The spectral fits for Annulus 2 (refer Table 3.1) of Abell 773 for the second pointing

(a) XIS 0

(b) XIS 1

(c) XIS 3
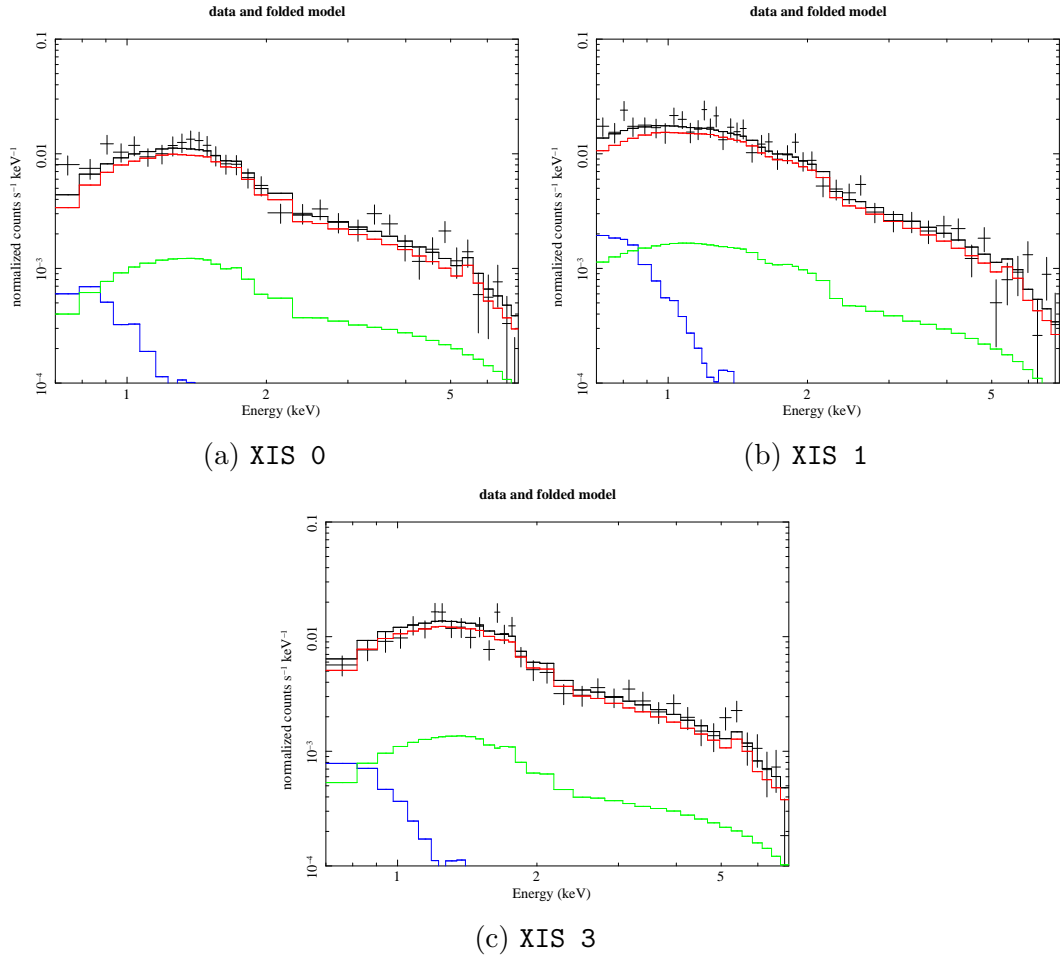
Figure A.42: The spectral fits for Annulus 2 (refer Table 3.1) of Abell 773 for the third pointing

133

(a) XIS 0

(b) XIS 1

(c) XIS 3
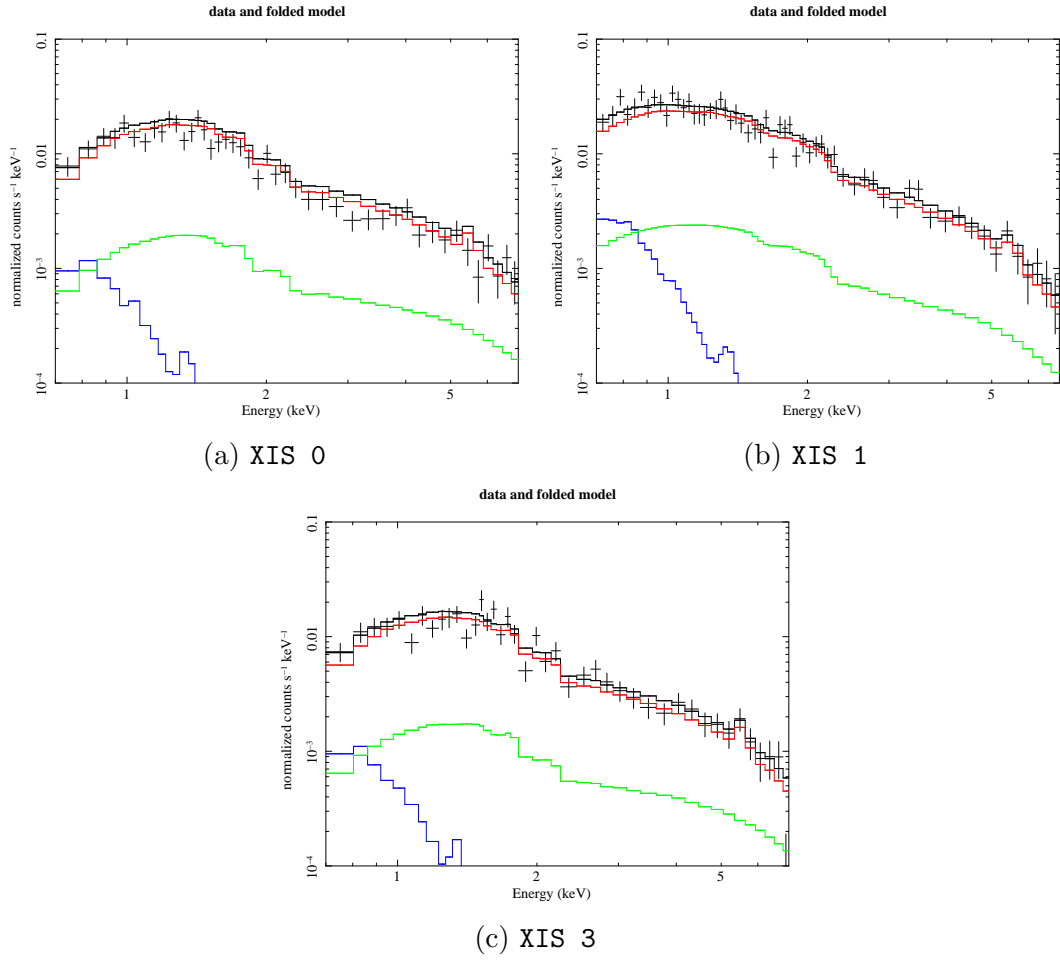
Figure A.43: The spectral fits for Annulus 2 (refer Table 3.1) of Abell 773 for the fourth pointing

134

(a) XIS 0

(b) XIS 1

(c) XIS 3
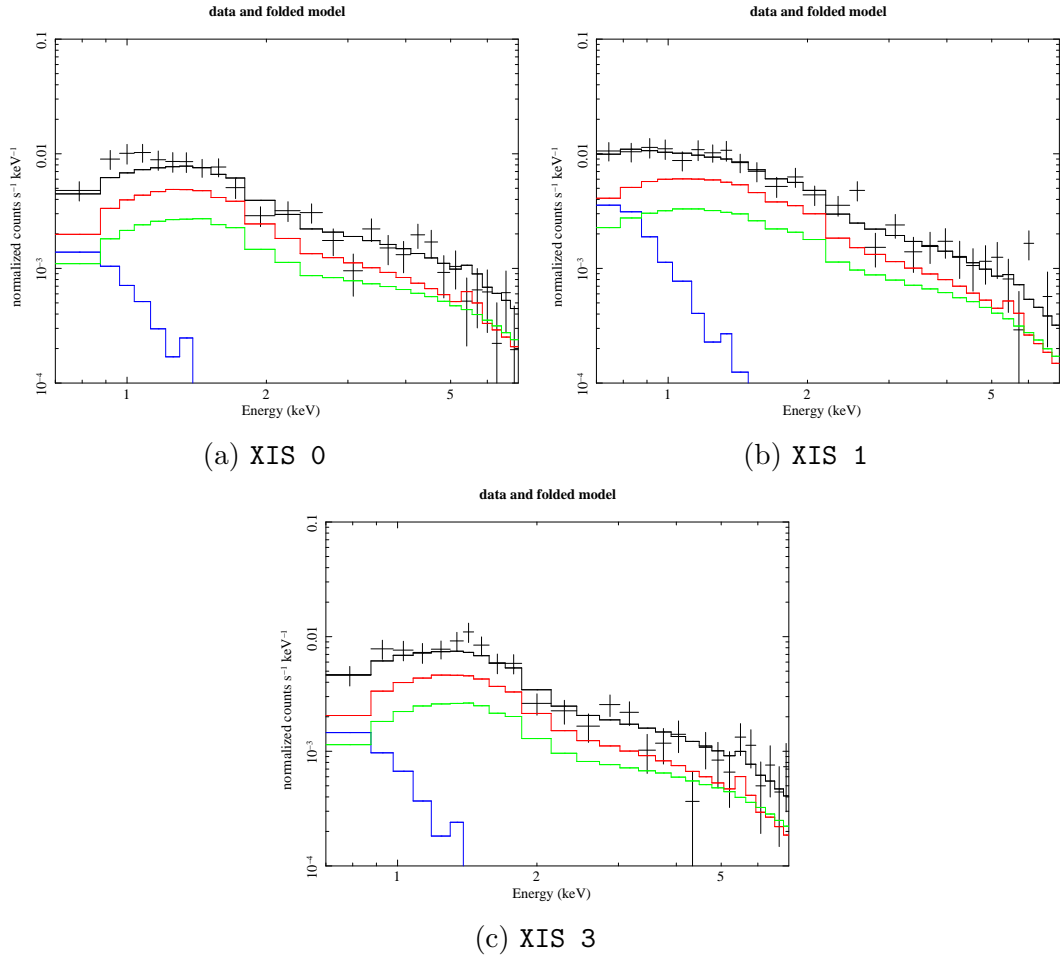
Figure A.44: The spectral fits for Annulus 3 (refer Table 3.1) of Abell 773 for the first pointing

135

(a) XIS 0

(b) XIS 1

(c) XIS 3
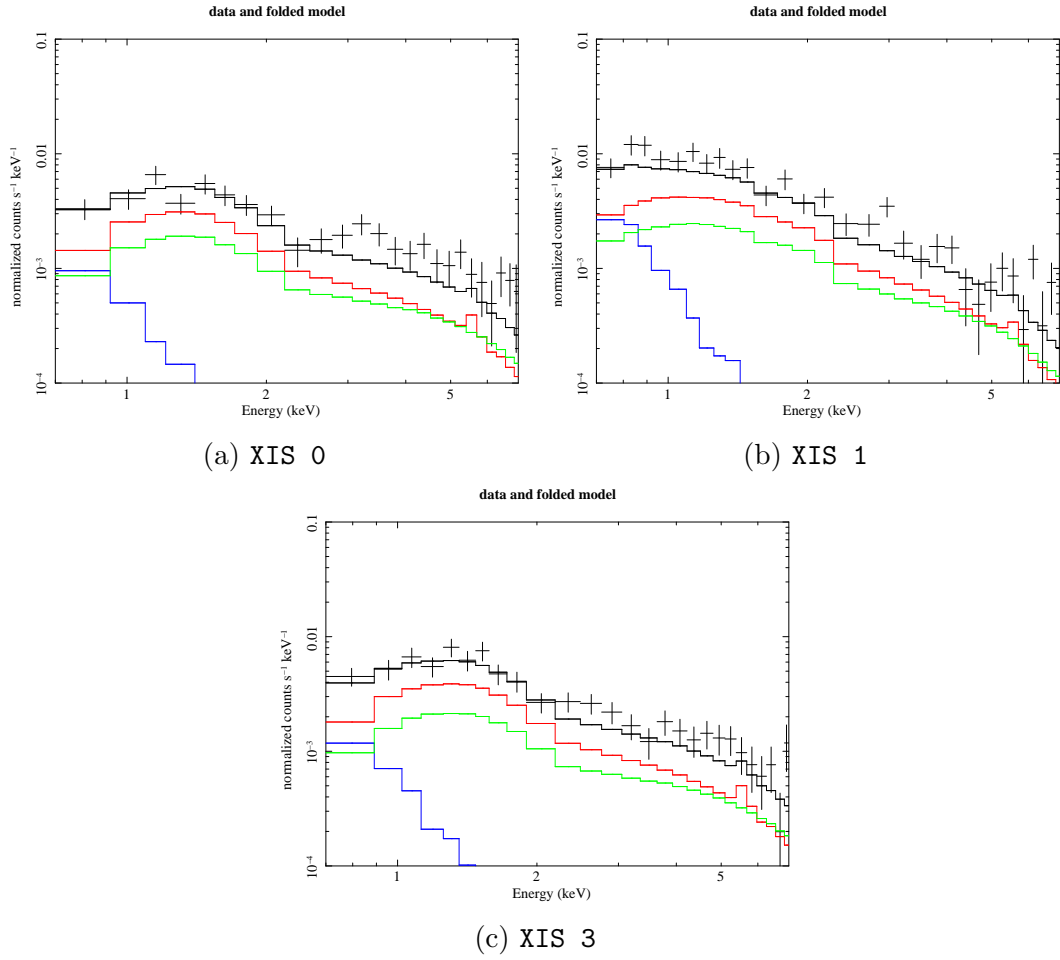
Figure A.45: The spectral fits for Annulus 3 (refer Table 3.1) of Abell 773 for the second pointing

(a) XIS 0

(b) XIS 1

(c) XIS 3
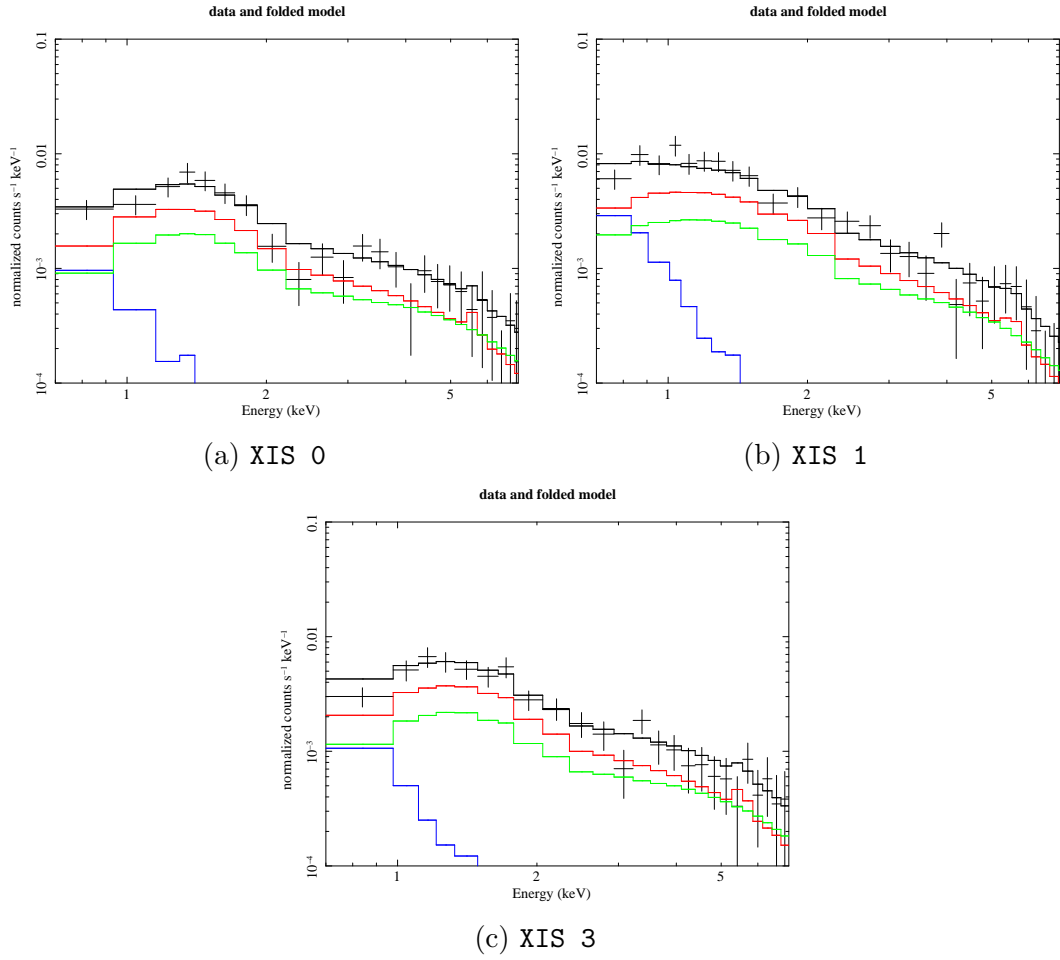
Figure A.46: The spectral fits for Annulus 3 (refer Table 3.1) of Abell 773 for the third pointing

137

(a) XIS 0

(b) XIS 1

(c) XIS 3
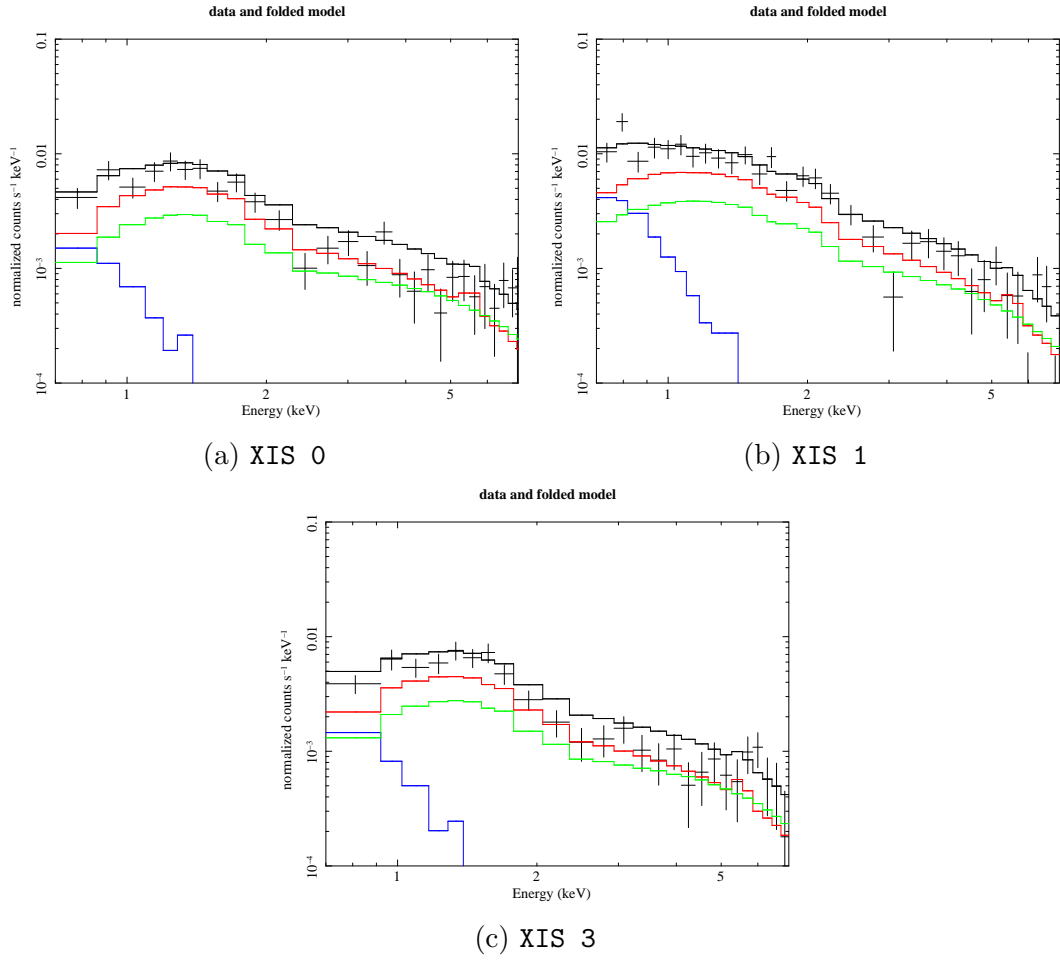
Figure A.47: The spectral fits for Annulus 3 (refer Table 3.1) of Abell 773 for the fourth pointing

(a) XIS 0

(b) XIS 1

(c) XIS 3
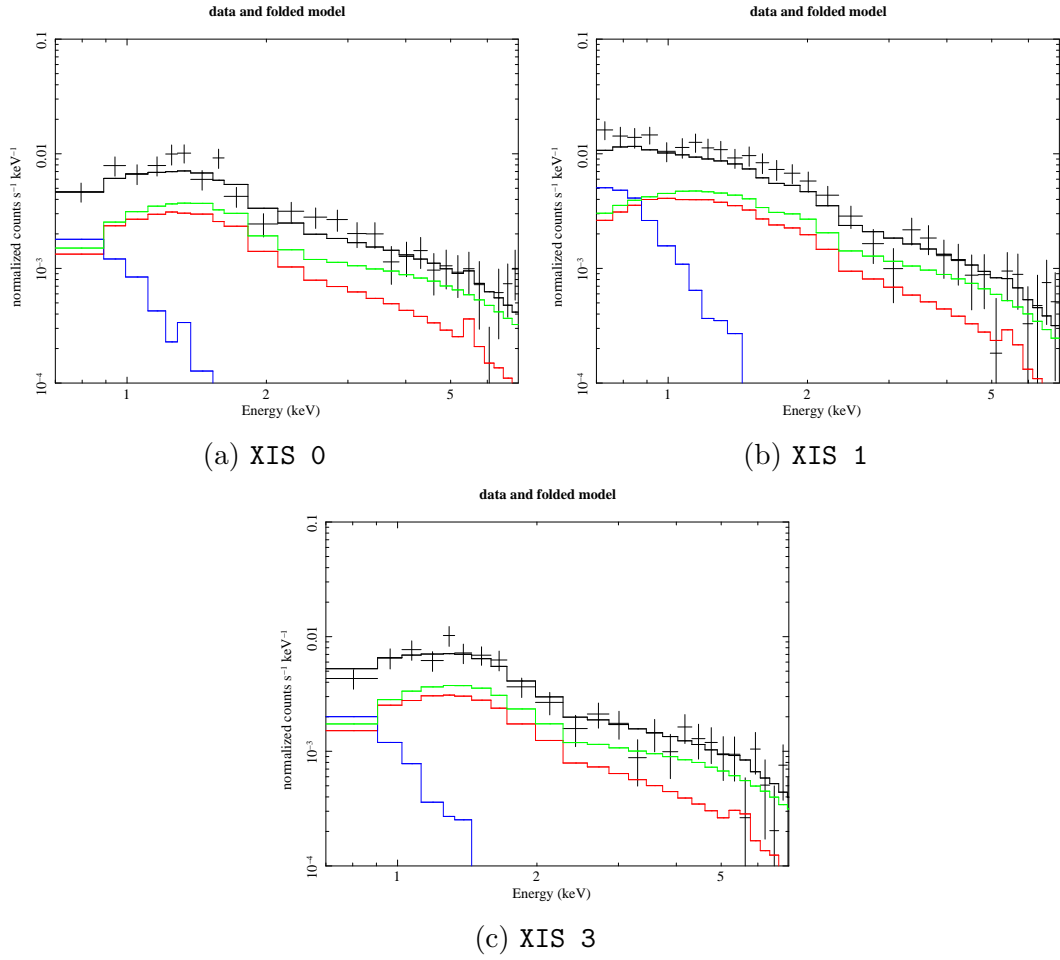
Figure A.48: The spectral fits for Annulus 4 (refer Table 3.1) of Abell 773 for the first pointing

139

(a) XIS 0

(b) XIS 1

(c) XIS 3
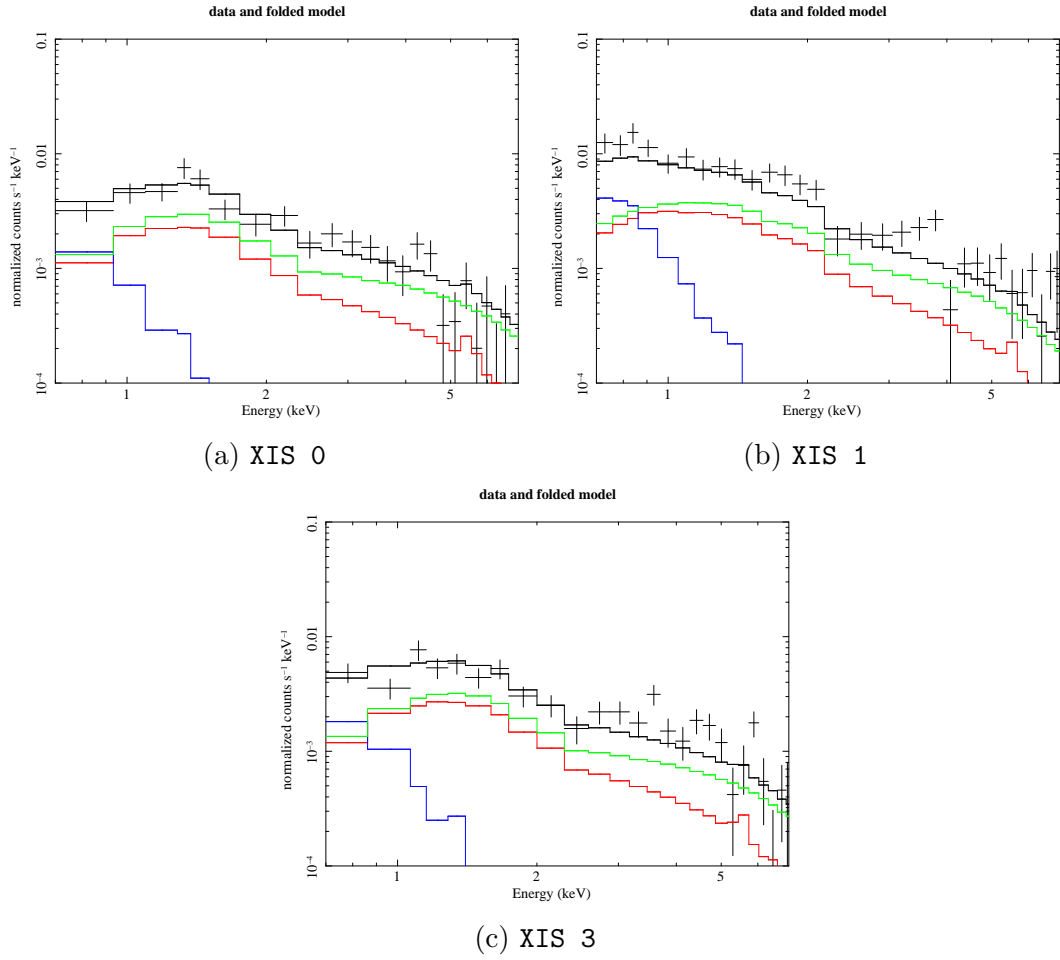
Figure A.49: The spectral fits for Annulus 4 (refer Table 3.1) of Abell 773 for the second pointing

(a) XIS 0

(b) XIS 1

(c) XIS 3
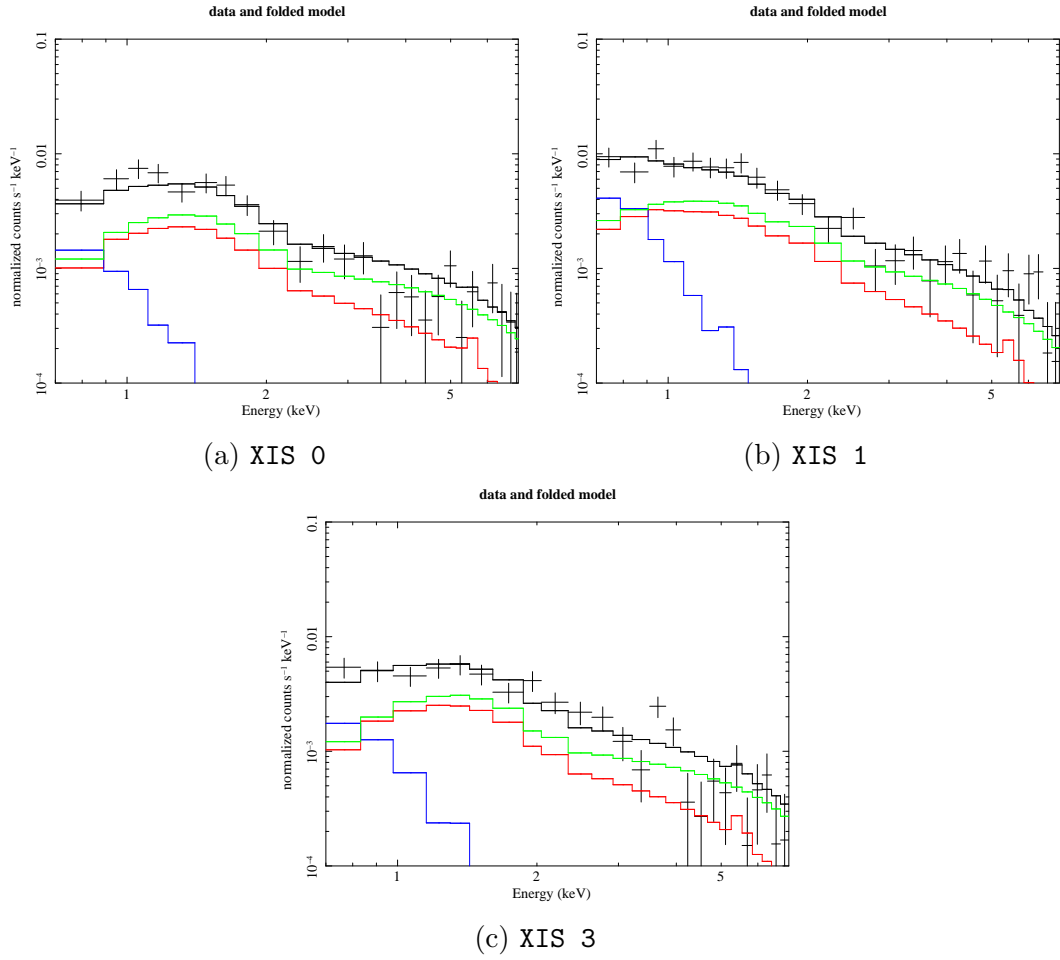
Figure A.50: The spectral fits for Annulus 4 (refer Table 3.1) of Abell 773 for the third pointing

(a) XIS 0

(b) XIS 1

(c) XIS 3
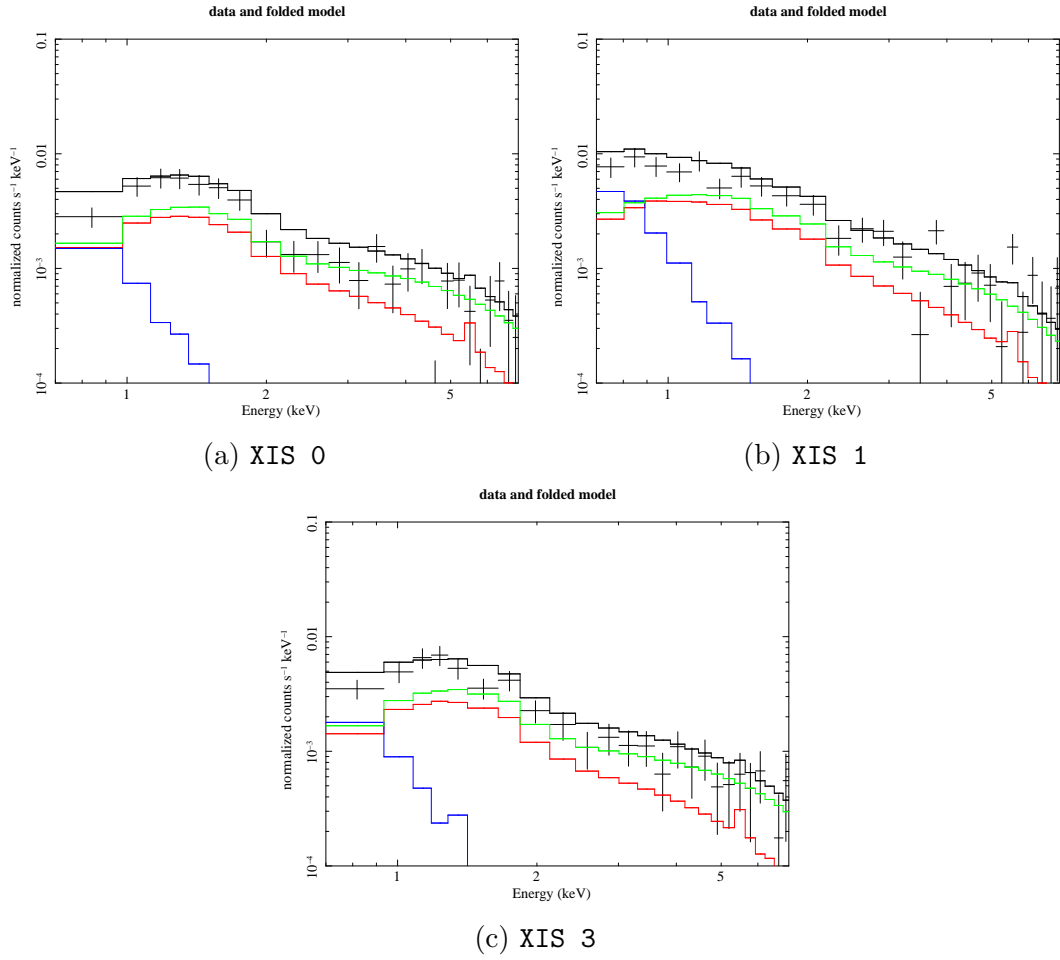
Figure A.51: The spectral fits for Annulus 4 (refer Table 3.1) of Abell 773 for the fourth pointing

(a) XIS 0

(b) XIS 1

(c) XIS 3
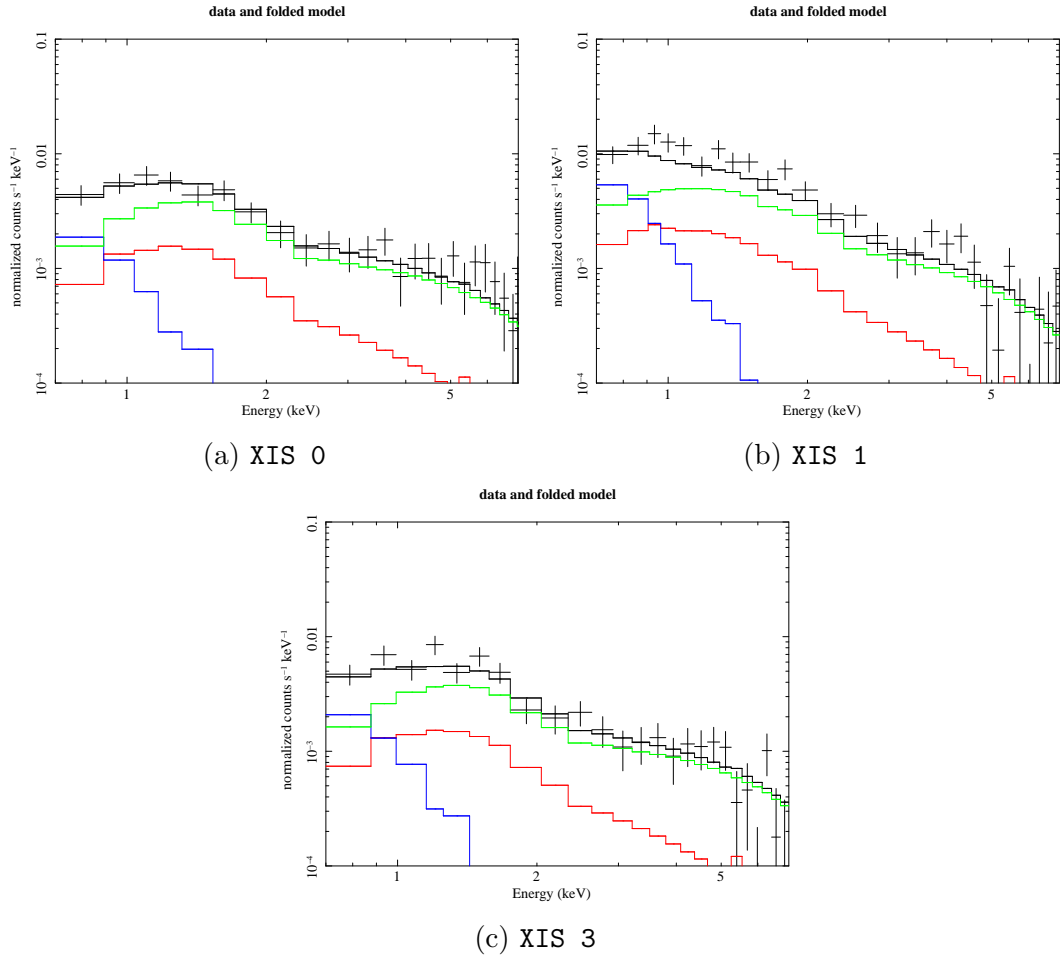
Figure A.52: The spectral fits for Annulus 5 (refer Table 3.1) of Abell 773 for the first pointing

143

(a) XIS 0

(b) XIS 1

(c) XIS 3
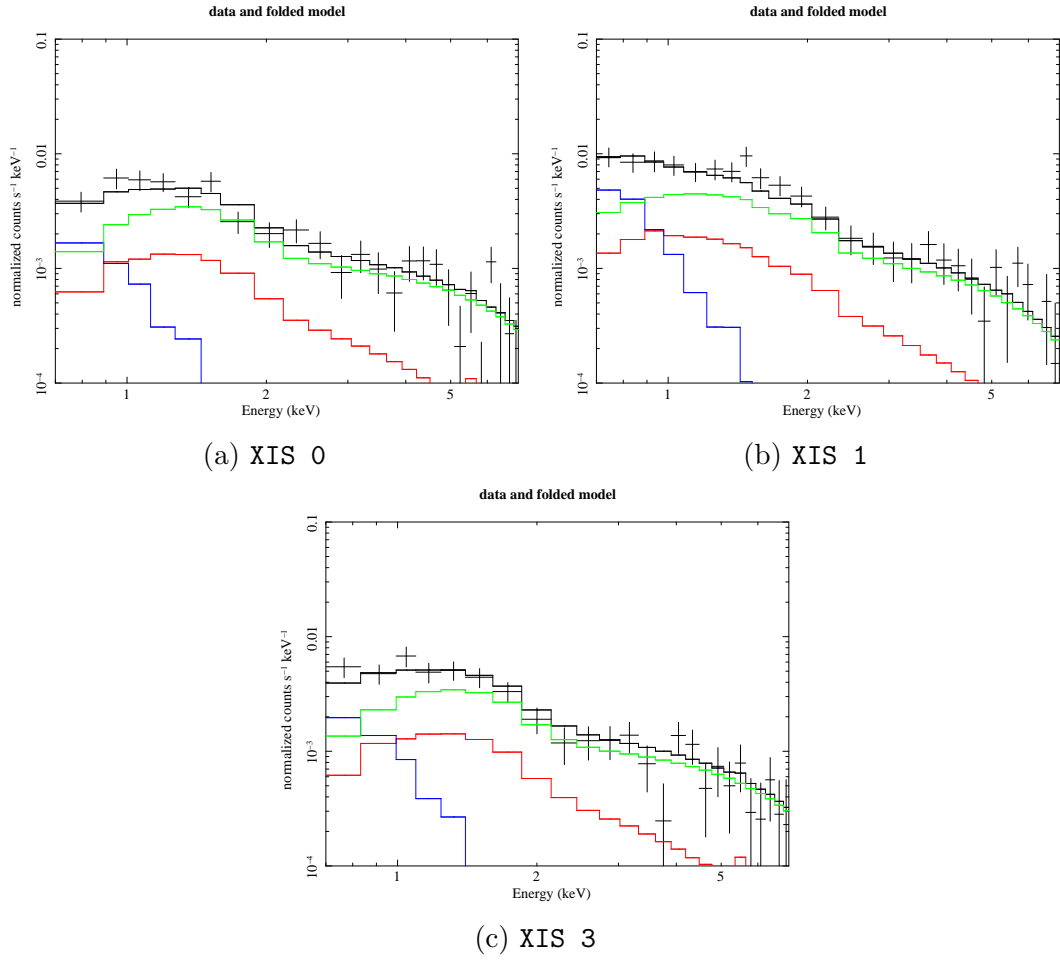
Figure A.53: The spectral fits for Annulus 5 (refer Table 3.1) of Abell 773 for the second pointing

144

(a) XIS 0

(b) XIS 1

(c) XIS 3
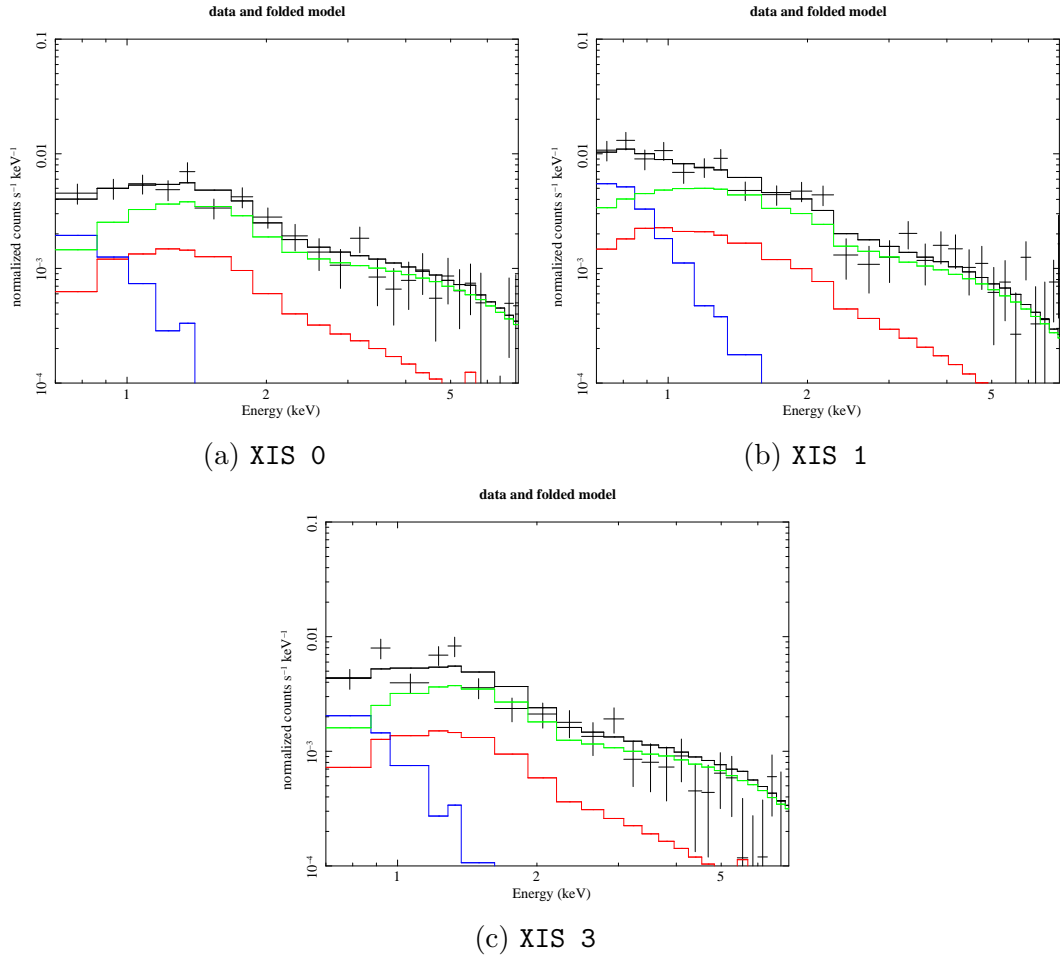
Figure A.54: The spectral fits for Annulus 5 (refer Table 3.1) of Abell 773 for the third pointing

(a) XIS 0

(b) XIS 1

(c) XIS 3
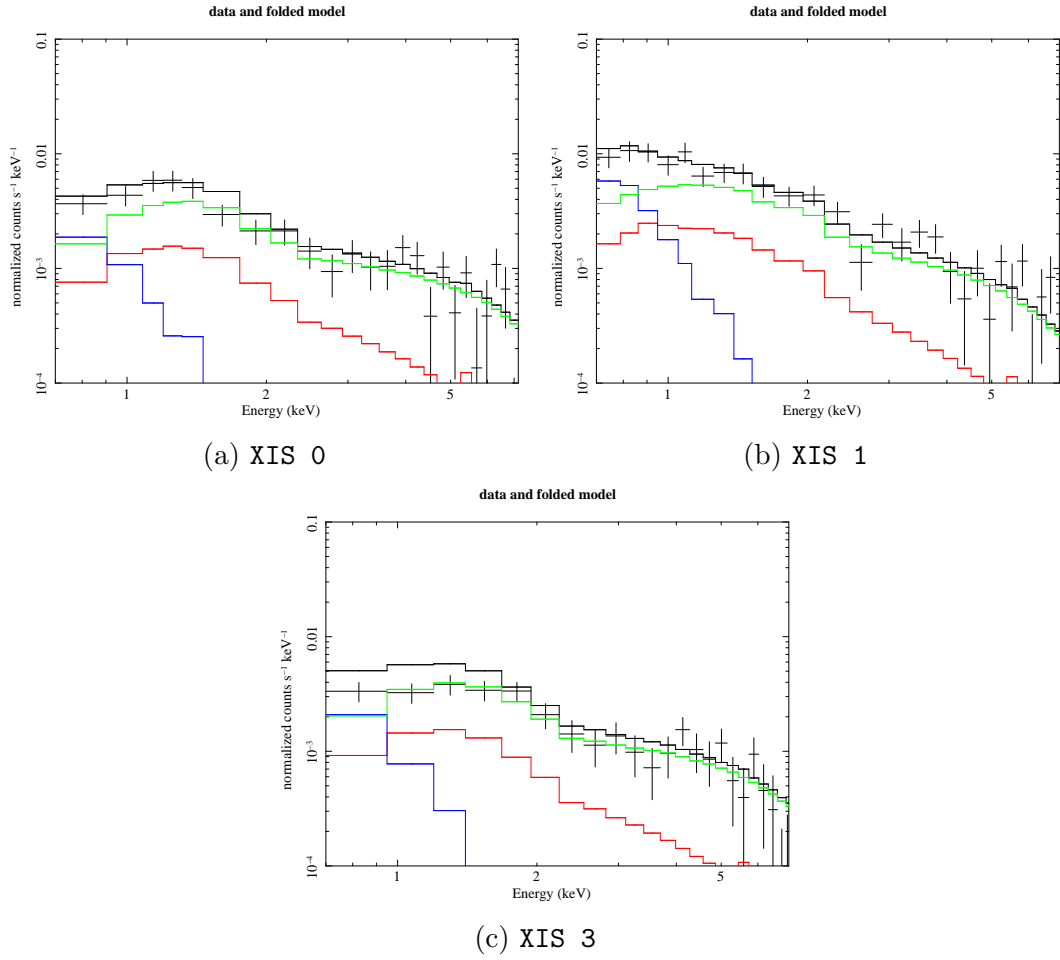
Figure A.55: The spectral fits for Annulus 5 (refer Table 3.1) of Abell 773 for the fourth pointing

(a) XIS 0

(b) XIS 1

(c) XIS 3
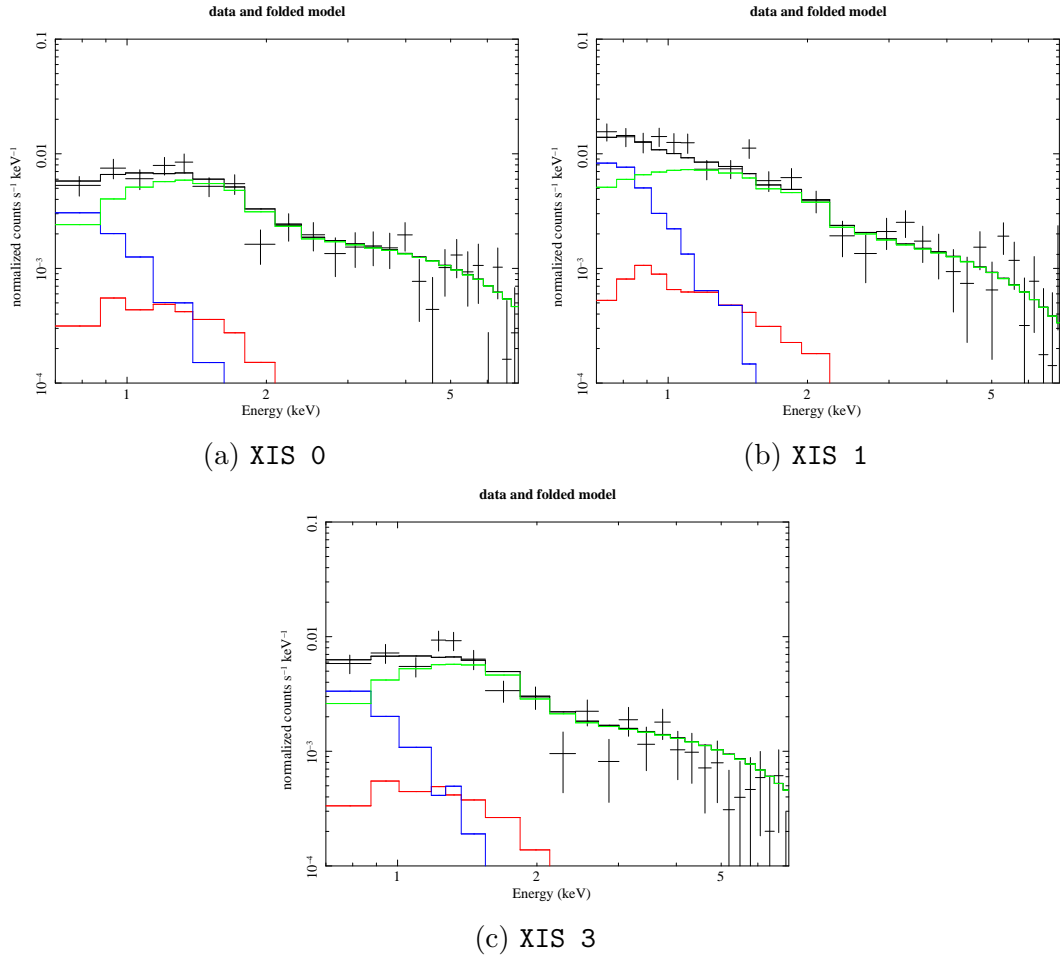
Figure A.56: The spectral fits for Annulus 6b (refer Table 3.1) of Abell 773 for the first pointing

(a) XIS 0

(b) XIS 1

(c) XIS 3
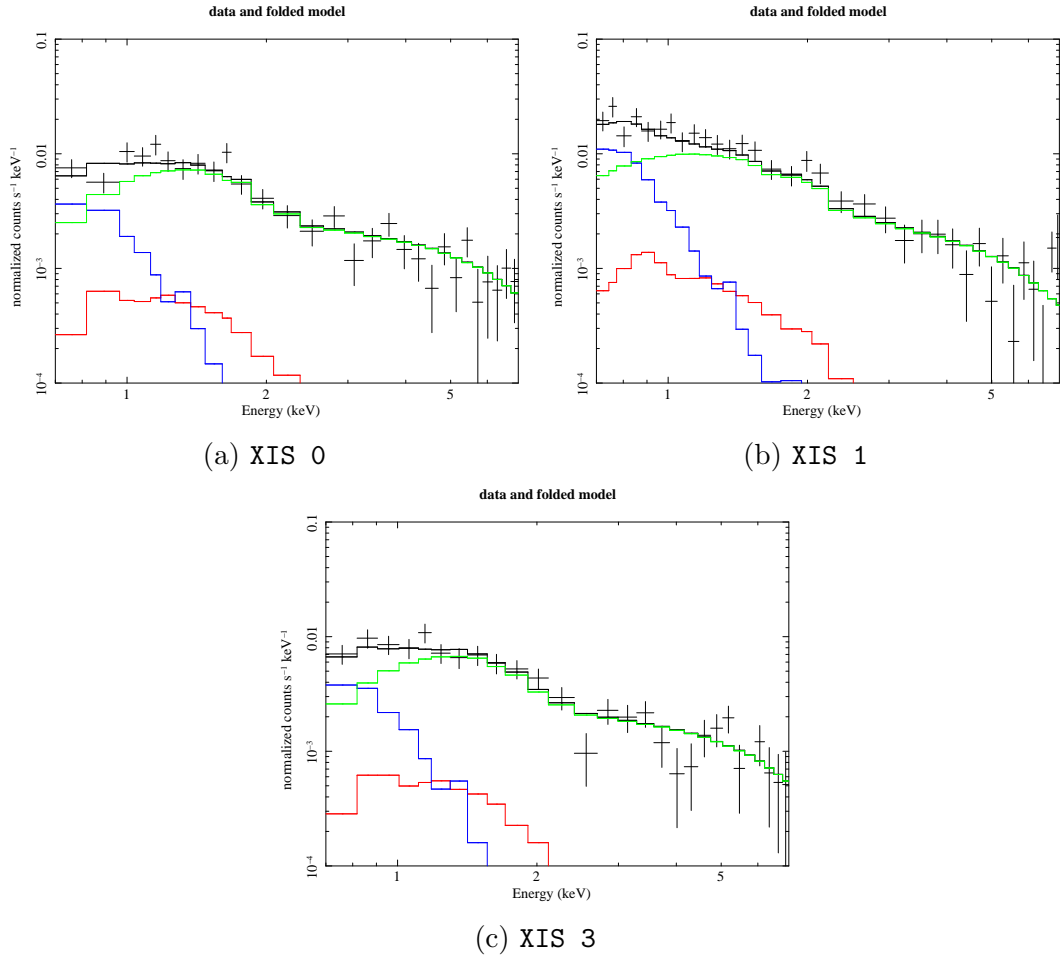
Figure A.57: The spectral fits for Annulus 6b (refer Table 3.1) of Abell 773 for the second pointing

148

(a) XIS 0

(b) XIS 1

(c) XIS 3
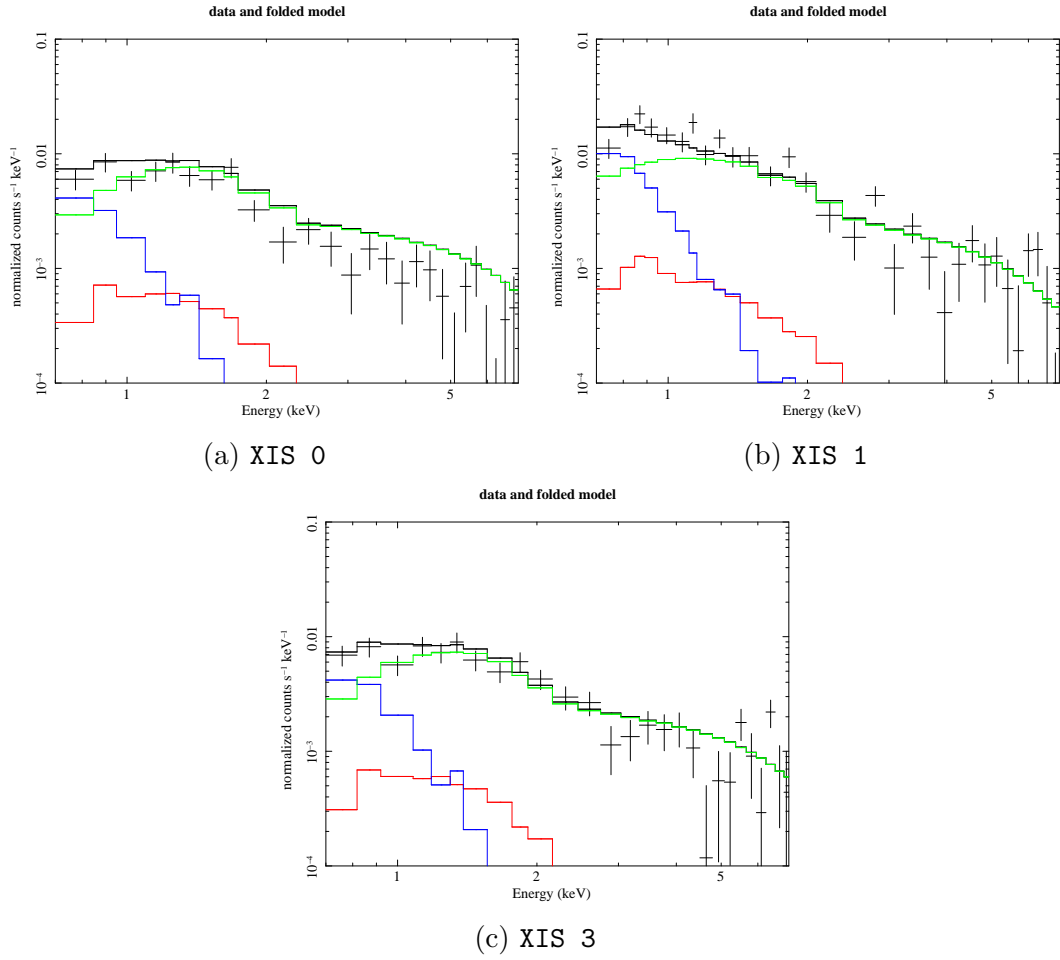
Figure A.58: The spectral fits for Annulus 6b (refer Table 3.1) of Abell 773 for the third pointing

(a) XIS 0

(b) XIS 1

(c) XIS 3
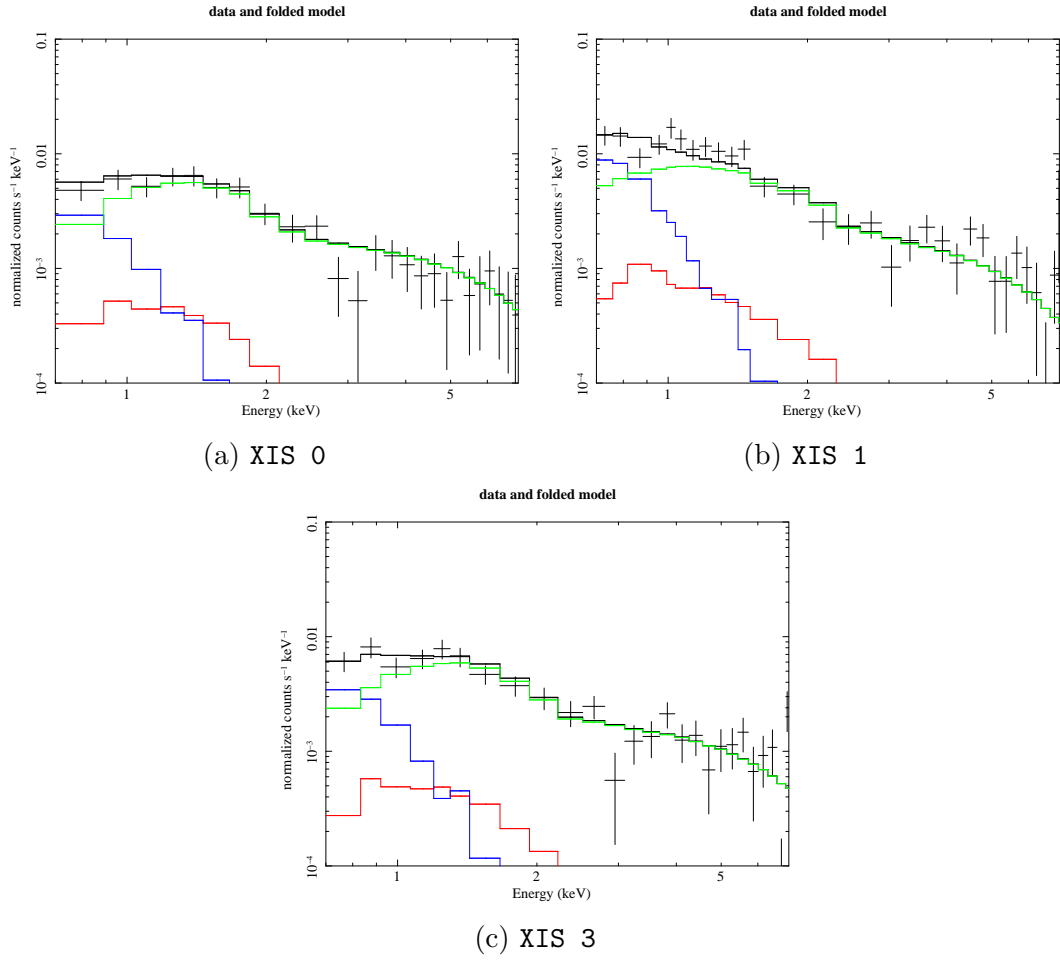
Figure A.59: The spectral fits for Annulus 6b (refer Table 3.1) of Abell 773 for the fourth pointing

A.4   Abell 383

Presented below are the *Suzaku* pointings for Abell 383 we utilized for this analysis. The observation details are shown below in Table A.4.

Pointing #	Observation ID	Comments
1	805062010	Proposed Data
2	805063010	Proposed Data
3	805064010	Proposed Data

Table A.4: The *Suzaku* data on Abell 383 used for this analysis

For all pointings, we use only detectors XIS 0, XIS 1 and XIS 3 for our analysis. This cluster only required three pointings for full azimuthal coverage out r_{200}.

(a) XIS 0

(b) XIS 1

(c) XIS 3
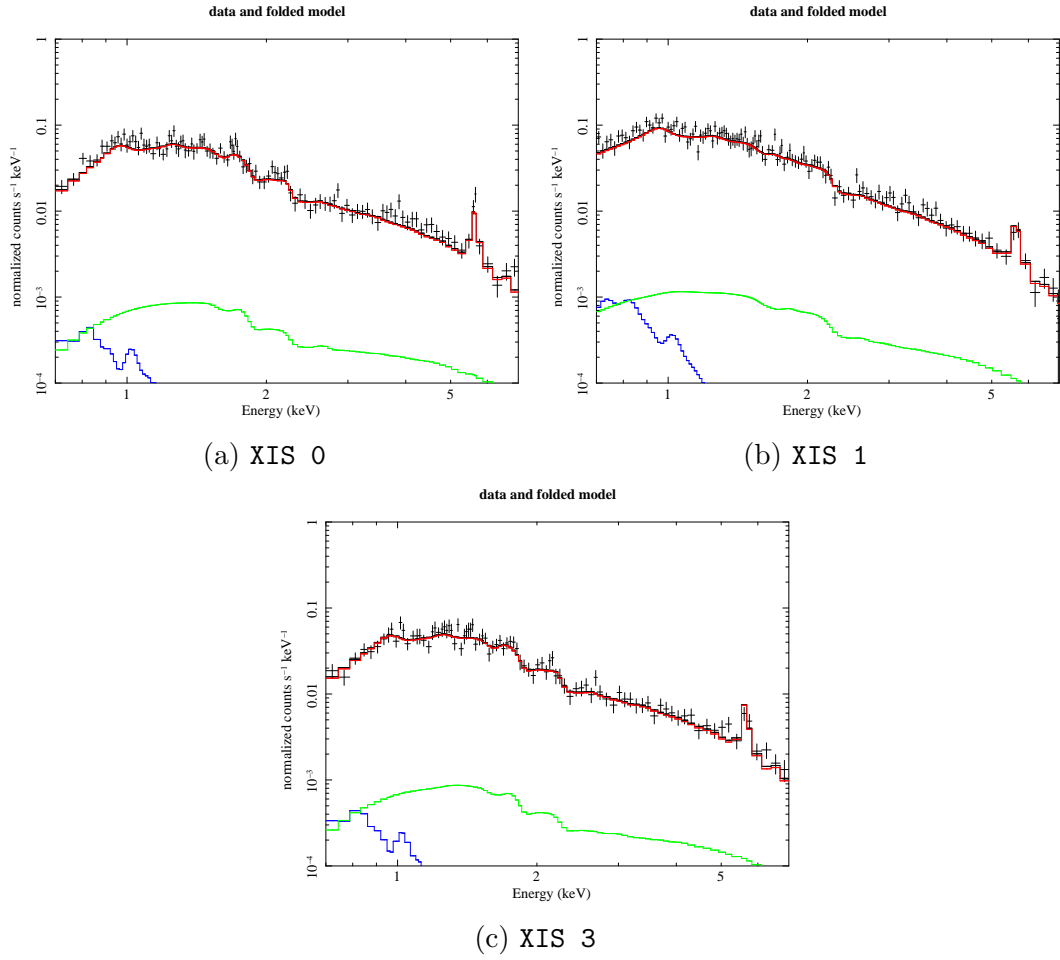
Figure A.60: The spectral fits for Annulus 1 (refer Table 3.1) of Abell 383 for the first pointing

152

(a) XIS 0   (b) XIS 1

(c) XIS 3
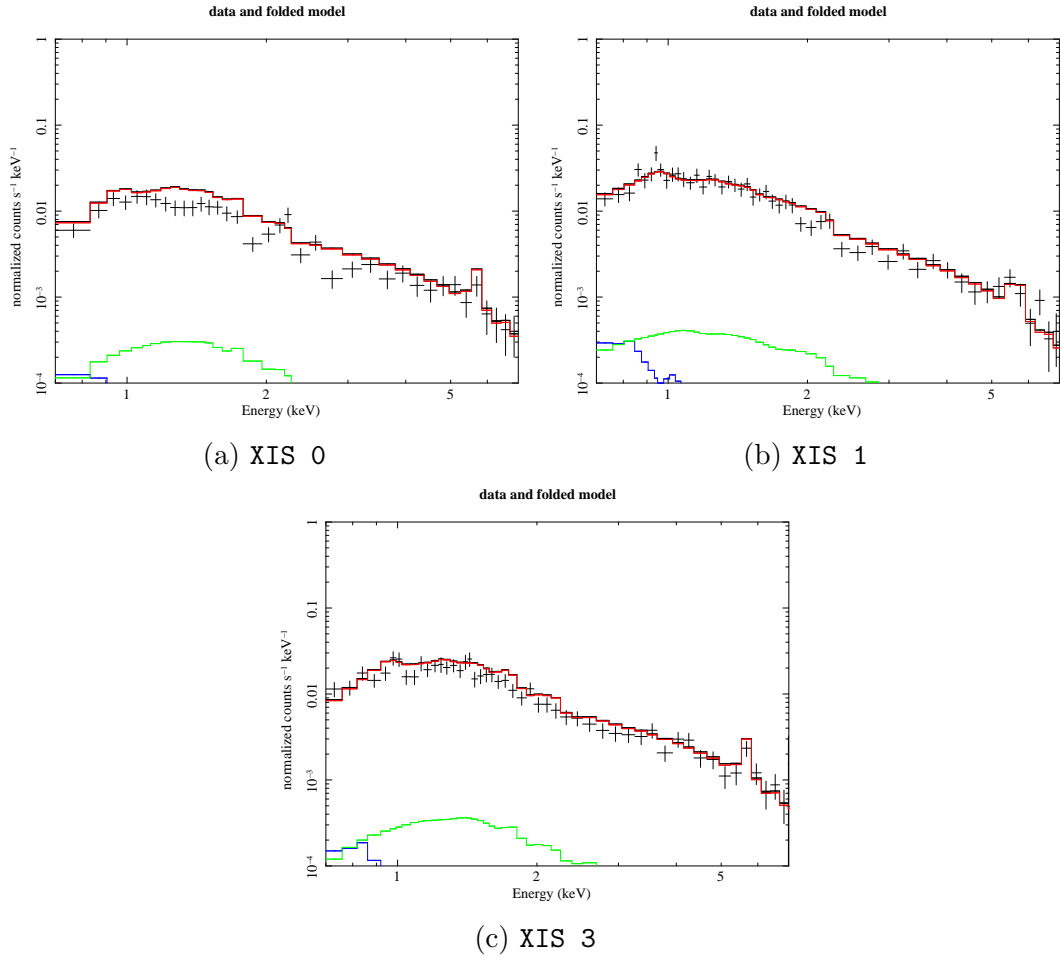
Figure A.61: The spectral fits for Annulus 1 (refer Table 3.1) of Abell 383 for the second pointing

(a) XIS 0   (b) XIS 1

(c) XIS 3
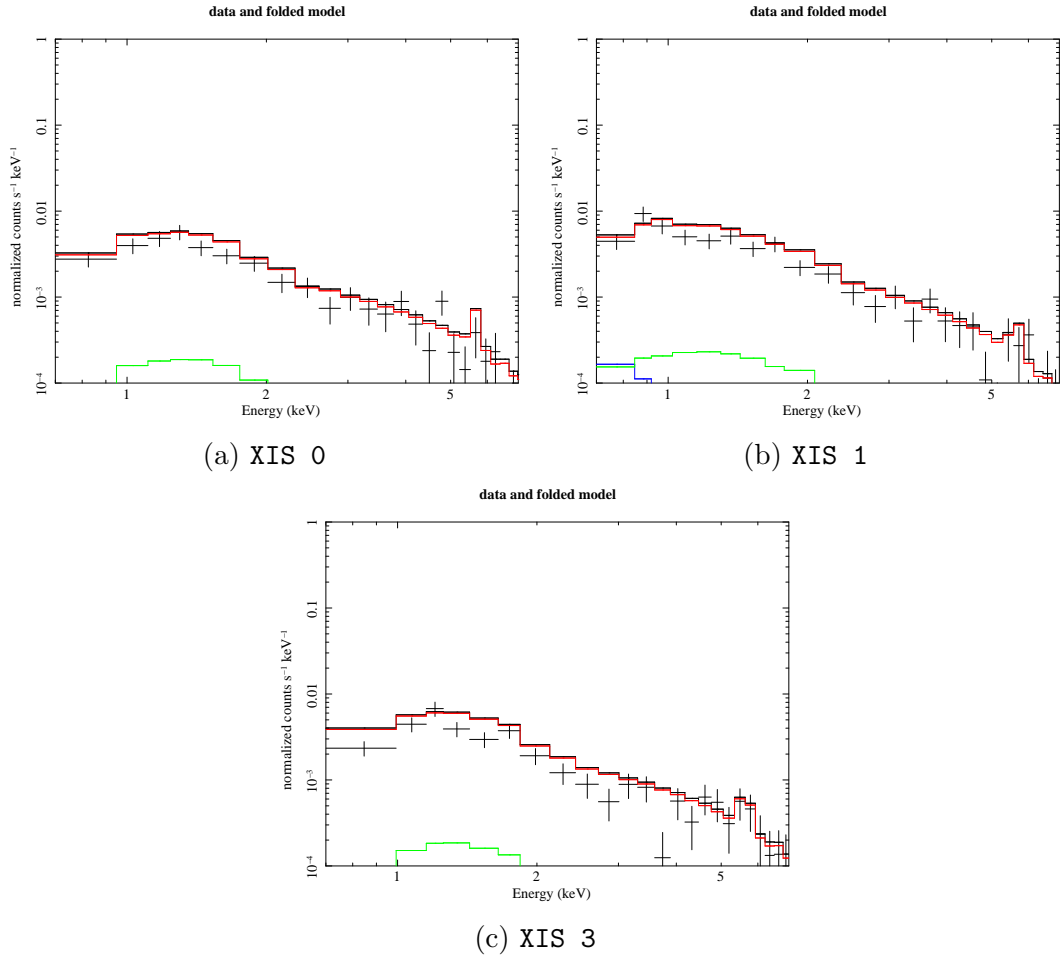
Figure A.62: The spectral fits for Annulus 1 (refer Table 3.1) of Abell 383 for the third pointing

(a) XIS 0

(b) XIS 1

(c) XIS 3
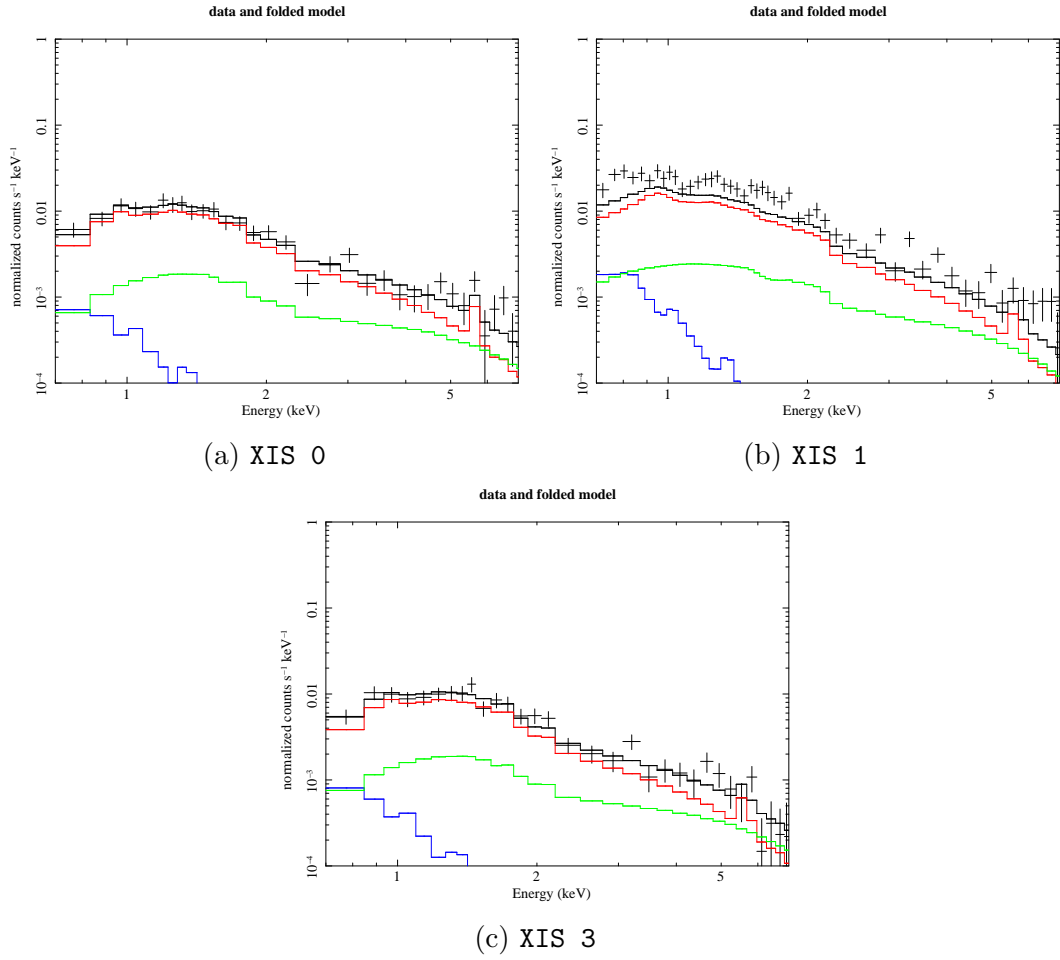
Figure A.63: The spectral fits for Annulus 2 (refer Table 3.1) of Abell 383 for the first pointing

155

(a) XIS 0

(b) XIS 1

(c) XIS 3
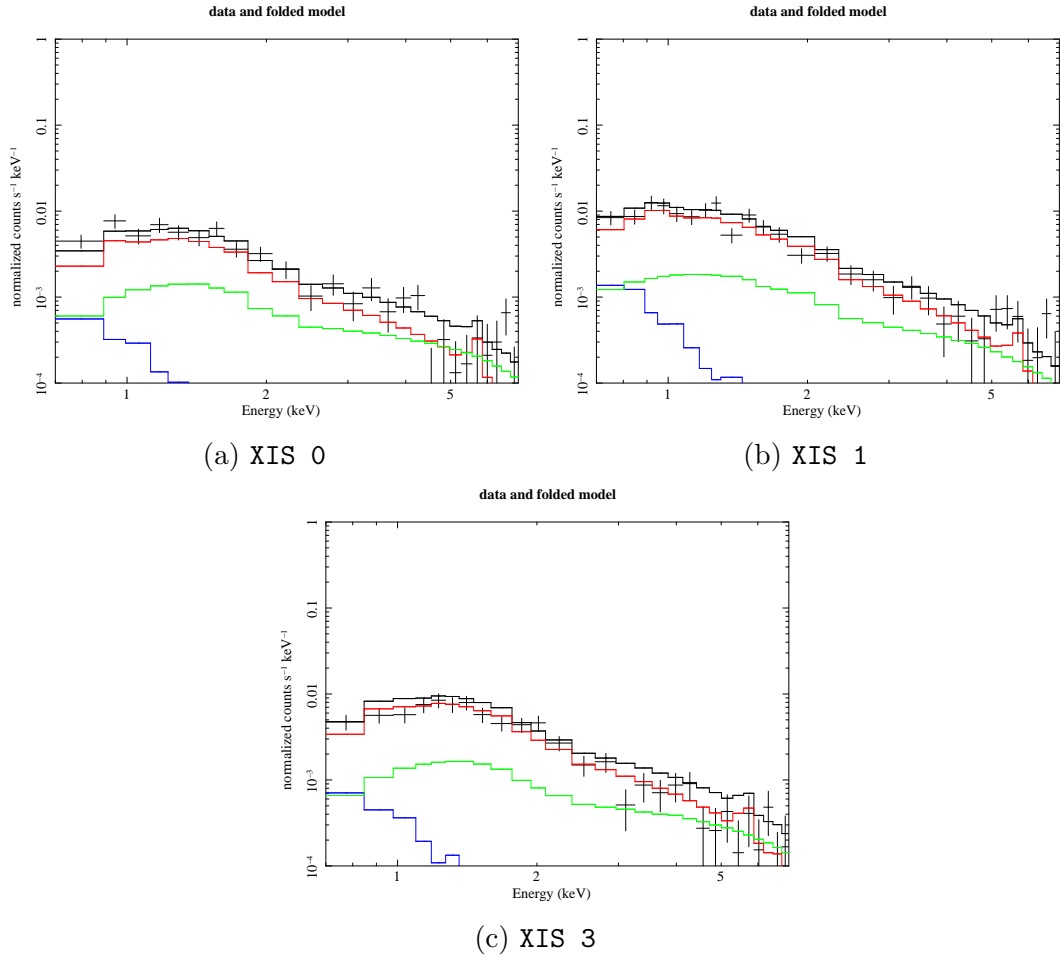
Figure A.64: The spectral fits for Annulus 2 (refer Table 3.1) of Abell 383 for the second pointing

(a) XIS 0

(b) XIS 1

(c) XIS 3
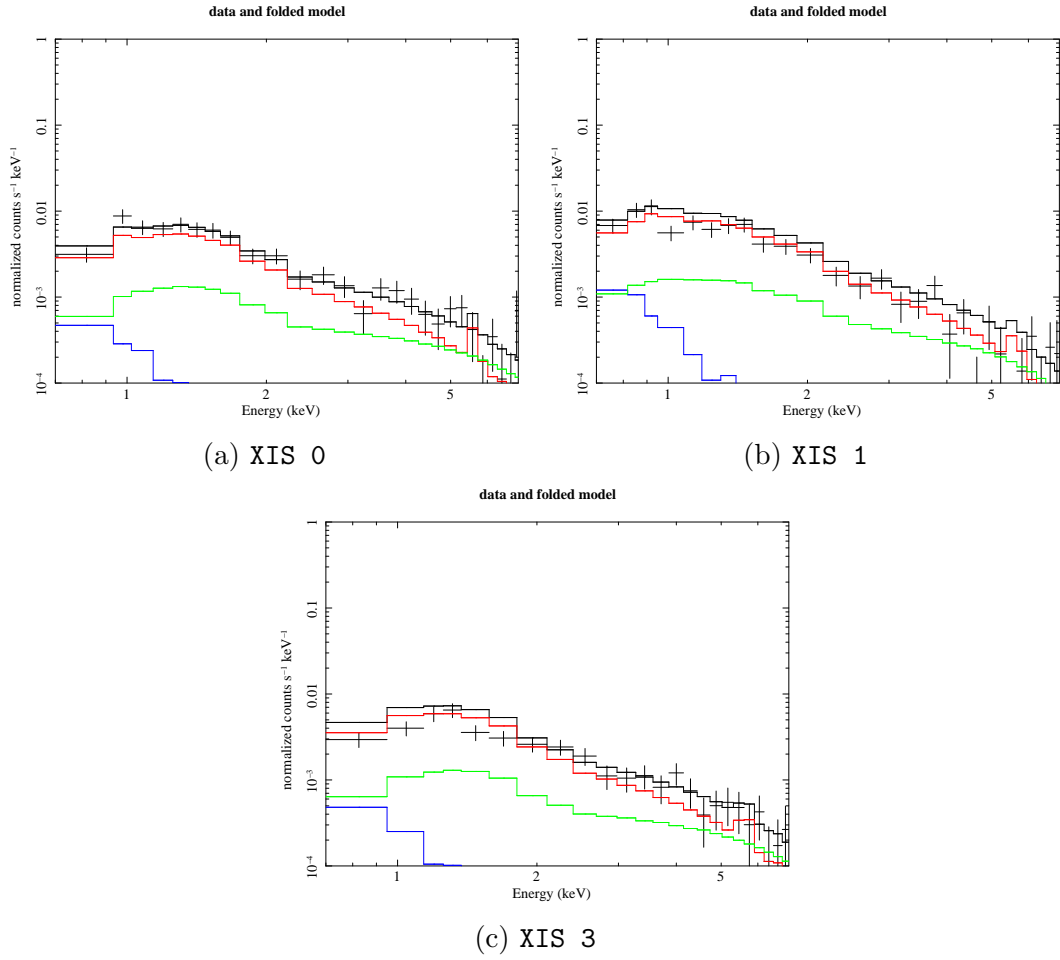
Figure A.65: The spectral fits for Annulus 2 (refer Table 3.1) of Abell 383 for the third pointing

(a) XIS 0

(b) XIS 1

(c) XIS 3
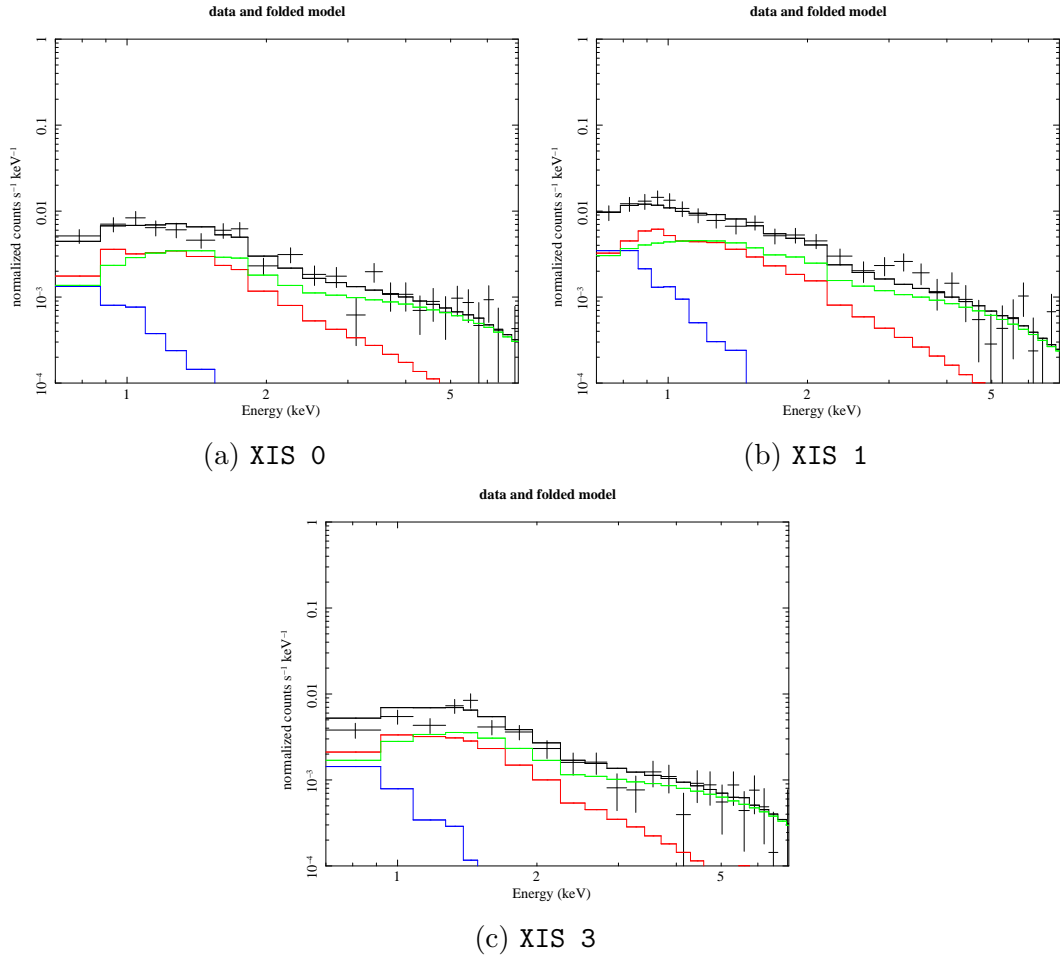
Figure A.66: The spectral fits for Annulus 3 (refer Table 3.1) of Abell 383 for the first pointing

(a) XIS 0

(b) XIS 1

(c) XIS 3
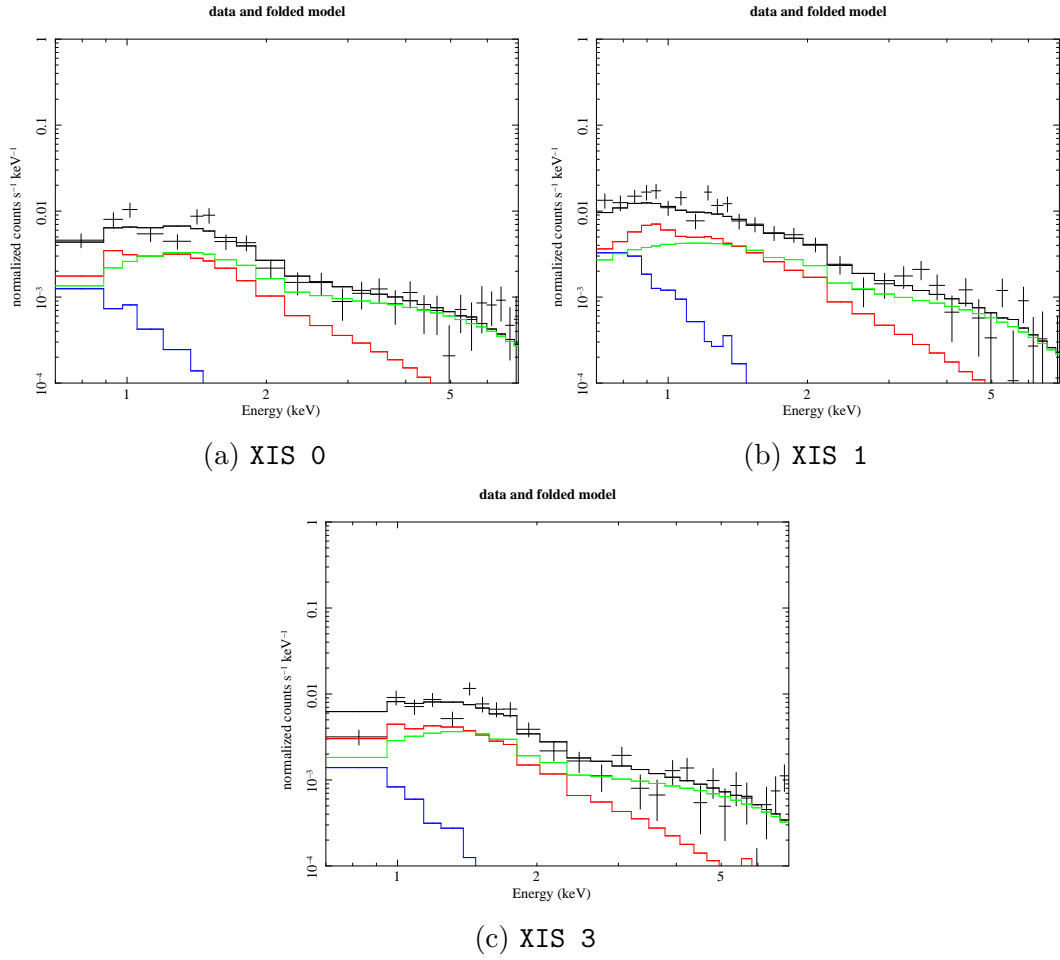
Figure A.67: The spectral fits for Annulus 3 (refer Table 3.1) of Abell 383 for the second pointing

159

(a) XIS 0

(b) XIS 1

(c) XIS 3
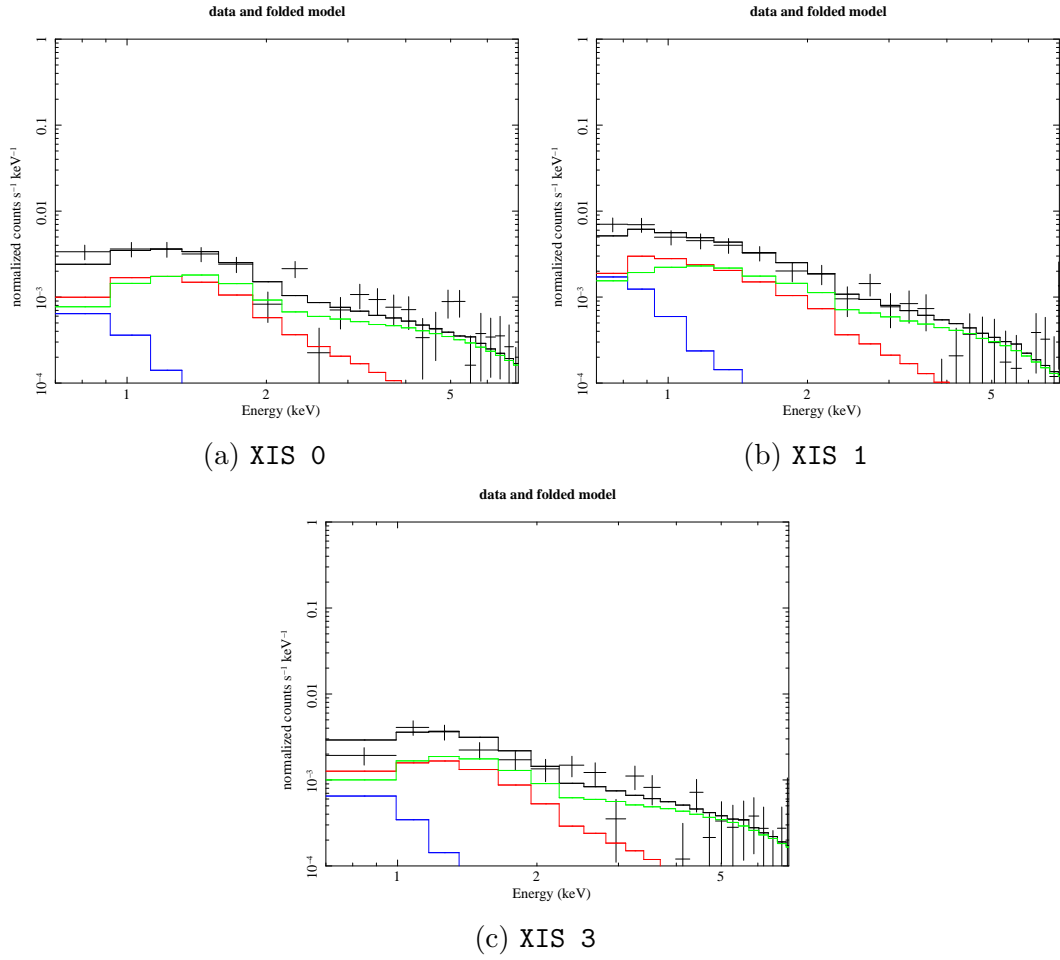
Figure A.68: The spectral fits for Annulus 3 (refer Table 3.1) of Abell 383 for the third pointing

160

(a) XIS 0

(b) XIS 1

(c) XIS 3
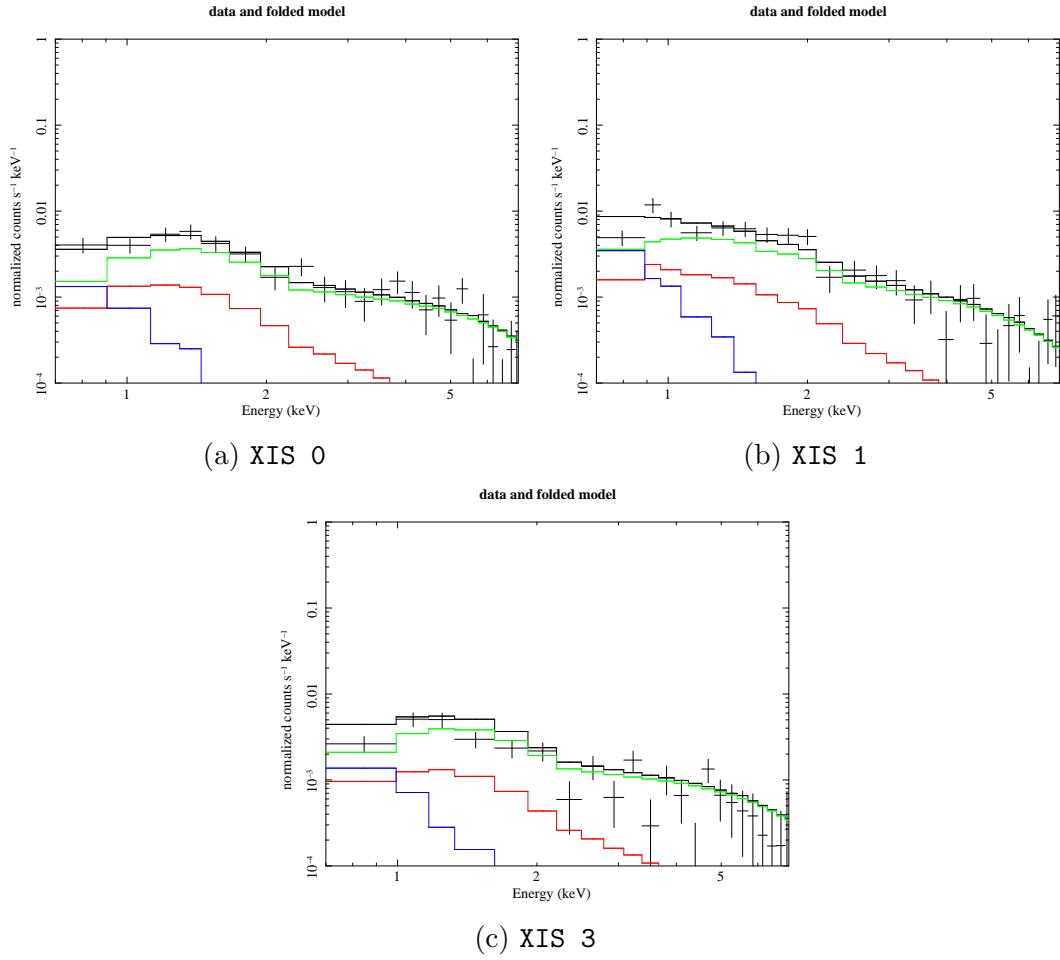
Figure A.69: The spectral fits for Annulus 4 (refer Table 3.1) of Abell 383 for the first pointing

(a) XIS 0   (b) XIS 1

(c) XIS 3
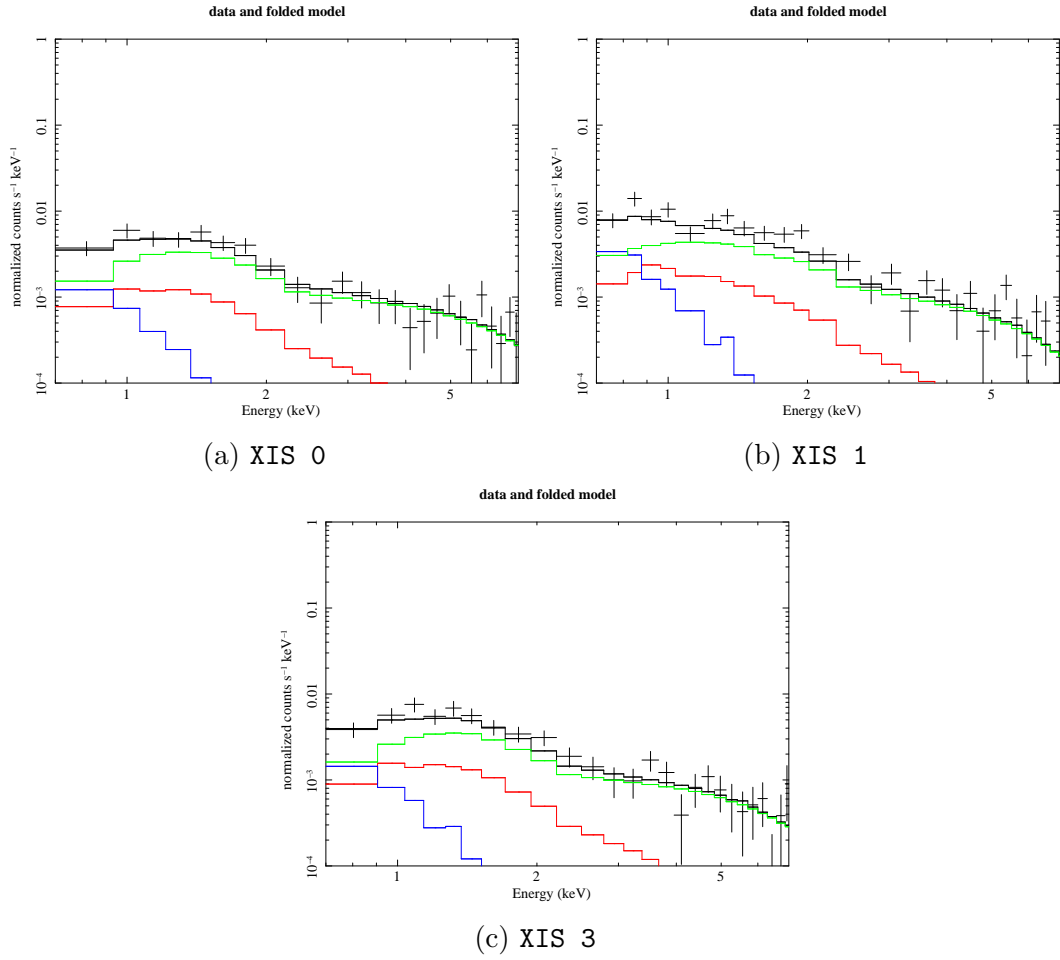
Figure A.70: The spectral fits for Annulus 4 (refer Table 3.1) of Abell 383 for the second pointing

(a) XIS 0

(b) XIS 1

(c) XIS 3
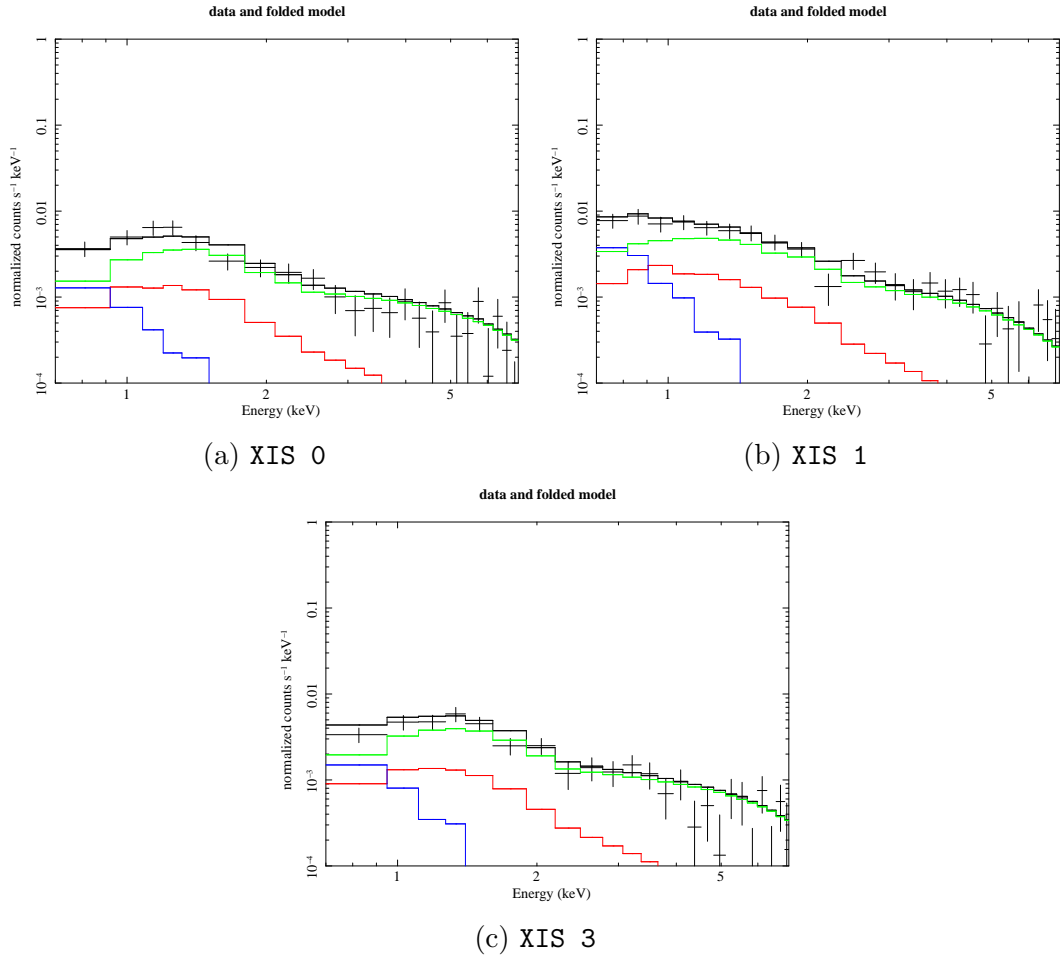
Figure A.71: The spectral fits for Annulus 4 (refer Table 3.1) of Abell 383 for the third pointing

(a) XIS 0

(b) XIS 1

(c) XIS 3
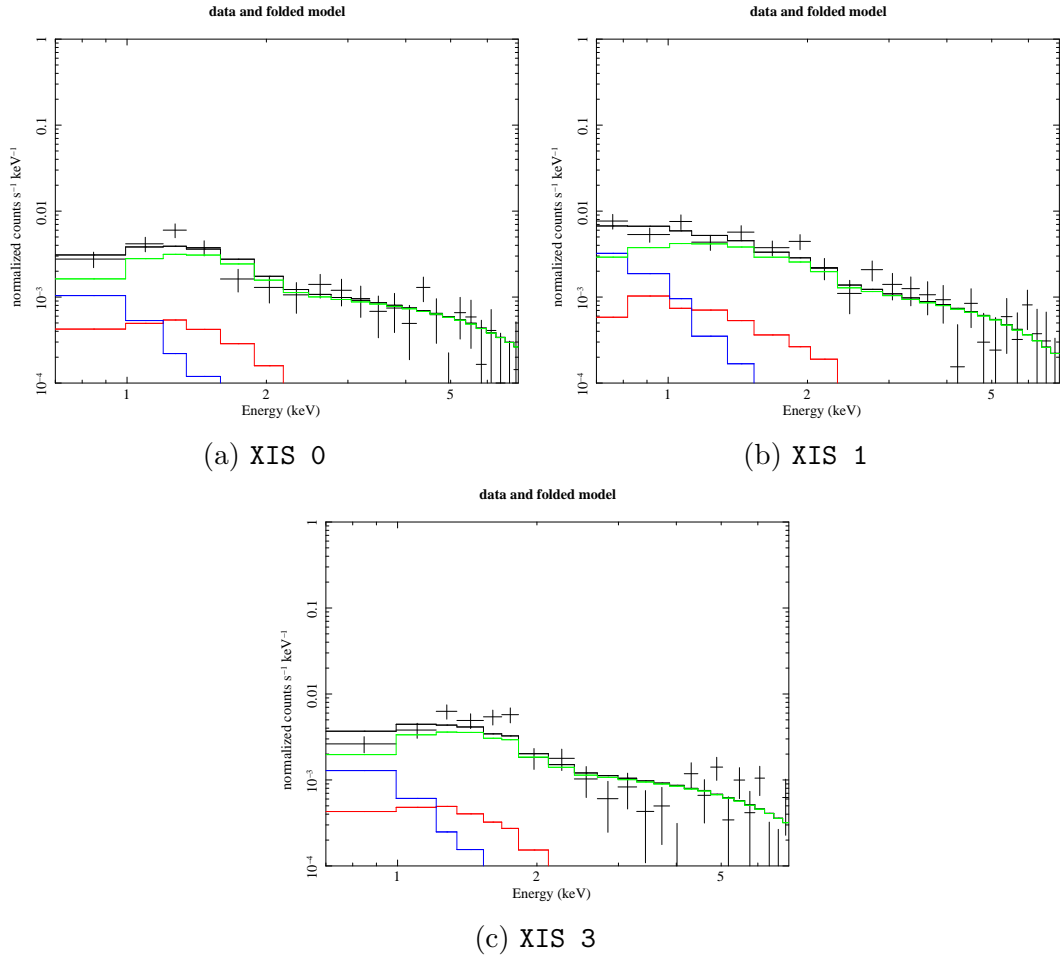
Figure A.72: The spectral fits for Annulus 5 (refer Table 3.1) of Abell 383 for the first pointing

(a) XIS 0

(b) XIS 1

(c) XIS 3
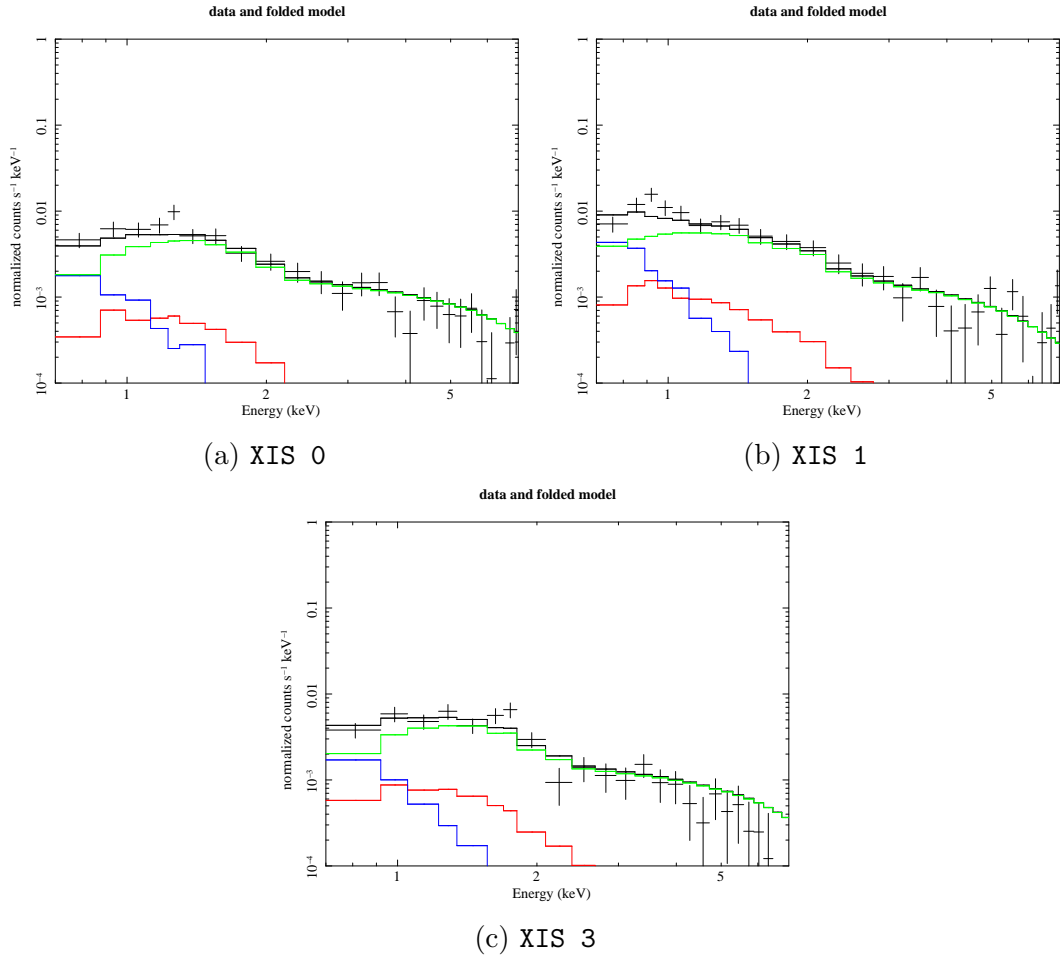
Figure A.73: The spectral fits for Annulus 5 (refer Table 3.1) of Abell 383 for the second pointing

data and folded model

(a) XIS 0

data and folded model

(b) XIS 1

data and folded model

(c) XIS 3
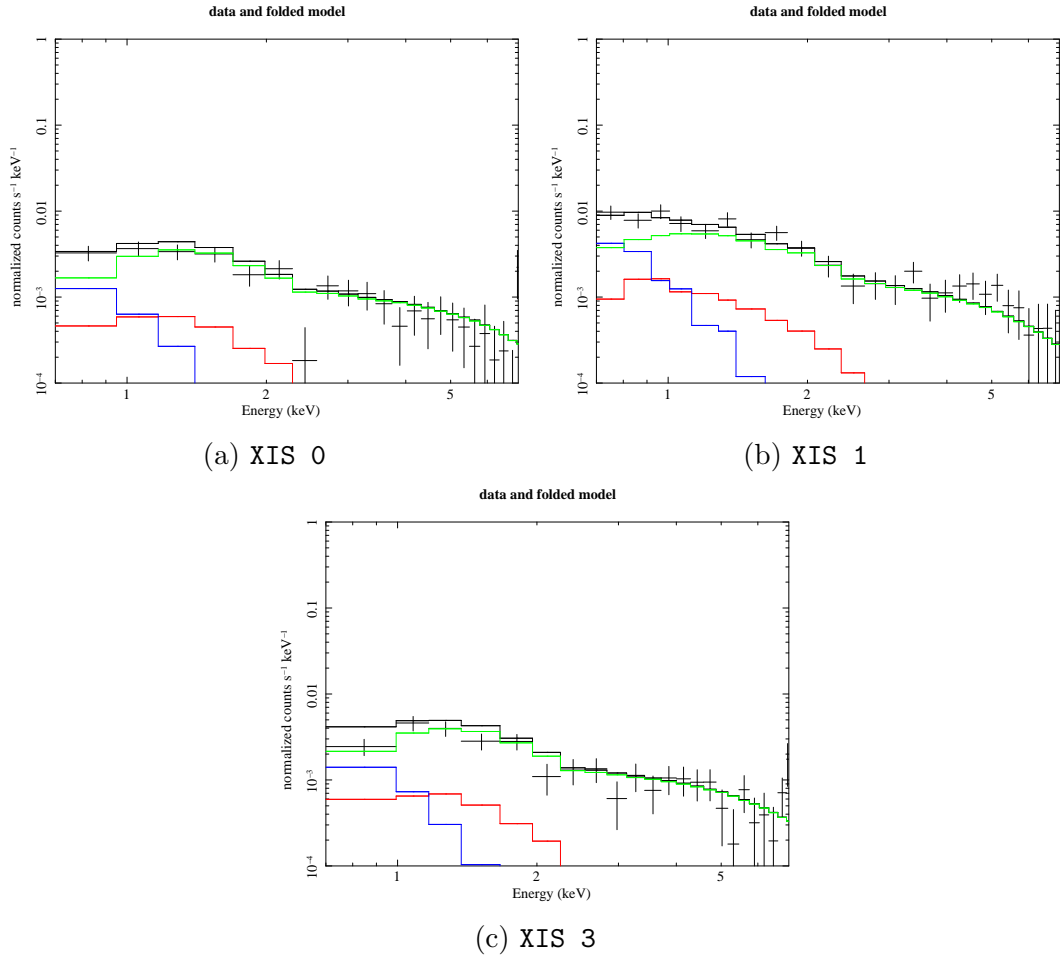
Figure A.74: The spectral fits for Annulus 5 (refer Table 3.1) of Abell 383 for the third pointing

Bibliography

S. L. Snowden, R. F. Mushotzky, K. D. Kuntz, and D. S. Davis. A catalog of galaxy clusters observed by XMM-Newton. *Astronomy & Astrophysics*, 478:615–658, February 2008. doi: 10.1051/0004-6361:20077930.

S. A. Walker, A. C. Fabian, J. S. Sanders, and M. R. George. Galaxy cluster outskirts: a universal entropy profile for relaxed clusters? *Monthly Notices of the Royal Astronomical Society*, 427:L45–L49, November 2012a. doi: 10.1111/j.1745-3933.2012.01342.x.

A. Simionescu, S. W. Allen, A. Mantz, N. Werner, and Y. Takei. Baryons in the outskirts of the X-ray brightest galaxy cluster. In R. Petre, K. Mitsuda, and L. Angelini, editors, *American Institute of Physics Conference Series*, volume 1427 of *American Institute of Physics Conference Series*, pages 5–12, March 2012. doi: 10.1063/1.3696143.

S. W. Allen, A. E. Evrard, and A. B. Mantz. Cosmological Parameters from Observations of Galaxy Clusters. *Annual Review of Astronomy and Astrophysics*, 49: 409–470, September 2011. doi: 10.1146/annurev-astro-081710-102514.

C. L. Sarazin. *X-ray emission from clusters of galaxies*. Cambridge University Press, 1988.

A. Vikhlinin, A. Kravtsov, W. Forman, C. Jones, M. Markevitch, S. S. Murray, and L. Van Speybroeck. Chandra Sample of Nearby Relaxed Galaxy Clusters: Mass, Gas Fraction, and Mass-Temperature Relation. *Astrophysical Journal*, 640: 691–709, April 2006. doi: 10.1086/500288.

C. L. Sarazin. X-ray emission from clusters of galaxies. *Reviews of Modern Physics*, 58:1–115, January 1986. doi: 10.1103/RevModPhys.58.1.

P. Tozzi and C. Norman. The Evolution of X-Ray Clusters and the Entropy of the Intracluster Medium. *Astrophysical Journal*, 546:63–84, January 2001. doi: 10.1086/318237.

G. M. Voit, S. T. Kay, and G. L. Bryan. The baseline intracluster entropy profile from gravitational structure formation. *Monthly Notices of the Royal Astronomical Society*, 364:909–916, December 2005. doi: 10.1111/j.1365-2966.2005.09621.x.

G. W. Pratt, M. Arnaud, R. Piffaretti, H. Böhringer, T. J. Ponman, J. H. Croston, G. M. Voit, S. Borgani, and R. G. Bower. Gas entropy in a representative sample of nearby X-ray galaxy clusters (REXCESS): relationship to gas mass fraction. *Astronomy & Astrophysics*, 511:A85, February 2010. doi: 10.1051/0004-6361/200913309.

A. Hoshino, J. P. Henry, K. Sato, H. Akamatsu, W. Yokota, S. Sasaki, Y. Ishisaki, T. Ohashi, M. Bautz, Y. Fukazawa, N. Kawano, A. Furuzawa, K. Hayashida, N. Tawa, J. P. Hughes, M. Kokubun, and T. Tamura. X-Ray Temperature and Mass Measurements to the Virial Radius of Abell 1413 with Suzaku. *Publications of the Astronomical Society of Japan*, 62:371–389, April 2010.

D. H. Rudd and D. Nagai. Nonequilibrium Electrons and the Sunyaev-Zel'Dovich Effect of Galaxy Clusters. *Astrophysical Journal Letters*, 701:L16–L19, August 2009. doi: 10.1088/0004-637X/701/1/L16.

A. Cavaliere, A. Lapi, and R. Fusco-Femiano. A Grand Design for Galaxy Clusters: Connections and Predictions. *Astrophysical Journal*, 742:19, November 2011. doi: 10.1088/0004-637X/742/1/19.

A. Lapi, R. Fusco-Femiano, and A. Cavaliere. Probing the astrophysics of cluster outskirts. *Astronomy & Astrophysics*, 516:A34, June 2010. doi: 10.1051/0004-6361/201014218.

E. T. Lau, A. V. Kravtsov, and D. Nagai. Residual Gas Motions in the Intracluster Medium and Bias in Hydrostatic Measurements of Mass Profiles of Clusters. *Astrophysical Journal*, 705:1129–1138, November 2009. doi: 10.1088/0004-637X/705/2/1129.

D. Nagai and E. T. Lau. Gas Clumping in the Outskirts of ΛCDM Clusters. *Astrophysical Journal Letters*, 731:L10, April 2011. doi: 10.1088/2041-8205/731/1/L10.

M. Takizawa and S. Mineshige. Evolution of X-Ray Clusters of Galaxies and Shock Heating of the Intracluster Medium. *Astrophysical Journal*, 499:82, May 1998. doi: 10.1086/305598.

T. H. Reiprich, K. Basu, S. Ettori, H. Israel, L. Lovisari, S. Molendi, E. Pointecouteau, and M. Roncarelli. Outskirts of Galaxy Clusters. *Space Science Reviews*, 177:195–245, August 2013. doi: 10.1007/s11214-013-9983-8.

A. Vikhlinin, W. Forman, and C. Jones. Outer Regions of the Cluster Gaseous Atmospheres. *Astrophysical Journal*, 525:47–57, November 1999. doi: 10.1086/307876.

D. M. Neumann. Tracing the X-ray emitting intra-cluster medium of clusters of galaxies beyond r$_{200}$. *Astronomy & Astrophysics*, 439:465–477, August 2005. doi: 10.1051/0004-6361:20053015.

M. Roncarelli, S. Ettori, K. Dolag, L. Moscardini, S. Borgani, and G. Murante. Simulated X-ray galaxy clusters at the virial radius: Slopes of the gas density, temperature and surface brightness profiles. *Monthly Notices of the Royal Astronomical Society*, 373:1339–1350, December 2006. doi: 10.1111/j.1365-2966.2006.11143.x.

D. Eckert, F. Vazza, S. Ettori, S. Molendi, D. Nagai, E. T. Lau, M. Roncarelli, M. Rossetti, S. L. Snowden, and F. Gastaldello. The gas distribution in the outer regions of galaxy clusters. *Astronomy & Astrophysics*, 541:A57, May 2012. doi: 10.1051/0004-6361/201118281.

M. Markevitch, W. R. Forman, C. L. Sarazin, and A. Vikhlinin. The Temperature Structure of 30 Nearby Clusters Observed with ASCA: Similarity of Temperature Profiles. *Astrophysical Journal*, 503:77–96, August 1998. doi: 10.1086/305976.

J. A. Irwin and J. N. Bregman. Radial Temperature Profiles of 11 Clusters of Galaxies Observed with BEPPOSAX. *Astrophysical Journal*, 538:543–554, August 2000. doi: 10.1086/309148.

S. W. Allen, R. W. Schmidt, and A. C. Fabian. The X-ray virial relations for relaxed lensing clusters observed with Chandra. *Monthly Notices of the Royal Astronomical Society*, 328:L37–L41, December 2001. doi: 10.1046/j.1365-8711.2001.05079.x.

G. W. Pratt, J. H. Croston, M. Arnaud, and H. Böhringer. Galaxy cluster X-ray luminosity scaling relations from a representative local sample (REXCESS). *Astronomy & Astrophysics*, 498:361–378, May 2009. doi: 10.1051/0004-6361/200810994.

D. Nagai, A. V. Kravtsov, and A. Vikhlinin. Effects of Galaxy Formation on Thermodynamics of the Intracluster Medium. *Astrophysical Journal*, 668:1–14, October 2007a. doi: 10.1086/521328.

Planck Collaboration, P. A. R. Ade, N. Aghanim, M. Arnaud, M. Ashdown, F. Atrio-Barandela, J. Aumont, C. Baccigalupi, A. Balbi, A. J. Banday, and et al. Planck intermediate results. V. Pressure profiles of galaxy clusters from the Sunyaev-Zeldovich effect. *Astronomy & Astrophysics*, 550:A131, February 2013a. doi: 10.1051/0004-6361/201220040.

T. H. Reiprich. *An X-Ray Flux-Limited Sample of Galaxy Clusters: Physical Properties and Cosmological Implications*. PhD thesis, Max-Planck-Institut für extraterrestrische Physik, P.O. Box 1312, Garching bei München, Germany, July 2001.

M. R. George, A. C. Fabian, J. S. Sanders, A. J. Young, and H. R. Russell. X-ray observations of the galaxy cluster PKS0745-191: to the virial radius, and beyond. *Monthly Notices of the Royal Astronomical Society*, 395:657–666, May 2009. doi: 10.1111/j.1365-2966.2009.14547.x.

S. A. Walker, A. C. Fabian, J. S. Sanders, and M. R. George. Further X-ray observations of the galaxy cluster PKS 0745-191 to the virial radius and beyond. *Monthly Notices of the Royal Astronomical Society*, 424:1826–1840, August 2012b. doi: 10.1111/j.1365-2966.2012.21282.x.

T. H. Reiprich, D. S. Hudson, Y.-Y. Zhang, K. Sato, Y. Ishisaki, A. Hoshino, T. Ohashi, N. Ota, and Y. Fujita. Suzaku measurement of Abell 2204's intracluster gas temperature profile out to 1800 kpc. *Astronomy & Astrophysics*, 501: 899–905, July 2009. doi: 10.1051/0004-6361/200810404.

M. W. Bautz, E. D. Miller, J. S. Sanders, K. A. Arnaud, R. F. Mushotzky, F. S. Porter, K. Hayashida, J. P. Henry, J. P. Hughes, M. Kawaharada, K. Makashima, M. Sato, and T. Tamura. Suzaku Observations of Abell 1795: Cluster Emission to r_{200}. *Publications of the Astronomical Society of Japan*, 61:1117–, October 2009. doi: 10.1093/pasj/61.5.1117.

M. Kawaharada, N. Okabe, K. Umetsu, M. Takizawa, K. Matsushita, Y. Fukazawa, T. Hamana, S. Miyazaki, K. Nakazawa, and T. Ohashi. Suzaku Observation of A1689: Anisotropic Temperature and Entropy Distributions Associated with the Large-scale Structure. *Astrophysical Journal*, 714:423–441, May 2010. doi: 10.1088/0004-637X/714/1/423.

H. Akamatsu, A. Hoshino, Y. Ishisaki, T. Ohashi, K. Sato, Y. Takei, and N. Ota. X-Ray Study of the Outer Region of Abell 2142 with Suzaku. *Publications of the Astronomical Society of Japan*, 63:1019, November 2011. doi: 10.1093/pasj/63.sp3.S1019.

T. Sato, T. Sasaki, K. Matsushita, E. Sakuma, K. Sato, Y. Fujita, N. Okabe, Y. Fukazawa, K. Ichikawa, M. Kawaharada, K. Nakazawa, T. Ohashi, N. Ota, M. Takizawa, and T. Tamura. Suzaku Observations of the Hydra A Cluster out to the Virial Radius. *Publications of the Astronomical Society of Japan*, 64:95, October 2012. doi: 10.1093/pasj/64.5.95.

S. A. Walker, A. C. Fabian, J. S. Sanders, M. R. George, and Y. Tawara. X-ray observations of the galaxy cluster Abell 2029 to the virial radius. *Monthly Notices of the Royal Astronomical Society*, 422:3503–3515, June 2012c. doi: 10.1111/j.1365-2966.2012.20860.x.

S. A. Walker, A. C. Fabian, J. S. Sanders, A. Simionescu, and Y. Tawara. X-ray exploration of the outskirts of the nearby Centaurus cluster using Suzaku and Chandra. *Monthly Notices of the Royal Astronomical Society*, 432:554–569, June 2013. doi: 10.1093/mnras/stt497.

A. Simionescu, N. Werner, O. Urban, S. W. Allen, A. C. Fabian, A. Mantz, K. Matsushita, P. E. J. Nulsen, J. S. Sanders, T. Sasaki, T. Sato, Y. Takei, and S. A. Walker. Thermodynamics of the Coma Cluster Outskirts. *ArXiv e-prints*, February 2013.

P. J. Humphrey, D. A. Buote, F. Brighenti, H. M. L. G. Flohic, F. Gastaldello, and W. G. Mathews. Tracing the Gas to the Virial Radius (R $_{100}$) in a Fossil Group. *Astrophysical Journal*, 748:11, March 2012. doi: 10.1088/0004-637X/748/1/11.

A. H. Gonzalez, S. Sivanandam, A. I. Zabludoff, and D. Zaritsky. Galaxy Cluster Baryon Fractions Revisited. *Astrophysical Journal*, 778:14, November 2013. doi: 10.1088/0004-637X/778/1/14.

X. Dai, J. N. Bregman, C. S. Kochanek, and E. Rasia. On the Baryon Fractions in Clusters and Groups of Galaxies. *Astrophysical Journal*, 719:119–125, August 2010. doi: 10.1088/0004-637X/719/1/119.

K. Koyama, H. Tsunemi, T. Dotani, M. W. Bautz, K. Hayashida, T. G. Tsuru, H. Matsumoto, Y. Ogawara, G. R. Ricker, J. Doty, S. E. Kissel, R. Foster, H. Nakajima, H. Yamaguchi, H. Mori, M. Sakano, K. Hamaguchi, M. Nishi-uchi, E. Miyata, K. Torii, M. Namiki, S. Katsuda, D. Matsuura, T. Miyauchi, N. Anabuki, N. Tawa, M. Ozaki, H. Murakami, Y. Maeda, Y. Ichikawa, G. Y. Prigozhin, E. A. Boughan, B. Lamarr, E. D. Miller, B. E. Burke, J. A. Gregory, A. Pillsbury, A. Bamba, J. S. Hiraga, A. Senda, H. Katayama, S. Kitamoto, M. Tsujimoto, T. Kohmura, Y. Tsuboi, and H. Awaki. X-Ray Imaging Spectrometer (XIS) on Board Suzaku. *Publications of the Astronomical Society of Japan*, 59:23–33, January 2007. doi: 10.1093/pasj/59.sp1.S23.

J. P. Henry, A. E. Evrard, H. Hoekstra, A. Babul, and A. Mahdavi. The X-Ray Cluster Normalization of the Matter Power Spectrum. *Astrophysical Journal*, 691: 1307–1321, February 2009. doi: 10.1088/0004-637X/691/2/1307.

A. Cavaliere and R. Fusco-Femiano. The Distribution of Hot Gas in Clusters of Galaxies. *Astronomy & Astrophysics*, 70:677, November 1978.

N. Grevesse and E. Anders. Solar-system abundances of the elements - A new table. In C. J. Waddington, editor, *Cosmic Abundances of Matter*, volume 183 of *American Institute of Physics Conference Series*, pages 1–8, 1989. doi: 10.1063/1.38013.

A. Moretti, S. Campana, D. Lazzati, and G. Tagliaferri. The Resolved Fraction of the Cosmic X-Ray Background. *Astrophysical Journal*, 588:696–703, May 2003. doi: 10.1086/374335.

K. D. Kuntz and S. L. Snowden. On the Contribution of Unresolved Galactic Stars to the Diffuse Soft X-Ray Background. *Astrophysical Journal*, 554:684–693, June 2001. doi: 10.1086/321421.

R. K. Smith, N. S. Brickhouse, D. A. Liedahl, and J. C. Raymond. Collisional Plasma Models with APEC/APED: Emission-Line Diagnostics of Hydrogen-like and Helium-like Ions. *Astrophysical Journal Letters*, 556:L91–L95, August 2001. doi: 10.1086/322992.

T. Yoshino, K. Mitsuda, N. Y. Yamasaki, Y. Takei, T. Hagihara, K. Masui, M. Bauer, D. McCammon, R. Fujimoto, Q. D. Wang, and Y. Yao. Energy Spectra of the Soft X-Ray Diffuse Emission in Fourteen Fields Observed with Suzaku. *Publications of the Astronomical Society of Japan*, 61:805–, August 2009. doi: 10.1093/pasj/61.4.805.

K. Jahoda, P. J. Serlemitsos, K. A. Arnaud, E. Boldt, S. Holt, F. E. Marshall, R. F. Mushotzky, R. Petre, W. T. Sanders, A. Smale, J. Swank, A. Szymkowiak, K. Weaver, and S. Yamauchi. BBXRT Observations of DXRB - First Results. In X. Barcons and A. C. Fabian, editors, *The X-ray Background*, page 240, 1992.

K. C. Gendreau, R. Mushotzky, A. C. Fabian, S. S. Holt, T. Kii, P. J. Serlemitsos, Y. Ogasaka, Y. Tanaka, M. W. Bautz, Y. Fukazawa, Y. Ishisaki, Y. Kohmura, K. Makishima, M. Tashiro, Y. Tsusaka, H. Kunieda, G. R. Ricker, and R. K. Vanderspek. ASCA Observations of the Spectrum of the X-Ray Background. *Publications of the Astronomical Society of Japan*, 47:L5–L9, April 1995.

R. V. Vasudevan, R. F. Mushotzky, and P. Gandhi. Can We Reproduce the X-Ray Background Spectral Shape Using Local Active Galactic Nuclei? *Astrophysical Journal Letters*, 770:L37, June 2013. doi: 10.1088/2041-8205/770/2/L37.

G. Schellenberger, T. H. Reiprich, L. Lovisari, J. Nevalainen, and L. David. XMM-Newton and Chandra Cross Calibration Using HIFLUGCS Galaxy Clusters. *ArXiv e-prints*, April 2014.

D. Davis. Abell 2204 xmm-newton analysis. Private Communication, 2013.

E. Anders and N. Grevesse. Abundances of the elements - Meteoritic and solar. *Geochimica et Cosmochimica Acta*, 53:197–214, January 1989. doi: 10.1016/0016-7037(89)90286-X.

D. Nagai, A. Vikhlinin, and A. V. Kravtsov. Testing X-Ray Measurements of Galaxy Clusters with Cosmological Simulations. *Astrophysical Journal*, 655:98–108, January 2007b. doi: 10.1086/509868.

E. Pointecouteau, M. Arnaud, J. Kaastra, and J. de Plaa. XMM-Newton observation of the relaxed cluster A478: Gas and dark matter distribution from $0.01R_{200}$ to $0.5R_{200}$. *Astronomy & Astrophysics*, 423:33–47, August 2004. doi: 10.1051/0004-6361:20035856.

J. F. Navarro, C. S. Frenk, and S. D. M. White. A Universal Density Profile from Hierarchical Clustering. *Astrophysical Journal*, 490:493, December 1997. doi: 10.1086/304888.

S. Ettori, F. Gastaldello, A. Leccardi, S. Molendi, M. Rossetti, D. Buote, and M. Meneghetti. Mass profiles and c-M_{DM} relation in X-ray luminous galaxy clusters. *Astronomy & Astrophysics*, 524:A68, December 2010. doi: 10.1051/0004-6361/201015271.

J. S. Sanders, A. C. Fabian, and G. B. Taylor. Giant cavities, cooling and metallicity substructure in Abell 2204. *Monthly Notices of the Royal Astronomical Society*, 393:71–82, February 2009. doi: 10.1111/j.1365-2966.2008.14207.x.

Planck Collaboration, P. A. R. Ade, N. Aghanim, C. Armitage-Caplan, M. Arnaud, M. Ashdown, F. Atrio-Barandela, J. Aumont, H. Aussel, C. Baccigalupi, and et al. Planck 2013 results. XXIX. Planck catalogue of Sunyaev-Zeldovich sources. *ArXiv e-prints*, March 2013b.

M. Arnaud, G. W. Pratt, R. Piffaretti, H. Böhringer, J. H. Croston, and E. Pointe-couteau. The universal galaxy cluster pressure profile from a representative sample of nearby systems (REXCESS) and the Y$_{SZ}$ - M$_{500}$ relation. *Astronomy & Astrophysics*, 517:A92, July 2010. doi: 10.1051/0004-6361/200913416.

D. Eckert, S. Ettori, S. Molendi, F. Vazza, and S. Paltani. The X-ray/SZ view of the virial region. II. Gas mass fraction. *Astronomy & Astrophysics*, 551:A23, March 2013. doi: 10.1051/0004-6361/201220403.

O. Urban, N. Werner, A. Simionescu, S. W. Allen, and H. Böhringer. X-ray spectroscopy of the Virgo Cluster out to the virial radius. *Monthly Notices of the Royal Astronomical Society*, 414:2101–2111, July 2011. doi: 10.1111/j.1365-2966.2011.18526.x.